Strengthening of cold-formed steel channels using different reinforcing options and innovative connections

Wei Wang

(*Email:* ww210@students.waikato.ac.nz)

Supervised by

Chief supervisor: Dr Krishanu Roy

Co-supervisors: Prof. James B.P. Lim,

Dr Arthur Fang,

Dr Hooman Rezaeian,

Dr Beulah Gnana Ananthi. G.

A thesis submitted in partial fulfilment of the requirements for the degree of Doctor of Philosophy in Engineering, The University of Waikato, 2026

To
my parents
&
my wife

Abstract

Cold-formed steel (CFS) has become an essential material in modern construction due to its lightweight, cost-effectiveness, and versatility. This study primarily investigated the web crippling capacity of channels with elongated edge-stiffened web holes. Compared to traditional circular edge-stiffened web holes, these elongated holes accommodate larger electrical conduits and water supply systems. The new Direct Strength Method (DSM) was developed to accurately predict their web crippling strength.

In addition, this research explored key advancements in CFS systems, including built-up box sections and trusses equipped with advanced Howick Rivet Connectors (HRCs). These high-performance connectors have demonstrated superior performance, providing greater connection strength than traditional self-drilling screws and better ductility than bolted connections. In this study, HRCs were utilized in truss systems and built-up box sections, offering critical data to support their practical application in engineering projects.

Furthermore, axial tests on telescopic studs and swaged sections were conducted to address installation challenges commonly encountered in real-world scenarios. Through experimental studies, numerical simulations, and parametric analyses, this research enhances the understanding of these systems, paving the way for more reliable and efficient applications in structural engineering. The findings are synthesized to highlight their implications and provide recommendations for integrating these insights into international design standards.

By bridging critical knowledge gaps, this thesis contributes to the broader adoption of advanced CFS systems in construction, fostering innovation, sustainability, and efficiency in structural design.

Preface

This thesis is submitted to the University of Waikato, New Zealand in fulfilment of the requirement for the degree of Doctor of Philosophy. The work contained in this thesis has not been previously submitted for a degree or diploma in any other higher educational institution. To the best of my knowledge and belief, the thesis contains no material previously published or written by another person except where due reference is made.

Publications

Journals

1. **Wang, W**., Roy, K., Rezaeian, H., Fang, Z., & Lim, J.B.P. (2025) Moment capacity of cold-formed steel trusses with Howick Rivet Connectors: Tests, modelling and design. Engineering Structures. (JCR Q1, Published)
2. **Wang, W**., Roy, K., Fang, Z., Ananthi. G.B.G., & Lim, J.B.P. (2023) Web crippling behaviour of cold-formed steel channel sections having elongated edge-stiffened web holes under interior-two-flange loading condition. Engineering Structures. (JCR Q1, Published)
3. **Wang, W**., Roy, K., Ananthi G.B.G., Lu, L., Fang, Z., & Lim, J.B.P. (2024) Simplified Direct Strength Method for the design of cold-formed steel channels with circular web openings under two-flange loadings. Engineering Structures. (JCR Q1, Published)
4. **Wang, W**., Roy, K., Fang, Z., Ananthi. G.B.G., & Lim, J.B.P. (2024) Web crippling behaviour of cold-formed steel channels with elongated un-stiffened and edge-stiffened web holes under end-two-flange loading condition. Thin-Walled Structures. (JCR Q1, Published)
5. **Wang, W**., Roy, K., Rezaeian, H. Kang H., Shubham T., & Lim, J.B.P. (2025) Experimental investigation and new design method for cold-formed steel built-up box columns with Howick Rivet Connectors. Thin-Walled Structures, (JCR Q1, Published)
6. **Wang, W**., Roy, K., Rezaeian, H., Fang, Z., & Lim, J.B.P. (2024) Experimental and numerical investigation of cold-formed steel telescopic studs under compression. Journal of Constructional Steel Research. (JCR Q1, Published)

7. **Wang, W**., Rezaeian, H., Roy, K., Fang, Z., & Lim, J.B.P. (2024) Axial capacity of a novel cold-formed steel swaged section: Experimental tests and design. Journal of Building Engineering. (JCR Q1，Published)
8. **Wang, W**., Roy, K., Rezaeian, H., & Lim, J.B.P. (2026) Structural behavior of cold-formed steel trusses incorporating built-up section chords. Thin-Walled Structures, (JCR Q1，Published)
9. **Wang, W**., Roy, K., Rezaeian, H & Lim, J.B.P. (2025) Experimental and numerical investigation of the axial load capacity in cold-formed steel studs featuring swaged sections. Structures, (JCR Q1，Published)
10. **Wang, W**., Roy, K., Ma R., Lu, L., Xie, Z., & Lim, J.B.P. (2026) Design recommendations for Howick Rivet Connectors in cold-formed steel connections. Journal of Constructional Steel Research. (JCR Q1，Published)
11. **Wang, W**., Roy, K., Fang, Z., Ananthi. G.B.G., & Lim, J.B.P. Web crippling capacity of CFS channels with elongated edge-stiffened web holes under one-flange loading. International Journal of Steel structure, (JCR Q3，Under Review)

Acknowledgements

I am profoundly grateful to my chief supervisor, Dr. Krishanu Roy, and my co-supervisors Prof. James B.P. Lim, Dr. Arthur Fang, Dr. Hooman Rezaeian, and Assoc. Prof. Beulah Gnana Ananthi. G., for their unwavering support, invaluable guidance, and expertise throughout my Ph.D. journey. Their encouragement has been instrumental in shaping the direction and quality of this research.

My sincere thanks go to my lab mates for their encouragement, collaboration, and support, which made this journey both productive and fulfilling.

I am deeply grateful to the China Scholarship Council of the Chinese government for their financial support, which allowed me to dedicate myself fully to my research.

Lastly, I wish to express my enduring gratitude to my parents for their unwavering belief in me and to my beloved girlfriend, Miss Huan Zhang, for her boundless love and encouragement. Their support and faith sustained me through the challenges and triumphs of this journey. This thesis is a testament to their enduring presence in my life.

Table of contents

List of Figures

List of Tables

Notations

E	Young's modulus
b_f	Overall flange width of section
b_l	Overall lip width of section
R_P	Web crippling strength reduction factor
R_{FEA}	Reduction factor predicted based on the results of finite element analysis
f_y	Yield strength
L	Specimen length
d	Overall web depth of the section;
d_1	Depth of the flat portion of the web;
d_w	Width of the elongated web holes
b_w	Length of the elongated web holes
N	Bearing plate lengths
q	Length of edge-stiffener
r_q	Inside fillet radius between web and hole edge-stiffener
t	Thickness of the section
Q	Ratio of the stiffener length to the depth of the flat portion of the web
D	Ratio of width of hole to depth of web
B	Aspect ratio of web hole
P_{EXP}	Experimental ultimate web crippling load
P_{FEA}	Web crippling strength predicted based on the results of finite element analysis
COV	Coefficient of variation
$P_{b,cr}$	Critical buckling load
$P_{b,y}$	Yield load
k	Critical buckling coefficient
r_m	Inside fillet radius from mid-thickness line
r_i	Inside fillet radius of section
N_m	Yield mechanism length
β	Reliability index
ϕ	Resistance factor

Chapter 1 Introduction

1.1. Background and problem statement

Cold-formed steel (CFS) channels are increasingly popular in the construction industry used as beams, floor joists, studs, purlins and other components due to their numerous advantages, including a high strength-to-weight ratio, durability, sustainability, and easy installation on site. Figure 1-1 shows the manufacturing process of CFS channels.

In residential and industrial construction, CFS channels often require web holes (see Figure 1-2) to allow services for piping, electric-wiring, and plumbing(Yu, 2012). The presence of web holes in CFS channels will cause changes in the stress distribution and consequently, there will be changes in the buckling characteristics and ultimate strength. However, such web holes will become more susceptible to web crippling failure (see Figure 1-3), particularly in the vicinity of a concentrated force (Uzzaman et al., 2020b), which need to be carefully evaluated when such CFS members are used in floor joists.

In recent years, a new generation of CFS channels with edge-stiffened web holes has been developed by the Howick Ltd. (2013) in New Zealand. As can be seen from Figure 1-4, the web holes are strengthened through a continuous lip around the web hole. It should be noted that traditional holes are normally flat punched without the edge. Such CFS channels with edge-stiffened web holes still provide services to be integrated within the floors, but significantly enhancing their web crippling bearing capacity. Notably, those channels are typically designed with nominal diameters of 90 mm and 140 mm. The holes are positioned at the mid-height of the web of the channel, and the length of edge-stiffener is 13 mm (Howick Ltd. 2013).

With the advancement of cold-formed member rolling technology, it is now possible to manufacture channels with elongated edge-stiffened web holes (see Figure 1-5) for larger

services to be accommodated. However, no research is available in the literature for such CFS channels with elongated holes investigating their web crippling strengths.

❖ Steel sheet coil-uncoiling and flattening

❖ Roller-forming, cutting, and pre-punching

Figure 1-1 Manufacturing process of CFS channels

Figure 1-2 CFS channels with web holes used in industry building (Chen et al., 2024)

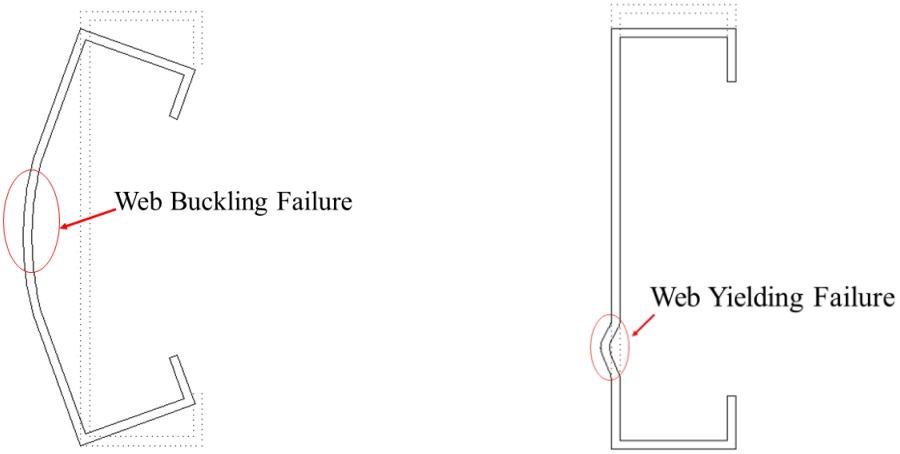

(a) Web buckling (b) Web yielding

Figure 1-3 Web crippling failure of CFS channels

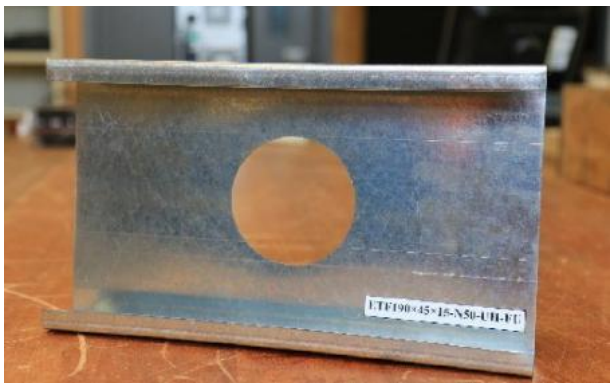

(a) Un-stiffened web hole

(b) Edge-stiffened web hole

Figure 1-4 CFS channels with circular web holes reported by (Chen et al., 2021)

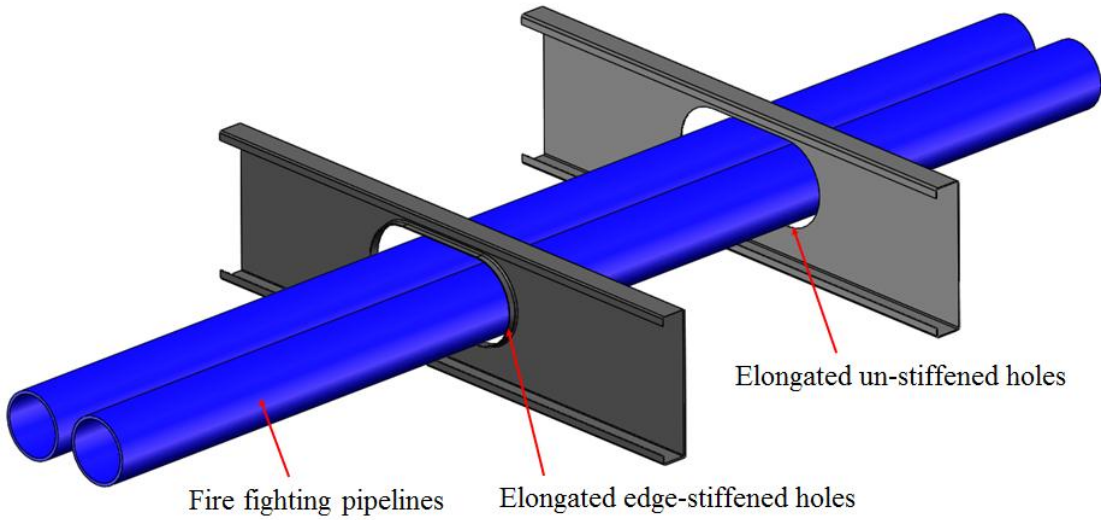

Figure 1-5 Elongated web holes for building services

Trusses constructed from CFS members are widely used in lightweight construction for their ability to span large distances while maintaining structural integrity. The integration of advanced connection systems, such as Howick Rivet Connectors (HRCs), has further enhanced the performance of CFS trusses. Key aspects include:

(1) Moment Capacity: Experimental studies on CFS trusses with HRCs have demonstrated increased moment capacity and ductility compared to conventional connections.

(2) Failure Modes: Common failure mechanisms include local buckling at chord members and shear failure at connections.

(3) Parametric Effects: Span-to-height ratios, lateral supports, and boundary conditions influence truss behaviour.

Built-up box sections, often formed by connecting U-sections and C-sections with fasteners such as screws or rivets, are increasingly used in high-capacity load-bearing applications. Their ability to sustain significant axial loads and resist buckling makes

them ideal for use in columns, roof trusses, and shear walls. However, the performance of these sections is heavily influenced by key parameters, including:

(1) Screw Spacing: The spacing between connectors significantly impacts the composite action and stiffness of the section.

(2) Thickness Variations: Differences in material thickness affect local, distortional, and global buckling behaviour.

(3) Slenderness Ratios: Longer columns with higher slenderness ratios are more prone to flexural buckling.

Experimental studies have shown that improper design or insufficient spacing of connectors can lead to premature failure, such as distortional or interactive buckling. Numerical studies, including finite element analysis (FEA), are essential for capturing these effects and proposing design improvements. For instance, recent findings highlight the need for modifications to existing design standards, such as the EWM and DSM, to accurately predict the performance of built-up box sections.

The telescopic stud system is a novel innovation in CFS construction, offering adjustable lengths to suit specific structural requirements. These systems are particularly useful in modular construction, where prefabrication and on-site assembly are critical. Telescopic studs typically consist of:

(1) Plain Channels (see Figure 1-6(a)): Outer members with pre-punched holes to accommodate screws.

(2) Sigma Channels (see Figure 1-6(b)): Inner members that slide within the plain channels for length adjustment.

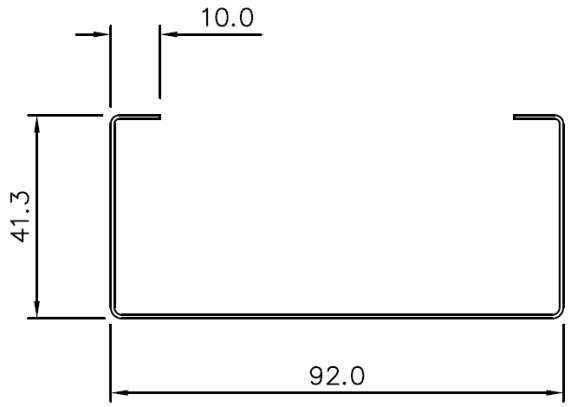

(a) Plain channel

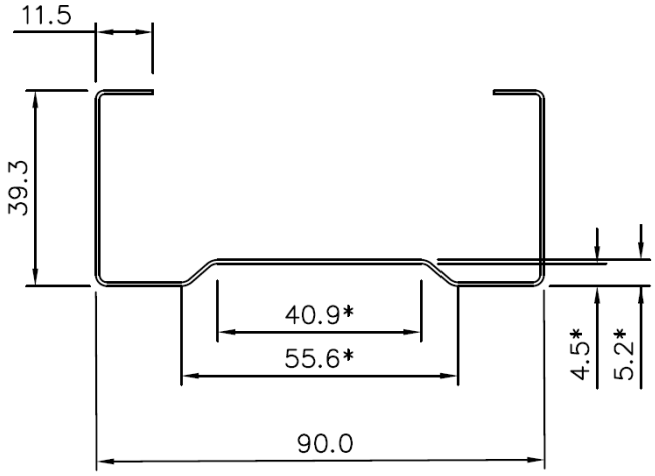

(b) Sigma channel

Figure 1-6 Cross-sectional configurations of CFS channels

Experimental investigations reveal that the number and arrangement of screws in the telescopic system significantly affect its axial capacity and failure modes. For example:

(1) Single-Screw Connections (see Figure 1-7(a)): Vulnerable to tilting and shear failure.

(2) Multi-Screw Configurations (see Figure 1-7(b)): Enhance strength by distributing loads more effectively.

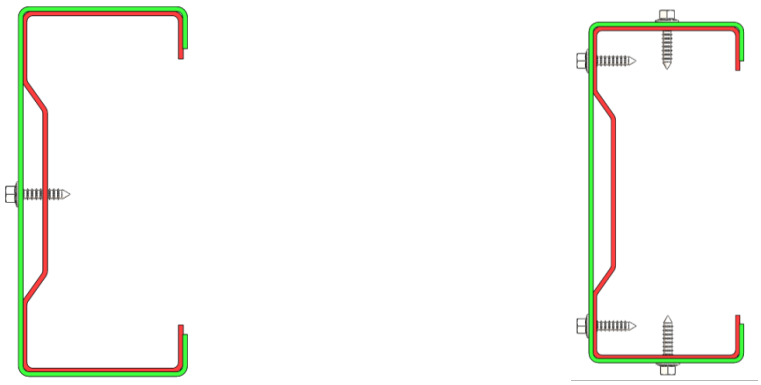

(a) Single-screw connection (b) Multi-screw configuration

Figure 1-7 Screw connection configurations of built-up CFS channels

Swaged sections represent a unique approach to improving the performance of CFS columns by narrowing the web width at specific locations, as shown in Figure 1-8. This modification allows easy nesting and alignment of components, making them particularly useful in frames and bracings. Experimental findings indicate:

(1) Axial Capacity: Swaged sections exhibit comparable or slightly reduced axial capacity compared to plain sections.

(2) Failure Modes: Global buckling dominates in long columns, while short columns are more susceptible to local buckling.

Numerical analyses have highlighted the need for tailored design equations to account for the unique geometry and stress distribution in swaged sections.

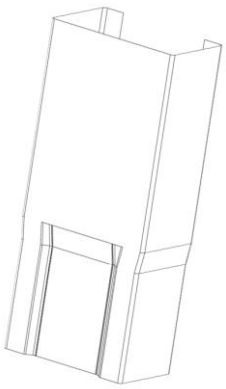

Figure 1-8 CFS channel having a swaged section

1.2. Aim and scope of the study

This thesis aims to provide a comprehensive understanding of the structural behaviour of CFS members and to develop reliable design methodologies for advanced systems. The study focuses on:

(1) CFS Channels with Web Holes: investigating the web crippling strength of CFS channels with elongated edge-stiffened web holes numerically and proposing modifications to DSM for accurate web crippling strength predictions of these channels.

(2) CFS Trusses: Analysing the moment capacity and failure modes of trusses with advanced connectors (HRCs) and exploring the truss strength design formula.

(3) CFS Built-Up Box Sections: Investigating the axial capacity, buckling behaviour, and connector performance using HRCs and screws and proposing modifications to DSM and EWM for accurate axial strength predictions of these CFS columns.

(4) CFS Telescopic Stud Systems: Evaluating the impact of screw configurations on connection strength.

(5) CFS Swaged Sections: Examining the axial and buckling behaviour of CFS columns with locally swaged geometries.

The research involves a combination of experimental tests, numerical simulations, and parametric studies to achieve these objectives.

1.3. Thesis outline

This thesis comprises eight chapters, as outlined below:

Chapter 1: Introduces the research topic, including the problem statement, objectives, and the method of investigation used in the study.

Chapter 2: Presents a detailed review of existing studies on CFS systems, highlighting research gaps and opportunities.

Chapter 3: Describes the numerical work conducted in this study to assess the web crippling performance of CFS channels with elongated edge-stiffened web holes under the four different loading condition.

Chapter 4: Analyses the performance of CFS trusses with HRCs, focusing on moment capacity and practical design considerations.

Chapter 5: Explores the experimental and numerical findings on the behaviour of built-up box sections connected by HRCs or Screws, emphasizing the role of connection configurations.

Chapter 6: Details the structural performance and failure mechanisms of telescopic studs under axial compression.

Chapter 7: Investigates the axial and buckling behaviour of swaged sections, proposing design improvements.

Chapter 8: Summarizes the research outcomes, provides conclusions, and offers recommendations for further research.

1.4. Summary

This chapter introduced the background and motivation for investigating advanced CFS structural systems. The application of CFS channels with web holes was discussed,

highlighting the increased susceptibility to web crippling failure and the limitations of existing design approaches when edge-stiffened and elongated web holes are used.

The chapter also outlined recent developments in CFS trusses, built-up box sections, telescopic stud systems, and swaged sections, emphasizing the significant influence of connection configurations, geometric characteristics, and slenderness on structural performance. The inadequacy of current design methods, including the Effective Width Method and the Direct Strength Method, in accurately predicting the behaviour of these systems was identified.

Finally, the aims, scope, and structure of the thesis were presented, providing a framework for the experimental, numerical, and parametric investigations described in the subsequent chapters.

Chapter 2 Literature review

CFS structural systems are widely used in low- and mid-rise residential buildings due to their high strength-to-weight ratio, ease of prefabrication, and rapid construction capability. In typical CFS residential buildings, structural members such as studs, floor joists, and roof trusses are formed from thin-walled sections and assembled through various types of connections. During service, these structural components are subjected to a wide range of loading conditions, including concentrated loads, distributed loads, and interaction effects between structural members and connections. In particular, concentrated loads transferred through floor systems or bearing reactions can induce web crippling in thin-walled sections, while the presence of service web openings may significantly influence the load-carrying capacity of these members.

Within this broader structural context, understanding the behaviour of CFS members with web openings and the performance of associated reinforcement and connection systems is essential for ensuring the safety and efficiency of CFS residential structures. The research presented in this thesis investigates several structural aspects relevant to such building systems, including the behaviour of CFS members under localized loading conditions, the effectiveness of reinforcement methods for web openings, and the performance of high-performance connection systems used in assembled structural components. To support these research objectives, this chapter reviews the existing literature on the web crippling behaviour of CFS channels with web openings and the corresponding reinforcement techniques. In addition, previous studies on high-performance connections in cold-formed steel structures are discussed to establish the background for the connection systems investigated in this thesis. The review also

summarizes current design approaches and identifies existing research gaps related to web reinforcement and connection performance in CFS structural members.

2.1. Web crippling capacity of CFS channels with web holes

2.1.1. CFS plain channels

Since 1940, numerous studies have focused on investigating the web crippling behaviour of various CFS plain channels, including C-shaped sections, Z-shaped sections, and hat sections, under four loading conditions: interior one-flange (IOF), end one-flange (EOF), interior two-flange (ITF), and end two-flange (ETF), as shown in Figure 2-1. The first experimental study on web crippling failure in CFS beams was conducted by Winter and Pian (1946), who performed laboratory tests to evaluate the web crippling capacity of CFS channels under IOF, EOF, ITF, and ETF. Building upon their work, Hetrakul and Yu (1978) developed more comprehensive design formulations for calculating the web crippling capacity of CFS channels.

Wing (1981) and Schuster (1986) proposed new design equations to calculate the web crippling capacity of CFS plain sections with multiple webs under IOF, ITF, and ETF loading conditions. Additionally, the interaction between bending and web crippling was investigated. Their research highlighted that the ratios of inside bend radius to web thickness and bearing length to web thickness had a significant impact on the ultimate web crippling capacity.

Santaputra et al. (1989) conducted both analytical and experimental studies on the behaviour and design of high-strength CFS hat sections and I-beams subjected to web crippling. Their laboratory test results revealed that existing design codes were inadequate for high-strength materials with elevated yield strengths. Consequently, new

design equations were developed for various loading cases, utilizing experimental data with material yield strengths ranging from 207 MPa to 1,138 MPa.

Rhodes and Nash (1998) conducted a theoretical study to investigate the web crippling capacity of CFS plain lipped channels under IOF and ITF loading conditions. The study evaluated the accuracy of design guidelines for CFS channels by comparing web crippling strengths obtained from numerical analysis, finite strip analysis, and the AISI (1996) design guidelines. Their findings highlighted the significant impact of bearing length and web height on the web crippling capacity of these channels. Additionally, the study proposed a design approach incorporating the European column curves.

Young and Hancock (1998, 2000) conducted experimental studies on the web crippling performance and design of CFS unlipped plain channels under IOF, EOF, ITF, and ETF loading conditions. Laboratory test results were compared with the AISI Specification (1996) for CFS members. Their findings demonstrated that the design strengths predicted by the AISI (1996) guidelines were overly conservative for determining the web crippling capacity of unlipped channels. In their study, they developed simple plastic mechanism equations to more accurately calculate the web crippling capacity of unlipped channels.

Young and Hancock (2001) conducted a series of experimental tests to investigate the web crippling capacity of CFS unlipped channels with relatively stocky webs under ITF and ETF loading conditions. The experimental results were compared with the design strengths predicted by the AISI (1996) specifications. The findings revealed that the design strengths provided by the AISI (1996) guidelines were unconservative for predicting the web crippling capacity of unlipped channels. Consequently, new design equations were developed based on a simple plastic mechanism model to improve the accuracy of web crippling strength predictions for these beams.

Holesapple and LaBoube (2003) conducted a study reporting 29 experimental results on C-shaped and Z-shaped channels (see Figure 2-2) to examine the effect of overhang length on the web crippling strength of CFS channels. The findings indicated that the EOF web crippling capacities predicted by the AISI (1996) guidelines were conservative for CFS channels with overhang lengths ranging from 0.5*h* to 1.5*h*, where *h* represents the web height. To address this, new design equations incorporating a modification factor for the EOF loading condition were proposed.

In 2004, Young and Hancock conducted web crippling experiments on CFS unlipped channels with flanges either restrained or unrestrained at the supports, under ETF and ITF loading conditions. To simulate restrained flanges, the flanges of the channels were bolted to bearing plates during testing. The experimental results were compared with the design strengths predicted by the AISI (1996) guidelines. It was found that the unrestrained design rules in the AISI (1996) guidelines generally provided conservative predictions, while the restrained design rules yielded unconservative estimates.

Macdonald et al. (2011) conducted 36 laboratory tests to investigate the web crippling capacity of CFS lipped channels. A comparison of experimental results, finite element (FE) simulations, and the plastic mechanism approach revealed that the FE models closely replicated the web crippling failure behaviour observed during tests. Furthermore, the study identified that bearing length, corner radius, and clear web height significantly influenced the web crippling capacity of channels, particularly under IOF and EOF loading conditions.

Keerthan et al. (2014) conducted 28 laboratory tests to investigate the web crippling capacity and design of CFS hollow flange channels under ETF and ITF loading conditions. Based on the results from these tests, they developed Direct Strength Method

(DSM)-based equations to calculate the web crippling capacities of hollow flange channels. The study demonstrated that the proposed equations closely predicted the web crippling capacity of these channels.

Steau et al. (2015) extended their previous research to rivet-restrained rectangular hollow flange channels. Laboratory tests revealed that these channels failed due to web crippling, flange crushing, or a combination of both. A comparison of the ultimate web crippling capacities with the design strengths predicted by AISI (2012) showed that the existing design equations were unconservative for calculating the web crippling strength of such channels. As a result, new equations were developed to calculate the web crippling capacities of rivet-restrained rectangular hollow flange channel beams, and these new equations were found to closely predict the web crippling capacity of these sections.

Janarthanan et al. (2015) conducted 28 web crippling experiments on CFS unlipped channels with flanges restrained to bearing plates under EOF and IOF loading conditions. For comparison, specimens with unrestrained flanges were also tested. Based on the results from this study, a new equation was proposed, utilizing the DSM, to determine the web crippling strength of CFS unlipped channels with flanges restrained to supports.

Gunalan and Mahendran (2015) conducted an experimental investigation into the web crippling capacity and design of CFS unlipped channels with stocky webs under ITF and ETF loading conditions. In the study, DuraGal sections with a nominal yield stress of 450 MPa were tested to examine the effects of different web slenderness ratios and bearing lengths on the capacity of these channels. The laboratory test results revealed that the AISI (2012) design guidelines were unconservative for these stocky channels under ETF and ITF loading conditions. Consequently, new design equations were proposed, based

on the DSM design rules, to more accurately predict the web crippling capacities of CFS channels.

Sundararajah et al. (2017) conducted experimental and numerical investigations to study the web crippling capacity and design of CFS plain channels under two-flange loading conditions. Based on the results from both the numerical and experimental studies, they proposed improved unified web crippling design equations. Additionally, they developed web crippling design rules based on the DSM, which closely predict the web crippling capacity of such CFS plain channels.

Janarthanan et al. (2019) investigated based on the recently developed AISI S909 web crippling test guidelines experimentally and numerically. Using the results of both experiments and FEA, new equations were proposed to determine the web crippling capacities of plain lipped and unlipped channels and SupaCee sections (see Figure 2-3). Additionally, suitable DSM-based web crippling design equations were developed.

Lan et al. (2024) reported the web crippling and structural design of high-strength steel unlipped channels under ETF loading, based on both experimental and numerical investigations. The experimental program consisted of six S690 grade specimens and four S960 grade specimens, with detailed reporting on the test setup, procedures, and results. It was found that the design methods in the current standards provide inaccurate and scattered resistance predictions for high-strength steel unlipped channels. Consequently, a modified AISI (2016) design method and a slenderness-based design method were proposed, both of which outperform the existing codified design methods.

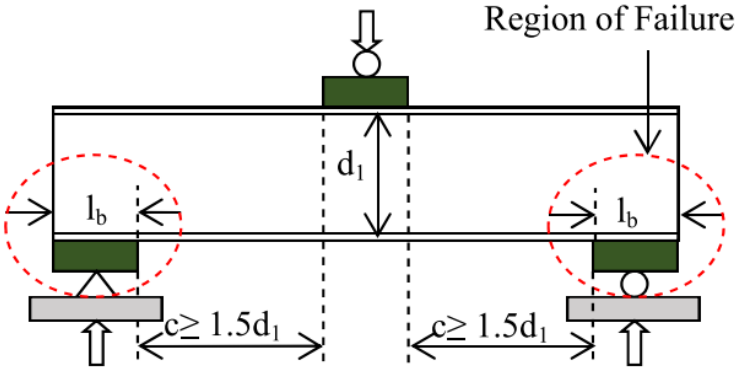

(a) EOF

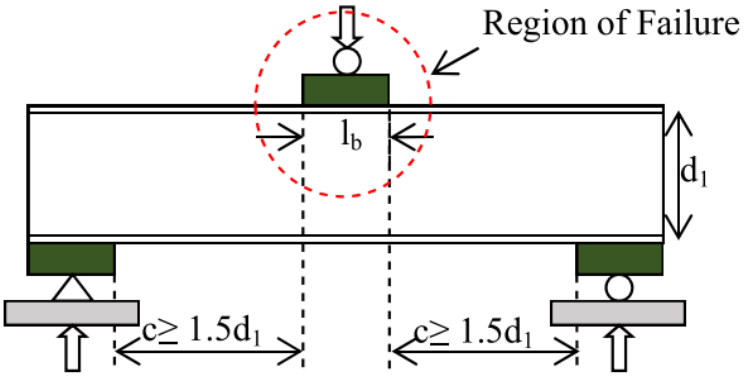

(b) IOF

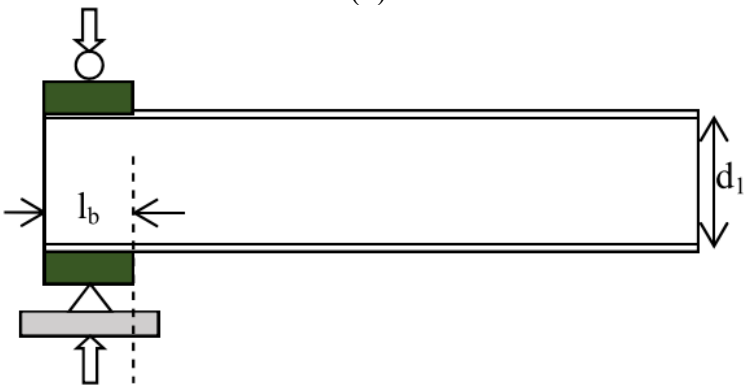

(c) ETF

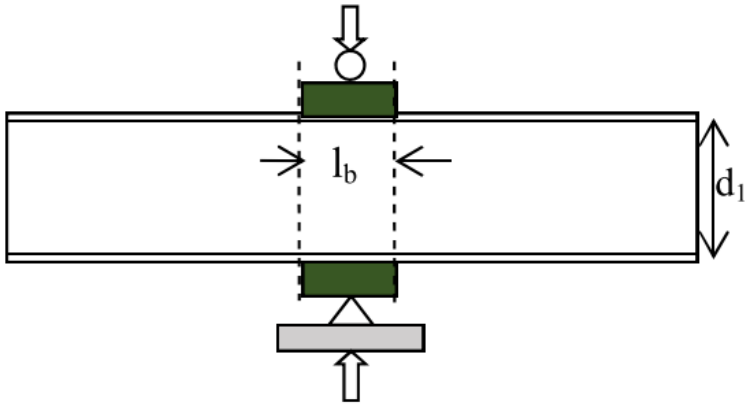

(d) ITF

Figure 2-1 Four loading conditions of web crippling tests (Janarthanan et al. 2019)

Figure 2-2 Z-shaped channels under EOF loading condition (Holesapple & LaBoube, 2003)

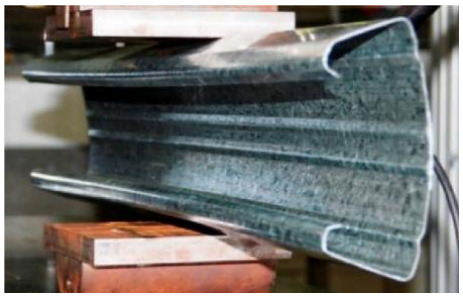

Figure 2-3 SupaCee section under ITF loading condition (Janarthanan et al., 2019)

2.1.2. CFS channels with un-stiffened web holes

Numerous studies have investigated the web crippling capacity and design of CFS channels with un-stiffened web holes. In an early study by Yu and Davis (1973), both circular and square unstiffened web holes were examined, positioned centrally beneath the bearing plate with the flange unrestrained against it. Laboratory tests were conducted with a bearing length of 89 mm. Based on the experimental results, design equations incorporating a capacity reduction factor were proposed; however, their applicability was restricted to the specified bearing length.

Uzzaman et al. (2012a, b, 2013) explored the effects of un-stiffened web holes on the reduced web crippling capacity of CFS lipped channels under ETF and ITF loading

conditions through a combination of experimental and numerical studies. To examine the influence of flange restraint on web crippling capacity, tests were conducted on specimens with both fastened and un-fastened flanges. For specimens with holes, the holes were either positioned centrally above the bearing plates or offset horizontally at a clear distance from the bearing plates. The experimental setup employed in Uzzaman et al.'s (2012a, b, c, 2013) tests is illustrated in Figure 2-4(a) and (b). Based on their findings, they proposed new equations for calculating the capacity reduction factor of CFS channels with un-stiffened web holes.

Lian et al. (2016, 2017) expanded upon the work of Uzzaman et al. (2012a, b, 2013), investigating the reduced web crippling capacity of CFS lipped channels with un-stiffened web holes under IOF and EOF loading conditions. Both fastened and un-fastened flange conditions were examined, and plain channels were tested for comparison. For specimens with web holes, the holes were either positioned centrally above the bearing plates or offset horizontally at a clear distance. Additionally, new design equations incorporating capacity reduction factors were proposed. The experimental setup employed by Lian et al. (2016, 2017) for testing CFS channels with un-stiffened web holes under EOF and IOF loading conditions is shown in Figure 2-4(c) and (d).

A comprehensive dataset was compiled from prior literature studies focusing on the web crippling behaviour of CFS lipped channels with circular web openings under four different loading conditions, as outlined in Table 2-1. This table encompasses variations in flange fastening conditions and the placement of circular web openings. Detailed parameters are presented in Figure 2-4.

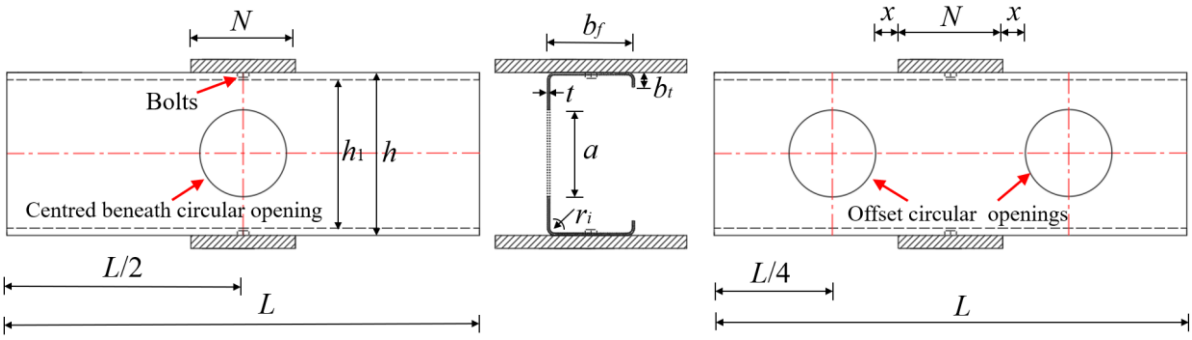

(a) ITF

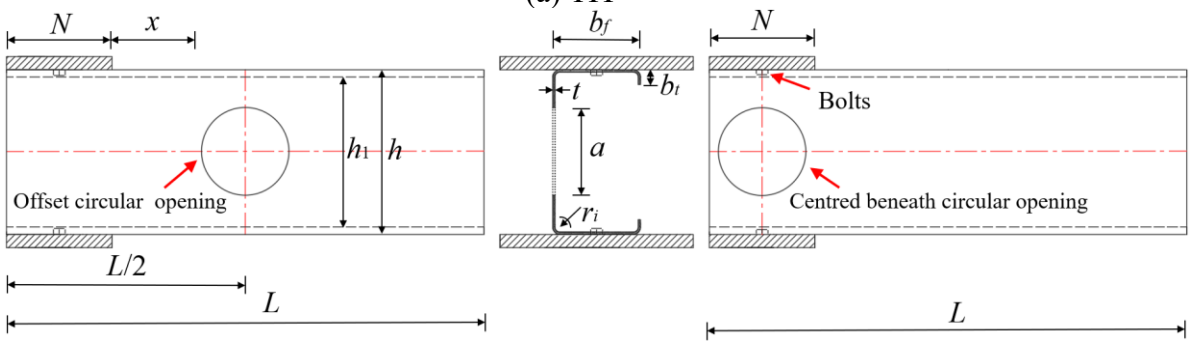

(b) ETF

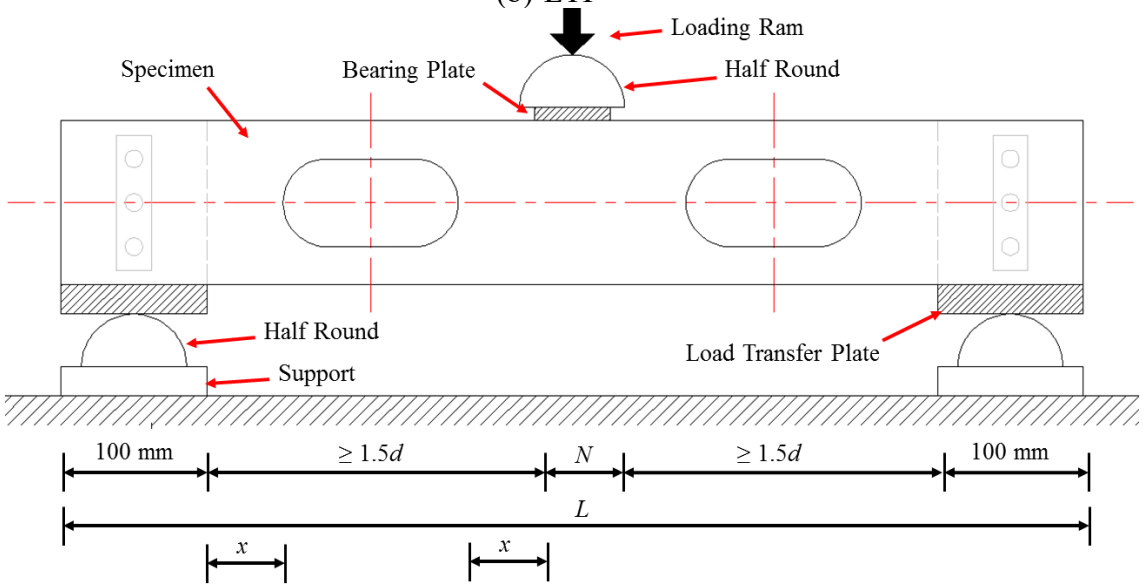

(c) IOF

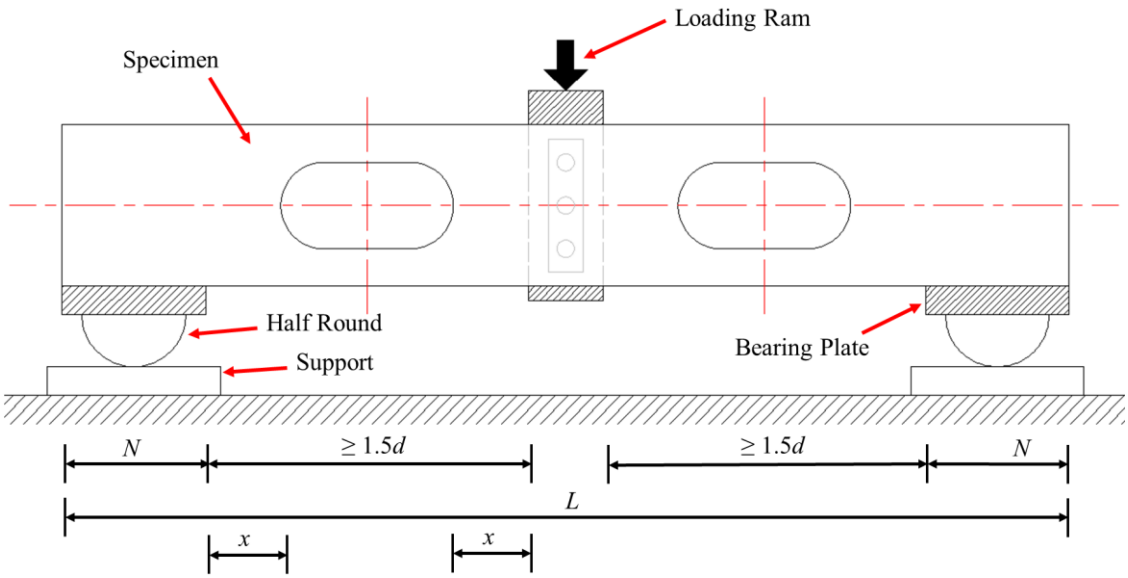

(d) EOF

Figure 2-4 Different load cases and variables

Table 2-1 Statistical web crippling tests of CFS channels with circular web holes

Authors	Load cases	Opening location	Flange Fastened	Web height h mm	Bearing length N mm
(Uzzaman et al., 2012a)	ITF & ETF	Central	Yes & No	142 - 262	90 - 150
(Uzzaman et al., 2013)	ETF	Offset	Yes & No	142 - 302	30 - 65
(Uzzaman et al., 2020a)	ETF	Offset & Central	No	240 - 290	50 - 100
(Uzzaman et al., 2012b)	ITF	Offset	Yes	142 - 302	30 - 90
(Uzzaman et al., 2020b)	ITF	Offset & Central	No	240 - 290	50 - 100
(Chen et al., 2021)	ITF & ETF	Offset & Central	Yes & No	190	50 - 100
(Lian et al., 2016)	EOF	Offset & Central	Yes & No	142 - 302	100 - 150
(Lian et al., 2017)	IOF	Offset & Central	Yes & No	142 - 302	100 - 150

2.1.3. CFS channels with edge-stiffened web holes

Uzzaman et al., (2017a, 2020a, b) conducted experimental and numerical investigations on the web crippling capacity of CFS channels with edge-stiffened web holes (see Figure 2-5) under ITF, ETF, IOF, and EOF loading conditions. The results from laboratory tests and numerical analyses demonstrated that edge-stiffened web holes significantly improve the web crippling capacity of such channels. Based on these findings, new design equations in the form of capacity reduction factors were proposed, which were shown to be conservative when compared to both experimental and numerical results.

Chen et al. (2021) reported 36 new web crippling tests conducted on CFS channels with edge-stiffened web holes under fastened support conditions and subjected to two-flange loading (see Figure 2-5). For comparison, specimens without holes and with unstiffened web holes were also tested. The test results revealed that specimens with fastened flanges exhibited significantly higher ultimate capacity compared to those with un-fastened flanges. Specifically, the web crippling capacity increased by 71% under ETF loading and by 33% under ITF loading for fastened flanges.

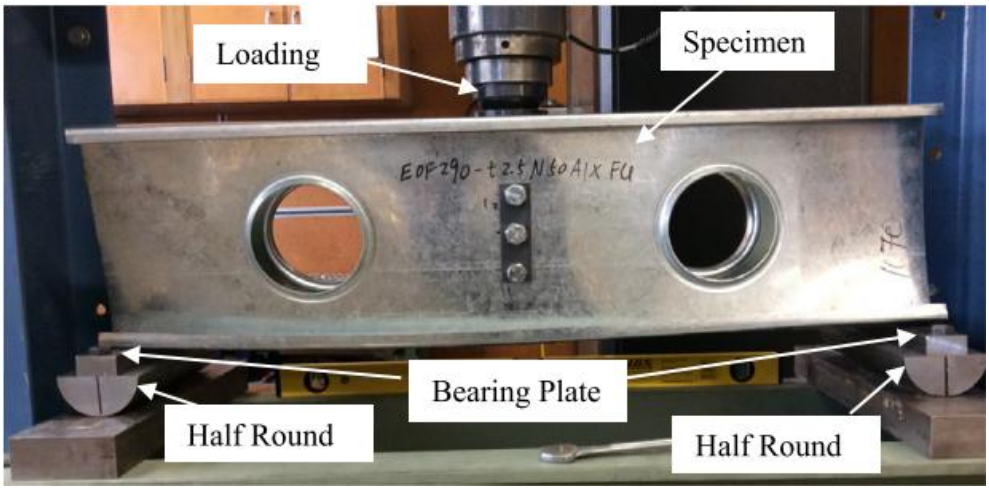

(a) Uzzaman et al. (2017b)

(b) Chen et al. (2021)

Figure 2-5 CFS channels with edge-stiffened web holes

2.1.4. Current design equations for CFS channels in web crippling

For CFS plain channels, unified web crippling design equations with specific coefficients are provided in the current AS/NZS (2018) and AISI (2016) standards. These coefficients C, C_r, C_l, and C_w vary depending on the loading cases, support conditions, and flange

types. The effect of fastened support is incorporated into the design rules outlined in both AS/NZS (2018) and AISI (2016) for CFS channels. The nominal web crippling capacity can be calculated using Equation 2.1. It should be noted that the design equations are not applicable to sections with larger r_i/t_w ratios, as such configurations may deviate from the assumptions used in deriving the equations, leading to inaccurate predictions of web crippling capacity.

$$R_b = Ct^2 f_y \sin\theta \left(1 - C_w\sqrt{\frac{h}{t}}\right)\left(1 - C_r\sqrt{\frac{r_i}{t}}\right)\left(1 + C_l\sqrt{\frac{N}{t}}\right) \quad \text{(Equation 2.1)}$$

Eurocode 3 provides design equations (Equations 2.2 and 2.3) for calculating the web crippling capacity of CFS plain channels under one-flange loading cases. In the equations, d_w is the web height; γ_{M1} represents the partial safety factor (=1). However, these equations are more complex compared to the unified web crippling design equations specified in AS/NZS (2018) and AISI (2016). Notably, Eurocode 3 uses the same design equations for both flange-fastened and flange-unfastened support conditions, disregarding any potential increase in web crippling capacity due to flanges being fastened to the supports. Additionally, the applicability of these equations is restricted to: $r_i/t \leq 6$ and $d_w/t \leq 200$.

$$R_b = (k_1 k_2 k_3 \left[6.66 - \frac{d_w/t}{64}\right]\left[1 + 0.01\frac{l_b}{t}\right] t^2 f_y) / \gamma_{M1} \quad \text{(Equation 2.2)}$$

$$R_b = (k_3 k_4 k_5 \left[21.0 - \frac{d_w/t}{16.3}\right]\left[1 + 0.0013\frac{l_b}{t}\right] t^2 f_y) / \gamma_{M1} \quad \text{(Equation 2.3)}$$

For CFS lipped channels with unstiffened web holes, AISI (2016) provides strength reduction factor equations (R_p) specifically for cases where the web hole has a horizontal

clear distance to the bearing plates. However, these equations apply only when the flanges are restrained against the bearing plates, addressing both IOF and EOF loading scenarios.

Uzzaman et al. (2012b, 2012a, 2013) proposed R_p equations for CFS channels with circular web openings across two-flange loading scenarios. These equations are summarized as follows in Equations 2.4 and 2.5, with their coefficients detailed in Table 2-2. However, for channels with varying dimensions and steel grades, the application of these equations may lead to suboptimal outcomes. This discrepancy arises due to the R_p equations' omission of critical parameters such as material yield strength (f_y), flange width (b_f), fillet radius (r_i), etc. Thus, there are notable limitations to the R_p equations' applicability scope: the dimensional limits are $h/t \leq 156$, $N/t \leq 84$, $N/h \leq 0.63$, $a/h \leq 0.8$.

For cantered beneath web holes:

$$R_P = n_1 - n_2\left(\frac{a}{h}\right) + n_3\left(\frac{N}{h}\right) \leq 1 \qquad \text{(Equation 2.4)}$$

For offset web holes:

$$R_P = n_1 - n_2\left(\frac{a}{h}\right) + n_3\left(\frac{x}{h}\right) \leq 1 \qquad \text{(Equation 2.5)}$$

Table 2-2 Coefficients for R_p equations (Uzzaman et al., 2012b, 2012a, 2013)

Load cases	Opening location	Flange Fastened	n_1	n_2	n_3
ITF	Central	No	1.05	0.54	0.01
ITF	Central	Yes	1.01	0.51	0.06
ITF	Offset	No	1.04	0.68	0.02
ITF	Offset	Yes	1.00	0.45	0.09
ETF	Central	No	0.90	0.60	0.12
ETF	Central	Yes	0.95	0.50	0.08
ETF	Offset	No	0.95	0.49	0.17
ETF	Offset	Yes	0.96	0.36	0.14

For specimens with edge-stiffened web holes, Uzzaman et al., (2017a, 2020a, b) developed design equations to calculate the capacity reduction factor (R_p) using bivariate linear regression analysis. These equations are specifically applicable to CFS channels

with un-fastened flanges subjected to two-flange loading conditions. The R_p for such channels can be determined using Equations 2.6 and 2.7.

$$R_P = 1.02 - 0.39\left(\frac{a}{h}\right) + 0.02\left(\frac{N}{h}\right) + 0.04\left(\frac{r_q}{t}\right) + 0.49\left(\frac{q}{h}\right) \leq 1 \quad \text{(Equation 2.6)}$$

$$R_P = 0.98 - 0.11\left(\frac{a}{h}\right) + 0.01\left(\frac{N}{h}\right) + 0.05\left(\frac{r_q}{t}\right) + 0.41\left(\frac{q}{h}\right) \leq 1 \quad \text{(Equation 2.7)}$$

2.2. A novel connector-Howick Rivet Connectors (HRCs)

CFS channels are commonly used as both chord and web members in trusses, typically joined with conventional self-drilling screws (Dizdar et al. (2019); Rajanayagam et al. (2021)). According to the North American Standard for Cold-Formed Steel Framing - Truss Design (AISI 2012), a minimum of four screws is recommended at each junction between web members and chords when screws are employed as fasteners. However, fabricators often prefer using a single fastener per connection for ease of alignment and precise positioning. Although bolts can satisfy the load requirements for truss connections, their shear strength frequently exceeds the bearing capacity of cold-formed thin steel, compromising the ductility of the connections.

To address this limitation, Howick Ltd., based in New Zealand, has developed an innovative connector called the Howick Rivet Connector (HRC). This connector is specifically designed to provide higher connection strength while accommodating the material properties of CFS trusses (Mathieson et al. 2014, 2016, 2019). The HRC consists of a hollow steel tube with two inner swaged collars strategically positioned between the connected CFS sections. The design of the HRC is illustrated in Figure 2-6, with additional depictions of the installation process and practical applications provided in Figures 2-7 and 2-8, highlighting its effectiveness in structural engineering.

Recent studies highlight that CFS T-stub connections employing HRCs demonstrate comparable performance to traditional bolted connections, with notable enhancements in load capacity and ductility. Specifically, HRC connections exhibit an average strength increase of 14.35% compared to bolted connections (Ahmadi et al. (2016)).

Mathieson et al. (2019) investigated the performance of HRCs versus conventional screws in CFS trusses spanning 1800 mm. Their results showed that trusses with HRCs significantly outperformed those with screws in terms of bearing capacity, initial stiffness, and ductility, as illustrated in Figures 2-9(a) and 2-9(b). Similarly, Roy et al. (2023) conducted 15 experimental tests on CFS T-stub connections using a combination of HRCs and screws to examine failure mechanisms and structural behaviour under tension.

Previous studies (Mathieson et al. (2019); Ahmadi et al. (2016); Roy et al. (2023)) have identified two primary failure modes for HRC connections: shear failure and bearing failure. In contrast, traditional screw connections are prone to additional failure modes, such as screw pull-out or tilting, as shown in Figure 2-9(a). These differences in failure mechanisms likely contribute to the higher connection strength observed in HRCs compared to conventional screws. However, despite these advancements, there remains a limited understanding of the moment capacity of CFS trusses featuring eccentric HRC connections at diagonal-to-chord joints, indicating the need for further research in this area.

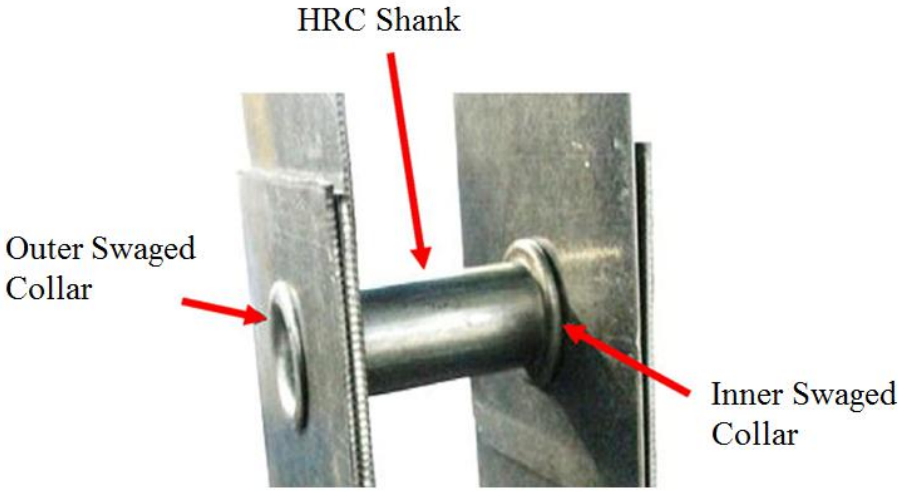

(a)Connection details reported by Roy et al. (2023)

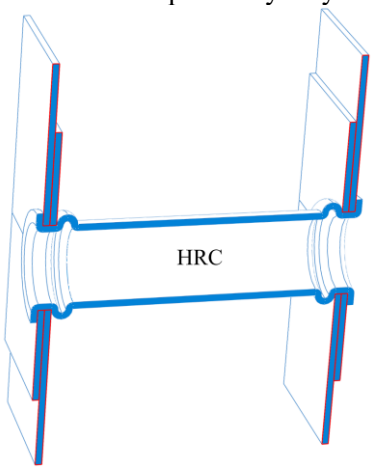

(b)Schematic view

Figure 2-6 Howick Rivet Connector (HRC)

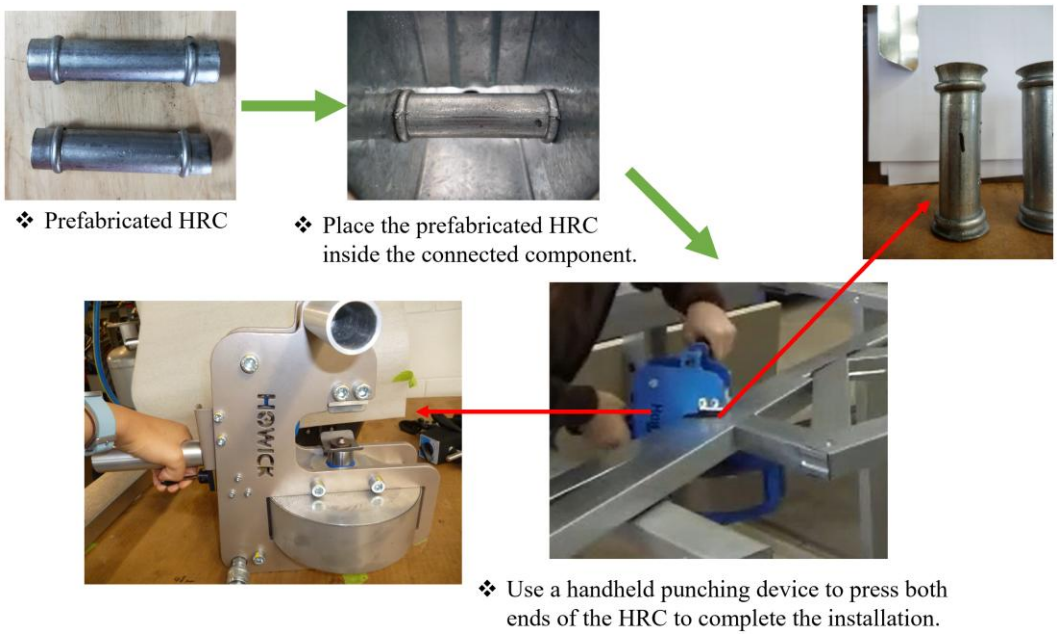

Figure 2-7 HRC installation process

Figure 2-8 HRCs used in roof trusses

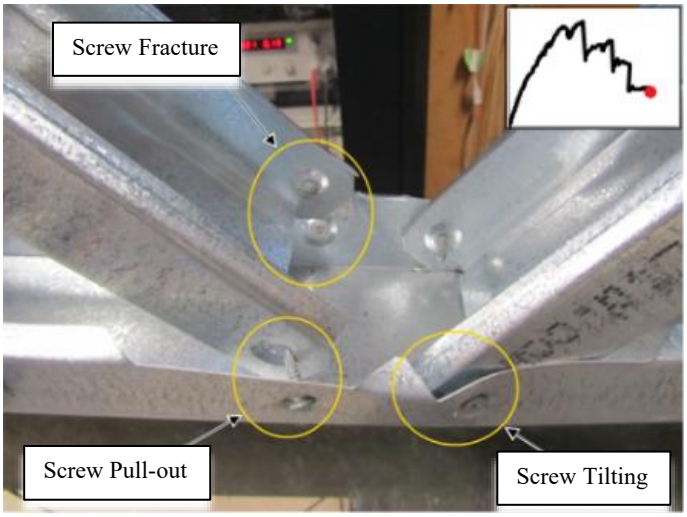

(a) Screw connections

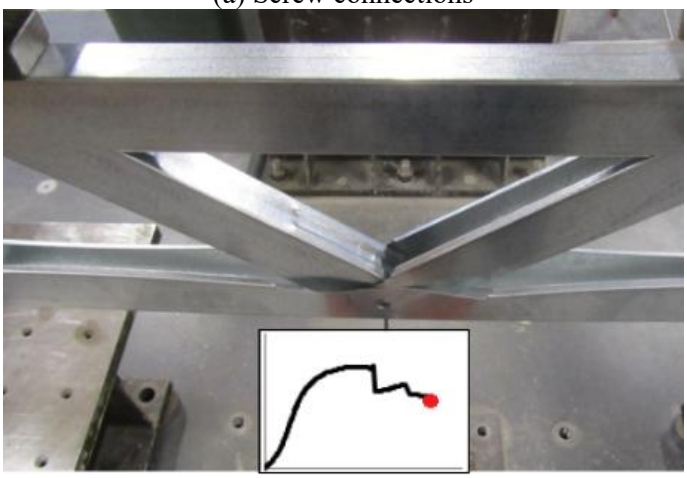

(b) HRC connections

Figure 2-9 Comparison of failure modes of screw and HRC connection in trusses reported by Mathieson et al. (2019)

2.3. CFS built-up box section

In cold-formed steel (CFS) structures, built-up box sections are extensively employed in critical structural components, such as roof trusses, floor joists, window frames, doorways, and shear wall studs, where they are required to withstand large concentrated loads. These sections are favoured in CFS construction for their exceptional load-bearing capacity, enhanced stability, and superior moment of inertia compared to back-to-back built-up sections (Roy et al. 2019). Additionally, the versatility of CFS channels enables the formation of built-up members with substantially increased capacities by combining multiple individual channels (Zhou et al. 2021). This flexibility not only enhances structural performance but also drives the continuous innovation in the application of standard CFS products (Craveiro et al. 2022).

Numerous experimental and numerical studies have examined the structural behaviour and axial capacity of built-up box section columns with various cross-sectional configurations. Commonly, these columns are composed of two C-sections (Roy et al. 2019; Guzman et al. 2021; Li et al. 2014; Mahar et al. 2023; Vy et al. 2021a, 2021b; Reyes et al. 2011), two U-sections (Mahar et al. 2022; Selvaraj et al. 2022), or a combination of one C-section and one U-section (Nie et al. 2020; Li et al. 2021, 2024), connected using either welding (Zhou et al. 2021; Guzman et al. 2021, Reyes et al. 2011) or self-drilling screws (Dai et al. 2024; Ananthi et al. 2023).

Nie et al. (2020) experimentally investigated the influence of cross-sectional shapes, lengths, and thicknesses under both concentric and eccentric axial compression. Their findings revealed that specimens subjected to eccentric compression about the strong axis experienced flexural-torsional buckling, whereas those compressed about the weak axis exhibited flexural buckling.

Li et al. (2021) conducted experimental and numerical analyses on nested built-up sections comprising C- and U-sections. They observed that C-sections primarily failed due to distortional buckling, while U-sections were prone to local buckling. Similarly, Zhou et al. (2021) studied built-up box sections experimentally, reporting failures dominated by local buckling and local-global interaction modes.

Recent studies have examined the structural behavior and ultimate strength of back-to-back built-up sections (Roy et al. 2019; Li et al. 2024; Chen et al. 2020; Li et al. 2022; Fratamico et al. 2018), as well as those comprising triple limbs or multiple channels (Roy et al. 2019; Deepak et al. 2021; Phan et al. 2021; Abbasi et al. 2023; Nie et al. 2020; Yang et al. 2022, 2024; Ma et al. 2024), through experimental testing and numerical analysis. Craveiro et al. (2022) conducted an experimental investigation into the behavior of innovative closed built-up cold-formed steel (CFS) short columns, evaluating four distinct built-up cross-sections formed from three individual shapes: C, U, and Σ. The study revealed that for built-up columns governed by local buckling, the fastener spacing must be equal to or smaller than the local buckling half-wavelength to achieve high composite action, thereby maximizing the load-bearing capacity of the built-up member.

The "plate group effect," introduced by Zhou et al. (2002) through theoretical analysis, describes the behaviour of built-up members under compression. This effect initially causes the weaker plate to buckle, while the stronger plate acts as a constraint, delaying the buckling of the weaker plate. However, once the weaker plate buckles, it exerts a destabilizing influence on the stronger plate, leading to a reduction in the critical buckling stress of the stronger plate while simultaneously increasing the critical buckling stress of the weaker plate.

Dar et al. (2021, 2022) investigated CFS battened closed-section columns composed of plain channels using experimental and numerical methods. The results of their study indicated that the arrangement of the channels in the built-up section influence the axial strengths as well as the buckling stability in CFS battened columns. The toe-to-toe configuration gives better performance over the back-to-back ones. Rahnavard et al. (2021, 2023) proposed an optimal layout for CFS built-up battened columns to enhance composite action between two individual lipped channels. They also developed design equations based on an extensive numerical parametric study.

Built-up members are recognized for their excellent strength-to-weight ratios and adaptability for various applications. However, as highlighted by Rasmussen et al. (2020), the design of these members is hindered by the lack of codified methodologies. AISI (2016) and AS/NZS (2018) provide two primary approaches for determining the ultimate axial capacity of CFS structural members: the EWM and DSM. The DSM equations included in these standards are semi-empirical and have been validated for a limited range of cross-sections. To address this limitation, researchers such as Li et al. (2021), Dai et al. (2024), and Li et al. (2022) have proposed modifications to the DSM for more accurate predictions of the ultimate strength of CFS built-up columns. Additionally, Roy et al. (2019) observed that the design strengths calculated using the EWM tended to be conservatively overestimated by approximately 17% for CFS built-up box columns. The variability in the effectiveness of the design methods specified in AISI (2016) and AS/NZS (2018) across different built-up sections underscores the need for re-evaluation when new built-up configurations are introduced.

2.4. CFS swaged section

In CFS channels, the swaging process is employed to reduce the width of the cross-sections, facilitating the nesting of these channels. Swaged channels (see Figure 2-10) are commonly utilized in various applications, including T-stud, brace-to-stud, and nogging-to-stud connections in CFS frames (see Figure 2-11). The axial capacities and deformed shapes of swaged CFS channels are expected to differ from those of plain channels; however, no experimental studies have been conducted to investigate these differences to date.

In recent years, extensive research on CFS channels reinforced with various web stiffeners has been reported, addressing not only compressive capacity (Wang et al. 2016; Manikandan et al. 2018; Ye et al. 2018a,2018b; Nguyen et al. 2009; Ananthi et al. 2021) but also flexural capacity (Wang et al. 2017; Roy et al. 2020) and shear capacity (Pham et al. 2015). Design recommendations for each of these capacities have also been proposed. However, these studies exclusively considered web stiffeners that span the full length of the test specimens. Additionally, the web height remained consistent between the CFS channels with web stiffeners and the plain channels used for comparison.

To ensure proper web support, cold-formed steel (CFS) channels with various web stiffeners and the same web height must possess sufficient rigidity; otherwise, the members may buckle prematurely, leading to a reduction in member strength (Wang et al. 2016). Manikandan et al. (2018) experimentally and numerically investigated the distortional buckling behaviour of CFS channels with various web stiffeners and the same web height (see Figure 2-12) under axial compression. Their findings revealed that intermediate web stiffeners significantly influence the strength and failure modes of the sections. Wang et al. (2016) conducted a series of compression tests and numerical

investigations on channels with two different types of web stiffeners and the same web height, as shown in Figure 2-13. Their results demonstrated that, compared to plain channels, the ultimate load-carrying capacity of Σ- and V-type sections was increased by 65% and 50%, respectively. Liang et al. (2022) reviewed and summarized a substantial body of literature to explore the optimization of CFS members with various configurations of web and edge stiffeners. Chen et al. (2019, 2020) investigated the effect of edge-stiffened web holes under axial compression.

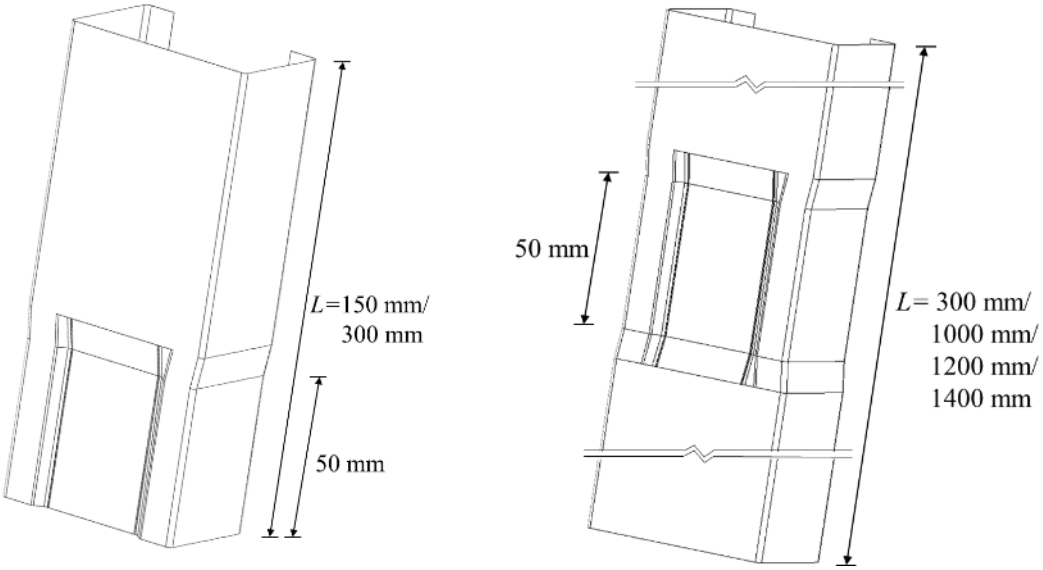

(a) Swaged section at the end of channel section

(b) Swaged section in the middle of channel section

Figure 2-10 CFS channels with swaged sections

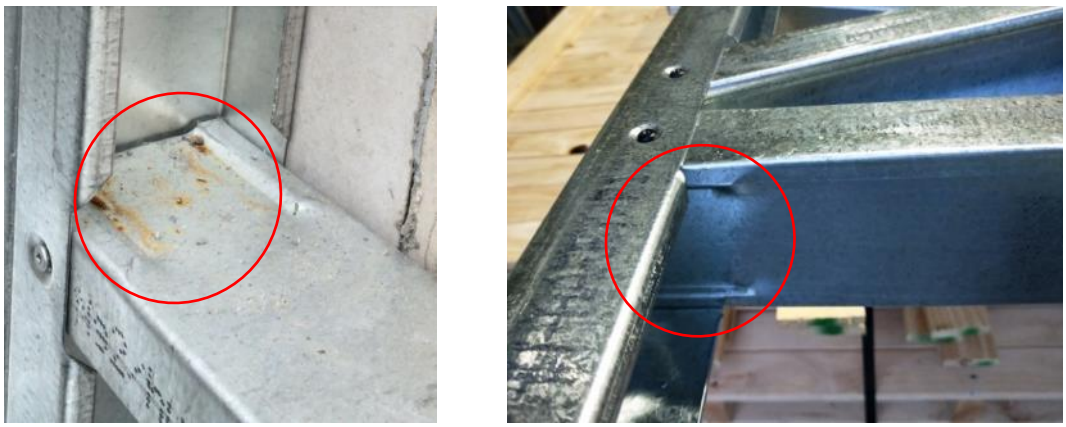

(a) T-stud

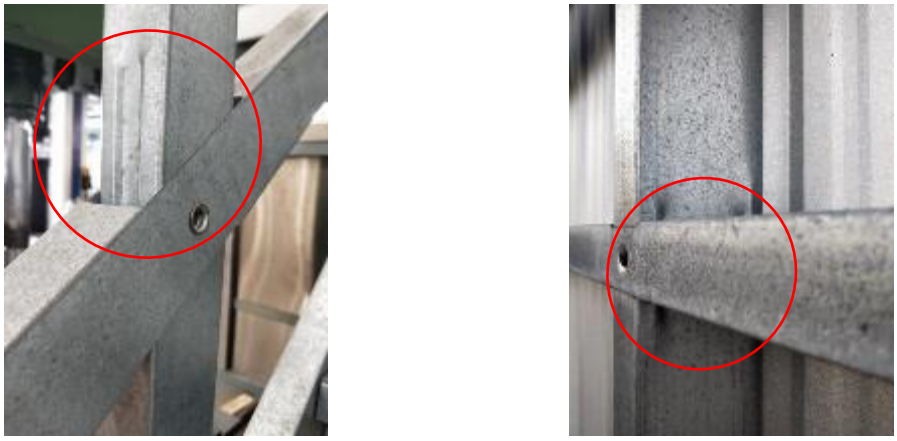

(b) Brace-to-stud (c) Nogging-to-stud

Figure 2-11 Application of CFS channels having a swaged section

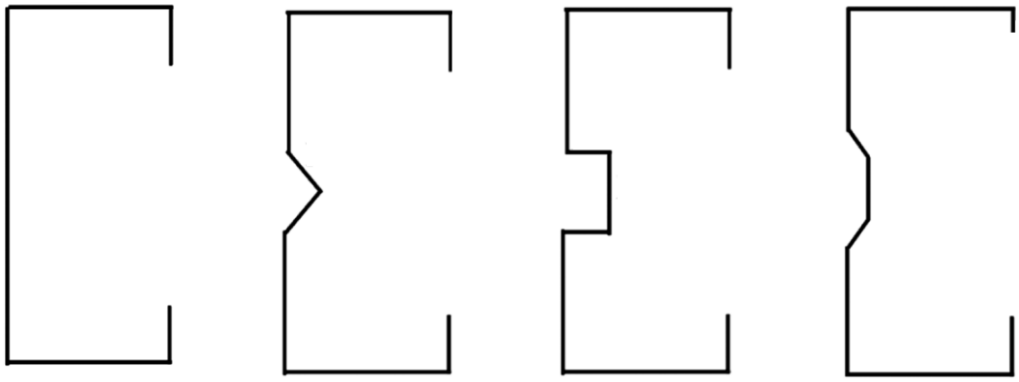

(a) Plain channel (b) V-type channel (c) U-type channel (d) Σ-type channel

Figure 2-12 Section geometries used by Manikandan et al. (2018)

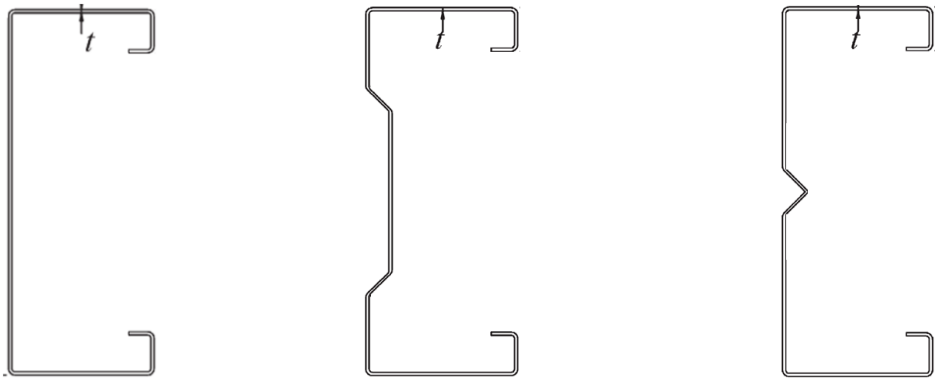

(a) Edge stiffeners (b) Edge stiffeners & Σ-type (c) Edge stiffeners & V-type

Figure 2-13 Cross sections used by Wang et al. (2016)

2.5. Summary

This chapter reviewed previous studies on the web crippling behaviour and design of CFS channels, with emphasis on members containing web holes. The development of web crippling research for plain channels under IOF, EOF, ITF, and ETF loading conditions was summarised, followed by a synthesis of experimental and numerical findings for

channels with un-stiffened and edge-stiffened web holes. Current design provisions were outlined, highlighting the scope and limitations of existing web crippling equations and reduction-factor models.

In addition, the chapter introduced the Howick Rivet Connector (HRC) and summarised its reported advantages over conventional screw connections, while noting outstanding research needs for truss joints with eccentric HRC connections. Literature on CFS built-up box sections and swaged sections was also reviewed, showing that member behaviour is strongly affected by cross-section configuration, connector detailing, and slenderness, and that existing approaches may require modification for new or advanced configurations. These identified gaps provide the basis for the investigations presented in the following chapters.

Chapter 3 Web crippling capacity of CFS channels with elongated edge-stiffened web holes

3.1. Introductory remarks

CFS channel sections are widely used in light-gauge steel construction, where web openings are often introduced to accommodate building services such as electrical conduits, plumbing pipes, and ventilation ducts. Elongated web holes are increasingly adopted in practice because they provide greater flexibility for service installation; however, their presence alters the stress distribution in the web and may significantly reduce the web crippling capacity when concentrated loads are applied. Edge stiffeners are commonly used around web openings to enhance the stiffness and strength of the web, yet the behaviour of CFS channels with elongated edge-stiffened web holes under web crippling loads remains insufficiently understood and is not explicitly addressed in current design standards. Therefore, this chapter presents a comprehensive numerical investigation using nonlinear FE analyses to study the web crippling behaviour of CFS channels with elongated web holes. The FE models were first validated against experimental results for sections with circular edge-stiffened web holes, showing good agreement in terms of load–displacement responses and deformed shapes. Based on the validated models, an extensive parametric study comprising 4,745 finite element analysis (FEA) cases was conducted for channels with elongated unstiffened and edge-stiffened web holes, and design equations were subsequently proposed in the form of web crippling reduction factors (R_p) and DSM-based equations.

3.2. Numerical study

3.2.1. General

No experimental studies were identified in the literature addressing the web crippling behavior of CFS channels with elongated un-stiffened and edge-stiffened web holes. Consequently, the web crippling test results for CFS channels with circular web holes under four different loading conditions (ITF, ETF, IOF and EOF), as reported by Chen et al. (2021) and Uzzaman et al. (2017), were utilized to validate the FE models developed in this study. The modelling techniques employed by Chen et al. (2021) and Uzzaman et al. (2017) were also adopted.

3.2.2. General description of FE model

The material properties were derived from tensile coupon tests reported by Chen et al. (2021) and Uzzaman et al. (2017). Following the guidelines in the ABAQUS manual, the engineering stress-strain curve was converted into a true stress-strain curve.

S4R shell elements with six degrees of freedom per node were used to model the CFS channels, while R3D4 rigid elements were chosen to model the bearing plates. Based on mesh sensitivity analysis results, a mesh size of 10 mm × 10 mm was used to simulate the bearing plates, while a mesh size of 5 mm × 5 mm was found to be appropriate for the channels. Mesh refinement was used around the elongated web holes and the section corners between the web and flanges. The FE meshing details were presented in Figure 3-1.

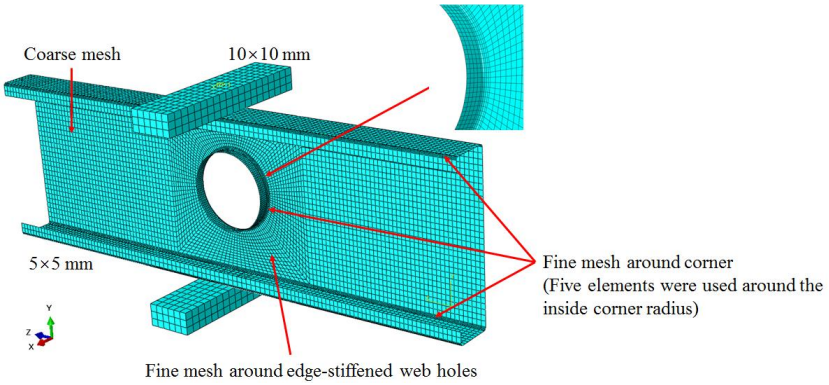

(a) ITF

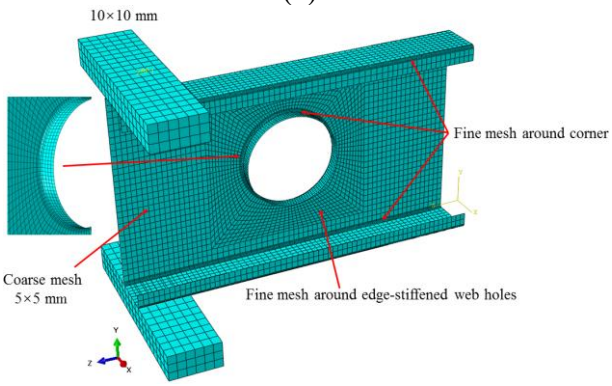

(b) ETF

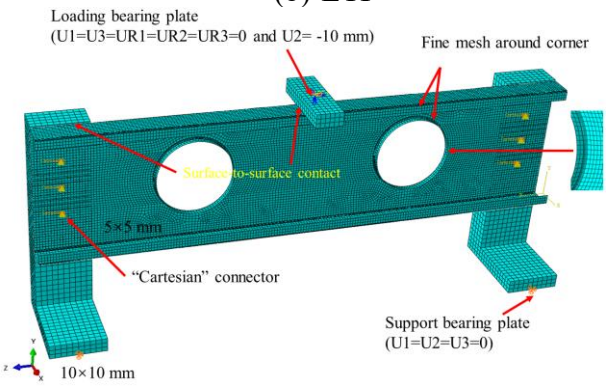

(c) IOF

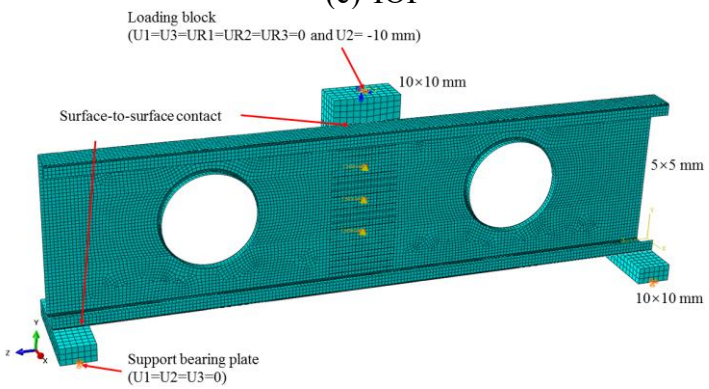

(d) EOF

Figure 3-1 CFS channels with edge-stiffened web holes

The interface between the CFS channels and the bearing plates was modeled using the "Surface-to-Surface" contact feature in ABAQUS. The stiffer bearing plate was designated as the master surface, while the flanges of the channels were assigned as the slave surface. To prevent the penetration of contact surfaces, the "node-to-surface" discretization method was employed. All degrees of freedom, except those associated with the loading direction, were constrained at the top bearing plate or loading block. Axial loading was applied through displacement control via a reference point located on the top bearing plate or loading block. For cases involving fastened flanges, bolt connections were modeled using the "Cartesian" connector. This connector element, defined by three nodes, is designed for rigid linkages and allows users to define translational and rotational degrees of freedom as well as axial stiffness between the connected nodes.

3.2.3. Validation of FE model

A comparison between the experimental results (P_{EXP}) reported by Chen et al. (2021) and Uzzaman et al. (2017) and the FEA results (P_{FEA}) from this study is summarized in Table 3-1. The specimens from Chen et al. (2021) and Uzzaman et al. (2017) were labeled as illustrated in Figure 3-3. The sharp peak observed in the FE load–displacement curves is mainly caused by an abrupt contact-status transition between the bearing plate and the channel flange, combined with the idealised contact assumptions in the numerical model (hard contact and simplified material law). In the tests, surface roughness, local indentation, gradual seating of the specimen–rig system and progressive yielding smear this transition, leading to a smoother response. As shown in Table 3-1, the mean ratios of P_{EXP}/P_{FEA} for ITF, ETF, IOF, and EOF are 1.00, 0.97, 0.99 and 0.99, with COVs of 0.03, 0.02, 0.02 and 0.02, respectively. Figures 3-4 and 3-5 compare the load-displacement

curves and deformed shapes obtained from the FEA and experimental results. These figures demonstrate that the deformed shapes and load-displacement responses from the FEA closely align with those from the experimental tests. Overall, the FE model developed in this study exhibited strong correlation with the experimental results.

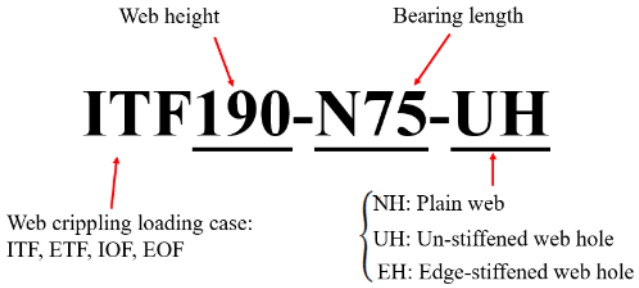

Figure 3-2 Specimen labelling for tests reported by Chen et al. (2021)

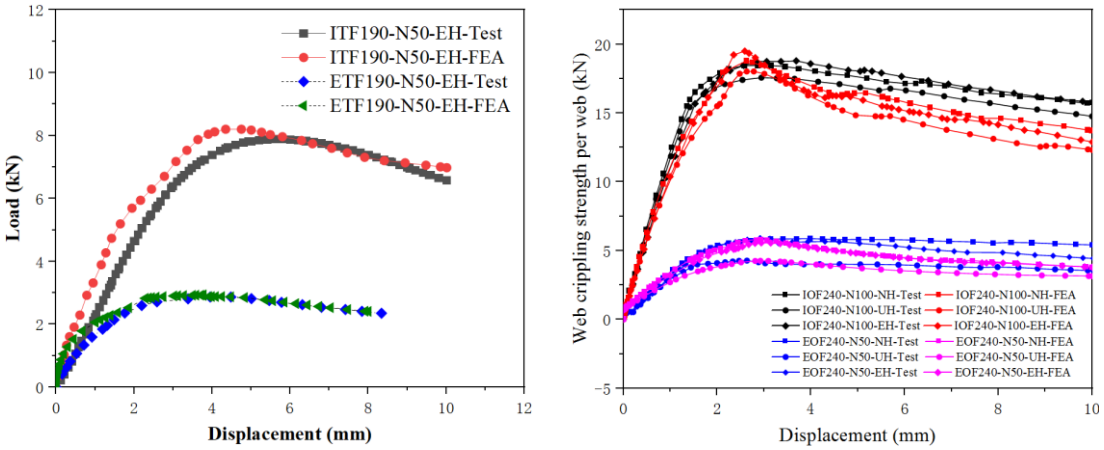

(a)Two-flange loads (b)One-flange loads

Figure 3-3 Comparison of load-displacement curve

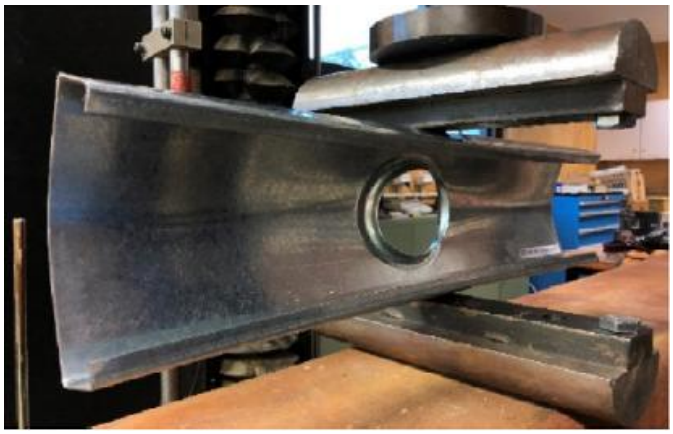

(i) ITF190-N50-EH-FU-Test (Chen et al., 2021)

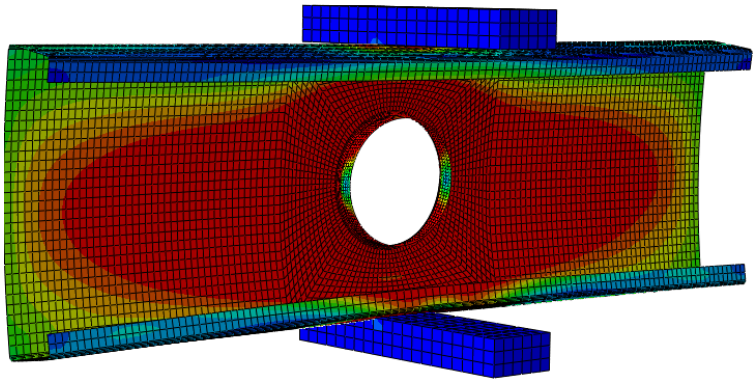

(ii) ITF190-N50-EH-FU-FEA

(a) ITF

(i) ETF190-N50-EH-Test

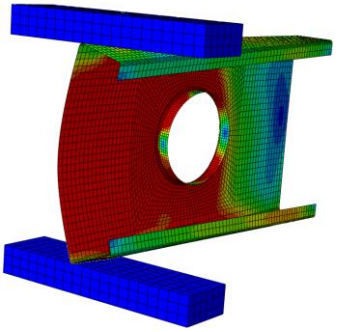

(ii) ETF190-N50-EH-FEA

(b) ETF

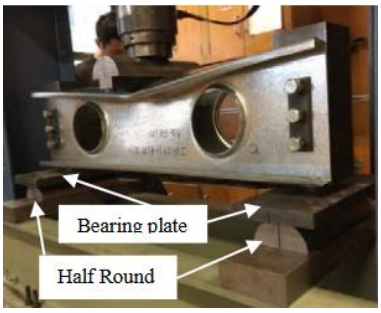

(i) Test

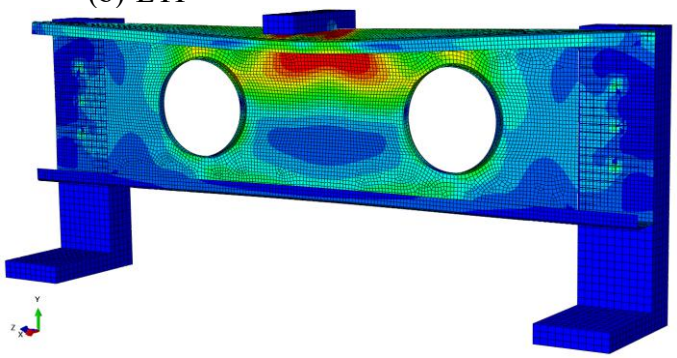

(ii) FEA

(c) IOF

(i) Test

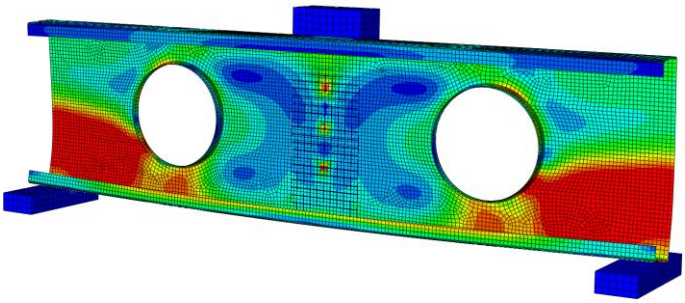

(ii) FEA

(a) EOF

Figure 3-4 Comparison of deformed shape

Table 3-1 Specimen dimensions and experimental ultimate loads from literature

Specimens	Web d (mm)	Flange b_f (mm)	Lip b_t (mm)	Length L (mm)	Bearing length N (mm)	Stiffener length q (mm)	Exp. load P_{EXP} (kN)	FEA. load P_{FEA} (kN)	P_{EXP} /P_{FEA}
(a) ITF									
ITF190-N50-UH	190.5	45.2	14.80	620.50	50	-	8.27	8.16	1.01
ITF190-N75-UH	190.3	45.0	15.00	645.00	75	-	8.78	8.28	1.06
ITF190-N100-UH	190.5	44.8	15.10	670.50	100	-	9.21	9.12	1.01
ITF190-N50-UH	190.0	45.0	14.90	621.00	50	-	6.45	6.39	1.01
ITF190-N75-UH	190.2	45.1	15.50	645.50	75	-	6.64	6.66	1.00
ITF190-N100-UH	190.5	45.5	15.50	670.00	100	-	6.89	6.96	0.99
ITF190-N50-EH	190.5	45.5	15.00	620.50	50	13	7.88	8.12	0.97
ITF190-N75-EH	190.1	45.0	14.80	645.00	75	13	8.29	8.53	0.97
ITF190-N100-EH	190.5	45.3	15.30	670.20	100	13	8.61	8.68	0.99
Mean									1.00
COV									0.03
(b) ETF									
ETF190-N50-NH	190.0	45.1	15.2	334.7	50	-	2.56	2.53	1.01
ETF190-N75-NH	189.8	45.5	14.8	360.5	75	-	2.77	2.88	0.96
ETF190-N100-NH	190.5	44.9	15.0	385.0	100	-	3.08	3.21	0.96
ETF190-N50-UH	189.5	44.9	15.2	334.8	50	-	1.98	2.02	0.98
ETF190-N75-UH	190.3	45.5	15.0	360.5	75	-	2.20	2.30	0.96
ETF190-N100-UH	189.7	44.8	14.8	384.5	100	-	2.45	2.53	0.97
ETF190-N50-EH	189.8	44.8	14.9	334.5	50	13	2.72	2.78	0.98
ETF190-N75-EH	190.2	45.2	15.2	360.5	75	13	3.08	3.16	0.97
ETF190-N100-EH	190.5	45.5	15.0	385.0	100	13	3.41	3.52	0.97
Mean									0.97
COV									0.02
(c) IOF									
IOF240-N50-NH	236.3	45.1	18.6	970.0	50	-	16.07	15.84	1.01
IOF240-N75-NH	238.2	44.8	17.6	994.7	75	-	17.30	17.17	1.01
IOF240-N100-NH	237.6	44.8	17.6	1020.0	100	-	18.50	18.79	0.98
IOF240-N50-UH	235.1	44.8	17.5	969.0	50	-	15.72	15.74	1.00
IOF240-N75-UH	236.5	45.2	17.8	994.3	75	-	16.64	17.01	0.98
IOF240-N100-UH	235.5	45.0	17.6	1020.2	100	-	17.60	18.02	0.98
IOF240-N50-EH	236.3	44.8	17.4	969.3	50	13	16.26	15.86	1.03
IOF240-N75-EH	236.7	44.8	17.8	994.3	75	13	17.54	18.19	0.96
IOF240-N100-EH	237.7	45.0	17.7	1020.9	100	13	18.83	19.50	0.97
Mean									0.99
COV									0.02
(d) EOF									
EOF240-N50-NH	237.33	44.35	17.72	920.0	50	-	5.82	5.81	1.00
EOF240-N75-NH	237.21	44.97	17.78	970.1	75	-	6.41	6.23	1.03
EOF240-N100-NH	237.58	45.10	17.81	1019.5	100	-	6.90	6.63	1.04
EOF240-N50-UH	236.73	44.84	17.48	920.1	50	-	4.22	4.26	0.99
EOF240-N75-UH	235.28	44.84	17.81	970.7	75	-	4.60	4.65	0.99
EOF240-N100-UH	236.32	45.10	17.78	1019.2	100	-	4.95	4.93	1.00
EOF240-N50-EH	238.00	44.93	17.74	919.3	50	13	5.74	5.57	1.03
EOF240-N75-EH	236.83	44.57	17.55	969.5	75	13	6.30	6.30	1.00
EOF240-N100-EH	237.50	44.80	17.47	1020.9	100	13	6.80	6.69	1.01
Mean									1.01
COV									0.02

3.3. Parametric study

A comprehensive parametric study was conducted on CFS channel sections with elongated unstiffened and edge-stiffened web holes (see Figure 2-4 and Figure 3–5) under four different loading conditions. These parameters included the ratio of hole width to the flat web depth (d_w/d_1), the ratio of hole length to hole width (b_w/d_w), the ratio of edge-stiffener length to flat web depth (q/d_1), the ratio of bearing length to section thickness (N/t), and the ratio of the inside fillet radius between the web and edge stiffener to flat web depth (r_q/d_1).

The values of the parameters investigated in the parametric study are summarized in Table 3-2. Appendix A-F presents the web crippling strengths of CFS channels with plain webs, unstiffened web holes, and edge-stiffened web holes, as determined from the FEA results. The labelling system for the specimens in the parametric study is illustrated in Figure 3-6.

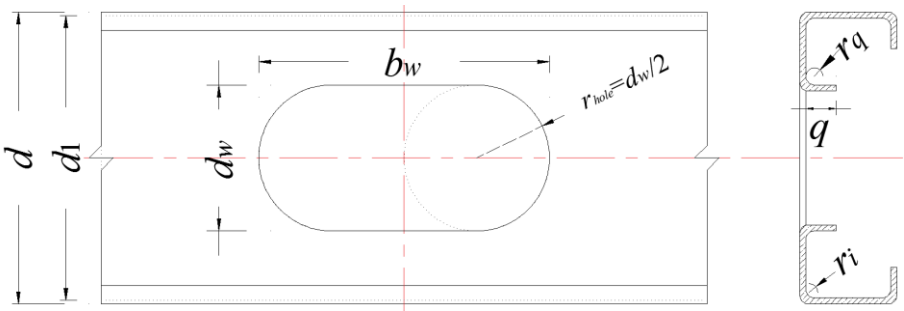

Figure 3-5 Elongated edge-stiffened web holes details

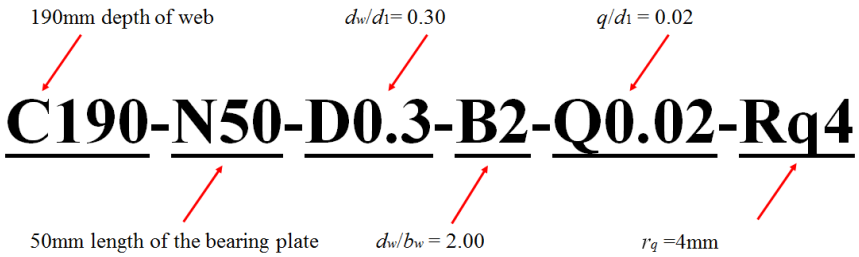

Figure 3-6 Specimen labelling in the parametric study

Table 3-2 Different variables used in the parametric study

Load cases	Sections (mm)	Elongated web holes		N (mm)	Q q/d_1	r_q (mm)	t (mm)
		d_w/d_1	b_w/d_w				
ITF	190×45×15, 240×45×15	0,0.3,0.5,0.7	2, 2.5, 3	50,75,100	0.02,0.06,0.10	2, 3, 4, 6	1.5
ETF	190×45×15	0,0.3,0.5,0.7	2, 2.25, 2.5, 2.75, 3	50,75,100	0.04, 0.06, 0.08, 0.10	2, 3, 4, 6	1,1.5
IOF	240×45×15	0, 0.2,0.4,0.6	1.4, 1.8, 2.2	50,75,100	0.04, 0.06, 0.08	2, 3, 4	1.5, 2, 2.5
EOF	240×45×15	0, 0.2,0.4,0.6	1.4, 1.8, 2.2	50,75,100	0.04, 0.06, 0.08	2, 3, 4	1.5, 2, 2.5

3.3.1. Effects of d_w/d_1 and b_w/d_w

The effect of d_w/d_1 on the R_P for the ITF loading case is illustrated in Figure 3-7(a). A decrease in R_P was observed for the channel section C190-N50-B2 as the d_w/d_1 ratio increased from 0.3 to 0.7. Figure 3-7(a) highlights the significant influence of d_w/d_1 on R_P, particularly for specimens with smaller edge-stiffener length ratios (i.e., Q0.02) and smaller edge-stiffener fillet radii (e.g., Rq2). For the ETF loads, a decrease of 37% of the web crippling strength for the specimen UH-N75-B2.5-T1.5 was observed when the values of d_w/d_1 increased from 0.3 to 0.7. For the CFS channels with elongated un-stiffened web holes, their web crippling strength could be increased by using edge-stiffened web holes. When the d_w/d_1 is equal to 0.7, the web crippling strength of the specimen EH-N75-B2.5-Q0.08-Rq4-T1.5 increases by 73% compared to the equivalent channel with an un-stiffened web hole, as shown in Figure 3-7(b). A decrease of 33% and 20% in the web crippling strengths was observed for the specimen UH-N100-B1.8-T2.0 under IOF and EOF loading conditions (see Figures 3-7(c) and 3-7(d)), respectively, as the d_w/d_1 values increased from 0.2 to 0.6. In the case of CFS channels with elongated un-stiffened web holes, their web crippling strengths were enhanced due to the presence of edge-stiffened web holes. Especially for large web openings, the primary compressive load transfer path within the web is significantly disrupted. As the opening approaches the bearing region, the effective web depth is substantially reduced, resulting in

pronounced strength degradation and a transition from conventional web crippling to a coupled failure mode involving hole-edge yielding, flange rotation, and localized web buckling, as observed in specimen UH-N100-B1.8-T2.0 in Figure 3-7(c). Consequently, the web crippling strength exhibits markedly higher sensitivity to both opening size and location. When the values of d_w/d_1 reached 0.6, the web crippling strengths of the specimen EH-N100-B1.8-Q0.06-Rq3-T2.0 under the IOF and EOF loading conditions, respectively, increased by 39% and 46% when compared to the equivalent channels with un-stiffened web holes.

In Figure 3-8(a), for the channels C190-N50-Rq2, when the d_w/b_w increased from 2.00 to 3.00, the R_P showed a downward trend with different q/d_1 and d_w/d_1. Compared to CFS sections with a plain web, for the case of an elongated un-stiffened web hole, the average reduction for sections with an aspect ratio of 2 and 3 was 39% and 49%, respectively. However, for an elongated edge-stiffened hole, the reduction in the web crippling strength was reduced to only 2% and 16%, respectively. It can be seen from Figure 3-8(b) that web crippling strengths showed a downward trend, especially for those specimens with un-stiffened web holes, when the d_w/b_w increased from 2 to 3. When the ratio of d_w/b_w is equal to 3, the web crippling strengths of the specimens UH-N75-D0.7-T1.5 and EH-N75-D0.7-Q0.08-Rq4-T1.5 decreased by 57% and 8%, respectively, compared to the specimen NH-N75-T1.5. Compared to sections having a plain web, for the case of an elongated un-stiffened web hole having an aspect ratio of two and three, the average reduction in web crippling strength was 21.23% and 35.67%, respectively. However, for an edge-stiffened hole, the reduction in the web crippling strength was only 4.56% and 7.54%, respectively. In Figure 3-8(c), when the b_w/d_w ratio was 2.2, the web crippling strengths of specimens UH-N75-D0.6-T2.0 and EH-N75-D0.6-Q0.06-Rq3-T2.0 under the IOF loading condition decreased by 43% and 9%, respectively, in comparison to the

specimen NH-N75-T2.0. It is noteworthy that for specimen UH-N75-D0.6-T2.0, a pronounced reduction in web crippling strength was observed as the b_w/d_w ratio increased from 1.8 to 2.2. This reduction is primarily attributed to the elongated web hole moving closer to the region of localized loading, whereby the unstiffened web opening becomes a critical weak point. This observation indicates that web crippling behaviour is highly sensitive to the location of web openings relative to the load application. In contrast, the use of edge-stiffened web holes effectively mitigates this adverse effect, significantly reducing the strength degradation associated with web openings. Similarly, for CFS channels with un-stiffened and edge-stiffened web holes under the EOF loading condition, the web crippling strengths were 44% and 15% lower than those of plain channels, respectively, as shown in Figure 3-8(d).

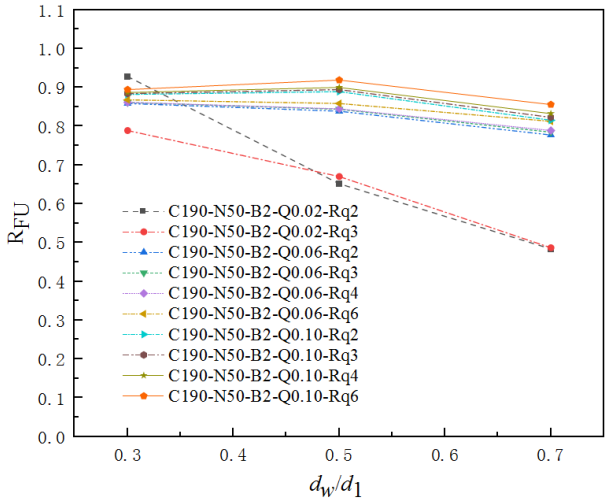

(a) ITF

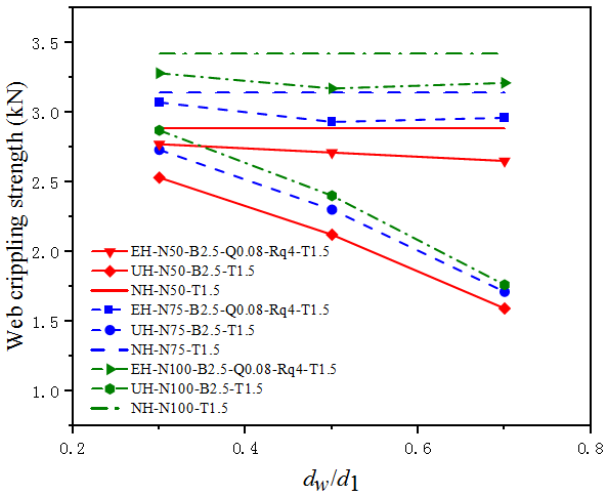

(b) ETF

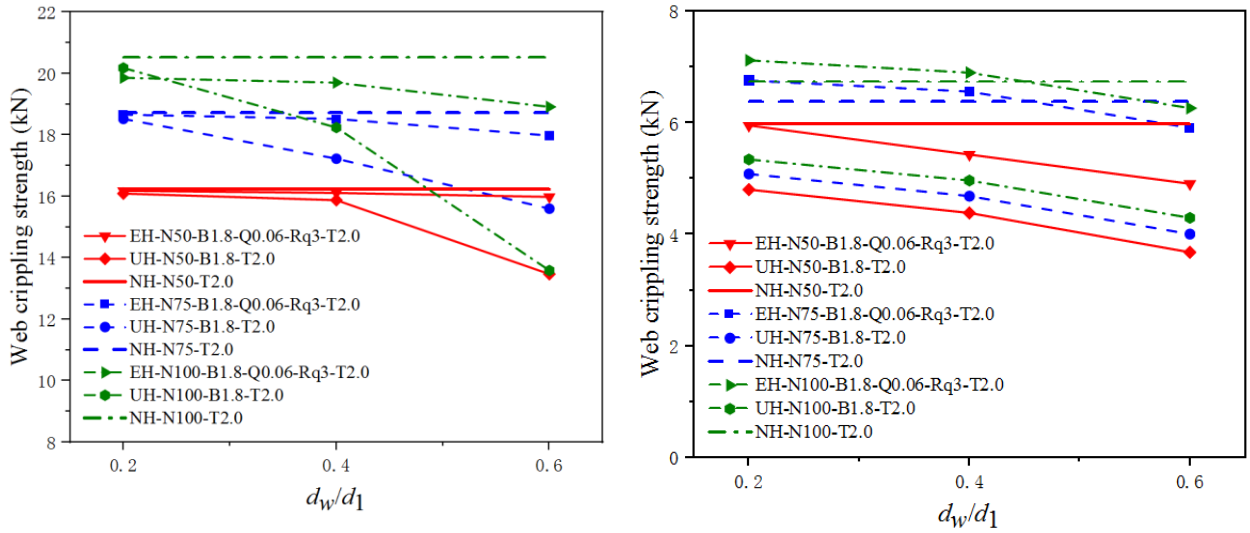

(c) IOF (d) EOF

Figure 3-7 Variation in reduction factor/web crippling strength with d_w/d_1

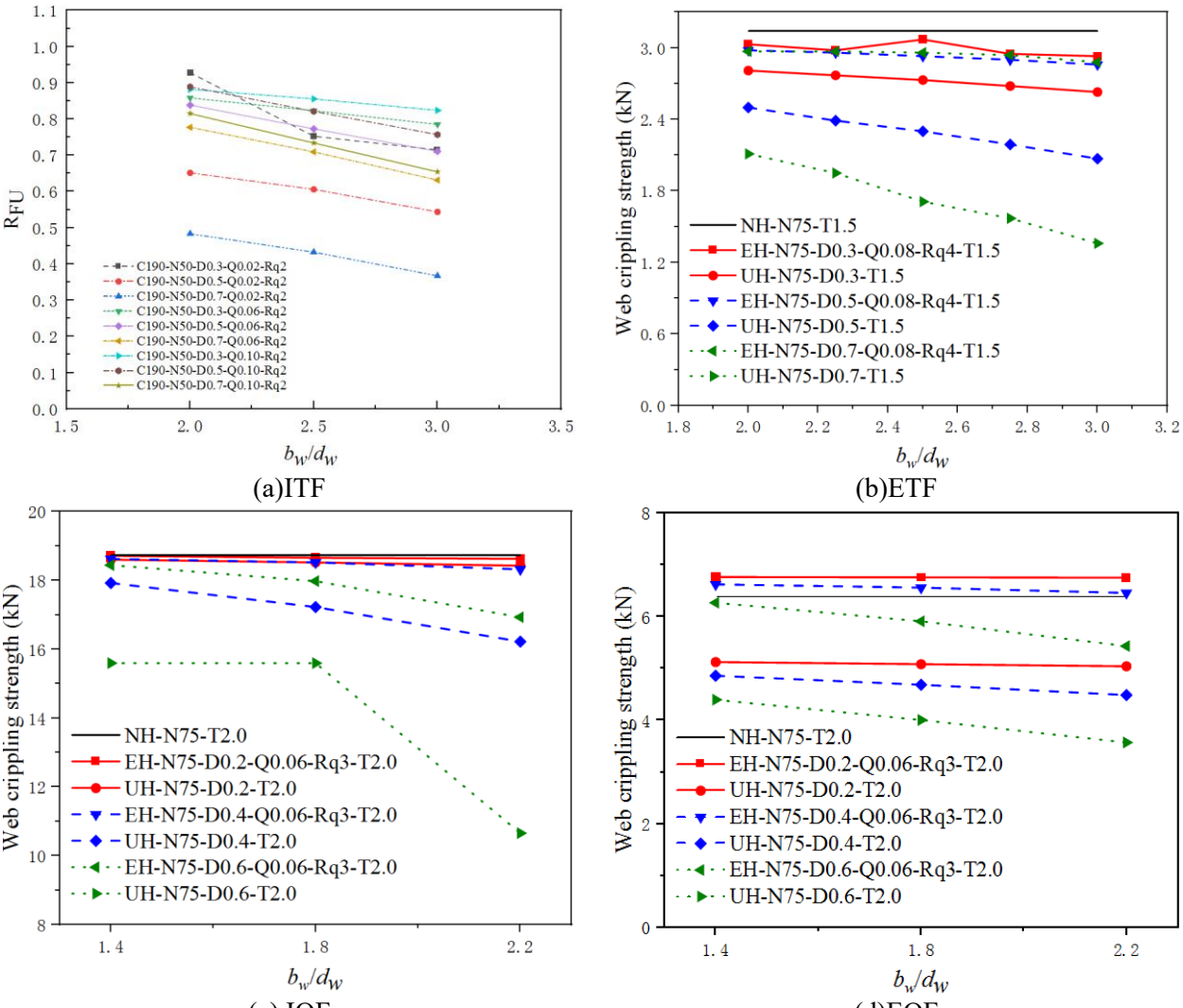

(a)ITF (b)ETF

(c) IOF (d)EOF

Figure 3-8 Variation in reduction factor/web crippling strength with b_w/d_w

3.3.2. Effects of r_q/t, N/d_1 and q/d_1

The effects of the r_q/t, N/d_1, and q/d_1 on the R_P/web crippling strength were shown in Figures 3-9, 3-10 and 3-11, respectively. It can be seen from Figure 3-9(a) that the values of the R_P for the channels C190-N50-D0.3 under ITF loading have a slight increase when the r_q/t increased from 1.33 to 4.00. The effect of r_q/t on the web crippling strength under ETF loading is shown in Figure 3-9(b). The r_q/t has a small effect on the web crippling strengths of the specimens with elongated edge-stiffened web holes. It is important to note that the web crippling strength of the specimen with an edge-stiffened web hole (EH-N75-D0.5-B2.5-Q0.08-T1.0) exceeded the web crippling strength of the equivalent section with a plain web (NH-N75-T1.0). In the case of web crippling, the use of elongated edge-stiffened holes almost results in the same strength as an equivalent channel-section with a plain web. The ratio r_q/t has a minor effect on the web crippling strengths of channels with elongated web holes for both IOF and EOF loading conditions as shown in Figures 3-9(c) and 3-9(d). It's worth noting that using an elongated edge-stiffened hole almost results in the same strength as an equivalent channel with a plain web. For example, the web crippling strength of the channel with an edge-stiffened web hole (EH-N75-D0.4-B1.8-Q0.06-T2.5) even exceeded that of the equivalent channel with a plain web (NH-N75-T2.5).

It can be seen from Figure 3-10(a) that the variation of N/d_1 has a slight effect on the R_P of the channels C190-Q0.02-Rq2. It can be seen from Figure 3-10(b) that web crippling strengths under ETF loadings all showed an increasing trend with increasing bearing lengths for CFS channels with edge-stiffened web holes, un-stiffened web holes, and plain webs. Similarly, the effect of N/d_1 ratio on the web crippling strengths is depicted in Figures 3-10(c) and 3-10(d). It is evident that as the bearing lengths increase, the web

crippling strengths of CFS channels with edge-stiffened web holes, un-stiffened web holes, and plain webs under IOF and EOF loading conditions exhibit an increasing trend.

The effect of the q/d_1 on the R_P was shown in Figure 3-11(a). It is important to note that for the channels C190-N50-Rq2, q/d_1 had a significant effect on the R_P, especially for those specimens with a large aspect ratio (i.e., B3.0) and a large ratio of the width of the hole to the depth of the web (i.e., D0.7). For instance, the R_P of channels C190-N50-D0.7-B3.0-Rq2 increased from 0.37 to 0.65 when the ratio q/d_1 increased from 0.02 to 0.10. The effect of q/d_1 on the web crippling strength under ETF loads is shown in Figure 3-11(b). The web crippling strength of the specimen EH-N75-D0.5-B2.5-Rq4-T1.5 increased by 4% when q/d_1 increased from 0.04 to 0.10. The effect of q/d_1 ratio on the web crippling strengths is shown in Figure 3-11(c) and 3-11(d). For the specimen EH-N75-D0.4-B1.8-Rq3-T2.0, subjected to IOF and EOF loading conditions, there was a respective 0.4% and 1.4% increase in web crippling strengths as the q/d_1 ratio increased from 0.04 to 0.08. From the FEA results, it is evident that among the five variables studied (d_w/d_1, b_w/d_w, r_q/t, N/d_1, and q/d_1), d_w/d_1, b_w/d_w, and N/d_1 ratios had the most significant effects on the web crippling strengths of these channels.

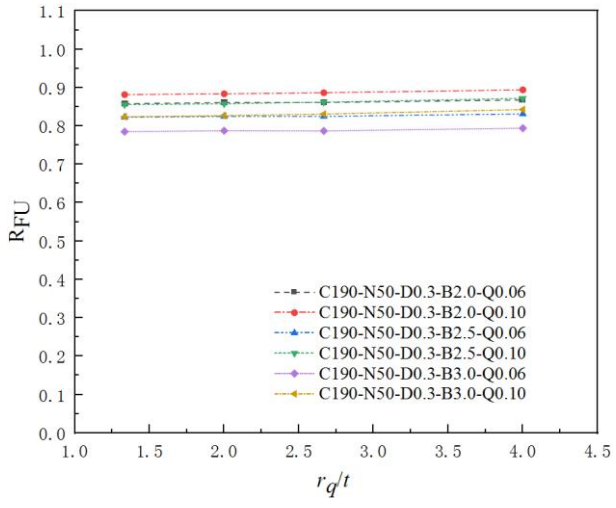

(a)ITF

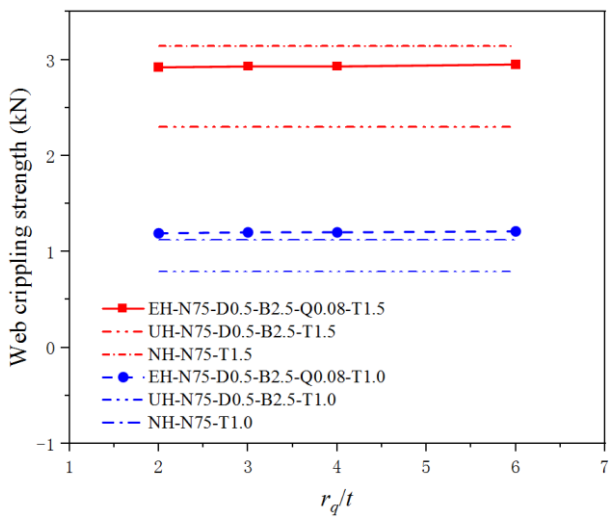

(b)ETF

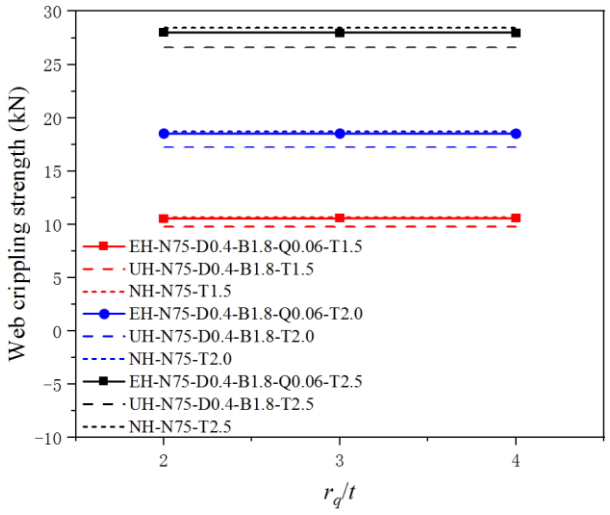

(c) IOF

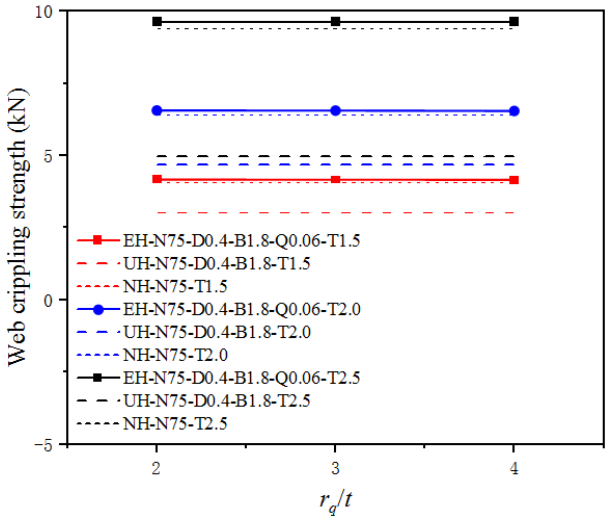

(d)EOF

Figure 3-9 Variation in reduction factor/web crippling strength with r_q/t

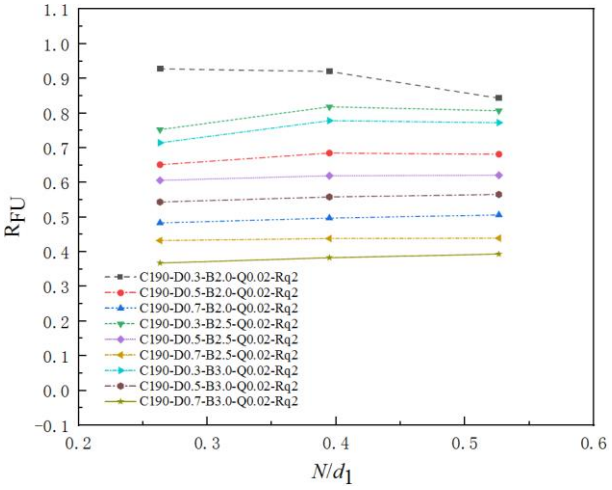

(a)ITF

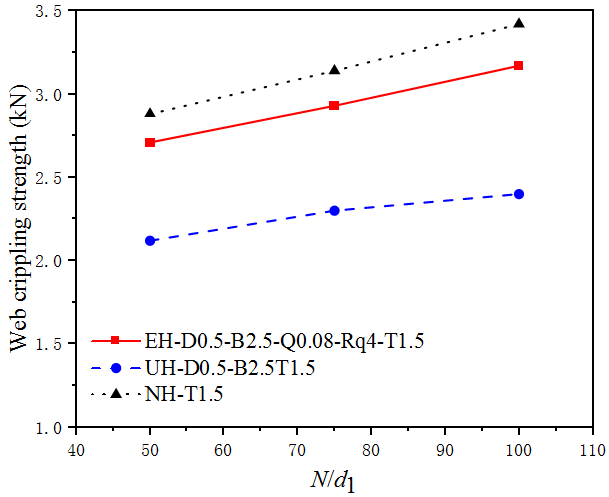

(b)ETF

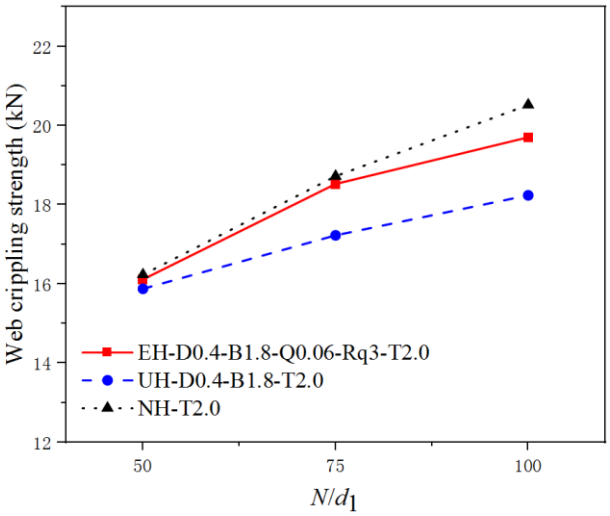

(c) IOF

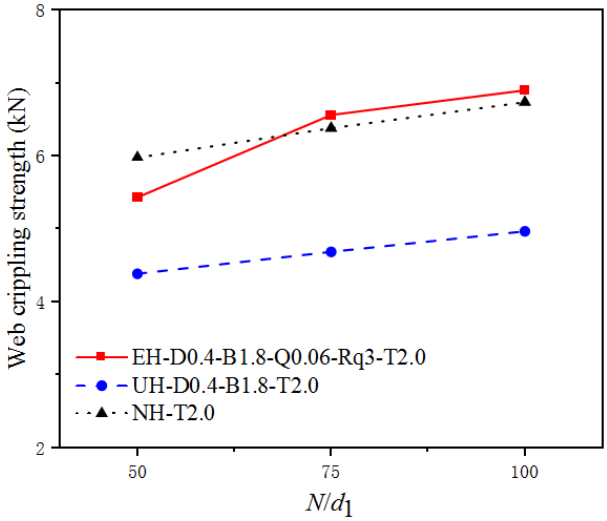

(d)EOF

Figure 3-10 Variation in reduction factor/web crippling strength with N/d_1

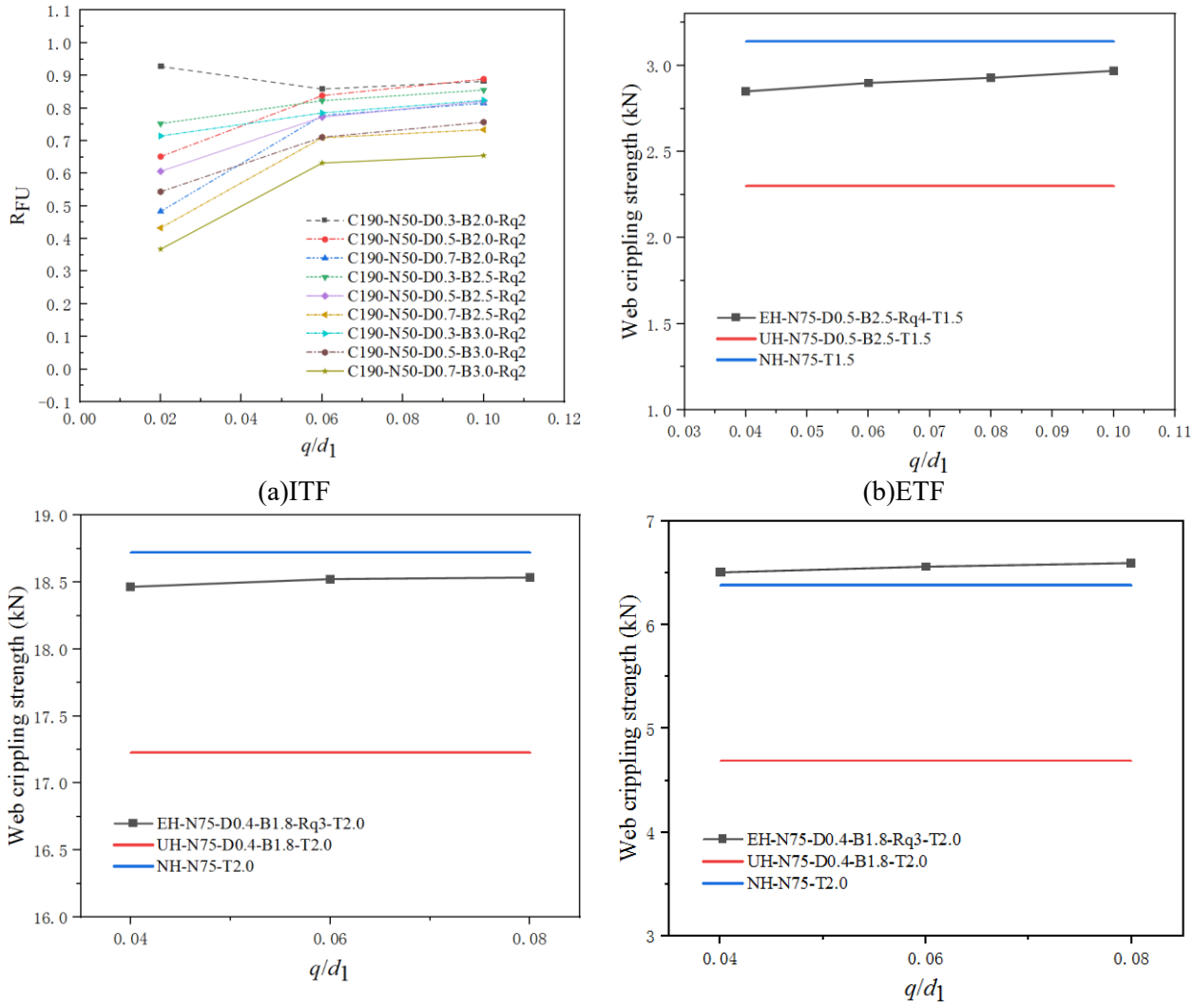

(a)ITF (b)ETF

(c) IOF (d)EOF

Figure 3-11 Variation in reduction factor/web crippling strength with q/d_1

3.4. Proposed web crippling design equations

3.4.1. Proposed R_p equations

The evaluation of numerical simulation results revealed that the parameters d_w/d_1, b_w/d_w, r_q/t, N/d_1, and q/d_1 significantly influenced the reduction factor (R_p) for CFS channels with elongated edge-stiffened web holes. Using regression analysis performed in Origin, equations were developed to predict R_p. These proposed equations are presented as follows:

For the CFS channels under ITF loadings,

$$R_{P1} = 1.13 - 0.41\left(\frac{d_w}{d_1}\right) - 0.11\left(\frac{b_w}{d_w}\right) - 0.16\left(\frac{N}{d_1}\right) + 0.01\left(\frac{r_q}{t}\right) + 2.04\left(\frac{q}{d_1}\right) \le 1 \quad \text{Equation 3.1}$$

For the CFS channels under ETF loadings,

$$R_{P2} = 1.00 - 0.04\left(\frac{d_w}{d_1}\right) - 0.04\left(\frac{b_w}{d_w}\right) - 0.03\left(\frac{N}{d_1}\right) + 0.03\left(\frac{r_q}{t}\right) + 0.88\left(\frac{q}{d_1}\right) \le 1 \quad \text{Equation 3.2}$$

For the CFS channels under IOF loadings,

$$R_{P3} = 1.14 - 0.11\left(\frac{d_w}{d_1}\right) - 0.04\left(\frac{b_w}{d_w}\right) - 0.23\left(\frac{N}{d_1}\right) + 0.004\left(\frac{r_q}{t}\right) + 0.30\left(\frac{q}{d_1}\right) \quad \text{Equation 3.3}$$

For the CFS channels under EOF loadings,

$$R_{P4} = 1.07 - 0.38\left(\frac{d_w}{d_1}\right) - 0.07\left(\frac{b_w}{d_w}\right) + 0.48\left(\frac{N}{d_1}\right) + 0.002\left(\frac{r_q}{t}\right) + 0.45\left(\frac{q}{d_1}\right) \quad \text{Equation 3.4}$$

It was found that the values of the web crippling strength reduction factor for ITF loadings were much larger than or much less than 1 when Q is 0.02, which means Equation 3.1 were no longer applicable. To accurately determine the range of application of these equations, the effects of q and r_q on R_{FEA}/R_{P1} were investigated in Appendix A(e), and it was found that the proposed equations were unreliable to predict the web crippling strength reduction factor when q/d_1 was less than 0.025. Overall, the limitations for the proposed equations are: $0.025 \le q/d_1 \le 0.10$, $0.30 \le d_w/d_1 \le 0.70$, $0.27 \le N/d_1 \le 0.54$, 2 mm $\le r_q \le$ 6 mm, and $2.00 \le b_w/d_w \le 3.00$. For Equation 3.2, the limitations are: $0.04 \le q/d_1 \le 0.10$, $0.30 \le d_w/d_1 \le 0.70$, $2.00 \le b_w/d_w \le 3.00$, $0.27 \le N/d_1 \le 0.54$, and 2 mm $\le r_q \le$ 6 mm. For Equations 3.3 and 3.4, the limitations are: $0.04 \le q/d_1 \le 0.08$, $0.20 \le d_w/d_1 \le 0.60$, $1.40 \le b_w/d_w \le 2.20$, $0.21 \le N/d_1 \le 0.43$, and 2 mm $\le r_q \le$ 4 mm. The comparison of web crippling capacities of CFS specimens from the parametric study with the proposed R_P equation in this chapter was shown in Figure 3-12.

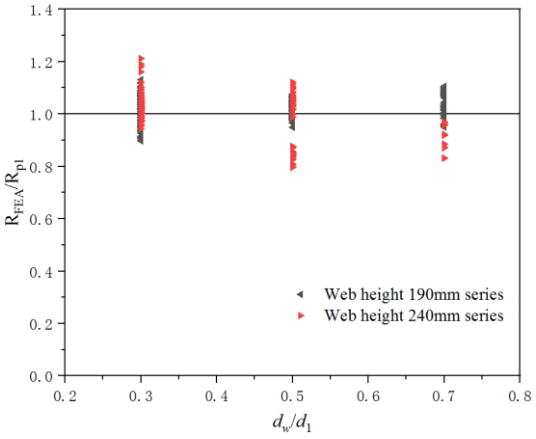

(a)Comparison of reduction factors for ITF loading condition

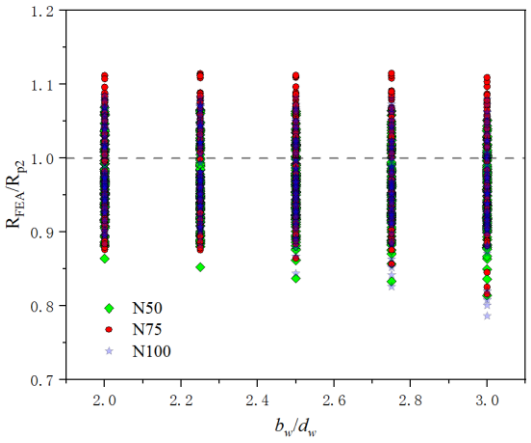

(b)Comparison of reduction factors for ETF loading condition

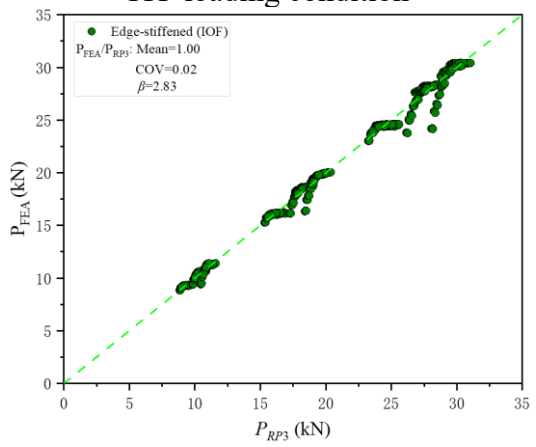

(c) Comparison of web crippling strength for IOF loading condition

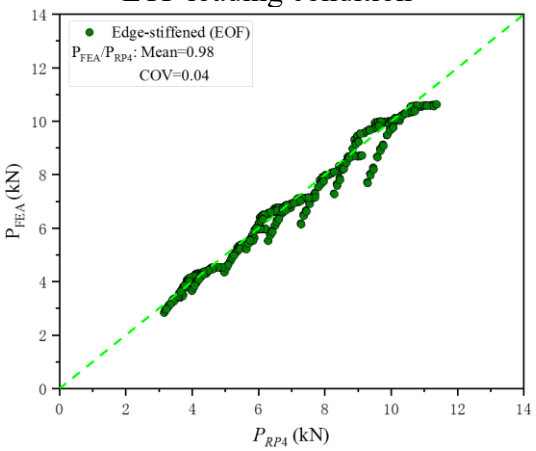

(d) Comparison of web crippling strength for EOF loading condition

Figure 3-12 Comparison of FEA results and R_p equations

3.4.2. Proposed DSM-based equations

The application of web crippling strength reduction factor equations was limited to some specific CFS channel sections and did not consider the effects of r_i, b_f and f_y. The DSM offers an alternative approach for predicting the web crippling strength of CFS channels, providing a more general framework as it encompasses all buckling modes within a single methodology. Previous studies on DSM have primarily focused on the web crippling behavior of CFS plain channels. However, the methodology can be adapted to the present study to investigate the effects of elongated edge-stiffened web holes on the web crippling behavior of CFS channels. Several researchers (Keerthan et al., 2014; Natário et al., 2016,

2017) have proposed DSM-based web crippling design equations using a format of Equation 3.5 for CFS plain channels under different loading conditions.

$$P_b = n_3 P_{b,y}\left[1 - n_1\left(\frac{P_{b,cr}}{P_{b,y}}\right)^{n_2}\right]\left(\frac{P_{b,cr}}{P_{b,y}}\right)^{n_2} \qquad \text{Equation 3.5}$$

The critical buckling load ($P_{b,cr}$) and the yield load ($P_{b,y}$) were two key parameters in Equation 3.3. Sundararajah 2017 proposed DSM-based equations to predict the web crippling capacities of CFS plain channels, and they determined the $P_{b,cr}$ using elastic buckling FEA and the $P_{b,y}$ using idealized failure mechanisms based on the deformed shapes observed in tests and FEA.

The critical buckling loads of CFS channels were derived from linear buckling analyses (Sundararajah 2017) using ABAQUS. The nodal forces were used to simulate the load at the junction between the web and the flange. The boundary conditions were shown in Figure 3-13. FE models were developed to obtain the elastic critical buckling loads ($P_{b,cr}$) of CFS channel sections having elongated un-stiffened and edge-stiffened web holes, and the details of such specimens were shown in the Appendix A. $P_{b,cr}$ were used to calculate the buckling coefficient (k_{FEA}) using Equation 3.6.

$$P_{b,cr} = \frac{\pi^2 Ekt^3}{12(1-\nu^2)d_1} \qquad \text{Equation 3.6}$$

where k represents the critical buckling coefficient and d_1 represents the clear height of web.

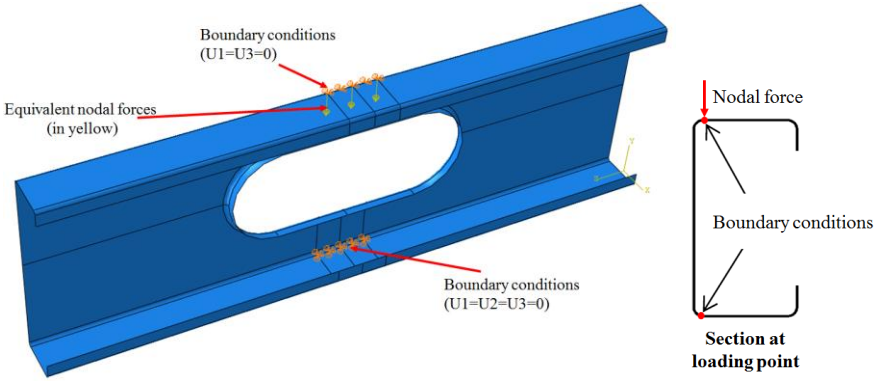

(a)ITF

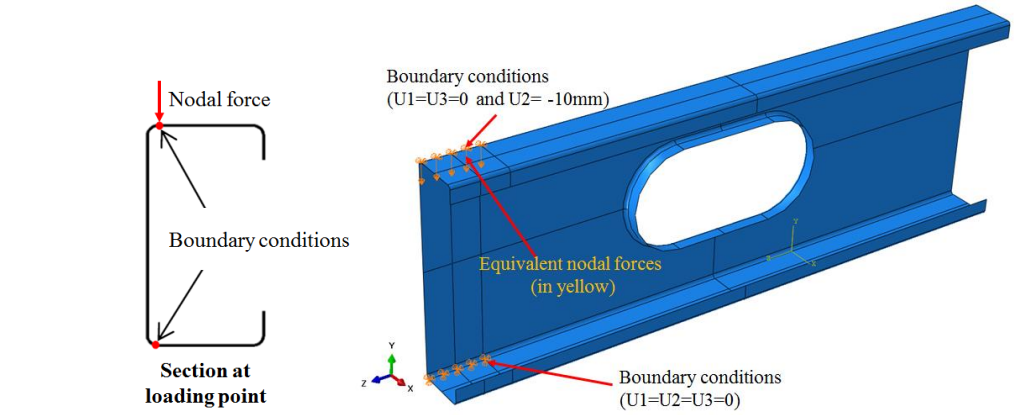

(b)ETF

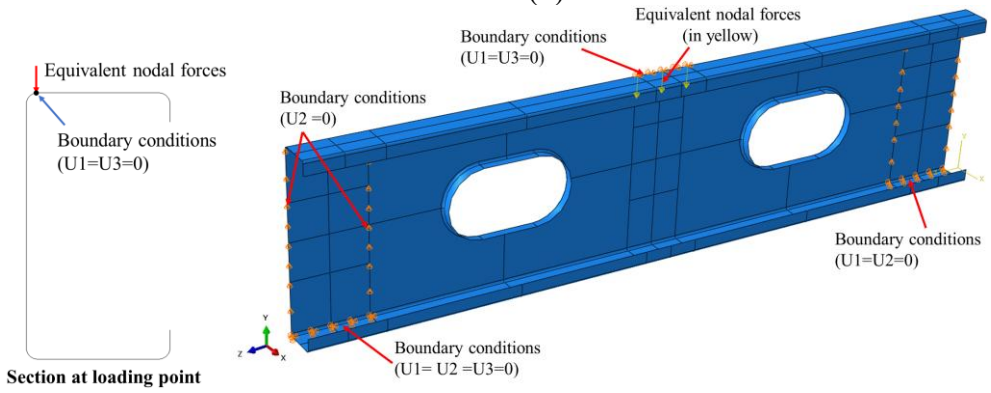

(c)IOF

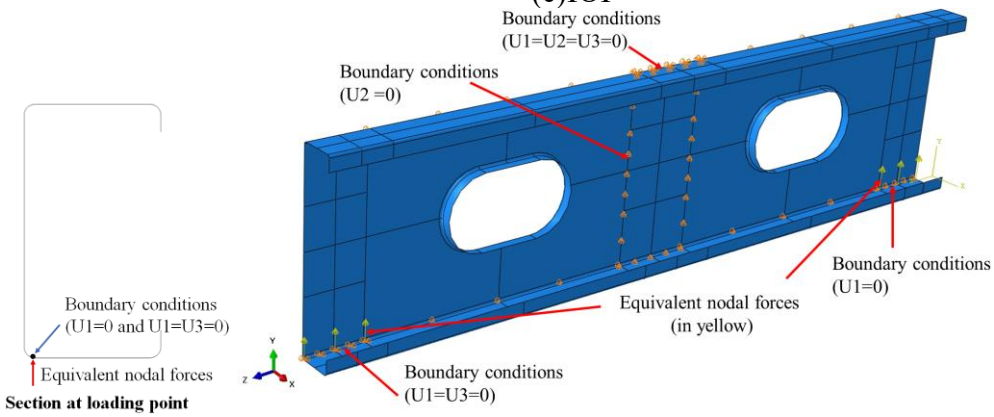

(d)EOF

Figure 3-13 Elastic buckling analysis

An equation considering the effects of elongated un-stiffened and edge-stiffened web holes on the web crippling strength of CFS channels was proposed with nine different coefficients linking the eight key parameters in the form of Equation 3.7 to calculate k_{prop}. The values of such coefficients were obtained based on the nonlinear regression analysis using Origin, as shown in Table 3-5.

$$k = C\left(1+C_1\sqrt{\frac{r_i}{t}}\right)\left(1+C_2\sqrt{\frac{d_1}{t}}\right)\left(1+C_3\sqrt{\frac{N}{t}}\right)\left(1+C_4\sqrt{\frac{b_f}{t}}\right)\left(1+C_5\sqrt{\frac{d_w}{t}}\right)\left(1+C_6\sqrt{\frac{b_w}{t}}\right)\left(1+C_7\sqrt{\frac{r_q}{t}}\right)\left(1+C_8\sqrt{\frac{q}{t}}\right) \quad \text{Equation 3.7}$$

where C represents the general coefficient, C_1, C_2, C_3, C_4, C_5, C_6, C_7 and C_8 were the coefficients of inside fillet radius of section to thickness ratio, web slenderness ratio, bearing length to thickness ratio, flange width to thickness ratio, width of the elongated web holes to thickness ratio, length of the elongated web holes to thickness ratio, inside fillet radius between web and hole edge-stiffener to thickness ratio and length of edge-stiffener to thickness ratio, respectively.

Table 3-3 Proposed buckling coefficients

Elongated web holes	C	C_1	C_2	C_3	C_4	C_5	C_6	C_7	C_8
Un-stiffened (ITF)	-3.47	0.25	-0.15	0.06	0.07	-0.05	-0.04	0	0
Edge-stiffened (ITF)	0.24	-0.30	-0.16	0.08	-3.25	0.07	-0.04	-0.01	0.03
Un-stiffened (ETF)	0.02	-0.16	0.61	0.05	1.21	0.01	-0.04	0	0
Edge-stiffened (ETF)	0.09	-0.14	0.16	0.05	0.33	0.03	-0.02	-0.01	0.03
Un-stiffened (IOF)	1.47	0.04	0.05	0.04	0.11	0.03	-0.05	0	0
Edge-stiffened (IOF)	2.49	-0.03	-0.02	0.04	0.06	0.01	0.00	0.01	0.03
Un-stiffened (EOF)	0.54	0.03	0.05	0.34	-0.08	0.03	-0.04	0	0
Edge-stiffened (EOF)	0.81	0.01	-0.02	0.29	-0.04	0.02	-0.02	0	0.02

Yield load ($P_{b,y}$) determination is difficult due to the complicated web crippling failure. Using the Principle of Virtual Work, some researchers (Natário et al., 2016, 2017) proposed a predictive equation in the form of Equation 3.8 for the calculation of $P_{b,y}$ using idealized plastic mechanisms for the case of unfastened flanges. Equations 3.9 - 3.16 were proposed to calculate N_m for CFS channels with elongated un-stiffened and edge-stiffened

web holes under four different loading cases, and the simplified yield mechanisms for the typical ultimate failure modes were shown in Figure 3-14.

$$P_{b,y} = f_y N_m \left(\sqrt{4r_m^2 + t^2} - 2r_m \right) \quad \text{Equation 3.8}$$

For CFS channels with un-stiffened web hole under ITF loadings,

$$N_{m1} = L - b_w \quad \text{Equation 3.9}$$

For CFS channels with edge-stiffened web hole under ITF loadings,

$$N_{m2} = \pi d_w \quad \text{Equation 3.10}$$

For CFS channels with un-stiffened web hole under ETF loadings,

$$N_{m3} = \frac{L - b_w}{2} \quad \text{Equation 3.11}$$

For CFS channels with edge-stiffened web hole under ETF loadings,

$$N_{m4} = \frac{L - b_w + \pi d_w}{2} \quad \text{Equation 3.12}$$

For CFS channels with un-stiffened web hole under IOF loadings,

$$N_{m5} = 1.5d + N + d_w - b_w \quad \text{Equation 3.13}$$

For CFS channels with edge-stiffened web hole under IOF loadings,

$$N_{m6} = 1.5d + N + \frac{\pi d_w}{2} - b_w \quad \text{Equation 3.14}$$

For CFS channels with un-stiffened web hole under EOF loadings,

$$N_{m7} = N + 0.45d_1 \quad \text{Equation 3.15}$$

For CFS channels with edge-stiffened web hole under EOF loadings,

$$N_{m8} = N + \frac{1.5d - b_w}{2} + \frac{\pi d_w}{4} \quad \text{Equation 3.16}$$

where r_m represents the inside fillet radius from the mid-thickness line ($r_m = r_i + t/2$).

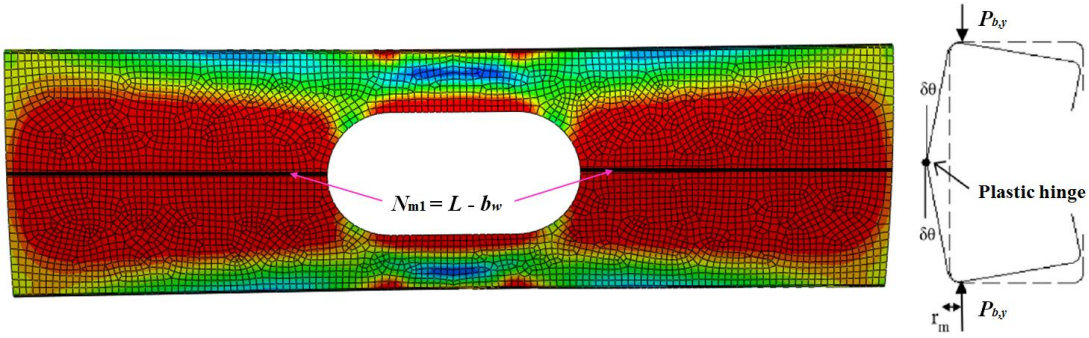

(i)Un-stiffened (C190-N100-D0.3-B2, t=1.5mm & f_y = 288 MPa)

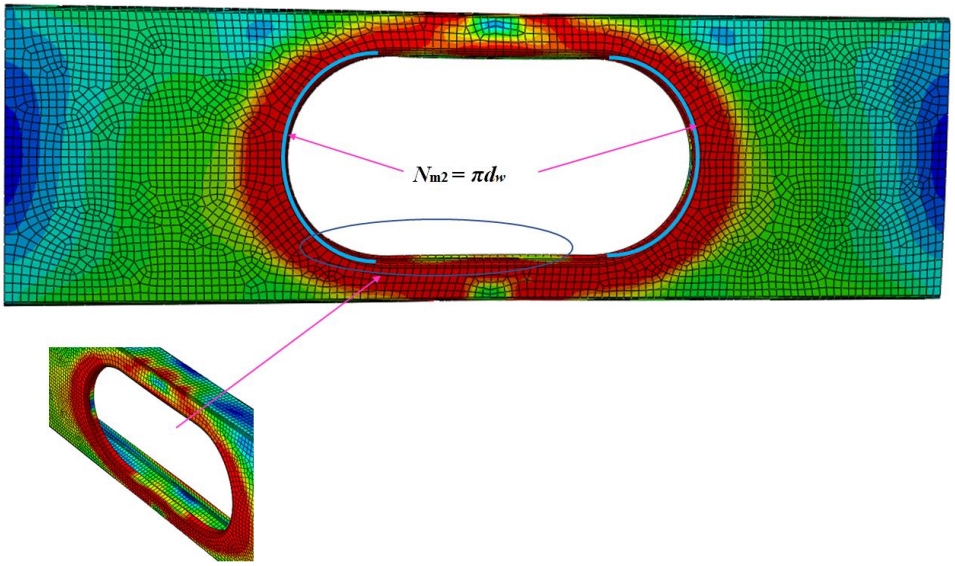

(ii)Edge-stiffened (C190-N50-D0.7-B2-Q0.06-Rq5, t=1.5mm & f_y = 288 MPa)

(a) ITF

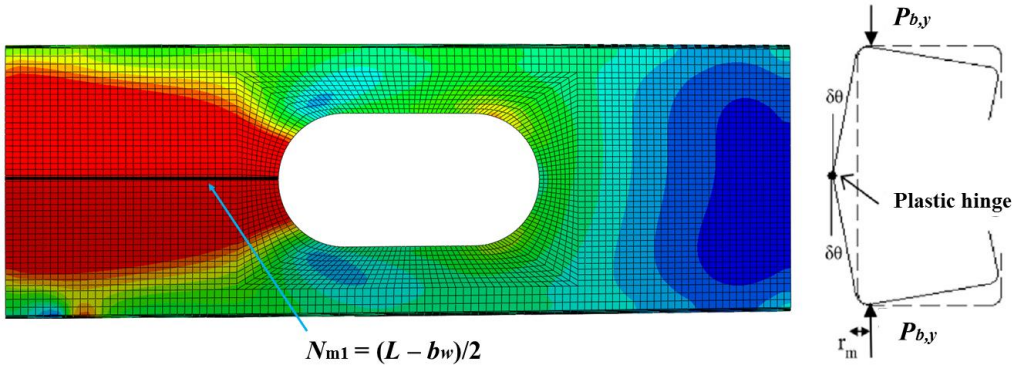

(i)Un-stiffened (UH-N50-D0.5-B2-T1.5, f_y = 288 MPa)

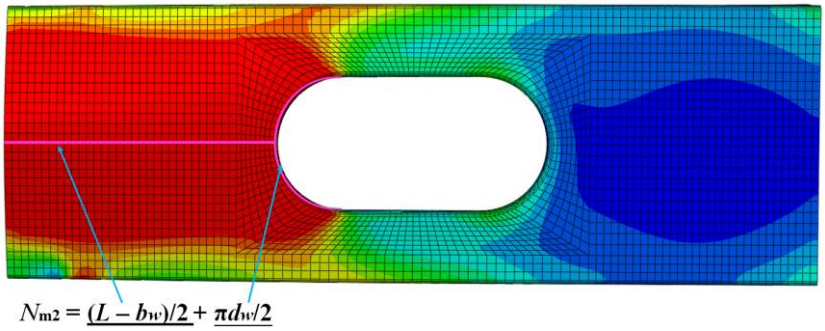

(ii)Edge-stiffened (EH-N50-D0.5-B2-Q0.06-Rq3-T1.5, f_y = 288 MPa)

(b) ETF

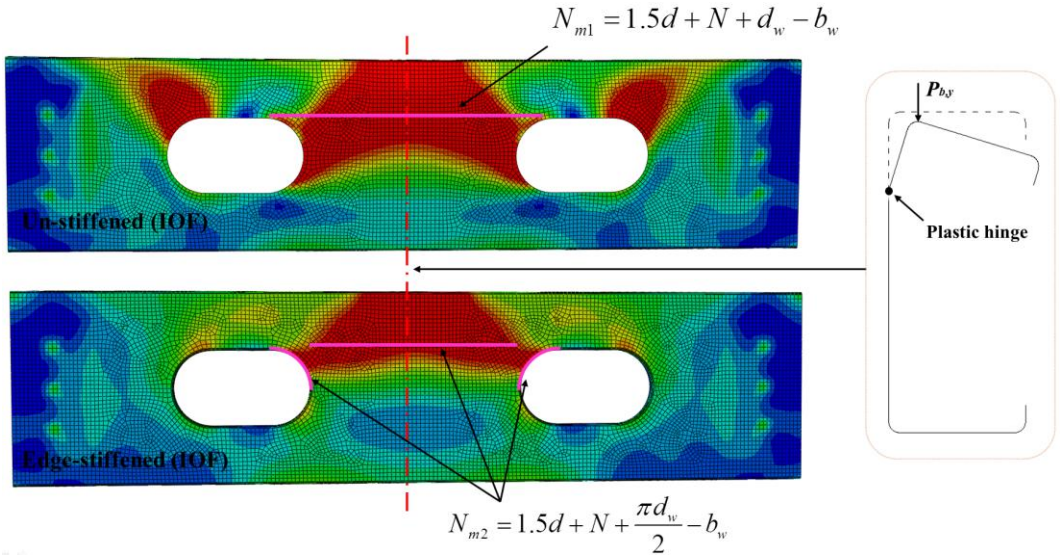

(c) IOF (N75-D0.4-B1.8 (-Q0.06-Rq3)-T2.0, f_y = 256.67 MPa)

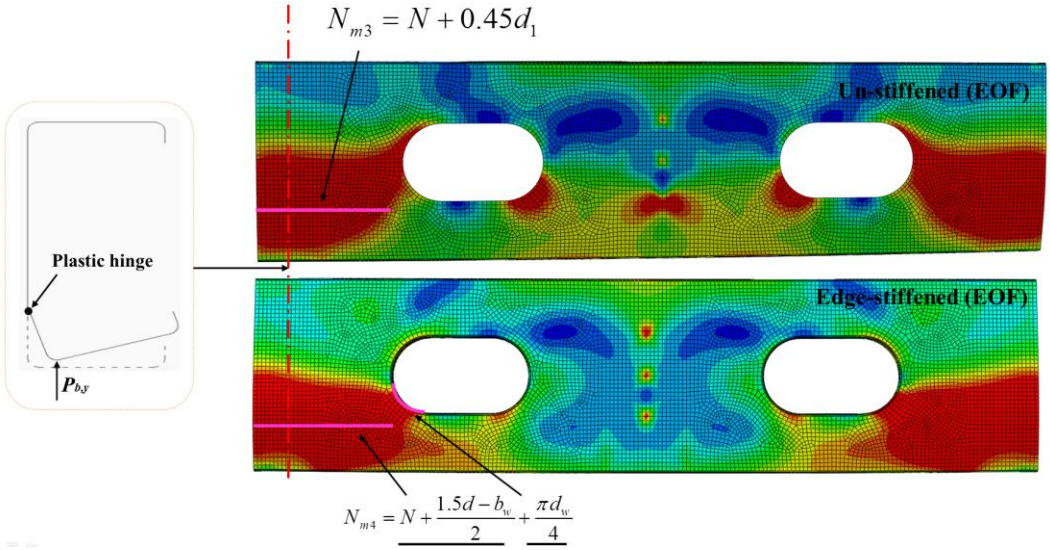

(d) EOF (N75-D0.4-B1.8 (-Q0.06-Rq3)-T2.0, f_y = 256.67 MPa)

Figure 3-14 Yield mechanism length

The unified DSM-based equations were proposed for CFS channels with elongated un-stiffened and edge-stiffened web holes to predict the web crippling strength. The suitable coefficients n_1 and n_2 need to be determined for the Equations 3.17 and 3.18, and these coefficients are summarized in Table 3-4. Using Origin, a regression analysis was performed to obtain such coefficients based on the results of the parametric study, and the DSM-based equations were then proposed. The comparison of web crippling capacities of CFS specimens from the parametric study with the proposed DSM-based equation in this work was shown in Figure 3-15. Table 3-5 showed the results of comparing the web crippling strength determined from proposed equations and the parametric study. The findings from Table 3-5 showed that the ratio P_{FEA}/P_{RP1} is 1.05 with a COV of 0.10, and the ratio P_{FEA}/P_b is 1.00 with a COV of 0.06. The DSM-based equation shows less variability compared to another equation.

For $\lambda \leq \alpha$, $P_b = P_{b,y}$ Equation 3.17

For $\lambda > \alpha$, $\frac{P_b}{P_{b,y}} = \left[1 - \delta\left(\frac{P_{b,cr}}{P_{b,y}}\right)^{\gamma}\right]\left(\frac{P_{b,cr}}{P_{b,y}}\right)^{\gamma}$ Equation 3.18

$\lambda = \sqrt{\frac{P_{b,y}}{P_{b,cr}}}$ Equation 3.19

Table 3-4 Proposed DSM-based equation coefficients

Elongated web holes (loading cases)	α	δ	γ
Un-stiffened (ITF)	0.938	0.11	1.07
Edge-stiffened (ITF)	0.938	0.11	1.07
Un-stiffened (ETF)	0.828	0.20	0.86
Edge-stiffened (ETF)	0.673	0.25	0.89
Un-stiffened (IOF)	0.38	0.24	0.28
Edge-stiffened (IOF)	0.44	0.25	0.41
Un-stiffened (EOF)	1.04	0.55	1.01
Edge-stiffened (EOF)	1.06	0.55	0.75

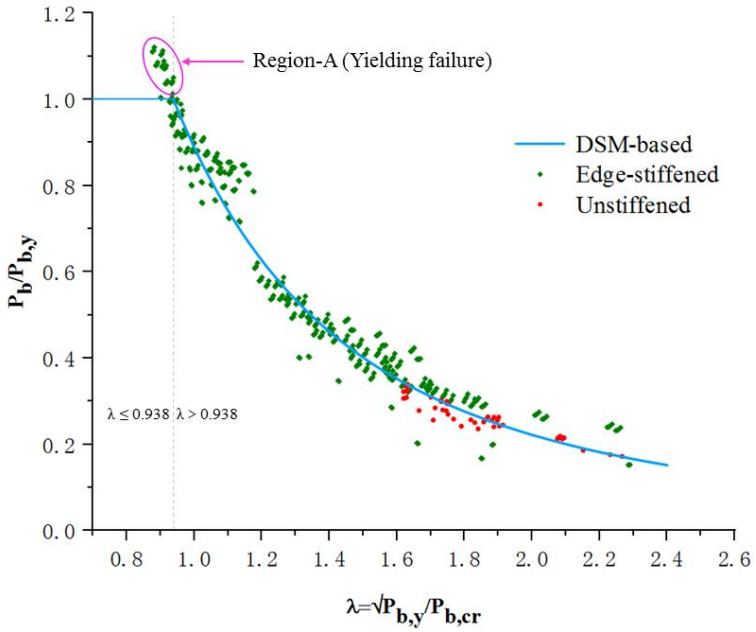

(a) ITF

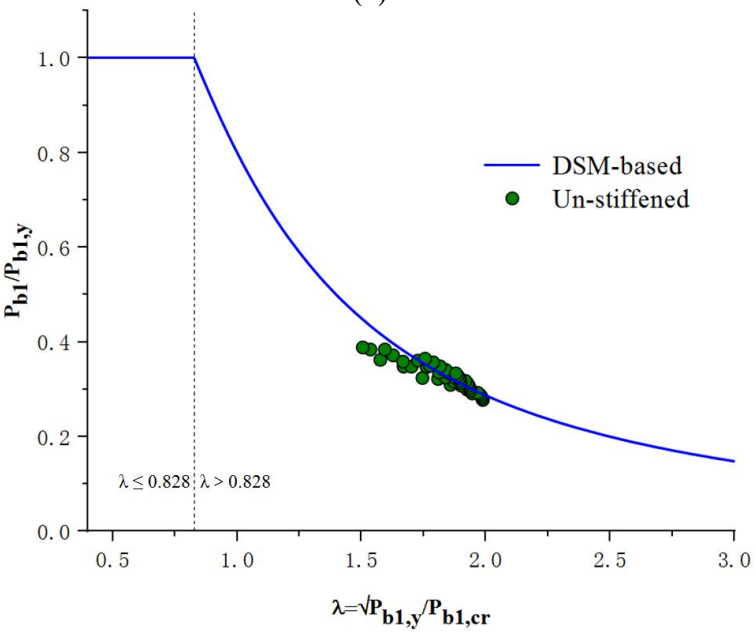

(i) Unstiffened

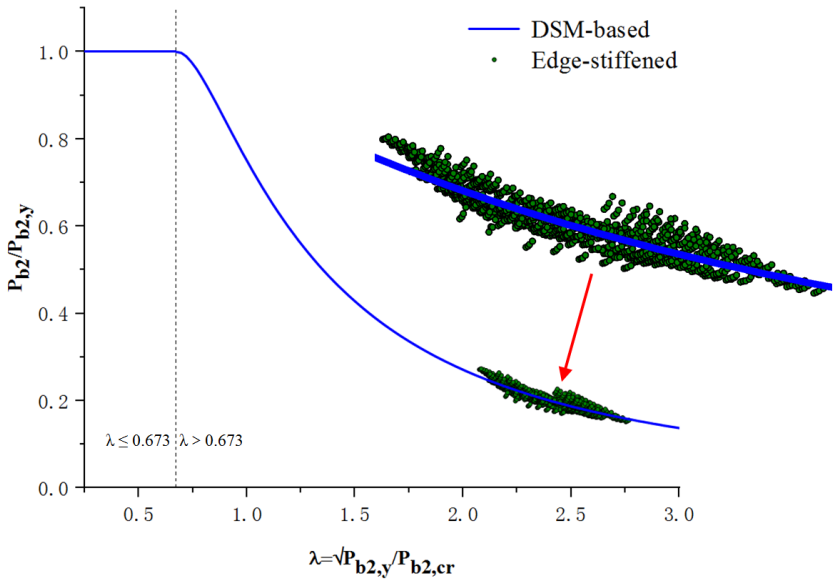

(ii) Edge-stiffened

(b) ETF

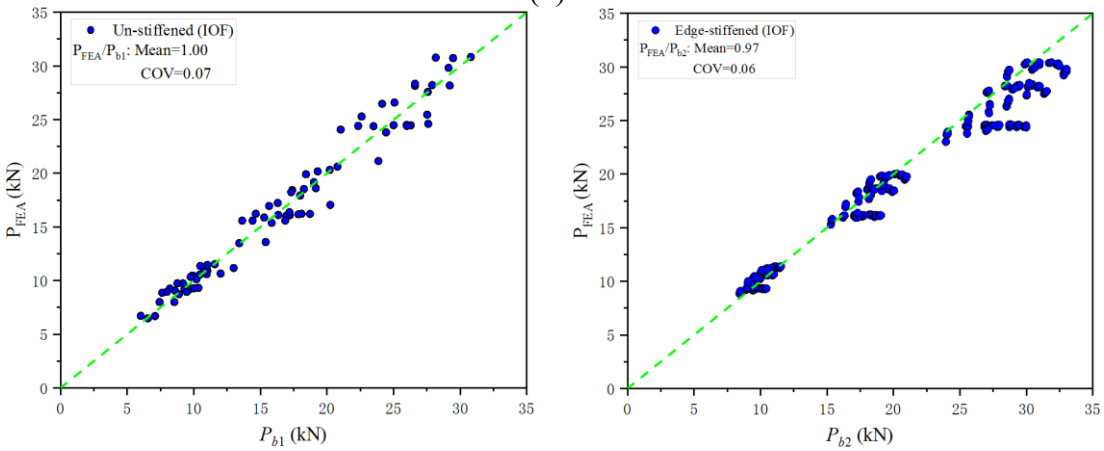

(i) Unstiffened (ii) Edge-stiffened

(c) IOF

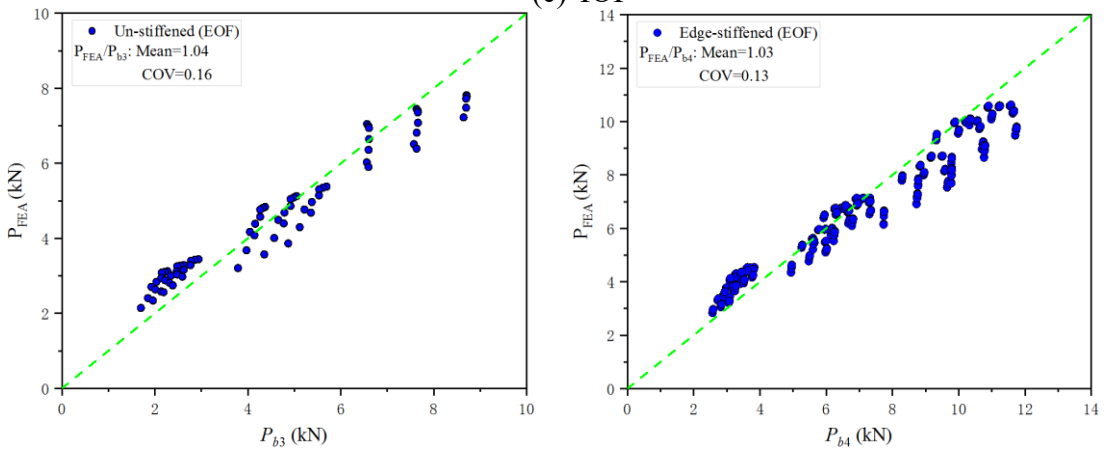

(i) Unstiffened (ii) Edge-stiffened

(d) EOF

Figure 3-15 Comparison of web crippling strength of specimens from a parametric study with proposed DSM-based equations

3.5. Reliability analysis

A reliability analysis was carried out to evaluate the reliability of the proposed design equations in the form of R_p and a DSM-based equation for CFS channels with elongated web holes. The reliability index (β) is a relative indicator of the design's safety, and AISI (2016) recommends a reliability index of 2.5 for CFS structural members. The design equations are considered dependable if the β is greater than or equal to 2.50. For the CFS structural members, the β could be determined using Equation 3.12.

$$\phi = 1.52\left(M_m F_m P_m\right) e^{-\beta\sqrt{V_M^2 + V_F^2 + C_P V_P^2 + V_Q^2}} \qquad \text{Equation 3.20}$$

$$C_P = \left(1 + \frac{1}{n}\right)\left(\frac{m}{m-2}\right) \qquad \text{Equation 3.21}$$

where M_m and V_M = mean values (1.10) and COV (0.1) of the material properties. F_m and V_F = mean values (1.00) and COV (0.05) of the fabrication factor. The statistical parameters P_m and V_P represent the load ratio's mean value and COV, respectively. V_Q = COV (0.21) of the load effect. A constant resistance factor (ϕ) of 0.85 was used in the reliability analysis. The correction factor (C_P) could be determined by Equation 3.21, and n and m are the number of specimens and degree of freedom ($m = n - 1$), respectively.

Table 3-5 summarizes the results of a reliability analysis. As a result, the β was higher than the desired value of 2.5, and the proposed equations could be used to predict web crippling strength the CFS channels with elongated edge-stiffened web holes under the four different loading conditions. The reliability of all the proposed DSM-based equations was demonstrated by means of statistical analyses, showing their suitability for incorporation into future revisions of international design codes for CFS structures. It is worth noting that, under EOF loading conditions, although the DSM-based design equations generally satisfy reliability requirements, a relatively large scatter in the

predicted strengths is still observed, with the coefficient of variation (COV) reaching up to 1.6 for specimens with un-stiffened web openings. This can be attributed to the highly complex response associated with this failure mode, which involves the interaction of local buckling, material yielding, and stress concentration around the elongated openings. Furthermore, the yield-line length calculation method proposed in this study requires further refinement when accounting for different elongated opening sizes. Additional parametric and experimental investigations are therefore recommended to improve the robustness of the proposed approach.

Table 3-5 Statistical analysis for proposed design equations

Statistical parameters	Load cases	Web holes	Mean, P_m	COV, V_p	Reliability index, β
P_{FEA}/P_{RP}	ITF	Edge-stiffened	1.01	0.07	2.53
P_{FEA}/P_{RP}	ETF	Edge-stiffened	1.00	0.06	2.73
P_{FEA}/P_{RP}	IOF	Edge-stiffened	1.00	0.02	2.83
P_{FEA}/P_{RP}	EOF	Edge-stiffened	0.98	0.04	2.72
P_{FEA}/P_b	ITF	Un-stiffened	1.01	0.06	2.64
P_{FEA}/P_b	ITF	Edge-stiffened	1.03	0.09	2.52
P_{FEA}/P_b	ETF	Un-stiffened	0.99	0.05	2.74
P_{FEA}/P_b	ETF	Edge-stiffened	1.00	0.05	2.79
P_{FEA}/P_b	IOF	Un-stiffened	1.00	0.07	2.72
P_{FEA}/P_b	IOF	Edge-stiffened	0.97	0.06	2.63
P_{FEA}/P_b	EOF	Un-stiffened	1.04	0.16	2.51
P_{FEA}/P_b	EOF	Edge-stiffened	1.03	0.13	2.60

3.6. Summary

This chapter presents the results of an investigation conducted on the web crippling behaviour of CFS channels with elongated edge-stiffened web holes under four different loading conditions. Nonlinear FE model was developed and validated against the experimental results reported by Chen et al. (2021) and Uzzaman et al. (2017). The results of the FEA and laboratory tests matched well. Using the validated FE model, a parametric study was carried out. The effects of q/d_1, d_w/d_1, b_w/d_w, N/d_1, and the r_q/t ratio on the web crippling strengths of CFS channels were investigated. The following conclusions can be drawn:

(1) From the results of the parametric study, it can be concluded that the ratios d_w/d_1, b_w/d_w, and N/d_1 have significant effects on the web crippling strengths of CFS channels. The dimensions of elongated web holes and the load distribution are critical variables for the web crippling strengths of these channels.

(2) The design equations for the R_P of CFS channels with elongated edge-stiffened web holes were proposed based on the linear regression analysis. The reliability analysis was conducted to show that the proposed R_P equation is reliable.

(3) The unified DSM-based equations were proposed for CFS channels with elongated un-stiffened and edge-stiffened web holes to determine the web crippling strength. Finally, a reliability analysis was conducted to show that the unified DSM-based equation is reliable.

Chapter 4 Moment capacity of cold-formed steel trusses with Howick Rivet Connectors

4.1. Introductory remarks

CFS trusses are widely used in lightweight building construction due to their high strength-to-weight ratio and ease of prefabrication. Recently, a new type of pin-jointed connection system, known as the Howick Rivet Connectors (HRCs), has been developed for assembling CFS trusses. Previous studies mainly focused on the behaviour of individual HRC connections, including T-stub connection tests and shear strength evaluations of CFS trusses with HRCs, providing initial insights into their structural performance. However, the moment capacity and global behaviour of CFS trusses assembled using HRCs remain insufficiently understood. Therefore, this chapter investigates the moment capacity of CFS trusses with HRCs through experimental testing and parametric analysis. A total of ten CFS trusses with HRCs were tested to determine their moment capacity. Two different cross-sections, namely lipped channel sections and hat sections, were used as truss chords. Variations in the number and locations of lateral supports were introduced to simulate different boundary conditions. In addition, a parametric study was conducted to investigate the effects of span-to-height ratio and the variability in lateral support locations on truss strength and failure modes. Finally, trusses with lipped channel section chords were designed according to AISI (2016) and AS/NZS (2018), yielding an average test-to-design strength ratio of 0.86.

4.2. Experimental investigation

4.2.1. Test specimens

In the experimental program, two main variables were considered: the cross-section of the chord and the number of lateral supports. The varying numbers of lateral supports were designed to represent different boundary conditions commonly encountered in engineering practice, and the program examined two specific configurations of lateral supports on trusses: one with two lateral supports and another with four lateral supports. A total of 10 tests were conducted on CFS trusses with HRCs, with specimen dimensions illustrated in Figure 4-1. Each eccentric diagonal-to-chord connection utilized two HRCs, spaced 67 mm apart to prevent overlap of the diagonal member. The overall length of each specimen is 3500 mm, suitable for meeting the span requirements of specific buildings or structures while ensuring the truss's load-bearing capacity and stability.

All specimens used 65 × 45 × 0.95 lipped channel sections for diagonal members (vertical and diagonal bracings), as shown in Figure 4-2(a). Chords in the trusses were designed using hat sections and lipped channel sections (see Figure 4-2). Notably, the diagonal members of the CFS trusses had swaged sections, 70 mm long at both ends, as depicted in Figure 4-3(a). During fabrication, flange holes for the HRCs were punched during the roll-forming process. The ends of the diagonal members were inserted into the chords, and the joint regions were reinforced using 12.7 × 0.95 mm (diameter × thickness) HRCs, as shown in Figure 4-3(b).

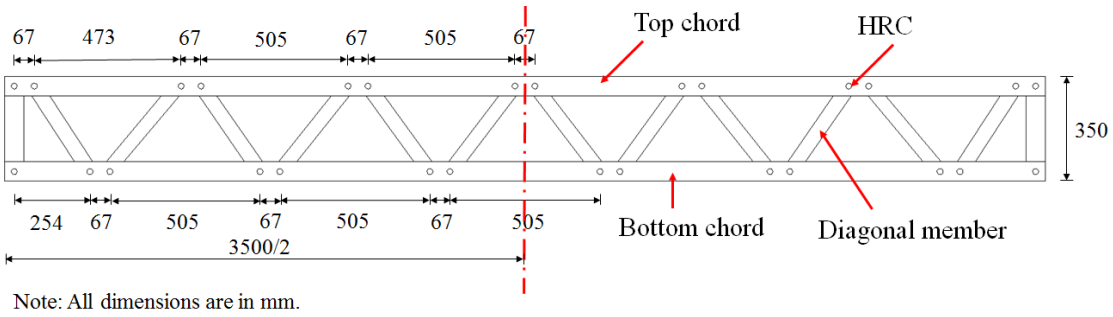

Note: All dimensions are in mm.

Figure 4-1 Details of test specimens

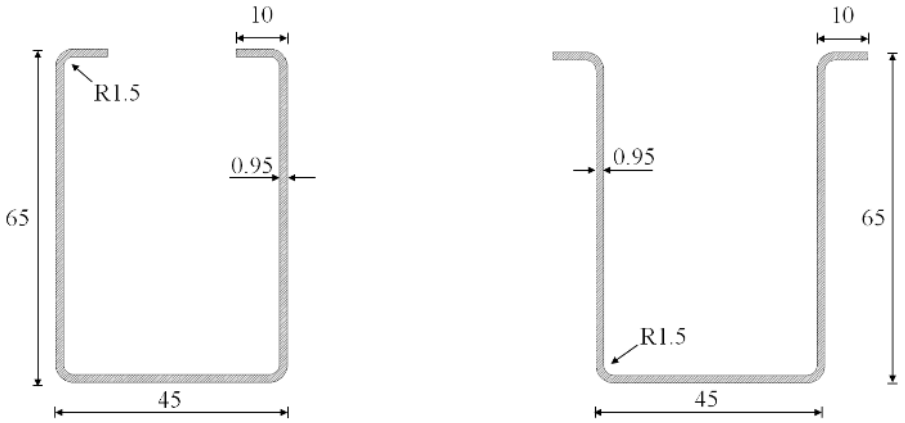

(a) Lipped channel section (b) Hat section

Figure 4-2 Different cross-sections used in the CFS trusses (all dimensions in mm)

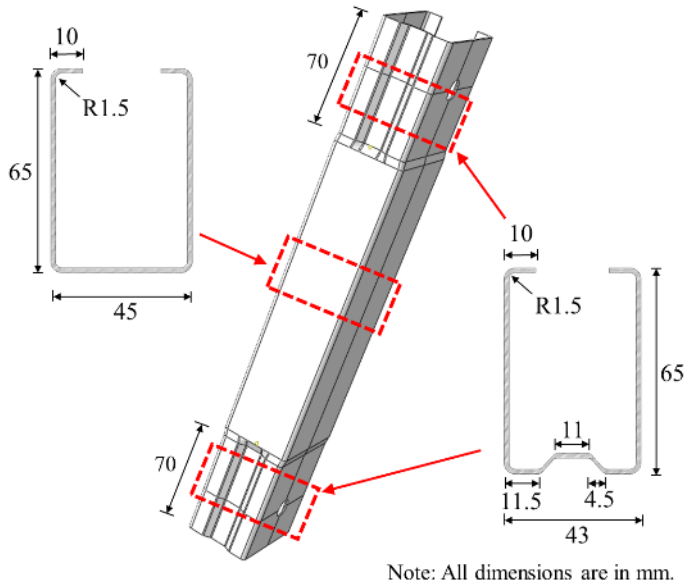

Note: All dimensions are in mm.

(a) Schematic diagram

(b) Photograph of a field test

Figure 4-3 Web member having swaged sections

4.2.2. Material testing

Three coupons were cut from the untested truss specimen, and tensile tests were performed using a 100 kN Instron machine (see Figure 4-4). These tests followed the guideline of EN ISO 6892-1:2019. The test results are presented in Table 1 and Figure 4-5, with the stress-strain curves shown in Figure 4-6. According to Table 1, the average yield strength ($\sigma_{0.2}$) was 682.95 MPa, and the ultimate strength (σ_u) was 684.27 MPa. These values are important for understanding the material properties of the specimens and the structural behaviour of the truss system with HRCs. The tensile properties of the corner regions were not directly measured in the material tests. In the finite element modelling, the constitutive conversion model proposed by Gardner and Yun (2018) was adopted to transform the material properties of the flat regions into equivalent corner properties, which were then assigned to the corner zones.

Figure 4-4 Setup of tensile coupon tests

Figure 4-5 Coupons

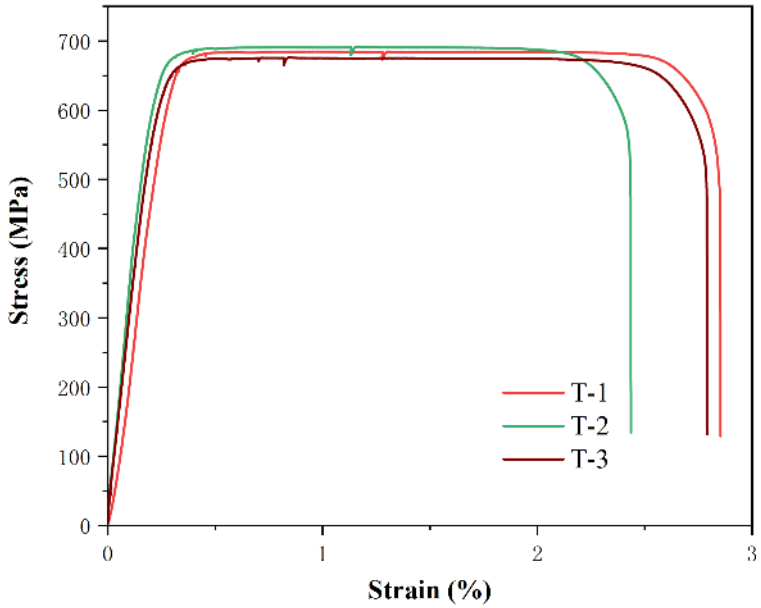

Figure 4-6 Stress-strain curves

Table 4-1 Material properties

Coupons	Thickness t (mm)	Yield stress $\sigma_{0.2}$ (MPa)	Ultimate stress σ_u (MPa)
T-1	0.96	683.22	684.76
T-2	0.95	690.59	691.82
T-3	0.96	675.04	676.24
Mean	0.96	682.95	684.27

4.2.3. Testing-rig and loading procedure

A 200 kN MTS machine was used to perform monotonically controlled four-point bending tests on CFS trusses with HRCs. The test setup, shown in Figures 4-7 and 4-8,

involved applying vertical loading to the truss specimens using a displacement-controlled method at a rate of 5 mm/min. The loading points were strategically placed at the joints between the chords and web members. Two hot-rolled steel beams acted as the bottom support and distribution beam. To ensure accurate measurement of the load-displacement relationship and to maintain repeatability of the experimental results, lateral supports made of steel plates were used to prevent lateral torsional buckling, which can be accentuated due to top chord loading. These lateral supports were positioned at various points along the shear spans, with specific details provided in Figure 4-8. The different configurations of lateral supports aimed to investigate various critical characteristics of the CFS trusses with HRCs. For measurement purposes, three linear variable displacement transducers (LVDTs) were employed to measure vertical displacement at mid-span and two additional joints. A data acquisition system recorded displacement and loads at regular intervals throughout the tests. This experimental setup was designed to evaluate the structural performance and behaviour of CFS trusses with HRCs under four-point loading conditions.

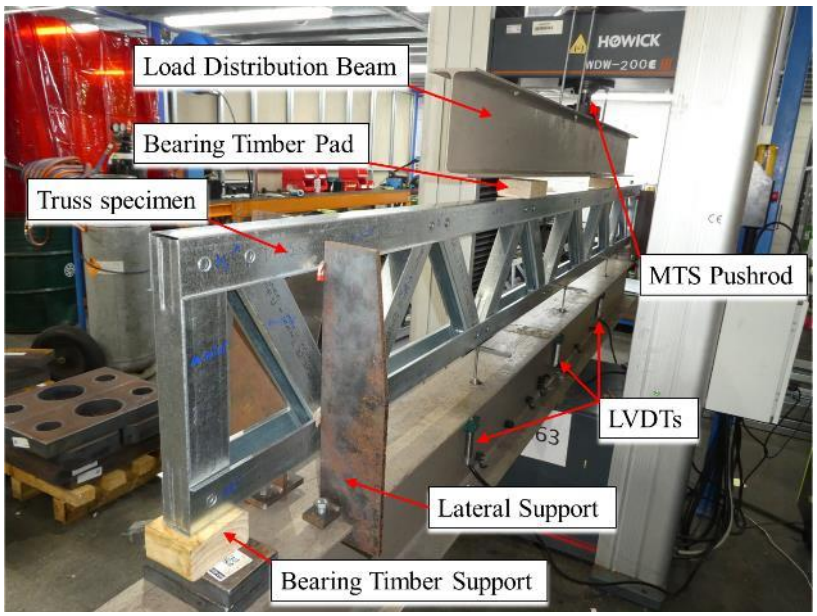

Figure 4-7 Picture of the experimental test setup

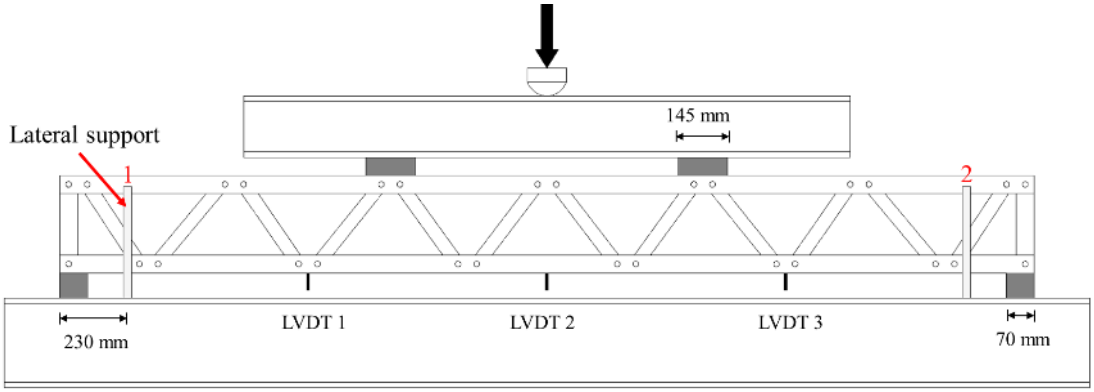

(a)Two lateral supports

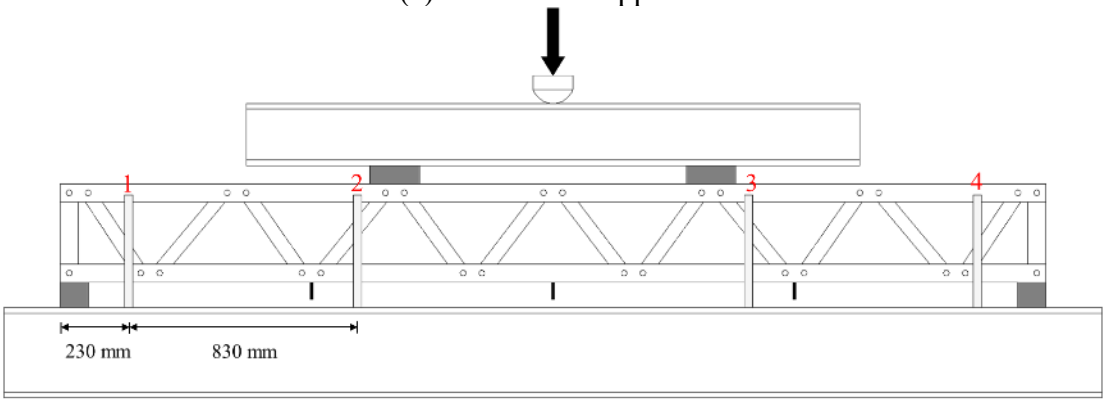

(b)Four lateral supports

Figure 4-8 Schematic diagram of different locations and numbers of lateral supports

4.2.4. Test results and discussions

During the experiments, several distinct failure modes were observed. The primary failure mode observed was local buckling in the top chord of the trusses. Interestingly, trusses with hat sections as chords demonstrated higher strength and exhibited different failure modes compared to those using lipped channel sections. Notably, none of the specimens experienced connection failure, indicating the effective contribution of HRCs to the overall connection capability. HRCs were found to provide sufficient shear strengths for diagonal-to-chord connections in CFS trusses. Additionally, some HRCs in the trusses exhibited minor inelastic deformations, which contributed to energy dissipation. This characteristic underscores why HRCs exhibit better ductility compared to conventional bolted connections, adding to their effectiveness in structural applications.

Table 4-2 provides a summary of all specimens, including their failure modes, peak loads, and specific details. The labeling of the specimens is illustrated in Figure 4-9. Additionally, Figure 4-10 presents the load-displacement curves for all standard trusses with HRCs. For specimens with two and four lateral supports, the average peak strength of trusses using hat sections as chords increased by 7.0% and 6.0%, respectively, compared to those using lipped channel sections. This difference can be attributed to modifications made to the chord lips of the lipped channel sections at the joints, which introduced local imperfections leading to a reduction in load-carrying capacity. It's noteworthy that trusses with hat sections exhibited better ductility than those with lipped channel sections serving as chords. At the peak load, the corresponding mid-span displacement for trusses with hat sections was approximately 46-51 mm, while for those with lipped channel sections, it was about 33-38 mm (see Figure 4-10). In comparison, specimens with four lateral supports showed average strength increases of 4.8% and 4.0% for lipped channel sections and hat sections serving as chords, respectively. These findings contribute to an understanding of the moment capacity and behaviour of CFS trusses with HRCs under different lateral support configurations.

Table 4-2 Details of the specimens and test results

Test ID	Test Details		Failure modes	Maximum loads P_{max} (kN)	Mean values $\bar{P}_{max}$ (kN)	Failure displacement of mid span δ_{max} (mm)	Mean values $\bar{\delta}_{max}$ (mm)
	Chords	Restraints					
C-L2-T1	Lipped C	2	L	19.98	19.46	38.30	35.60
C-L2-T2			L	18.73		33.36	
C-L2-T3			L	19.66		35.13	
C-L4-T1	Lipped C	4	L	20.42	20.39	38.30	41.40
C-L4-T2			L	20.46		41.30	
C-L4-T3			L	20.28		38.60	
H-L2-T1	Hat	2	D	20.51	20.83	45.80	47.00
H-L2-T2			L	21.16		51.45	
H-L2-T3			L+D	20.81		46.01	
H-L4-T1	Hat	4	L+D	21.66	21.66	54.65	56.52

Note: L represents local buckling in the top chord; D represents distortional buckling of diagonal members.

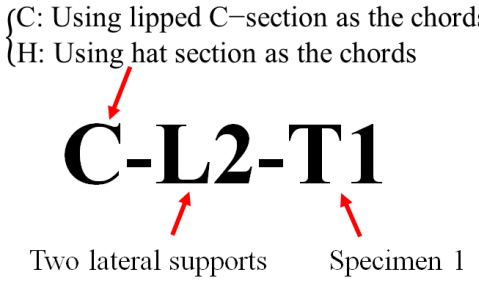

Figure 4-9 Specimen labelling

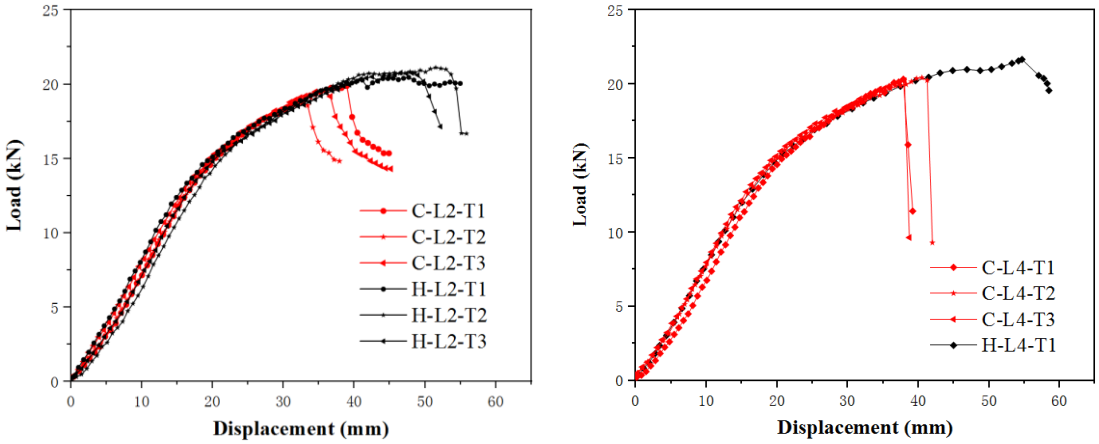

(a)Two lateral supports (b)Four lateral supports

Figure 4-10 Load-displacement curves for truss bending tests

The typical failure modes observed for CFS trusses using lipped channel sections as chords are illustrated in Figure 4-11. In specimen C-L2 (Figure 4-11(a)), the observed failure mode is local buckling in the top chord. The lack of sufficient lateral support resulted in a slight out-of-plane displacement in the loading point area. Although some HRCs exhibited slight deformation, no shear failure was observed. This indicates that HRCs can provide sufficient shear strength.

For specimen C-L4 (Figure 4-11(b)), like specimen C-L2, shear loads in the diagonal-to-chord connections caused deformation of the HRCs, but no shear failure occurred. The HRCs in the specimen with four lateral supports experienced more deformation than those with two supports, due to higher shear loads on the individual connections. However, from a load-bearing perspective, adding more lateral supports did not significantly enhance capacity. Both specimens, whether with two or four lateral supports,

exhibited local buckling with only minor differences in the buckling location, as shown in Figure 4-11.

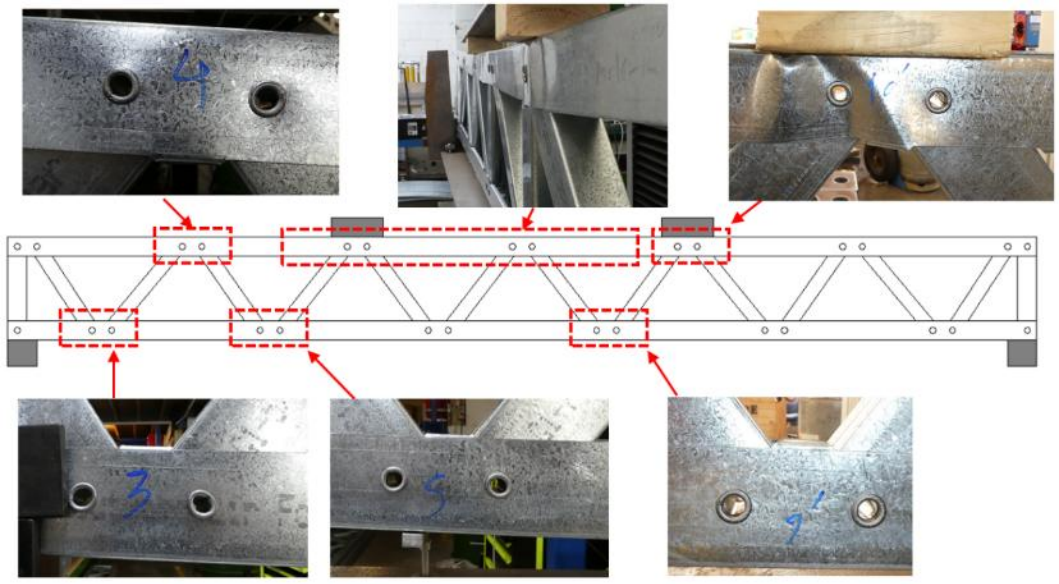

(a) C-L2-T1

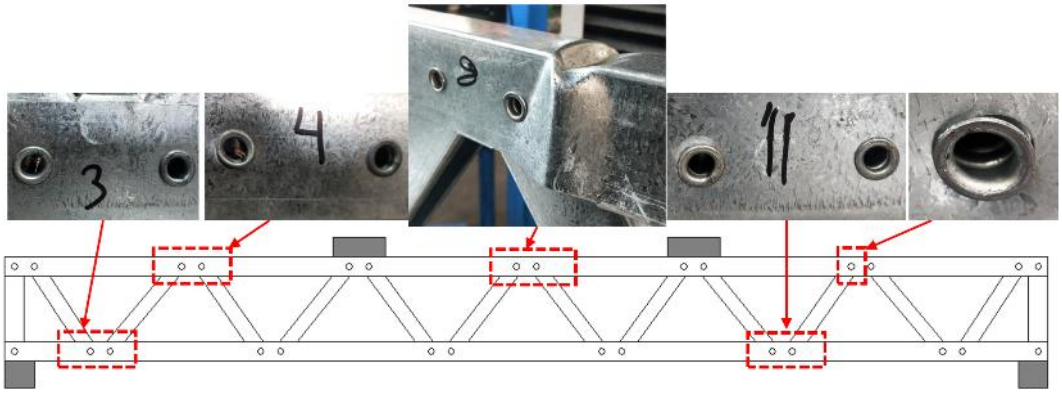

(b) C-L4-T1

Figure 4-11 Deformed shapes of CFS trusses with lipped channel sections as chords

The common failure modes observed in truss specimens utilizing hat sections as chords are depicted in Figure 4-12. In specimen H-2L, the primary mode of failure was local buckling in the top chord. However, distortional buckling of diagonal members was observed in specimens H-2L-T1 (Figure 4-12(a)) and H-2L-T3. Unlike lipped channel sections, which have portions of lips removed near the diagonal-to-chord connection, the hat section retains its full geometry with the truss, allowing it to withstand higher axial loads. As the deflection of the specimen increases, the load reaches the critical distortional

buckling load of diagonal members. Similarly, for specimen H-4L (Figure 4-12(b)), the observed failure modes were a combination of local buckling in the top chord and distortional buckling in the diagonal members. The combination of failure modes highlights the intricate response of the truss structure with hat sections as chords.

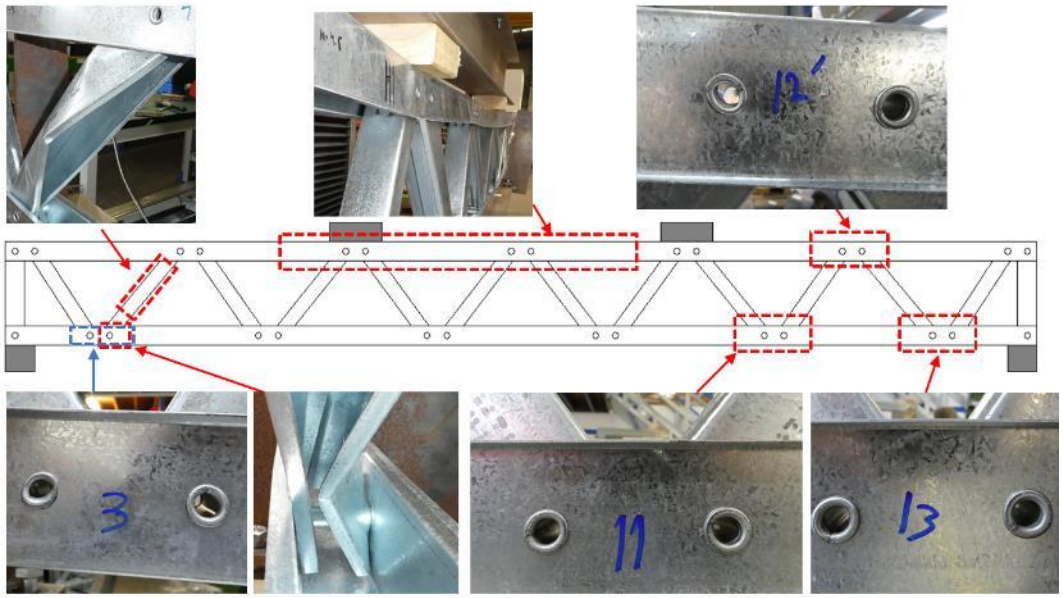

(a)H-L2-T1

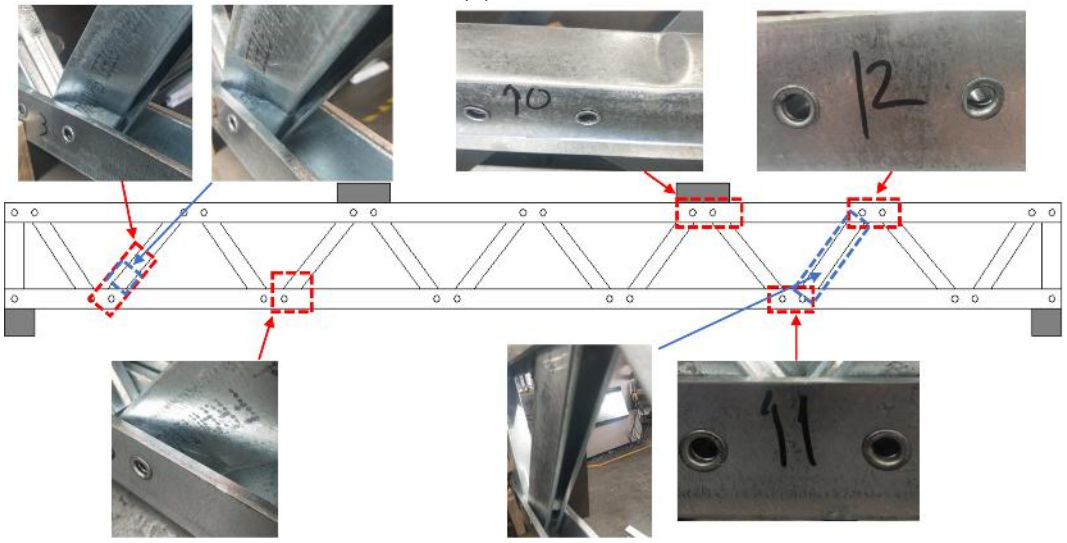

(b)H-L4-T1

Figure 4-12 Deformed shapes of CFS trusses with hat sections as chords

4.3. Numerical study

4.3.1. General description of FE model

In this section, a non-linear elastic-plastic FE model was developed with ABAQUS to simulate trusses. The new FE models were validated using the experimental results from this study. The non-linear material properties for flat CFS sections were determined through tensile coupon tests. To account for the enhanced material properties in the corner regions, standardized values of strain-hardening exponents proposed by Gardner and Yun, (2018) were used to develop the material curves based on flat coupon data. Based on ABAQUS manual, the engineering material curve was converted into a true material curve using the following equations.

$$\sigma_{true} = \sigma(1+\varepsilon) \qquad \text{Equation 4.1}$$

$$\varepsilon_{true(pl)} = \ln(1+\varepsilon) - \frac{\sigma_{true}}{E} \qquad \text{Equation 4.2}$$

The full geometry of HRCs, Chords and web members was modelled using the S4R shell element, which have six degrees of freedom per node. Mesh refinement was applied specifically at the section corners between the web and flange, as well as at the connection holes on the flanges of chords and web members. A mesh sensitivity analysis was conducted to find an optimal mesh size that balances computational time and accuracy. Notably, when the mesh size is too large, such as 10 mm x 10 mm, mesh intrusion may occur, which can lead to inaccurate results. The analysis showed that a mesh size of 5 mm x 5 mm was ideal for both the chords and web members. Detailed results are shown in Figure 4-13, and further information is provided in Figure 4-14.

Surface-to-surface contact with a friction coefficient of 0.2 was used to model the interface between the chords, HRCs, and web members. The load surface of the top chord

was coupled to two “RP” (reference points). A displacement control method was employed to apply vertical load through these reference points to the top chords at the physical load locations (see Figure 4-15). At the locations of the lateral supports, displacement in the out-of-plane direction was constrained.

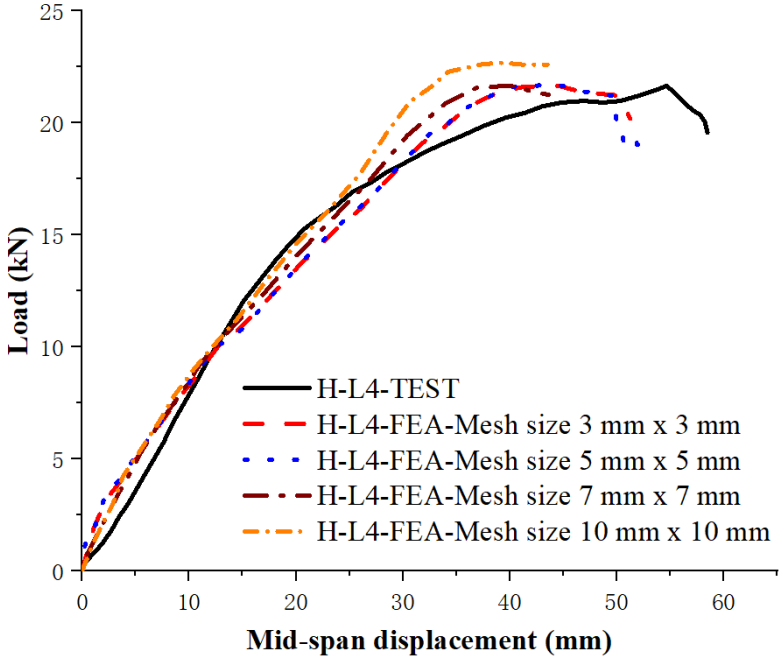

Figure 4-13 Result of a mesh sensitivity analysis

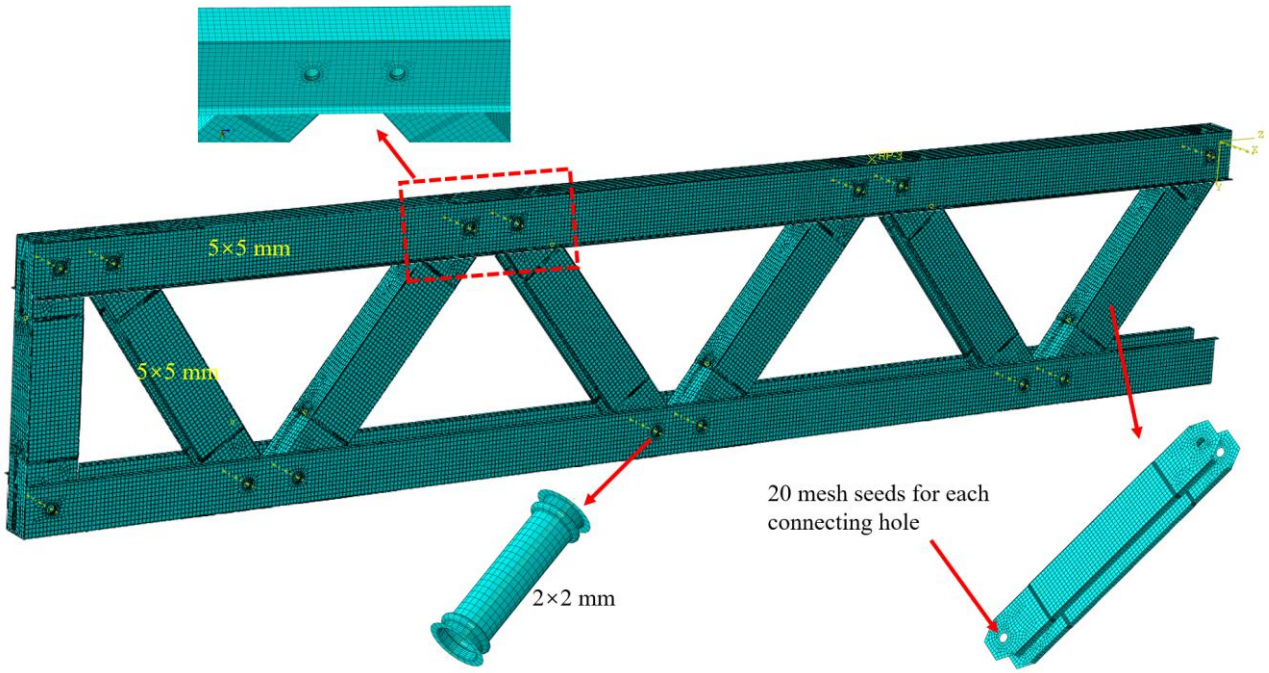

Figure 4-14 FE meshing

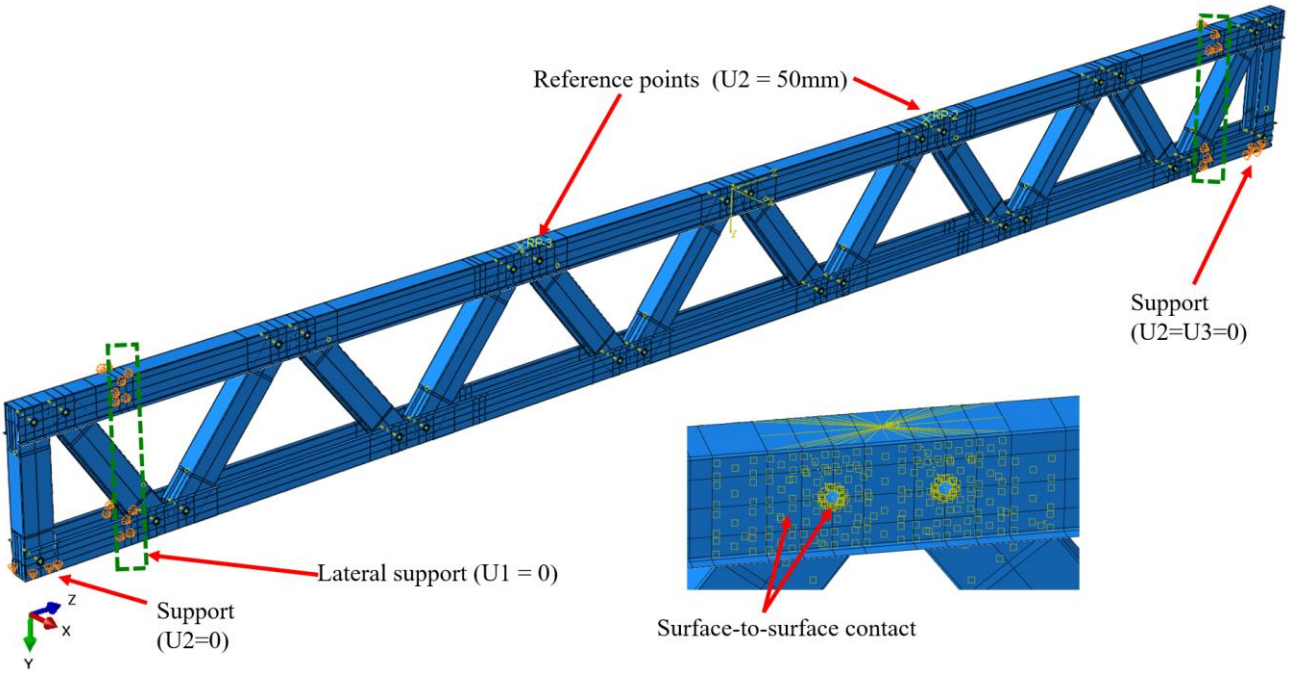

Figure 4-15 Boundary conditions and interactions

The effect of initial geometric imperfections on the behaviour of the entire trusses, not just the deformation of isolated chord members, was considered for all FE models in this study. Linear buckling analysis in ABAQUS was used to determine the critical buckling shapes of the trusses. The selected imperfection shapes (lowest buckling mode) were incorporated into the ideal models by modifying keywords, allowing the static analysis models to include these initial imperfections. The magnitude of the imperfections (e_0) was calculated using Equation 4.3 (Korcz-Konkol and Iwicki, 2023).

$$e_0 = \alpha_m L / 500 \qquad \text{Equation 4.3}$$

$$\alpha_m = \sqrt{0.5\left(1+1/m\right)} \qquad \text{Equation 4.4}$$

where L is the span of the restrained member and α_m is the coefficient that accounts for the irregularity of the geometrical imperfections of restrained members m, which can be determined by Equation 4.4.

4.3.2. Validation of FE model

In Table 4-3, a detailed comparison is presented between the FEA results (P_{FEA}) and the test results (P_{max}) for the CFS trusses with HRCs. The average value of the ratio P_{max}/P_{FEA} is 0.98, with a COV of 0.02, indicating close agreement between the numerical predictions and the experimental results. To further validate the FE model, the load-displacement curves and failure modes obtained from both the tests and FEA are compared in Figures 4-16 and 4-17. The results from the FEA align well with the laboratory tests in terms of failure modes and strengths, providing confidence in the accuracy and reliability of the developed FE model for CFS trusses with HRCs.

Table 4-3 Comparison of tests and FEA results

Test ID	Maximum load		P_{max}/P_{FEA}	Failure displacement of mid span		$\delta_{max}/\delta_{FEA}$	Failure modes	
	Test P_{max} (kN)	FEA P_{FEA} (kN)		Test δ_{max} (mm)	FEA δ_{FEA} (kN)		Test	FEA
C-L2-T1	19.98	20.34	0.98	38.30	34.91	1.10	L	L
C-L2-T2	18.73	20.34	0.92	33.36	34.91	0.96	L	L
C-L2-T3	19.66	20.34	0.97	35.13	34.91	1.01	L	L
C-L4-T1	20.42	20.80	0.98	40.15	36.63	1.10	L	L
C-L4-T2	20.46	20.80	0.98	43.36	36.63	1.18	L	L
C-L4-T3	20.28	20.80	0.98	40.68	36.63	1.11	L	L
H-L2-T1	20.51	21.11	0.97	45.80	40.33	1.14	D	L+D
H-L2-T2	21.16	21.11	1.00	49.20	40.33	1.22	L	L+D
H-L2-T3	20.81	21.11	0.99	46.01	40.33	1.14	L+D	L+D
H-L4-T1	21.66	21.72	1.00	56.52	43.90	1.29	L+D	L+D
Mean			0.98			1.12		
COV			0.02			0.08		

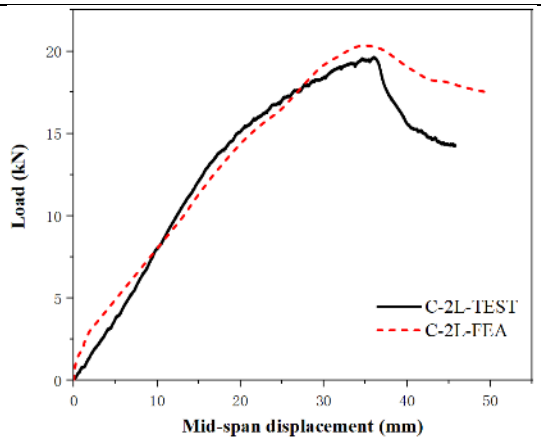

(a) Specimen C-L2

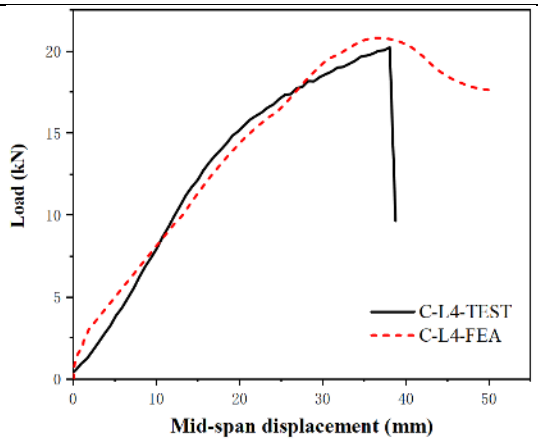

(b) Specimen C-L4

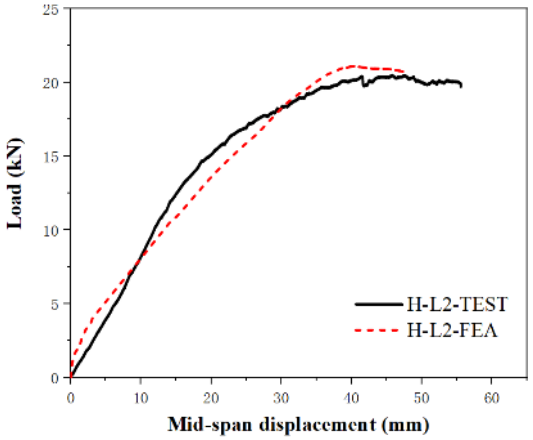

(c) Specimen H-L2

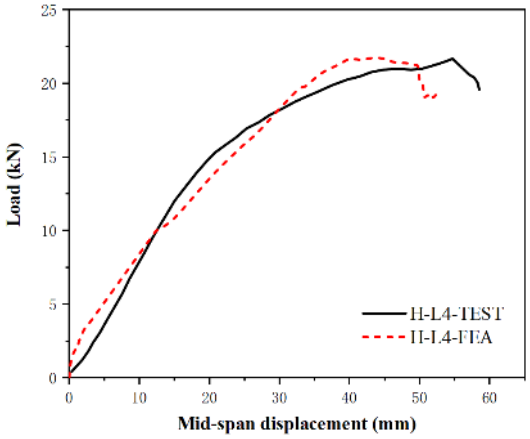

(d)Specimen H-L4

Figure 4-16 Comparison of load-displacement curves of tests and FEA

(i)Test

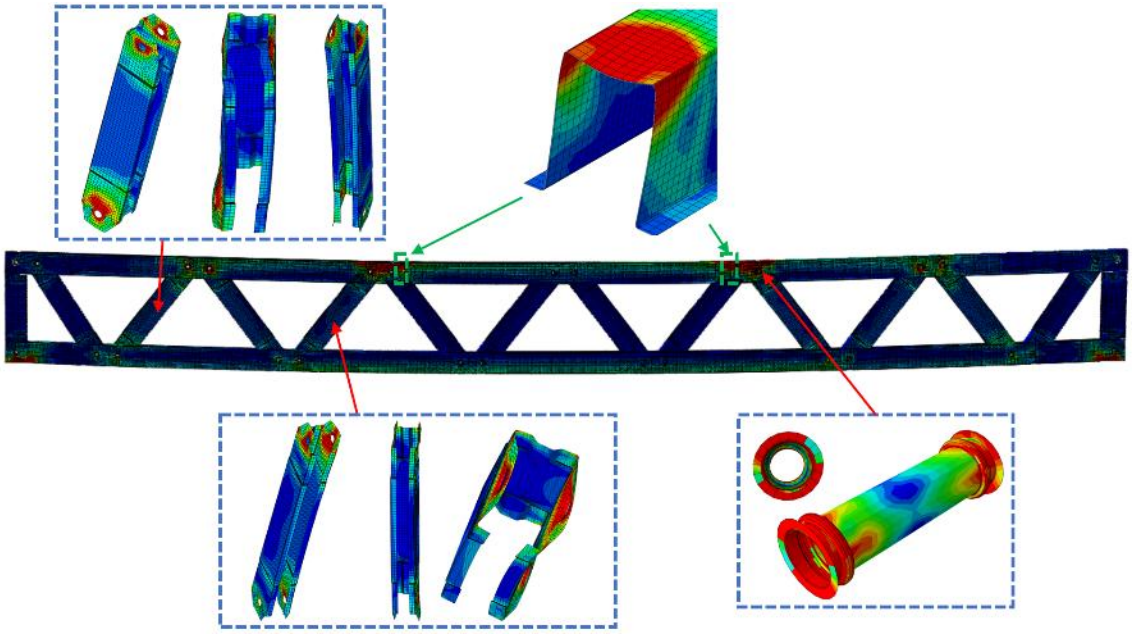

(ii)FEA

Figure 4-17 Failure modes of the specimen H-L4-T1 obtained from the tests and FEA

4.4. Parametric study

Following the validated model, a parametric study was conducted to investigate the effects of the span-height ratio and number of lateral supports on truss strength and failure modes. Based on the specimen H-L4, the new FE models were referenced and modified, and the specimen details and results are summarised in Table 4-4.

Table 4-4 Summary of specimen details and results of a parametric study

ID	Height of truss h (mm)	Span-height ratio	Lateral supports	$P_{max,FEA}$ (kN)	$\delta_{max,FEA}$ (mm)	Failure modes
H-L4	350	10.00	L4	21.66	54.65	L+D
1	300	11.67	L4	19.98	45.67	L+D
2	325	10.77	L4	19.53	35.06	L
3	375	9.33	L4	22.21	41.15	L+D+B
4	400	8.75	L4	22.53	42.66	L+D+B
5	350	10	L5	21.69	43.50	L+D
6	350	10	L7	21.64	43.74	L+D

Note: L represents local buckling in the top chord; D represents distortional buckling of diagonal members; B represents bearing failure at diagonal-to-chord connection; L4, L5, L7 indicate different layouts of lateral supports on the truss, as shown in Figure 4-20.

When the truss span is kept constant at 3500 mm, as in the tested specimen, new FE models were developed to compare variations in truss height from 300 mm to 400 mm. Details of the specimens are shown in Table 4-4. The results indicate that the failure mode and strength of the specimens vary significantly with different span-height ratios. The primary failure mode remains local buckling in the top chord of the truss. However, when the span-height ratio is lower than 9.33, bearing failure occurs at the diagonal-to-chord connections, as shown in Figure 4-18. This may be due to the changing angles between diagonal members and chords as the truss height varies, leading to a redistribution of internal forces and subjecting the diagonal-to-chord connections to greater shear forces. Therefore, increasing the height of the truss does not enhance its strength; instead, it decreases the strength (see Figure 4-19) due to the onset of shear failure.

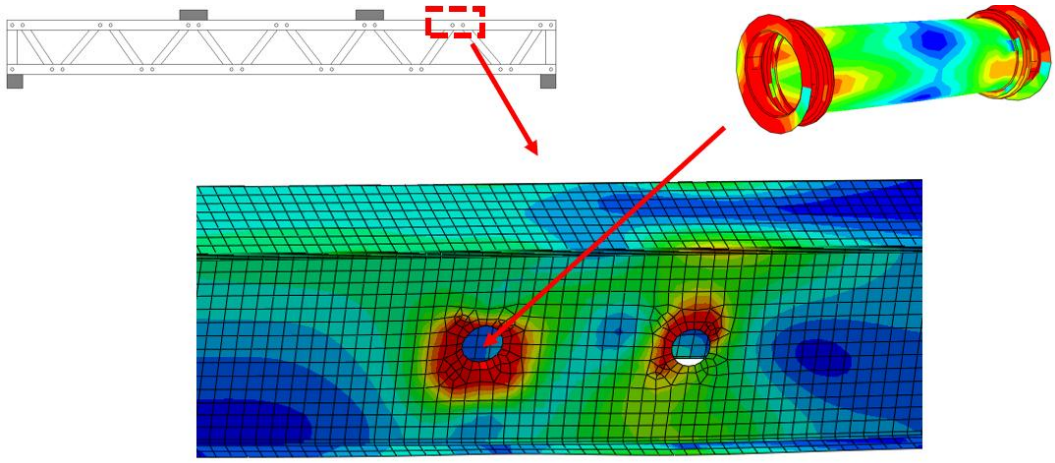

Figure 4-18 Bearing failure at diagonal-to-chord connection for Specimen 3

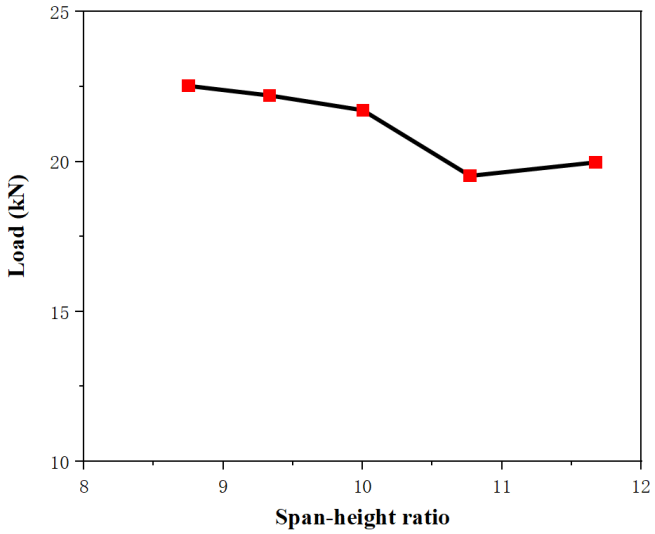

Figure 4-19 Relationship between truss strength and the span-height ratio

The number and locations of lateral supports on trusses represent various boundary conditions in practical engineering applications. Experimental results have demonstrated that these factors influence the strength, failure modes, and particularly the ductility of the trusses. In this section, new FE models were developed to explore the potential occurrence of local and/or distortional buckling modes under different lateral support configurations. Figure 4-20 shows the layouts of lateral supports L2 and L4, which were investigated in the tests, along with other modified layouts achieved by adjusting the number and/or positions of these supports.

According to Figure 4-21 and Table 4-4, the FEA results indicated that adding lateral supports did not affect the failure pattern. Additionally, increasing the number of lateral supports tends to slight enhance the strength of the truss. This improvement can be attributed to the reduction in out-of-plane displacement of the specimen when lateral supports are added from 2 to 4. However, when the number of lateral supports exceeds four, further increases do not lead to significant changes in the truss load, indicating that the specimen will not experience out-of-plane displacements affecting the load.

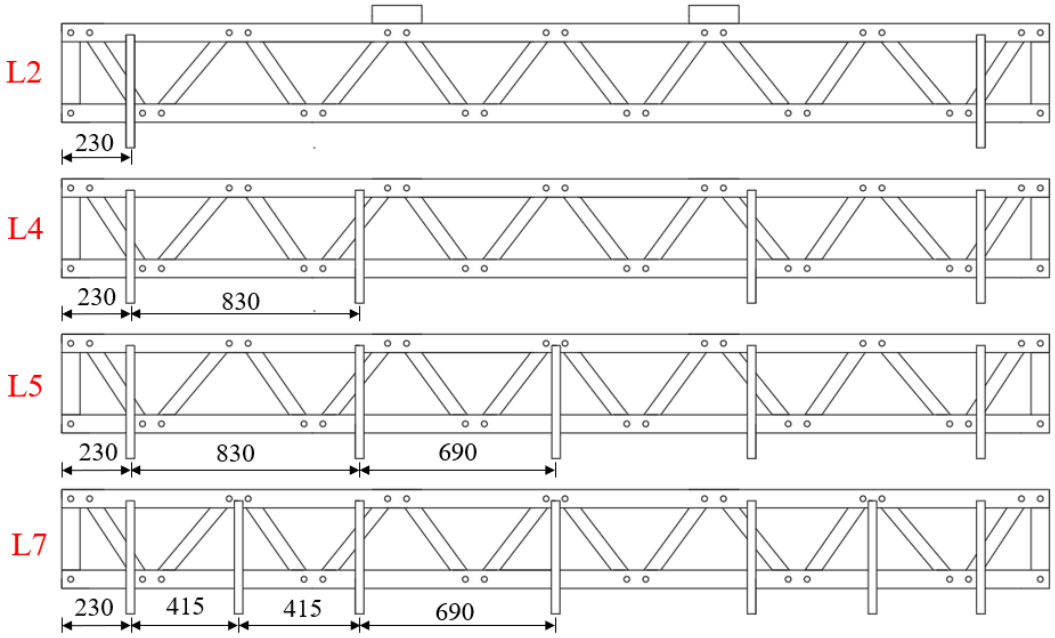

Figure 4-20 Layouts of lateral supports on trusses (all dimensions in mm)

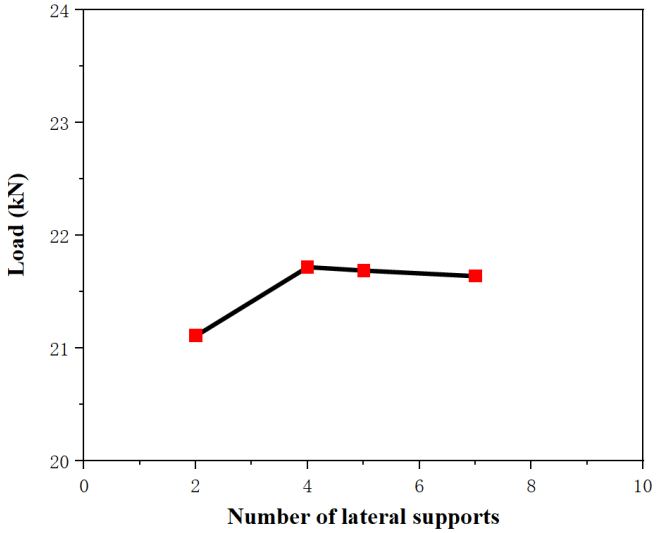

Figure 4-21 Relationship between truss strength and the number of lateral supports

4.5. Truss design strength

The distribution of forces acting through the members of the trusses is shown in Figure 4-22. In Figure 4-22, "+" indicates that the member is subjected to compression loads, while "-" indicates that the member is subjected to tension loads. To calculate the member internal forces, two adjacent HRCs are simplified and assumed to function as a whole. These member forces are based on an applied load of "*P*". In the subsequent sections, the

connection strength of the HRCs and the compressive strength of the top chord were calculated using the DSM based on AISI (2016) and AS/NZS (2018).

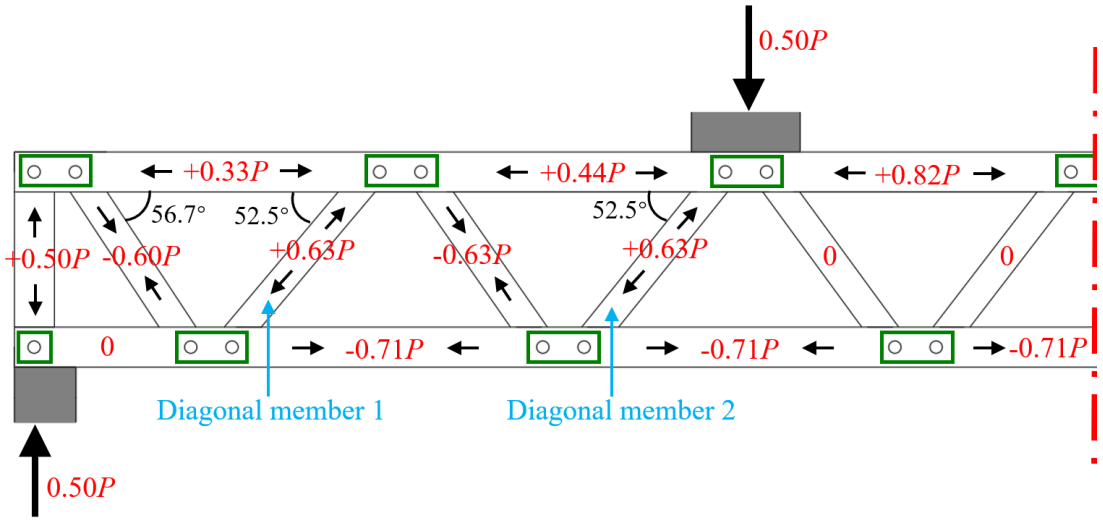

Figure 4-22 Relative internal forces of members in truss

4.5.1. Determining connection strength of HRCs

Based on the test results from Ahmadi et al. (2016) on Tee-stub connections with HRCs, it was observed that specimens experiencing shear failure exhibit significantly lower ductility compared to those undergoing bearing failure. Therefore, it is crucial to prevent shear failure in such connections. Following this, they developed a new formula to calculate connection strength, derived from the expression for bolt connections. This formula, shown in Equation 4.5, was derived from tests involving HRCs and CFS sections with the same cross-sections and steel strength examined in this chapter.

$$P_b = nCdtF_u \qquad 0.75 \le t \le 1.15 \text{ and } 11 \le d/t \le 22 \qquad \text{Equation 4.5}$$

$$C = 0.95 + \frac{1.88}{d/t} \qquad \text{Equation 4.6}$$

where C is the bearing constant and can be determined by Equation 4.6; d is the diameter of HRCs; t is the thickness of the HRCs; F_u represents the ultimate tensile strength of the

CFS sections and is limited to the range of 612–721 MPa; n is the number of connections, and a single HRC contains two connections.

Using Equation 4.5, the connection strength of a single HRC was determined to be 18.22 kN. From Figure 4-22, the maximum connection force observed in the tested specimens is 0.5P near the bottom support. A comparison of the test strength and design strength is presented in Table 4-5, showing that HRCs provide sufficient connection strength and have a large safety reserve. This explains why no shear failure was observed in the experiments.

Table 4-5 Comparison of test strength and design strength of HRCs

Test ID	Maximum load P_{max} (kN)	$0.5P_{max}$ (kN)	Design strength of single HRC P_b (kN)	$0.5P_{max}/P_b$
C-L2-T1	19.98	9.99	18.22	0.55
C-L2-T2	18.73	9.37	18.22	0.51
C-L2-T3	19.66	9.83	18.22	0.54
C-L4-T1	20.42	10.21	18.22	0.56
C-L4-T2	20.46	10.23	18.22	0.56
C-L4-T3	20.28	10.14	18.22	0.56
H-L2-T1	20.51	10.26	18.22	0.56
H-L2-T2	21.16	10.58	18.22	0.58
H-L2-T3	20.81	10.41	18.22	0.57
H-L4-T1	21.66	10.83	18.22	0.59

4.5.2. Determining truss strength

Ahmadi et al. (2016) and Roy et al. (2023) have established that HRCs provide a pinned connection between CFS sections through their flanges. Consequently, the strength of the truss chord can be determined by treating the segment between two adjacent diagonal-to-chord connections as a pin-ended compression member. This approach is conservative as the chord member is continuous and restrained at the ends of such segments. Standards such as AISI (2016) and AS/NZS (2018) provide the DSM for calculating the axial compressive capacity of CFS members.

Based on the physical length of the member between the diagonal-to-chord connections, the elastic critical loads of 505 mm long chords and 360 mm long diagonal members with a pin-ended boundary condition were determined using the DSM. Lipped channel sections, hat sections, and unlipped sections were considered separately. The THIN-WALL-2 V2.0 program was used to determine their elastic local buckling loads (P_{crl}), distortional buckling loads (P_{crd}), and flexural buckling loads (P_{cre}). The design strengths (P_{DSM}) calculated by DSM are presented in Table 4-6.

For the CFS trusses with lipped section chords, Table 4-6 shows a comparison of capacities that reveals notable differences in behaviour between lipped and unlipped channels. Local buckling is the primary failure mode for both types. Figure 4-22 indicates that the maximum chord axial force for the tested specimens is $0.82P_{max}$ near the loading plates. Table 4-7 provides the ratios of $0.82P_{max}/P_{DSM}$, showing that the design strength significantly exceeds the test strength, with an average ratio of 0.38 when considering the influence of the lips. When the influence of the lips is disregarded, the design strength more closely matches the test strength, with an average ratio of 0.86. Consequently, this chapter recommends ignoring the influence of the lips when designing for axial force in lipped section chords.

For the CFS trusses with hat section chords, it was observed that tested specimens experienced distortional buckling in diagonal members 1 and 2 (see Figure 4-22), in addition to local buckling in the top chords. Axial strengths for 505 mm long hat section chords and 360 mm long diagonal members were determined using the same method as described above, as shown in Tables 4-6 and 4-8. Based on the relative internal forces of truss members shown in Figure 4-22, the mean value ratios of $0.82P_{max}/P_{DSM}$ for hat section chords and $0.63P_{max}/P_{DSM}$ for diagonal members were found to be 0.53 and 0.29,

respectively. This suggests that the current design standards (AISI 2016 and AS/NZS 2018) do not accurately predict the ultimate strength of the trusses.

Table 4-6 Axial strength calculated according to DSM

Specimens	F_y (MPa)	P_{crl} (kN)	P_{crd} (kN)	P_{cre} (kN)	P_{nl} (kN)	P_{nd} (kN)	P_{ne} (kN)	Min P_n (kN)
505 mm long chords								
Lipped C	682.95	33.92	29.34	74.57	42.73	46.33	61.48	42.73
Hat	682.95	33.87	-	46.74	32.70	-	40.99	32.70
Un-Lipped	682.95	6.45	-	49.74	18.87	-	43.53	18.87
360 mm long diagonal members								
Lipped C	682.95	33.92	29.34	146.05	53.11	46.33	85.91	46.33

Table 4-7 Comparison of measured and calculated response of specimens with lipped section chords

Specimens	Maximum load P_{max} (kN)	$0.82P_{max}$ (kN)	Design strength of 505mm long sections according to DSM, P_{DSM} (kN)		Strength ratio, $0.82P_{max}/P_{DSM}$	
			Lipped C	Unlipped	Lipped C	Unlipped
C-L2-T1	19.98	16.38	42.73	18.87	0.38	0.87
C-L2-T2	18.73	15.36	42.73	18.87	0.36	0.81
C-L2-T3	19.66	16.12	42.73	18.87	0.38	0.85
C-L4-T1	20.42	16.74	42.73	18.87	0.39	0.89
C-L4-T2	20.46	16.78	42.73	18.87	0.39	0.89
C-L4-T3	20.28	16.63	42.73	18.87	0.39	0.88
Mean					0.38	0.86
COV					0.01	0.03

Table 4-8 Comparison of measured and calculated response of specimens with hat section chords

Specimens	Maximum load P_{max} (kN)	Design strength according to DSM, P_{DSM} (kN)			
		505 mm long chords	$0.82P_{max}/P_{DSM}$	360 mm diagonal member	$0.63P_{max}/P_{DSM}$
H-L2-T1	20.51	32.70	0.51	46.33	0.28
H-L2-T2	21.16	32.70	0.53	46.33	0.29
H-L2-T3	20.81	32.70	0.52	46.33	0.28
H-L4-T1	21.66	32.70	0.54	46.33	0.29
Mean			0.53		0.29
COV			0.01		0.02

4.6. Summary

This study presents findings from an experimental and numerical investigation into the moment capacity of CFS trusses with HRCs. Ten tests were conducted, employing two different cross-sections (lipped channel sections and hat sections) as chords for the CFS trusses with HRCs. The study also explored the effect of varying lateral support

configurations on the moment capacity experimentally. A nonlinear elastic-plastic FE model was developed and validated against the test results. Using the validated FE model, a parametric study was conducted which investigate the effects of the span-height ratio and the number of lateral supports on the truss strength and failure modes. Finally, the design methods based on the standards AISI (2016) and AS/NZS (2018) were used to calculate the capacity of these trusses with HRCs. The following conclusions can be drawn from the outcomes of this study:

(1) None of the specimens experienced connection failure in tests, indicating that a single HRC can offer sufficient shear strength for the diagonal-to-chord connections. There is a safety reserve in connection strength.

(2) Specimens with two and four lateral supports showed average peak strength increase of 7% and 6%, respectively, for CFS trusses using hat sections as chords compared to those using lipped channel sections.

(3) Specimens with four lateral supports showed average strength increases of 4.8% and 4.0% for lipped channel sections and hat sections as chords, respectively, compared to those with two lateral supports.

(4) The results of the parameter study suggest that the strength of the truss tends to decrease with increasing height due to the emergence of bearing failure at the diagonal-to-chord connections.

(5) The design method based on the current DSM suggests that the influence of lips should be ignored, when determining the axial strengths of the lipped section chords. The average ratio of test strength to design strength is 0.86, with a COV of 0.03.

Chapter 5 CFS built-up box columns connected with Howick Rivet Connectors

5.1. Introductory remarks

CFS built-up box columns are increasingly used in lightweight steel structures because built-up configurations can improve the load-carrying capacity and stability of thin-walled members. Recently, Howick Rivet Connectors (HRCs) have been introduced as an alternative fastening system for assembling CFS members, offering potential advantages in connection efficiency and structural performance. However, the axial behaviour of CFS built-up box columns assembled using HRCs has not been fully investigated, and their design provisions are not clearly addressed in existing standards. Therefore, this chapter examines the axial strength and failure modes of a new CFS built-up box column connected using HRCs under pin-ended boundary conditions (see Figure 5-1). For comparison, specimens with traditional screw connections were also considered. A total of 112 specimens were designed and tested to evaluate the influence of key parameters, including thickness, type of fastener, fastener spacing, and slenderness ratios, on buckling behaviour and ultimate axial strength. The test results were used to evaluate two commonly used design methods — the EWM and DSM. The findings revealed that these existing methods do not accurately predict the axial strength of such columns. To address this, the study proposes a new design approach that combines DSM and EWM. The validity of the proposed design equations was further confirmed through statistical analysis, demonstrating their accuracy in predicting the axial strength of CFS built-up box columns.

5.2. Experimental investigation

5.2.1. Test specimens

A total of 112 compression tests were conducted on CFS built-up box section columns, each consisting of a C-section and a U-section nested face-to-face and fastened by HRCs or screws along their long flanges. The dimensions of the C- and U-sections are shown in Figure 5-2, with an internal corner radius (r) of 1.5 mm. The C-section is nested within the U-section, with HRCs or screws connecting the midpoints of the C-section flanges, and the lips of the C-section are positioned near the web of the U-section.

The strong and weak axes of the built-up section are illustrated in Figure 5-2. In general, for CFS built-up columns, rotation is typically allowed around the weak axis. However, when these columns are integrated into a CFS structural system, the boundary conditions illustrated in Figure 5-3 are commonly used. The top track and bottom track are typically fixed to the beam system, allowing the built-up column to rotate only around the strong axis. To reflect these boundary conditions in practical applications, this study includes specimens with HRCs designed to allow rotation around either the strong or the weak axis. Additionally, two nominal thicknesses for the built-up sections were considered: 0.95 and 1.15 mm. Column lengths of 700, 1300, 1900, and 2500 mm were tested (see Figure 5-4), encompassing a broad range of modified slenderness ratios (λ_m) from 45 to 136, as calculated using Equation 5.1.

$$\left(\frac{KL}{r_{\min}}\right)_m = \sqrt{\left(\frac{KL}{r_{\min}}\right)_o^2 + \left(\frac{a}{r_i}\right)^2} \text{ when, } \left(\frac{a}{r_i}\right) \le 0.5\left(\frac{KL}{r_{\min}}\right)_o \qquad \text{Equation 5.1}$$

where $K = 1$ represents the effective length factor for pin-ended columns as specified in AISI (2016); L is the laterally unbraced length of the CFS member, equal to the calculated member length; a represents the intermediate fastener spacing; and $r_{\min}$ is the minimum

radius of gyration of the full unreduced cross-section about the centroid axis. To satisfy Equation 5.1, a must be limited so that the ratio a/r_i does not exceed half of the controlling slenderness ratio of the built-up member. Calculations indicate that only the 700 mm long specimen with a 600 mm fastener spacing does not meet this fastener spacing requirement. Tables 5-1, 5-2, and 5-3 provide the measured dimensions of the specimens with HRCs and screws, with the specimen labels shown in Figure 5-5.

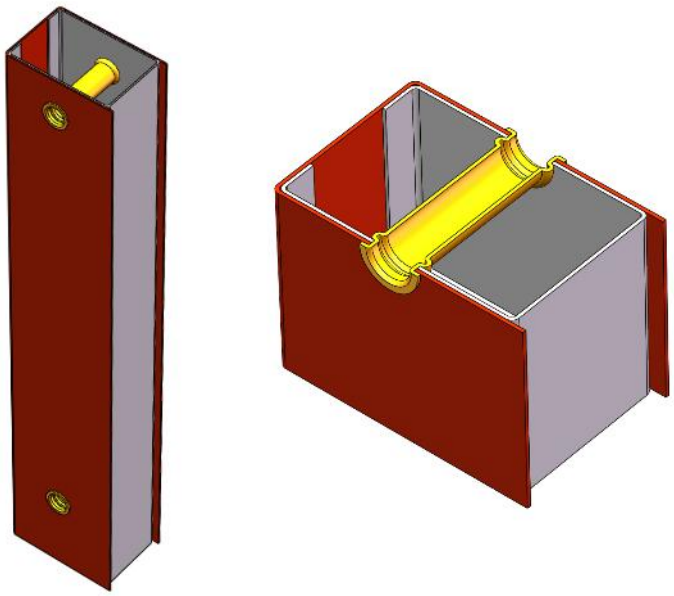

Figure 5-1 3D view of the novel CFS built-up column with HRCs

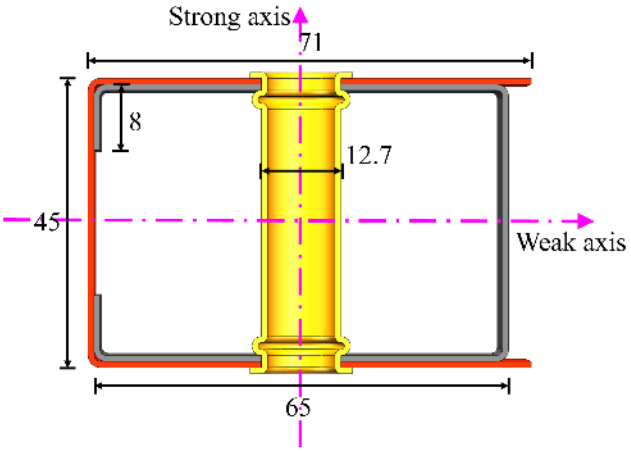

Figure 5-2 Nominal dimensions of the built-up box section (all dimensions in mm)

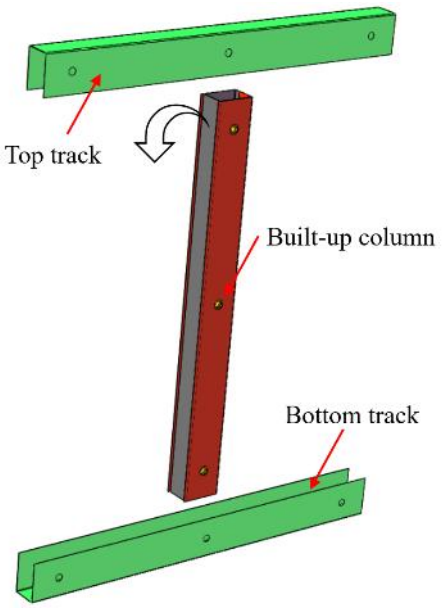

Figure 5-3 The application of built-up columns in CFS structural systems

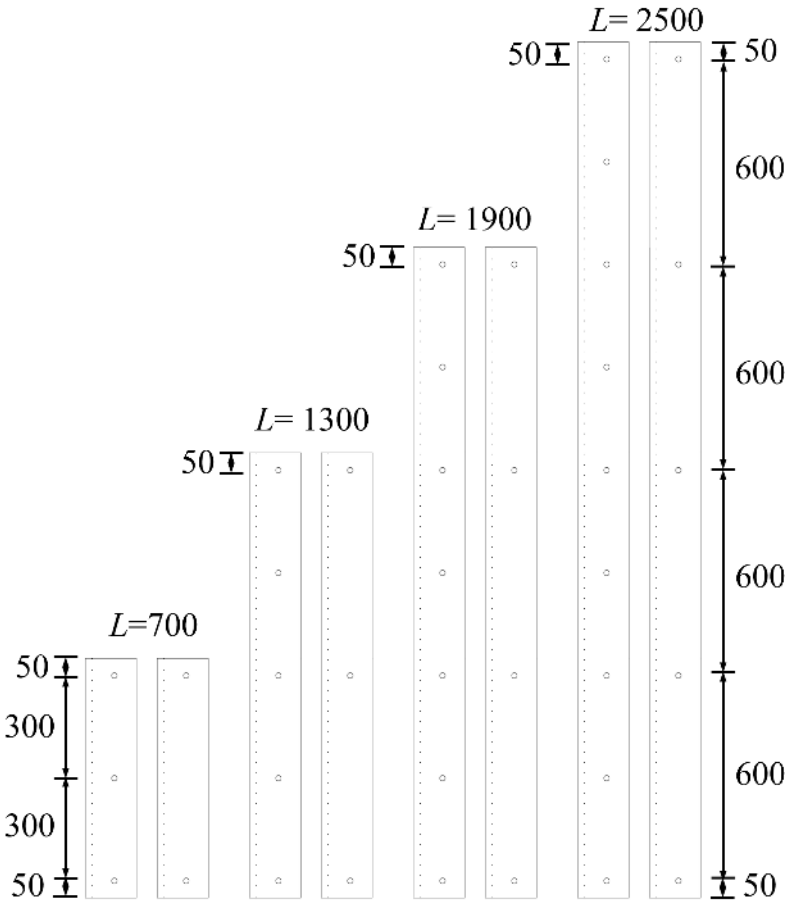

Figure 5-4 Nominal lengths of the specimens and fastener spacing (all dimensions in mm)

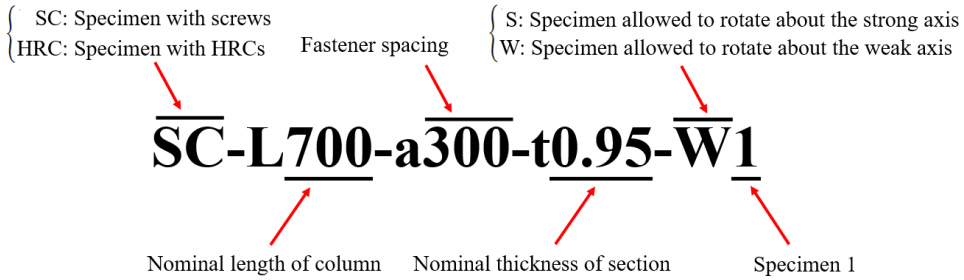

Figure 5-5 Specimen labelling

Table 5-1 Measured cross-sectional dimensions of specimens with a thickness of 0.95 mm

Specimens	Single C-section				Single U-section /Built-up box section			Length
	Web d mm	Flange b mm	Lip l mm	Thickness t mm	Web d mm	Flange b mm	Thickness t mm	L mm
(a) Specimens allowed to rotate about the weak axis								
HRC-L700-a300-t0.95-W1	45.54	64.82	8.86	1.07	45.34	70.89	1.03	700.0
HRC-L700-a300-t0.95-W2	45.53	64.61	8.22	1.08	45.46	70.80	1.06	699.9
HRC-L700-a600-t0.95-W1	45.36	64.95	8.74	0.98	45.35	71.16	1.04	699.6
HRC-L700-a600-t0.95-W2	45.54	64.41	8.80	1.02	45.31	70.84	1.03	700.3
HRC-L1300-a300-t0.95-W1	45.40	65.16	8.07	1.05	45.45	71.42	1.05	1300.5
HRC-L1300-a300-t0.95-W2	45.29	65.43	7.35	0.95	44.81	70.63	0.96	1300.1
HRC-L1300-a600-t0.95-W1	45.31	65.55	8.20	0.97	45.11	71.23	1.02	1300.4
HRC-L1300-a600-t0.95-W2	45.13	65.35	8.23	1.06	45.76	71.37	1.00	1300.0
HRC-L1900-a300-t0.95-W1	45.09	64.86	8.66	0.96	45.71	70.97	1.04	1900.9
HRC-L1900-a300-t0.95-W2	45.48	65.07	8.80	1.02	46.20	71.11	0.99	1900.5
HRC-L1900-a600-t0.95-W1	44.88	65.36	7.75	1.00	45.32	70.62	1.00	1900.3
HRC-L1900-a600-t0.95-W2	45.23	64.78	8.23	1.01	45.51	70.80	1.03	1900.2
HRC-L2500-a300-t0.95-W1	45.26	64.77	8.10	0.99	45.56	70.76	1.02	2499.3
HRC-L2500-a300-t0.95-W2	44.93	64.98	7.99	1.01	44.79	70.68	1.02	2500.1
HRC-L2500-a600-t0.95-W1	45.70	64.83	8.21	0.98	45.07	70.75	1.00	2500.7
HRC-L2500-a600-t0.95-W2	45.29	65.44	8.11	1.03	45.68	71.10	1.01	2500.0
(b) Specimens allowed to rotate about the strong axis								
HRC-L700-a300-t0.95-S1	45.12	64.99	8.39	1.07	44.96	71.40	1.00	699.6
HRC-L700-a300-t0.95-S2	45.50	66.10	8.06	1.07	45.43	70.91	1.06	700.1
HRC-L700-a600-t0.95-S1	45.29	66.13	8.10	1.02	45.41	70.92	1.00	700.0
HRC-L700-a600-t0.95-S2	44.85	65.14	7.98	0.99	45.10	71.08	1.03	699.9
HRC-L1300-a300-t0.95-S1	45.12	65.64	7.56	1.03	46.31	71.07	1.00	1300
HRC-L1300-a300-t0.95-S2	45.28	65.29	7.46	1.04	46.40	71.68	1.04	1300.1
HRC-L1300-a600-t0.95-S1	45.45	65.56	7.59	1.02	45.55	70.63	0.96	1299.8
HRC-L1300-a600-t0.95-S2	45.29	65.07	8.12	1.02	45.25	71.25	0.99	1299.8
HRC-L1900-a300-t0.95-S1	45.01	65.86	8.14	1.00	45.19	70.91	0.96	1900.0
HRC-L1900-a300-t0.95-S2	44.97	65.28	7.89	0.99	45.04	70.85	0.96	1900.1
HRC-L1900-a600-t0.95-S1	45.06	65.53	7.99	0.97	45.25	71.38	0.98	1900.3
HRC-L1900-a600-t0.95-S2	45.25	65.50	8.14	0.99	45.69	71.05	0.99	1900.1
HRC-L2500-a300-t0.95-S1	45.44	65.70	7.98	1.00	45.83	71.18	1.03	2500.3
HRC-L2500-a300-t0.95-S2	45.85	65.30	8.06	1.02	45.65	71.20	1.00	2500.6
HRC-L2500-a600-t0.95-S1	45.43	65.35	8.12	1.01	45.67	71.06	0.98	2500.0
HRC-L2500-a600-t0.95-S2	45.04	65.51	8.05	1.01	45.56	70.98	1.03	2500.5

Table 5-2 Measured cross-sectional dimensions of specimens with a thickness of 1.15 mm

Specimens	Single C-section				Single U-section /Built-up box section			Length
	Web *d* mm	Flange *b* mm	Lip *l* mm	Thickness *t* mm	Web *d* mm	Flange *b* mm	Thickness *t* mm	*L* mm
(a) Specimens allowed to rotate about the weak axis								
HRC-L700-a300-t1.15-W1	45.67	64.85	8.29	1.22	45.61	71.11	1.23	699.6
HRC-L700-a300-t1.15-W2	45.77	65.86	8.37	1.21	45.76	70.75	1.22	699.9
HRC-L700-a600-t1.15-W1	45.55	66.18	9.20	1.20	45.20	70.61	1.19	700.0
HRC-L700-a600-t1.15-W2	45.35	64.67	8.78	1.22	45.69	71.16	1.14	699.7
HRC-L1300-a300-t1.15-W1	45.31	65.18	8.47	1.24	45.11	70.62	1.24	1300.2
HRC-L1300-a300-t1.15-W2	45.46	65.62	8.14	1.24	45.28	71.18	1.26	1299.9
HRC-L1300-a600-t1.15-W1	45.31	65.11	8.35	1.25	45.56	70.73	1.23	1300.4
HRC-L1300-a600-t1.15-W2	45.09	65.05	8.49	1.24	45.06	70.94	1.21	1300.0
HRC-L1900-a300-t1.15-W1	45.50	64.46	8.22	1.25	45.39	70.70	1.25	1900.5
HRC-L1900-a300-t1.15-W2	45.20	65.04	8.15	1.27	45.66	70.50	1.26	1299.7
HRC-L1900-a600-t1.15-W1	45.21	65.26	8.15	1.19	45.33	71.44	1.27	1900.2
HRC-L1900-a600-t1.15-W2	45.13	65.69	7.96	1.24	45.71	71.67	1.26	1900.1
HRC-L2500-a300-t1.15-W1	45.24	65.83	7.97	1.19	46.01	71.52	1.25	2500.0
HRC-L2500-a300-t1.15-W2	45.51	65.12	8.10	1.24	45.64	70.59	1.24	2500.6
HRC-L2500-a600-t1.15-W1	45.16	65.02	7.90	1.24	45.08	70.68	1.25	2500.2
HRC-L2500-a600-t1.15-W2	45.59	65.40	8.03	1.25	45.12	70.91	1.21	2500.1
(b) Specimens allowed to rotate about the strong axis								
HRC-L700-a300-t1.15-S1	45.43	65.35	8.33	1.23	45.49	71.33	1.24	700.0
HRC-L700-a300-t1.15-S2	44.87	65.17	8.01	1.20	45.85	71.73	1.21	700.0
HRC-L700-a600-t1.15-S1	44.92	64.64	7.89	1.19	45.50	70.87	1.21	700.1
HRC-L700-a600-t1.15-S2	45.93	64.67	8.05	1.28	45.21	71.21	1.23	699.8
HRC-L1300-a300-t1.15-S1	45.24	65.65	8.14	1.22	46.50	70.53	1.23	1300.1
HRC-L1300-a300-t1.15-S2	45.35	64.88	8.31	1.23	45.83	71.59	1.22	1300.2
HRC-L1300-a600-t1.15-S1	44.78	64.91	8.11	1.20	45.47	72.38	1.17	1299.0
HRC-L1300-a600-t1.15-S2	45.80	65.62	8.16	1.24	45.68	71.74	1.25	1300.2
HRC-L1900-a300-t1.15-S1	45.56	65.36	7.89	1.24	45.56	71.47	1.26	1900.2
HRC-L1900-a300-t1.15-S2	45.35	65.64	7.46	1.21	45.78	71.56	1.26	1900.0
HRC-L1900-a600-t1.15-S1	45.35	64.60	7.95	1.21	45.42	70.39	1.21	1900.8
HRC-L1900-a600-t1.15-S2	45.40	65.00	7.99	1.20	45.66	70.88	1.21	1900.2
HRC-L2500-a300-t1.15-S1	45.45	65.21	8.05	1.25	45.80	70.95	1.22	1901.0
HRC-L2500-a300-t1.15-S2	45.29	65.04	8.24	1.21	45.79	72.09	1.18	1900.9
HRC-L2500-a600-t1.15-S1	45.71	65.31	8.49	1.21	45.93	71.68	1.19	1900.0
HRC-L2500-a600-t1.15-S2	45.29	65.27	7.98	1.21	45.74	71.51	1.25	1899.9

Table 5-3 Measured cross-sectional dimensions of specimens with screws

Specimen	Single C-section				Single U-section /Built-up box section			Length
	Web *d* mm	Flange *b* mm	Lip *l* mm	Thickness *t* mm	Web *d* mm	Flange *b* mm	Thickness *t* mm	*L* mm
(a) Thickness of 0.95 mm								
SC-L700-a300-t0.95-W1	44.79	65.51	7.27	0.96	44.78	70.47	0.97	700.0
SC-L700-a300-t0.95-W2	44.71	65.53	7.58	0.97	45.35	71.03	1.08	699.0
SC-L700-a300-t0.95-W3	45.34	65.27	8.07	0.98	44.46	71.13	0.98	700.0
SC-L700-a600-t0.95-W1	45.39	65.46	7.90	0.97	44.60	71.29	0.97	699.0
SC-L700-a600-t0.95-W2	44.40	64.75	7.64	0.98	45.90	70.24	1.06	700.5
SC-L700-a600-t0.95-W3	44.90	65.25	8.10	1.01	45.22	70.89	0.97	700.0
SC-L1300-a300-t0.95-W1	44.84	65.86	7.69	1.05	45.20	70.50	1.05	1300.0
SC-L1300-a300-t0.95-W2	45.27	65.94	7.65	1.07	45.09	70.96	1.08	1300.0
SC-L1300-a300-t0.95-W3	45.32	66.08	7.28	0.97	45.12	70.65	1.06	1300.0
SC-L1300-a600-t0.95-W1	45.35	65.63	7.80	1.05	45.34	70.78	1.05	1300.0
SC-L1300-a600-t0.95-W2	46.11	65.91	7.90	1.08	45.18	71.73	0.99	1301.0
SC-L1300-a600-t0.95-W3	45.17	65.89	7.62	0.95	45.41	71.08	0.98	1300.0
SC-L1900-a300-t0.95-W1	45.35	64.90	8.45	0.98	45.16	71.02	0.98	1900.5
SC-L1900-a300-t0.95-W2	45.43	65.84	8.69	0.99	44.99	71.85	0.99	1900.0

SC-L1900-a300-t0.95-W3	45.09	64.80	8.97	1.01	44.78	70.68	0.96	1901.0
SC-L1900-a600-t0.95-W1	44.67	64.62	8.84	0.98	44.83	70.81	1.09	1900.5
SC-L1900-a600-t0.95-W2	44.72	64.92	8.12	1.02	44.82	71.10	0.98	1900.5
SC-L1900-a600-t0.95-W3	44.84	65.35	8.33	0.99	44.68	70.63	0.97	1899.5
SC-L2500-a300-t0.95-W1	44.65	65.69	8.36	1.02	44.55	70.68	1.04	2500.0
SC-L2500-a300-t0.95-W2	44.67	65.37	8.33	1.02	45.01	70.87	0.99	2500.5
SC-L2500-a300-t0.95-W3	45.33	65.02	7.86	1.01	44.73	70.86	0.96	2499.5
SC-L2500-a600-t0.95-W1	44.89	65.59	8.55	1.03	44.92	70.80	1.01	2501.0
SC-L2500-a600-t0.95-W2	45.36	64.83	8.49	0.98	45.02	70.30	1.01	2500.2
SC-L2500-a600-t0.95-W3	44.73	65.33	8.37	0.97	44.58	70.55	1.06	2500.5
(b) Thickness of 1.15 mm								
SC-L700-a300-t1.15-W1	44.30	64.88	8.25	1.14	44.70	70.46	1.31	700.0
SC-L700-a300-t1.15-W2	44.88	65.54	8.58	1.18	44.91	70.78	1.21	700.0
SC-L700-a300-t1.15-W3	44.65	64.88	7.81	1.21	44.73	70.68	1.23	699.5
SC-L700-a600-t1.15-W1	44.96	65.43	7.90	0.97	44.79	71.56	1.29	699.5
SC-L700-a600-t1.15-W2	44.40	64.81	8.33	1.06	44.74	70.74	1.23	700.0
SC-L700-a600-t1.15-W3	44.76	65.09	7.83	1.23	44.96	71.27	1.20	700.0
SC-L1300-a300-t1.15-W1	44.77	65.44	8.28	1.21	45.11	71.24	1.23	1300.0
SC-L1300-a300-t1.15-W2	44.68	64.97	7.99	1.23	45.06	71.17	1.25	1300.5
SC-L1300-a300-t1.15-W3	44.74	65.09	7.90	1.19	45.04	71.53	1.26	1300.5
SC-L1300-a600-t1.15-W1	44.75	65.19	7.94	1.23	44.95	71.71	1.29	1300.0
SC-L1300-a600-t1.15-W2	44.85	65.23	8.29	1.24	45.03	71.31	1.20	1299.5
SC-L1300-a600-t1.15-W3	44.51	65.10	8.28	1.23	44.87	71.52	1.27	1300.5
SC-L1900-a300-t1.15-W1	44.79	65.02	8.20	1.28	44.96	71.33	1.25	1900.5
SC-L1900-a300-t1.15-W2	44.83	65.08	7.95	1.22	44.75	71.28	1.29	1900.5
SC-L1900-a300-t1.15-W3	44.98	64.73	7.98	1.21	44.64	71.41	1.28	1900.5
SC-L1900-a600-t1.15-W1	44.62	65.02	8.13	1.22	45.07	71.52	1.26	1899.5
SC-L1900-a600-t1.15-W2	44.85	65.05	8.07	1.19	45.09	71.42	1.25	1899.5
SC-L1900-a600-t1.15-W3	44.87	64.58	8.04	1.20	45.25	71.58	1.24	1900.0
SC-L2500-a300-t1.15-W1	44.79	64.84	7.99	1.19	45.30	71.53	1.24	2500.5
SC-L2500-a300-t1.15-W2	44.82	64.78	7.90	1.17	44.71	71.46	1.22	2500.5
SC-L2500-a300-t1.15-W3	44.81	65.14	7.82	1.23	45.09	71.41	1.28	2500.3
SC-L2500-a600-t1.15-W1	44.52	64.91	8.20	1.21	44.89	71.45	1.20	2499.8
SC-L2500-a600-t1.15-W2	44.98	65.03	9.15	1.19	45.41	70.57	1.27	2500.0
SC-L2500-a600-t1.15-W3	44.73	65.50	8.01	1.18	44.90	71.20	1.25	2500.7

5.2.2. Material testing

The actual material properties of the CFS sections were obtained through tensile testing. Two sets of coupons, representing different nominal thicknesses, were extracted from the untested web along the length of the specimen. The dimensions of these coupons are shown in Figure 5-6. An Instron machine with a capacity of 100 kN was used to conduct the tensile coupon tests, as shown in Figure 5-7. According to the latest calibration certificate, the repeatability error of the 100 kN load cell is 0.06%. The strain of the coupons under tension was measured using an extensometer with a gauge length of 25 mm. The repeat error of the strain gauge is 0.006%, and the measurement uncertainty is 0.002 mm.

The photos after fracture and actual stress-strain curves for both thicknesses are shown in Figures 5-8 and 5-9, with the results summarized in Table 5-4. The initial linear elastic portion of the stress-strain curve is offset by 0.2% strain; the stress at which this line intersects the curve is taken as the yield stress (f_y). For the thickness of 0.95 mm, the average f_y is 691.59 MPa and the ultimate strength (f_u) is 693.61 MPa. For the thickness of 1.15 mm, these values are 588.38 MPa and 601.38 MPa, respectively. The nominal steel grade of the coupons, which have two different thicknesses, is G550. However, due to differences in production batches for the two thicknesses, significant variations in material properties were observed.

The AS/NZS (2018) standard recommends that the total elongation of a tensile coupon should be at least 10% for a 50 mm gauge length. However, there are no detailed specifications for a 25 mm gauge length. Although the elongation may not meet the AS/NZS (2018) recommendation, similar levels of ductility in high-strength CFS with less than 10% elongation have also been reported by Dai et al. (2024) and Zhong et al. (2023).

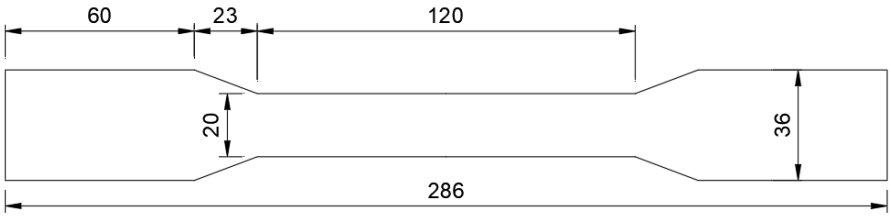

Figure 5-6 Dimensions of tensile coupons

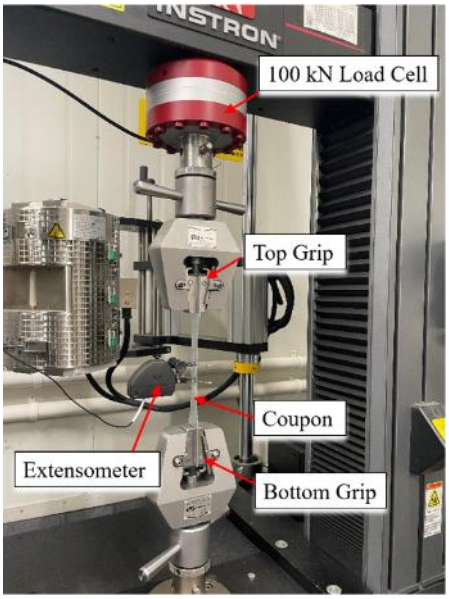

Figure 5-7 Setup of the tensile coupon tests

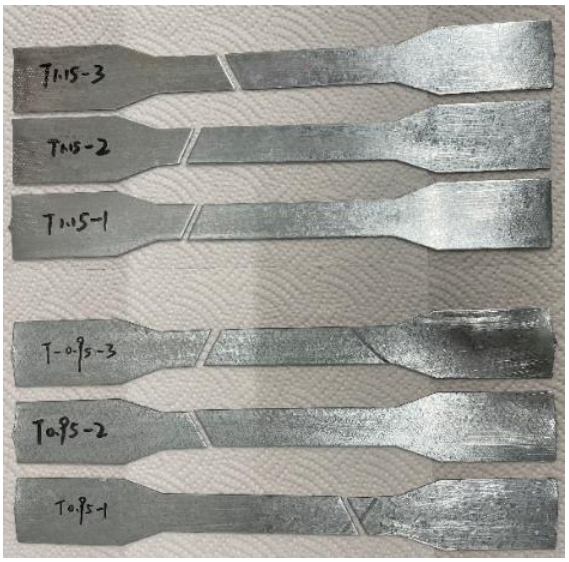
Figure 5-8 Photos of the coupons after failure

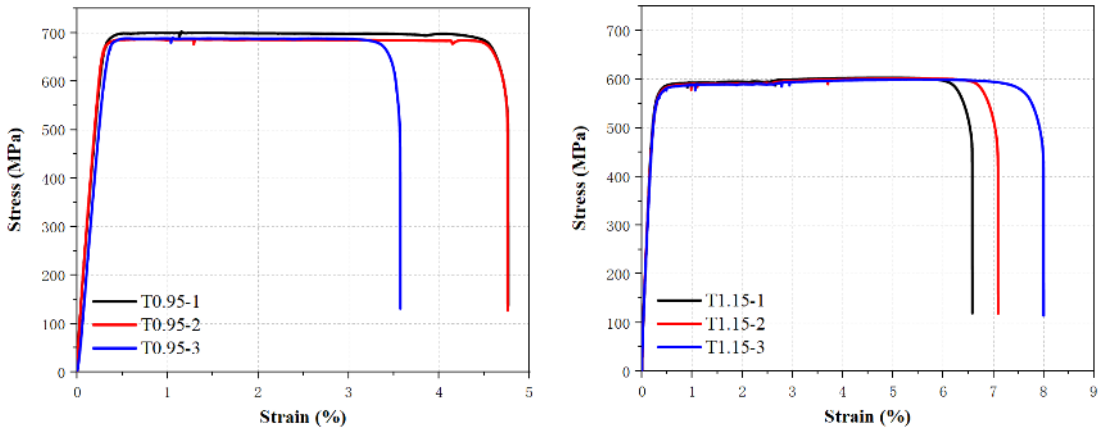

(a)Thickness of 0.95 mm (b) Thickness of 1.15 mm

Figure 5-9 Stress-strain curves obtained from the tensile coupon tests

Table 5-4 Measured material properties of the coupons

Coupons	Thickness t mm	Yield stress f_y MPa	Ultimate stress f_u MPa	Young's modulus E $\times 10^5$ MPa	Elongation %
T0.95-1	0.98	699.67	702.78	2.06	4.8
T0.95-2	0.97	686.87	688.09	2.13	4.8
T0.95-3	0.97	688.24	689.97	2.01	4.1
Mean	0.97	691.59	693.61	2.06	4.6
COV	0.006	0.010	0.012	0.029	0.088
T1.15-1	1.17	591.41	603.06	2.08	6.6
T1.15-2	1.17	588.04	601.67	1.96	7.1
T1.15-3	1.18	585.69	599.42	2.03	8.0
Mean	1.17	588.38	601.38	2.02	7.2
COV	0.005	0.005	0.003	0.030	0.098

5.2.3. Initial geometric imperfection measurements

In practical engineering, CFS members are susceptible to initial deformation and inherent geometric imperfections caused by factors such as manufacturing, transportation, and installation. The presence of these imperfections can significantly influence their failure modes and load-bearing capacity. Therefore, measuring the initial geometric imperfections of the specimens before the axial compression tests is essential.

The measurement setup used in this study is shown in Figure 5-10(a). The primary function of this measuring device is to allow the linear variable differential transformer (LVDT) to slide smoothly along the guide rail. Due to the challenges in achieving perfect parallel alignment between the specimen and the guide rail, the initial inclination of the specimen must be subtracted to determine the actual imperfections. Figure 5-10(b) illustrates the measurement principle of the initial geometric imperfection, where d_1 to d_n represent the measured values from the LVDT. The gray dotted line indicates the actual plane of the specimen to be measured, which serves as the running track for the LVDT. It is important to note that the LVDT readings were reset to zero before each measurement. Therefore, the actual initial geometric imperfections y_1 to y_{n-1} of the built-up column were calculated using Equation 5.2.

$$y_x = d_x - d_n x / L_m$$ Equation 5.2

where y_x represents the actual initial geometric imperfections of the specimen, d_n is the measured value at the endpoint of the measurement, d_x is the measured value during the measurement, x is the distance of the LVDT's movement, and L_m is the actual length of specimens.

Bending of the member occurs along the x-axis of the built-up sections due to the pin-end boundary conditions, which involve strong-axis fixation and weak-axis hinge support, as shown in Figure 5-10(c). The initial geometric imperfections were measured on four faces of the specimens, establishing a total of ten measuring points. The precise locations for measuring the initial imperfections are displayed in Figure 5-10(c). Figure 5-11 plots the imperfection profile of two specimens. The global initial bending (F_{U3} and F_{U4}) of the specimen resembles a half-wave sine curve, with multiple half-wave deformations occurring simultaneously. The global flexural imperfection (δ_{global}) of the bult-up section columns around the minor axis was determined as the maximum value of the imperfection measurements F_{U3} and F_{U4}. The maximum out-of-plane imperfections δ_{max} were defined as the maximum value of all measured imperfections (W_{C1}-W_{C3}, W_{U1}-W_{U3}, and F_{U1}-F_{U4}). According to AS/NZS (2018), δ_{max} should be taken as 1/1,000 of the member length in numerical analysis. Table 5-5 lists the values of δ_{global} and δ_{max} for each measured specimen; both δ_{global}/L_m and δ_{max}/L_m for the specimens were lower than the value recommended by AS/NZS (2018).

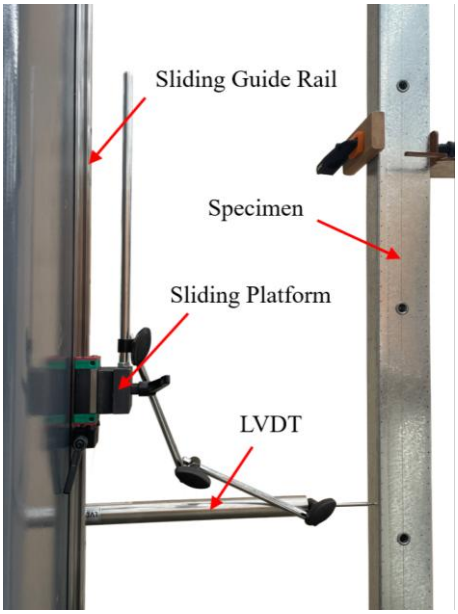

(a) Imperfection measurement setup

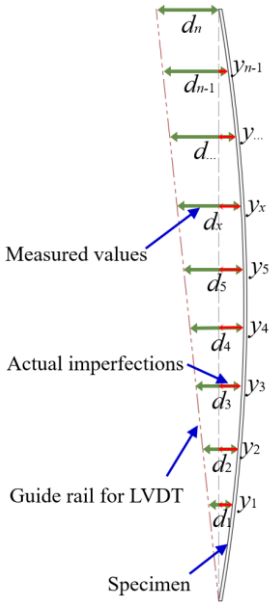

(b) Measurement principle

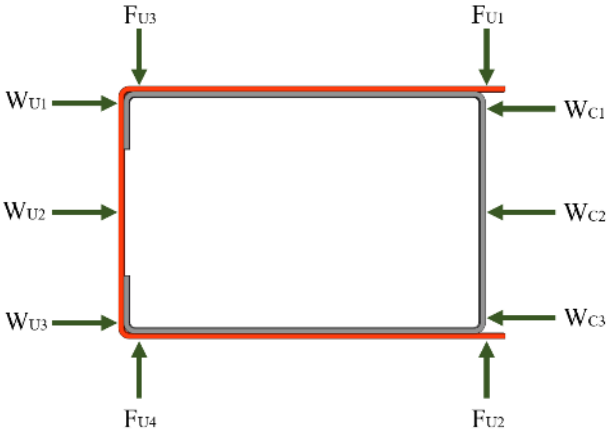

(c)Imperfection measurement paths

Figure 5-10 Initial imperfection measurements

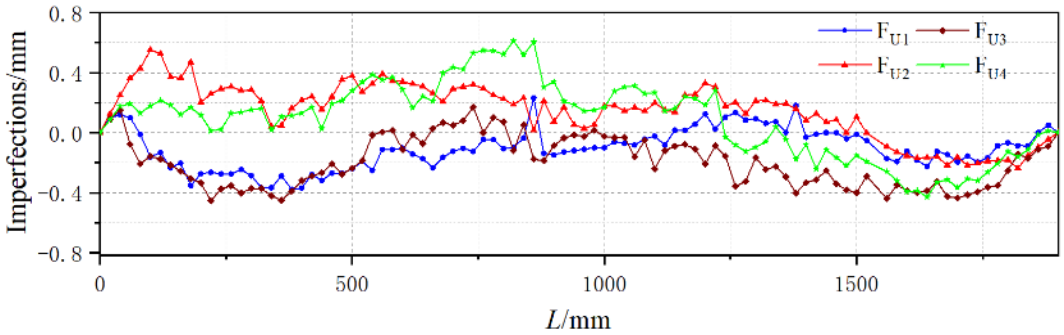

(i)Imperfections of F_{U1}, F_{U2}, F_{U3}, and F_{U4}

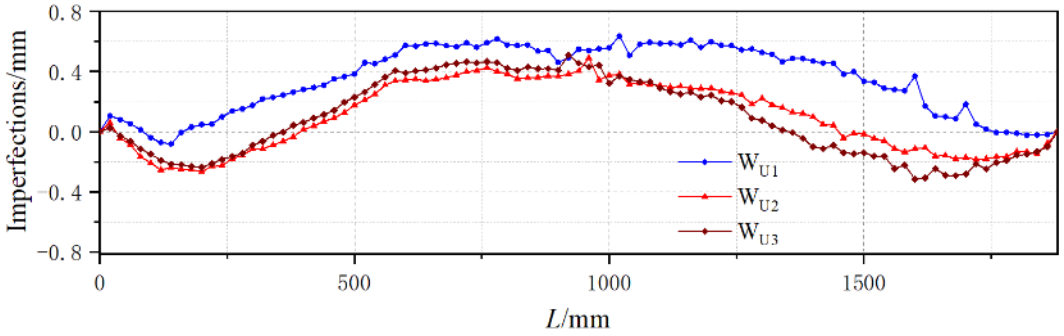

(ii)Imperfections of W_{U1}, W_{U2}, and W_{U3}

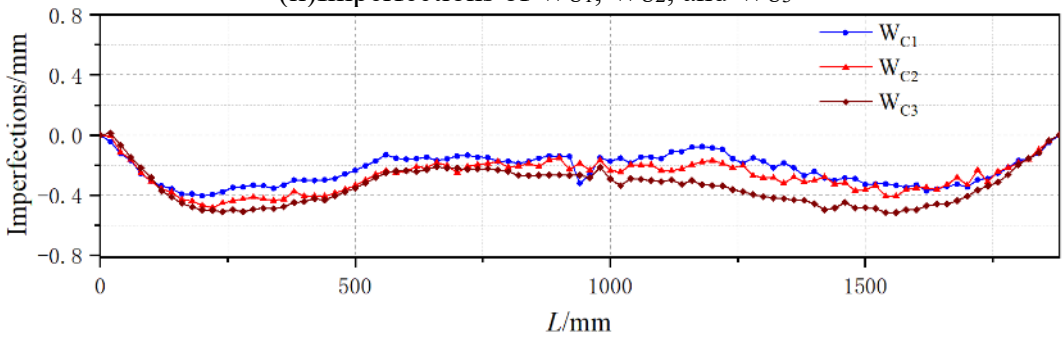

(iii)Imperfections of W_{C1}, W_{C2}, and W_{C3}

(a) SC-L1900-a300-t0.95

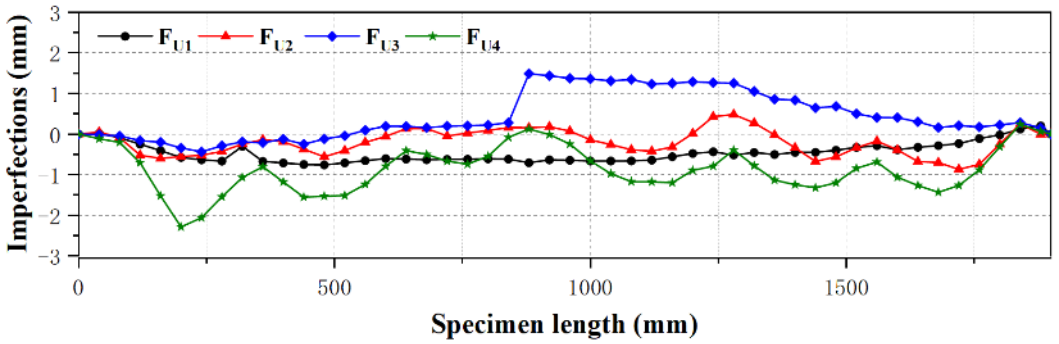

(i)Imperfections of F_{U1}, F_{U2}, F_{U3}, and F_{U4}

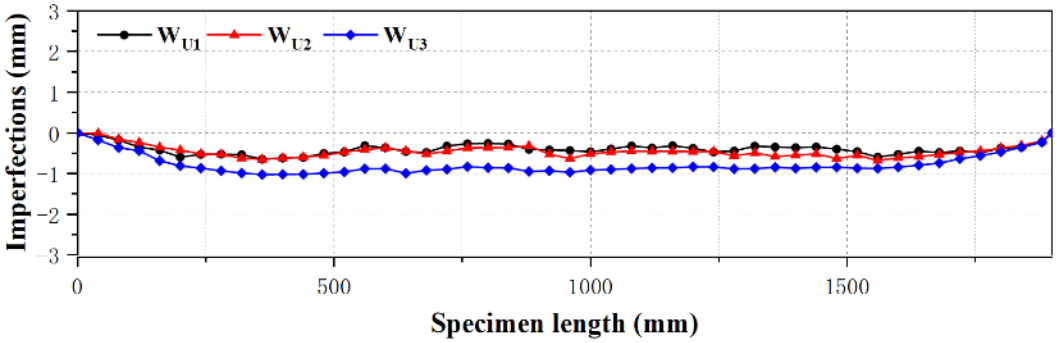

(ii)Imperfections of W_{U1}, W_{U2}, and W_{U3}

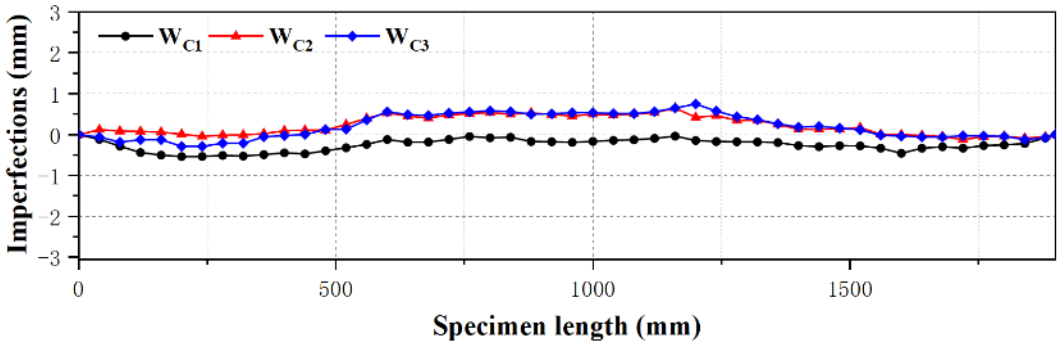

(iii)Imperfections of W_{C1}, W_{C2}, and W_{C3}

(b) HRC-L1900-a300-t0.95

Figure 5-11 Typical imperfection profile

Table 5-5 Maximum amplitude of measured imperfections

Specimens	δ_{global} mm	δ_{global}/L_m ‰	δ_{max} mm	δ_{max}/L_m ‰
HRC-L700-a300-t0.95	0.96	1.37	0.96	1.37
HRC-L700-a600-t0.95	0.72	1.02	0.72	1.02
HRC-L700-a300-t1.15	0.59	0.84	0.65	0.93
HRC-L700-a600-t1.15	0.39	0.56	1.04	1.49
HRC-L1300-a300-t0.95	0.72	0.55	1.66	1.28
HRC-L1300-a600-t0.95	0.74	0.57	0.74	0.57
HRC-L1300-a300-t1.15	0.47	0.36	0.76	0.58
HRC-L1300-a600-t1.15	0.65	0.50	0.71	0.55
HRC-L1900-a300-t0.95	1.49	0.78	1.49	0.78
HRC-L1900-a600-t0.95	2.06	1.08	2.06	1.08
HRC-L1900-a300-t1.15	1.08	0.57	1.09	0.57
HRC-L1900-a600-t1.15	0.87	0.46	1.39	0.73
HRC-L2500-a300-t0.95	1.67	0.67	2.88	1.15
HRC-L2500-a600-t0.95	1.02	0.41	1.72	0.69
HRC-L2500-a300-t1.15	1.20	0.48	1.52	0.61
HRC-L2500-a600-t1.15	1.12	0.45	1.78	0.71
SC-L700-a300-t0.95	0.53	0.76	0.53	0.76
SC-L700-a600-t0.95	0.76	1.09	0.85	1.21
SC-L700-a300-t1.15	0.35	0.50	0.57	0.81
SC-L700-a600-t1.15	0.36	0.51	0.44	0.63
SC-L1300-a300-t0.95	0.82	0.63	1.03	0.79
SC-L1300-a600-t0.95	0.42	0.32	0.50	0.38
SC-L1300-a300-t1.15	0.44	0.34	0.50	0.38
SC-L1300-a600-t1.15	0.42	0.32	0.58	0.45
SC-L1900-a300-t0.95	1.62	0.85	1.86	0.98
SC-L1900-a600-t0.95	1.50	0.79	1.50	0.79
SC-L1900-a300-t1.15	0.61	0.32	0.64	0.34
SC-L1900-a600-t1.15	0.49	0.26	0.76	0.40
SC-L2500-a300-t0.95	2.42	0.97	2.42	0.97
SC-L2500-a600-t0.95	2.30	0.92	2.30	0.92
SC-L2500-a300-t1.15	1.47	0.59	1.48	0.59
SC-L2500-a600-t1.15	1.28	0.51	1.86	0.74

5.2.4. Testing-rig and loading procedure

An axial load was applied to the specimens using a servo-controlled hydraulic system at a displacement rate of 0.2 mm/min, as illustrated in Figure 5-12(a). To achieve pin-ended boundary conditions along the specimen's weak and strong axes, respectively, pin-ended supports were installed at each end, as illustrated in Figures 5-12(b) and 5-12(c). Fastening devices were used to secure the supports, ensuring stability and preventing movement during loading or specimen exchanges. The hinge centre was positioned 70 mm from the specimen's end, resulting in a calculated column length for the built-up section equal to the specimen length plus this offset. Two LVDTs were installed at the top support and mid-height of the specimen to measure axial shortening and lateral displacement.

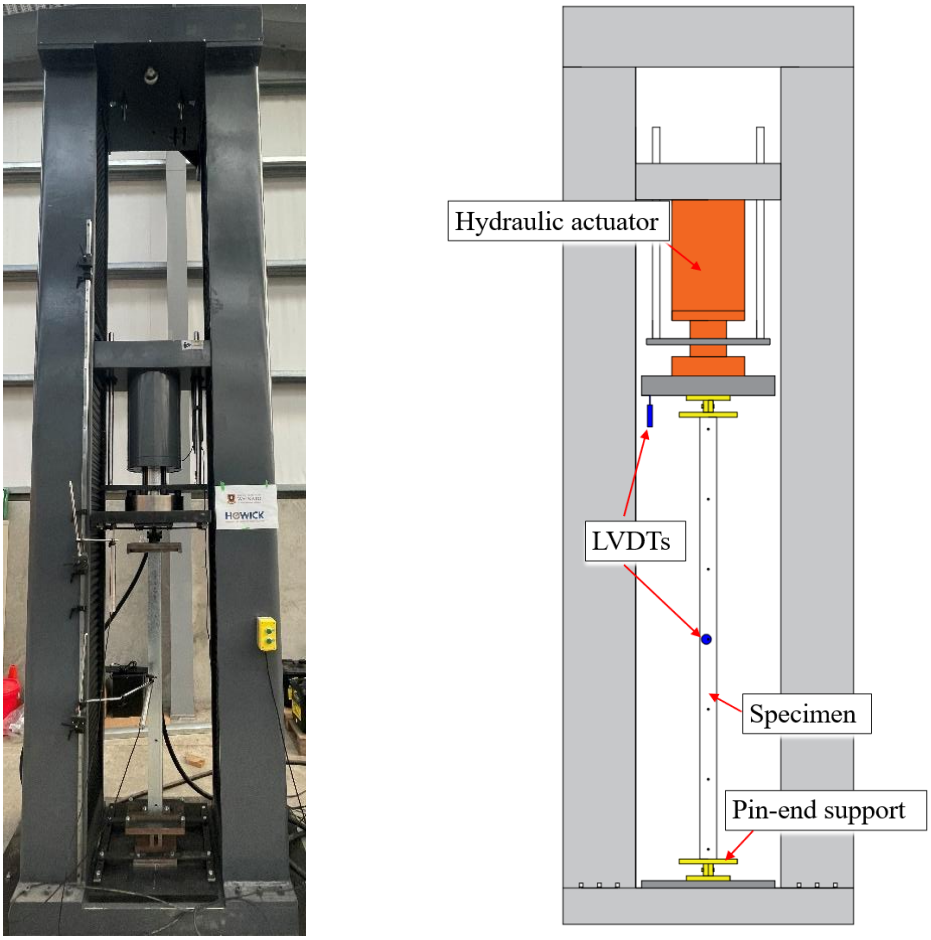

(a)Hydraulic universal testing machine

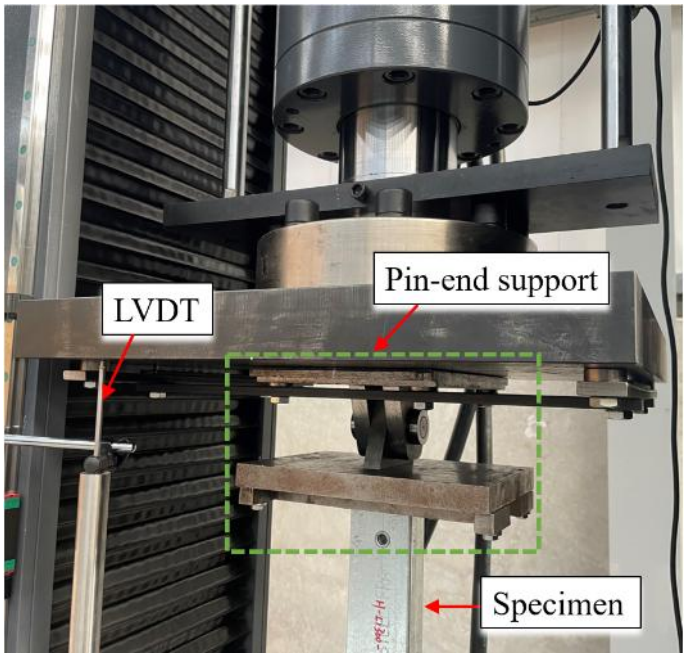

(b) Allowed rotation around the weak axis

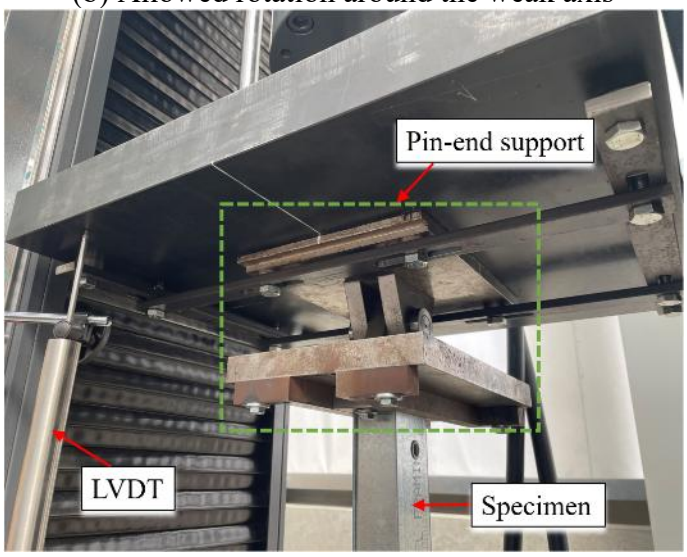

(c)Allowed rotation around the strong axis

Figure 5-12 Test setup for compression tests

5.2.5. Test results and discussions

5.2.5.1. Specimens with HRCs

The axial strength (P_{EXP}) of the built-up columns was investigated for various thicknesses, HRC spacings, and slenderness ratios. The experimental results are summarized in Tables 5-6 and 5-7, where "L" indicates local buckling, "D" represents distortional buckling in

the C-section, and "F_S" and "F_W" denote flexural buckling about the strong and weak axes, respectively.

Table 5-6 Test results of specimens with a thickness of 0.95 mm

Specimen ID	Test			FEA		P_{EXP}/P_{FEA}
	Loads P_{EXP} /kN	Mean $\bar{P}_{EXP}$ /kN	Failure modes	Loads P_{FEA} /kN	Failure modes	
(a) Specimens allowed to rotate about the weak axis						
HRC-L700-a300-t0.95-W1	74.70	76.25	L+D	81.9	L+D	0.91
HRC-L700-a300-t0.95-W2	77.80		L+D			0.95
HRC-L700-a600-t0.95-W1	78.25	75.63	L+D	80.2	L+D	0.98
HRC-L700-a600-t0.95-W2	73.00		L+D			0.91
HRC-L1300-a300-t0.95-W1	76.55	74.00	L+F_S	75.3	L+D+F_W	1.02
HRC-L1300-a300-t0.95-W2	71.45		L+D+F_W			0.95
HRC-L1300-a600-t0.95-W1	67.85	67.15	L+D+F_S	74.8	L+D+F_W	0.91
HRC-L1300-a600-t0.95-W2	66.45		L+F_W			0.89
HRC-L1900-a300-t0.95-W1	60.50	62.35	L+F_W	62.1	L+F_W	0.97
HRC-L1900-a300-t0.95-W2	64.20		L+D+F_S			1.03
HRC-L1900-a600-t0.95-W1	54.80	57.93	L+F_W	60.1	L+F_W	0.91
HRC-L1900-a600-t0.95-W2	61.05		L+F_W			1.02
HRC-L2500-a300-t0.95-W1	37.80	43.55	L+F_W	48.3	L+F_W	0.78
HRC-L2500-a300-t0.95-W2	49.30		F_W			1.02
HRC-L2500-a600-t0.95-W1	46.60	47.48	F_W	47.9	L+F_W	0.97
HRC-L2500-a600-t0.95-W2	48.35		F_W			1.01
(b) Specimens allowed to rotate about the strong axis						
HRC-L700-a300-t0.95-S1	79.35	76.75	L+D	81.9	L+D	0.97
HRC-L700-a300-t0.95-S2	74.15		L+D			0.91
HRC-L700-a600-t0.95-S1	75.70	74.65	L+D	80.2	L+D	0.94
HRC-L700-a600-t0.95-S2	73.60		L+D			0.92
HRC-L1300-a300-t0.95-S1	74.00	73.80	L+D	75.3	L+D+F_W	0.98
HRC-L1300-a300-t0.95-S2	73.60		L+D			0.98
HRC-L1300-a600-t0.95-S1	74.55	74.78	L+F_S	74.8	L+D+F_W	1.00
HRC-L1300-a600-t0.95-S2	75.00		L+D+F_W			1.00
HRC-L1900-a300-t0.95-S1	63.30	62.58	L+F_W	62.1	L+F_W	1.02
HRC-L1900-a300-t0.95-S2	61.85		L+F_S			1.00
HRC-L1900-a600-t0.95-S1	61.95	61.13	L+F_S	60.1	L+F_W	1.03
HRC-L1900-a600-t0.95-S2	60.30		L+F_S			1.00
HRC-L2500-a300-t0.95-S1	47.35	46.38	L+F_W	48.3	L+F_W	0.98
HRC-L2500-a300-t0.95-S2	45.40		L+F_W			0.94
HRC-L2500-a600-t0.95-S1	46.65	47.00	L+F_W	47.9	L+F_W	0.97
HRC-L2500-a600-t0.95-S2	47.35		L+F_W			0.99
Mean						0.97
COV						0.06

Table 5-7 Test results of specimens with a thickness of 1.15 mm

Specimen ID	Test			FEA		P_{EXP}/P_{FEA}
	Loads P_{EXP} /kN	Mean $\bar{P}_{EXP}$ /kN	Failure modes	Loads P_{FEA} /kN	Failure modes	
(a) Specimens allowed to rotate about the weak axis						
HRC-L700-a300-t1.15-W1	92.05	94.63	L+D	104.7	L+D	0.88
HRC-L700-a300-t1.15-W2	97.20		L			0.93
HRC-L700-a600-t1.15-W1	101.30	99.43	L+D	97.6	L+D	1.04
HRC-L700-a600-t1.15-W2	97.55		L+D			1.00

HRC-L1300-a300-t1.15-W1	96.90	93.75	$L+F_W$	100.2	L+D	0.97
HRC-L1300-a300-t1.15-W2	90.60		$L+F_W$			0.90
HRC-L1300-a600-t1.15-W1	85.40	89.50	$L+F_W$	94.2	L+D	0.91
HRC-L1300-a600-t1.15-W2	93.60		$L+D+F_S$			0.99
HRC-L1900-a300-t1.15-W1	77.50	86.55	$L+F_W$	81.3	$L+F_W$	0.95
HRC-L1900-a300-t1.15-W2	95.60		$L+F_W$			1.18
HRC-L1900-a600-t1.15-W1	64.60	65.38	$L+F_W$	80.8	$L+F_W$	0.80
HRC-L1900-a600-t1.15-W2	66.15		$L+F_W$			0.82
HRC-L2500-a300-t1.15-W1	53.95	63.93	$L+F_W$	62.0	$L+F_W$	0.87
HRC-L2500-a300-t1.15-W2	73.90		$L+F_S$			1.19
HRC-L2500-a600-t1.15-W1	62.30	62.35	F_W	60.9	$L+F_W$	1.02
HRC-L2500-a600-t1.15-W2	62.40		F_W			1.02
(b) Specimens allowed to rotate about the strong axis						
HRC-L700-a300-t1.15-S1	103.10	101.15	L	104.7	L+D	0.98
HRC-L700-a300-t1.15-S2	99.20		L+D			0.95
HRC-L700-a600-t1.15-S1	92.70	93.80	L+D	97.6	L+D	0.95
HRC-L700-a600-t1.15-S2	94.90		L+D			0.97
HRC-L1300-a300-t1.15-S1	93.60	94.35	L+D	100.2	L+D	0.93
HRC-L1300-a300-t1.15-S2	95.10		L+D			0.95
HRC-L1300-a600-t1.15-S1	92.40	93.00	L+D	94.2	L+D	0.98
HRC-L1300-a600-t1.15-S2	93.60		L+D			0.99
HRC-L1900-a300-t1.15-S1	82.45	83.10	$L+F_W$	81.3	$L+F_W$	1.01
HRC-L1900-a300-t1.15-S2	83.75		$L+F_W$			1.03
HRC-L1900-a600-t1.15-S1	88.90	84.93	$L+F_W$	80.8	$L+F_W$	1.10
HRC-L1900-a600-t1.15-S2	80.95		$L+F_W$			1.00
HRC-L2500-a300-t1.15-S1	59.20	59.38	$L+F_W$	62.0	$L+F_W$	0.95
HRC-L2500-a300-t1.15-S2	59.55		$L+F_W$			0.96
HRC-L2500-a600-t1.15-S1	63.40	62.85	F_W	60.9	$L+F_W$	1.04
HRC-L2500-a600-t1.15-S2	62.30		$L+F_W$			1.02
Mean						0.97
COV						0.07

Tables 5-6 and 5-7 indicate that variations in boundary conditions have minimal influence on the strength of the specimens. Similarly, the specimen strength showed a slight variation as the HRC spacing changes from 30 mm to 600mm. This is likely due to the comparable web widths of the C- and U-sections, along with the significant friction between their contact surfaces, which enhances their composite action. Notably, in some cases, specimens with an HRC spacing of 600 mm exhibited higher ultimate strength than those with a spacing of 300 mm. This suggests that the influence of initial imperfections may outweigh the effect of HRC spacing. The ultimate axial strength, however, is primarily governed by the slenderness ratio and the specimen thickness.

In Figure 5-13, as expected, the axial strength decreases as the slenderness ratio increases. When the slenderness ratio exceeds 80, the axial ultimate strength declines significantly, likely due to changes in the dominant buckling behaviour of the specimens.

Figure 5-14 illustrates the axial displacement versus load curves for the specimens. During the initial loading stage, the overall axial stiffness of the specimens was relatively low, which may be attributed to potential gaps between the specimens and the test setup. Another possible contributing factor is the slight misalignment of the C- and U-sections at both ends during assembly. Such misalignment can reduce the initial stiffness compared to a scenario where the loading plate fully contacts the built-up column. Beyond a load of approximately 10 kN, the axial displacement increased linearly with the applied load, and specimens of the same length exhibited comparable axial stiffness.

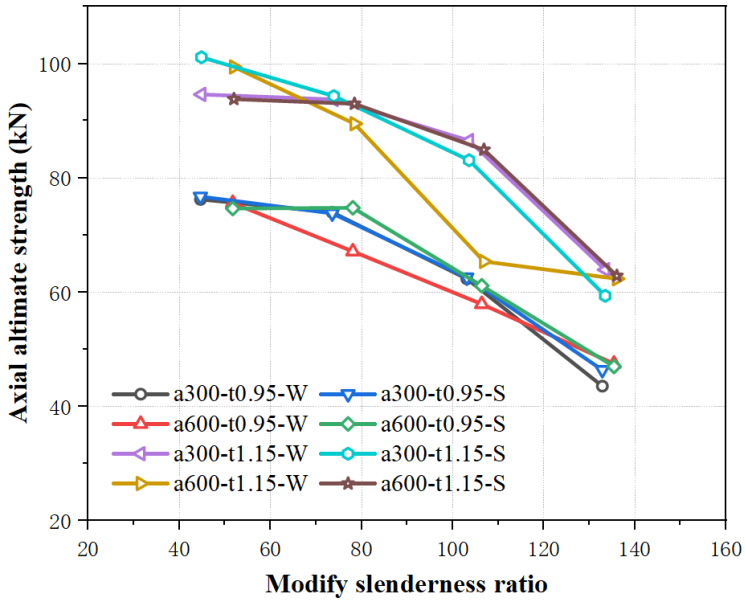

Figure 5-13 Load versus modified slenderness ratio

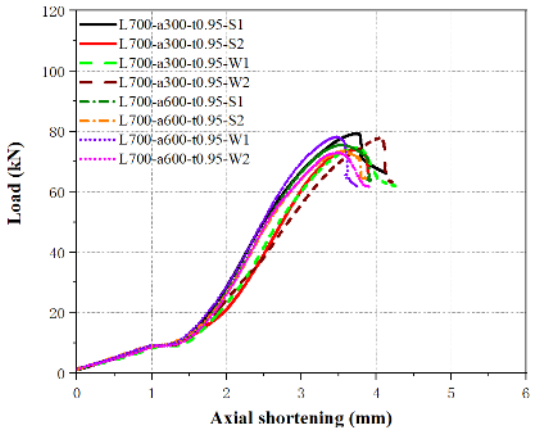

(a) HRC-L700-t0.95

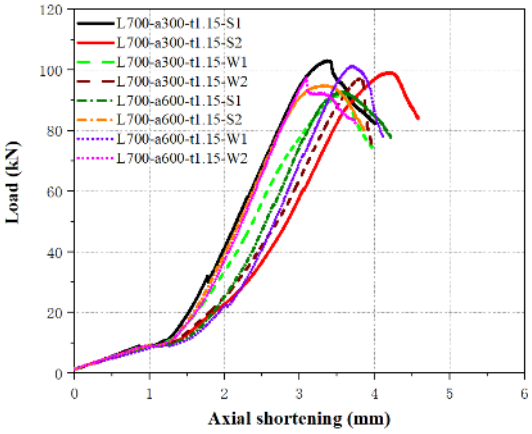

(b) HRC-L700-t1.15

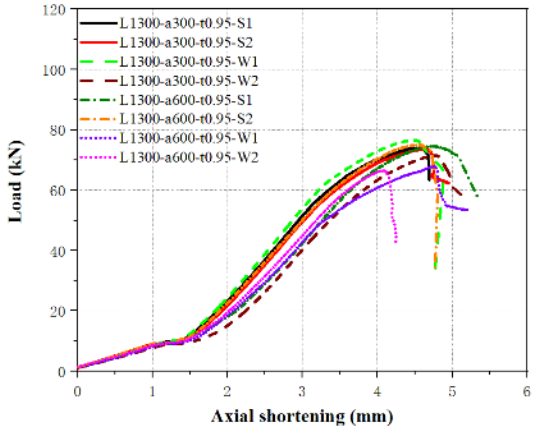

(c) HRC-L1300-t0.95

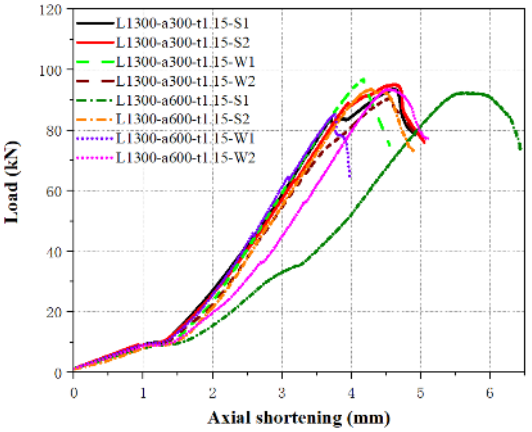

(d) HRC-L1300-t1.15

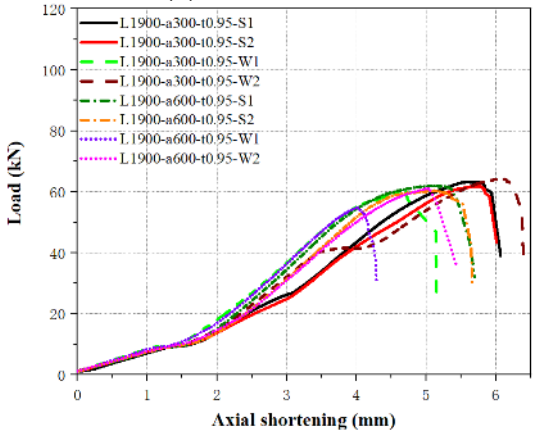

(e) HRC-L1900-t0.95

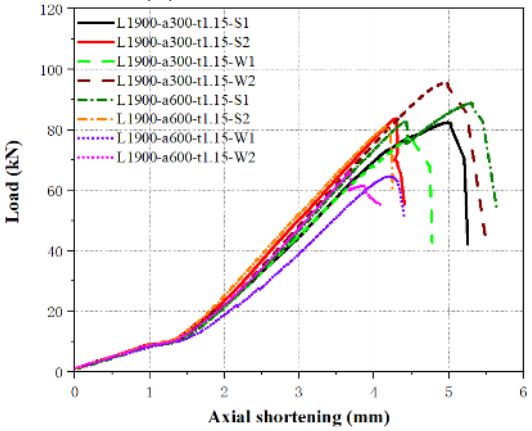

(f) HRC-L1900-t1.15

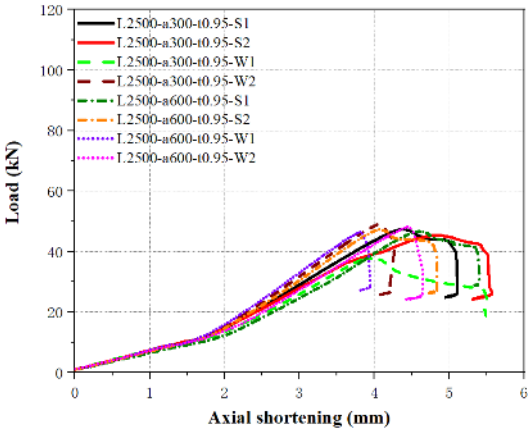

(g) HRC-L2500-t0.95

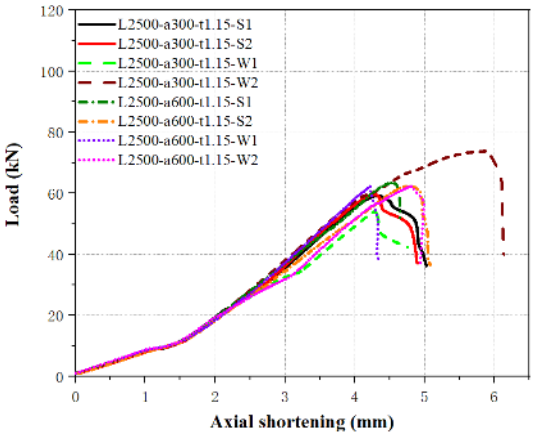

(h) HRC-L2500-t1.15

Figure 5-14 Load versus axial displacement curve

A summary of all specimens is provided in Tables 5-6 and 5-7, with the final failure modes of selected representative specimens illustrated in Figures 5-15 and 5-16. The HRC spacings, thicknesses, and boundary conditions at the end supports had a relatively minor effect on the buckling behaviour of the specimens, while the slenderness ratio played a dominant role in determining the failure mode. Throughout testing, no significant deformation or shear failure of the HRCs was observed in any specimens, indicating that the fasteners provided sufficient connection strength to prevent slippage between the connected flanges. Regardless of whether the end supports allowed rotation about the strong or weak axis, specimens exhibiting flexural buckling predominantly rotated about the weak axis. However, the specimens with a thickness of 0.95 mm were more likely to experience strong-axis rotation failures, as shown in Figure 5-16. These thinner specimens were more susceptible to larger deformations, which weakened the composite action of the built-up sections and reduced interface friction.

For short columns (700 mm in length), failure was primarily characterized by local-distortional interactive buckling, with distortional buckling predominantly occurring in the C-section (see Figure 5-15). Medium-length specimens (1300 mm) exhibited local-distortional or local-flexural interactive buckling as their primary failure modes, with

some specimens showing a combination of local, distortional, and global buckling. For long columns (1900 mm and 2500 mm in length), local buckling occurred in almost all specimens, except for those that displayed only global buckling. Examples include specimens HRC-L2500-a600-t0.95-W2, HRC-L2500-a600-t0.95-W1, and HRC-L2500-a600-t1.15-S1. These specimens demonstrated similar failure processes, particularly after unloading, where the elastic local buckling waves disappeared, and the specimens nearly returned to their pre-test condition.

(a) HRC-L700-a300-t1.15-W1

(b) HRC-L700-a600-t1.15-W1

(c) HRC-L700-a300-t1.15-S1

(d) HRC-L700-a600-t1.15-S1

Figure 5-15 Distortional buckling in the C-section of the specimens

HRC-L700-W1

HRC-L1300-W1

HRC-L1900-W1

HRC-L2500-W1

HRC-L700-S1 HRC-L1300-S1 HRC-L1900-S1 HRC-L2500-S1

Figure 5-16 Failure modes of specimens with 300 mm HRC spacing and 0.95 mm thickness

5.2.5.2. Specimens with screws

For comparison with specimens with HRCs, the experimental axial compression capacities (P_{EXP}) of built-up columns with varying thicknesses, screw spacing, and slenderness ratios were examined in this study. The experimental test results are summarized in Table 5-8, with further details provided in the following paragraphs:

Axial displacement versus load curves for the specimens are shown in Figure 5-17. The different post-peak responses observed in Figure 5-17 are primarily attributed to the occurrence of distinct failure modes in the built-up columns, which govern the softening behaviour after reaching the ultimate load. In addition, owing to the relatively small cross-sectional dimensions of the specimens, the post-peak response is highly sensitive to unavoidable initial imperfections and minor load eccentricities introduced, which further contributes to the observed variability in post-peak behaviour. In the initial loading stage, the overall axial stiffness of the specimen was relatively low, likely due to potential gaps between the specimen and the test setup and misalignment between individual components. The primary reason for the observed bi-linear stiffness before peak may be the "plate group effect," as mentioned in the Introduction. Based on the configuration of the built-up section used in this study, the flange of the U-section acts as a weak plate, while the C-section functions as a strong plate. This effect initially leads to the buckling of the weak plate. The strong plate provides a constraining effect on the weak plate, thereby delaying its buckling. However, once the weak plate buckles, it induces the buckling of the strong plate, and subsequently, the entire built-up section undergoes deformation. During this process, the stiffness of the built-up member changes. After the weak and strong plates jointly resist deformation, the load on the specimen gradually increases until it eventually reaches its peak value. This bi-linear stiffness phenomenon has also been reported in previous studies (Roy et al. 2019; Yang et al. 2022,

2024). After reaching a load of about 10 kN, the axial displacement increased linearly with the load, and specimens of the same length exhibited similar axial stiffness.

The ultimate axial strength was highly dependent on the slenderness ratio and thickness of the specimens. It was also observed that fastener spacing had a relatively small impact on the ultimate strength. This is because the C- and U-sections have similar web widths, and the significant friction between their contact surfaces contributes to the composite action of the two sections. Specifically, in some cases, the ultimate strength of specimens with a screw spacing of 600 mm was higher than that of those with 300 mm spacing, which may suggest that the effect of initial imperfections outweighs the impact of screw spacing. The load-displacement curves for specimens SC-L1900-a600-t0.95-W1, SC-L1900-a600-t0.95-W2, SC-L1900-a600-t0.95-W3, and SC-L2500-a600-t1.15-W1 deviated from others in the same group, primarily due to their distinct failure modes.

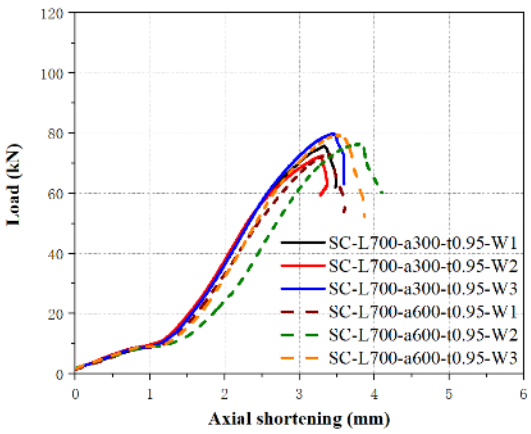

(a) SC-L700-t0.95

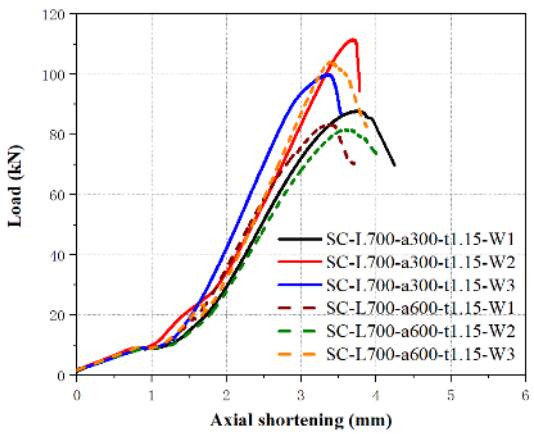

(b) SC-L700-t1.15

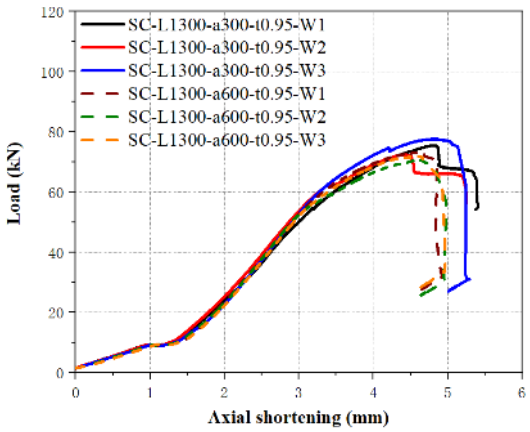

(c) SC-L1300-t0.95

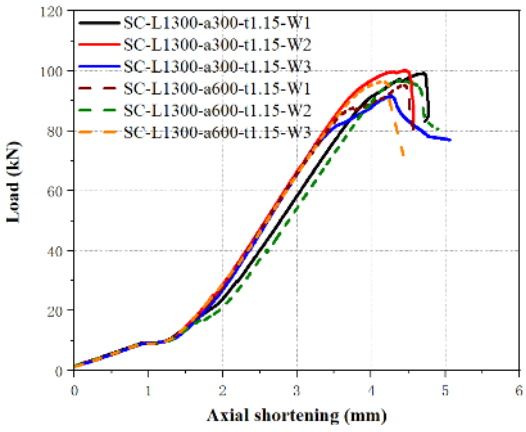

(d) SC-L1300-t1.15

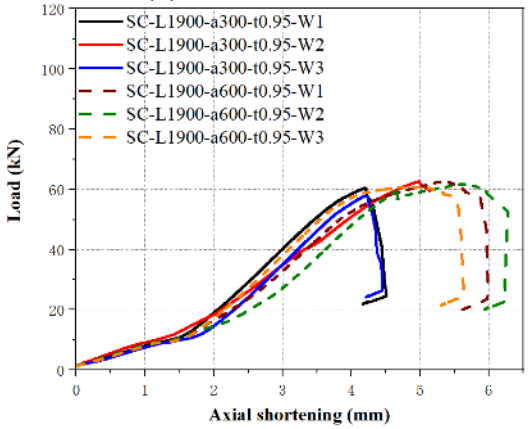

(e) SC-L1900-t0.95

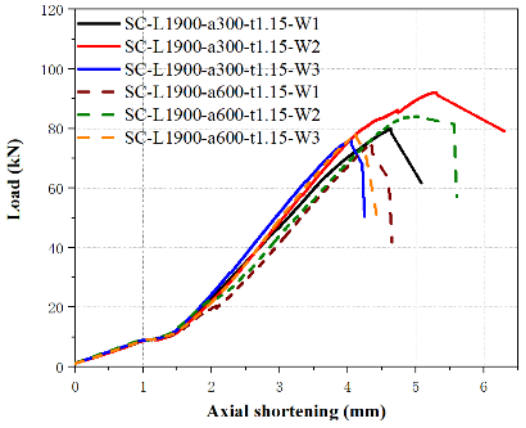

(f) SC-L1900-t1.15

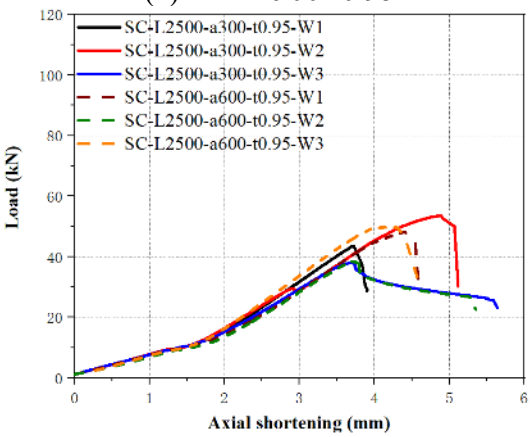

(g) SC-L2500-t0.95

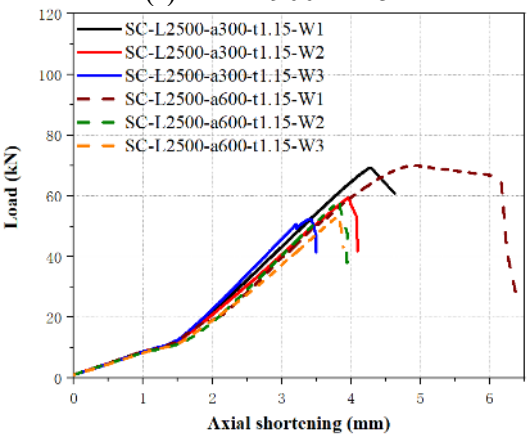

(h) SC-L2500-t1.15

Figure 5-17 Load versus axial displacement curves

Table 5-8 Comparison of test results with FE results

Specimen ID	Non-dimensional slenderness ratio λ_c	Test			FEA		P_{EXP}/P_{FEA}
		Loads P_{EXP} kN	Mean $\overline{P_{EXP}}$ kN	Failure modes	Loads P_{FEA} kN	Failure modes	
(a) Thickness of 0.95 mm							
S-L700-a300-t0.95-T1	0.8	75.6		$L+D_c$			0.92
S-L700-a300-t0.95-T2	0.8	72.4	75.9	L	81.9	$L+D_c$	0.88
S-L700-a300-t0.95-T3	0.8	79.8		L			0.97

S-L700-a600-t0.95-T1	1.0	73.1		$L+D_c$			0.91
S-L700-a600-t0.95-T2	1.0	76.4	76.3	$L+D_c$	80.2	$L+D_c$	0.95
S-L700-a600-t0.95-T3	1.0	79.4		$L+D_c$			0.99
S-L1300-a300-t0.95-T1	1.4	75.5		$L+D_c$			1.00
S-L1300-a300-t0.95-T2	1.4	72.4	75.2	$L+D_c$	75.3	$L+D_c+F_W$	0.96
S-L1300-a300-t0.95-T3	1.4	77.7		$L+D_c+F_S$			1.03
S-L1300-a600-t0.95-T1	1.5	73.1		$L+F_S$			0.98
S-L1300-a600-t0.95-T2	1.5	70.6	72.3	$L+F_S$	74.8	$L+D_c+F_W$	0.94
S-L1300-a600-t0.95-T3	1.5	73.1		$L+D_c+F_S$			0.98
S-L1900-a300-t0.95-T1	2.0	60.4		$L+F_W$			0.97
S-L1900-a300-t0.95-T2	2.0	56.3	58.2	$L+F_W$	62.1	$L+F_W$	0.91
S-L1900-a300-t0.95-T3	2.0	57.8		$L+F_W$			0.93
S-L1900-a600-t0.95-T1	2.0	62.5		$L+F_S$			1.04
S-L1900-a600-t0.95-T2	2.0	61.7	61.7	$L+F_S$	60.1	$L+F_W$	1.03
S-L1900-a600-t0.95-T3	2.0	60.8		$L+F_S$			1.01
S-L2500-a300-t0.95-T1	2.5	43.5		$L+F_W$			0.90
S-L2500-a300-t0.95-T2	2.5	53.5	45.0	$L+F_W$	48.3	$L+F_W$	1.11
S-L2500-a300-t0.95-T3	2.5	38.0		$L+F_W$			0.79
S-L2500-a600-t0.95-T1	2.6	48.2		$L+F_W$			1.01
S-L2500-a600-t0.95-T2	2.6	38.4	45.4	$L+F_W$	47.9	$L+F_W$	0.80
S-L2500-a600-t0.95-T3	2.6	49.7		$L+F_W$			1.04
(b) Thickness of 1.15 mm							
S-L700-a300-t1.15-T1	0.8	87.8		L			0.84
S-L700-a300-t1.15-T2	0.8	111.6	99.8	L	104.7	$L+D_c$	1.07
S-L700-a300-t1.15-T3	0.8	100.0		$L+D_c$			0.96
S-L700-a600-t1.15-T1	0.9	83.4		$L+D_c$			0.85
S-L700-a600-t1.15-T2	0.9	81.9	89.8	$L+D_c$	97.6	$L+D_c$	0.84
S-L700-a600-t1.15-T3	0.9	104.2		$L+D_c$			1.07
S-L1300-a300-t1.15-T1	1.3	99.3		$L+D_c$			0.99
S-L1300-a300-t1.15-T2	1.3	100.1	97.0	$L+D_c$	100.2	$L+D_c$	1.00
S-L1300-a300-t1.15-T3	1.3	91.6		$L+D_c$			0.91
S-L1300-a600-t1.15-T1	1.4	95.3		$L+D_c$			1.01
S-L1300-a600-t1.15-T2	1.4	96.8	96.2	$L+D_c$	94.2	$L+D_c$	1.03
S-L1300-a600-t1.15-T3	1.4	96.4		$L+D_c$			1.02
S-L1900-a300-t1.15-T1	1.8	79.9		$L+F_W$			0.98
S-L1900-a300-t1.15-T2	1.8	92.2	82.7	$L+F_W$	81.3	$L+F_W$	1.13
S-L1900-a300-t1.15-T3	1.8	76.1		$L+F_W$			0.94
S-L1900-a600-t1.15-T1	1.9	74.5		$L+F_W$			0.92
S-L1900-a600-t1.15-T2	1.9	84.1	78.8	$L+F_W$	80.8	$L+F_W$	1.04
S-L1900-a600-t1.15-T3	1.9	77.9		$L+F_W$			0.96
S-L2500-a300-t1.15-T1	2.4	69.3		$L+F_W$			1.12
S-L2500-a300-t1.15-T2	2.4	59.5	60.4	$L+F_W$	62.0	$L+F_W$	0.96
S-L2500-a300-t1.15-T3	2.4	52.4		$L+F_W$			0.85
S-L2500-a600-t1.15-T1	2.4	70.0		$L+F_S$			1.15
S-L2500-a600-t1.15-T2	2.4	57.9	60.3	$L+F_W$	60.9	$L+F_W$	0.95
S-L2500-a600-t1.15-T3	2.4	52.9		$L+F_W$			0.87
Mean							0.97
COV							0.09

Note: L denotes local buckling, D_c represents distortional buckling in the C-section, and F_S and F_W correspond to flexural buckling about the strong and weak axes, respectively.

The failure modes of the specimens showed similarities. For example, Figure 5-18 illustrates the entire failure process of specimen SC-L1300-a600-t1.15-W1. The testing process can be divided into the following stages: (1) Local buckling waves first appeared on the U-section flanges after the specimen made full contact with the end supports. At

this point, the load on the load-displacement curve corresponded to the region after the slope change, with the initial buckling waves occurring near the outermost screw at the end of the specimen; (2) As the load increased linearly with an axial displacement, additional local buckling waves were observed along the U-section flanges; (3) The load then entered the plastic phase; (4) Upon reaching the peak load, local buckling also occurred in the web of the C-section component; (5) The load-displacement curve subsequently entered the descending phase, accompanied by further deformation in the local buckling of the C-section web, eventually leading to specimen failure; (6) During unloading, the local buckling waves gradually disappeared, leaving behind an unrecoverable plastic yield zone in the C-section web. Distortional buckling in the flanges and lips of the C-section, which were enclosed within the specimen, could not be captured during the test. The final failure mode of specimen SC-L1300-a600-t1.15-W1 was identified as local-distortional interactive buckling. Throughout the testing process, no deformation, shearing, pulling, or tilting of the self-drilling screws was observed in any of the specimens, indicating that the screws provide sufficient connection strength at the screw connection area. The final failure modes of selected representative specimens are illustrated in Figure 5-19, and a summary of all specimens is presented in Table 5-8.

In Figure 5-19(a), when the slenderness ratio of the specimen was 42 (with a length of 700 mm), the specimens failed by local or local-distortional interactive buckling. Distortional buckling mainly occurred in the C-section flanges and the adjacent corner near the outermost screw. The thickness of the specimen and the screw spacing primarily influenced the location of the buckling.

For medium-length specimens, the primary failure mode is local and distortional interactive buckling. Like the 700 mm long specimen, the location of the distortional

buckling is close to the ends. However, for the specimen with a screw spacing of 600 mm and a thickness of 0.95 mm, the failure mode shifts to local-flexural interactive buckling. The specimens that undergo flexural buckling rotate around their strong axis, as depicted in Figure 5-19(b). This occurs because the composite action of built-up section primarily relies on the shear provided by the screws and the friction between the C- and U-sections. As significant deformation occurs, the friction at the composite interface gradually decreases, weakening the composite action for specimens with larger screw spacings. As a result, these built-up sections exhibit local-flexural interactive buckling, which manifest as rotation around the strong axis in the final failure mode. This failure mode is reflected in the load-displacement curves, where the ductility of the specimen increases. After entering the plastic zone, the specimen gradually reaches its peak after undergoing a certain amount of displacement.

In Figure 5-19(c) and (d), the failure progression of the 1900- and 2500-mm long columns in the experiment are similar to that of specimen SC-L1300-a600-t1.15-W1. However, after the load reaches its peak, significant elastic-plastic overall buckling occurs, preventing the specimen from bearing any further load and ultimately leading to its failure. Upon unloading, the local and flexural buckling waves partially disappeared, and an unrecoverable plastic yield zone formed near the mid-height of specimens. The flexural buckling of both specimen SC-L1900-a600-t0.95-W1 and SC-L2500-a600-t1.15-W1 involves rotation around the strong axis. Similarly, this failure mode occurs exclusively in specimens with a screw spacing of 600 mm, as shown in Figure 5-19(c) and (d).

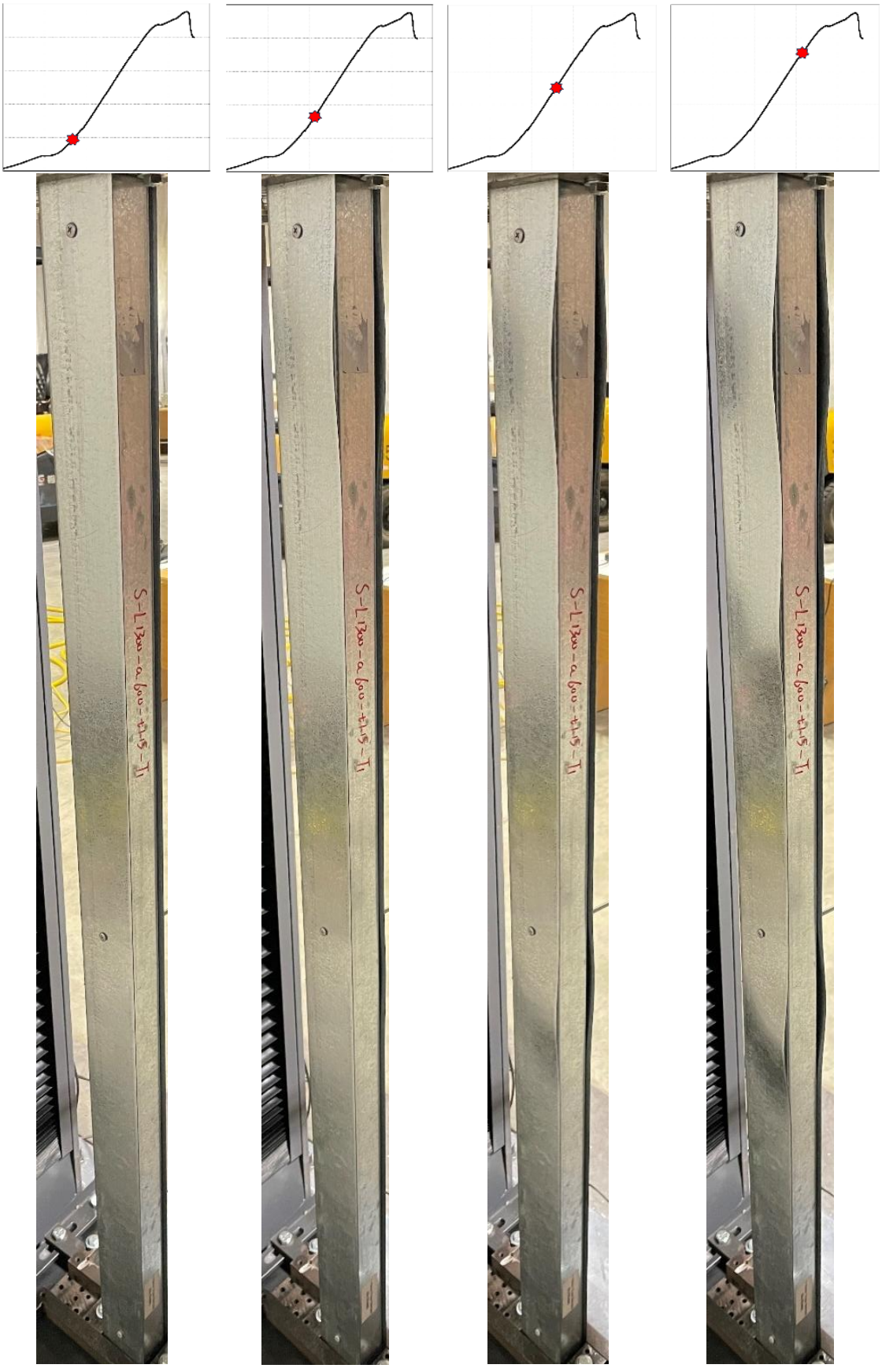
S-L-1300-α600-t1.5-T1
S-L-1300-α600-t1.5-T1
S-L-1300-α600-t1.5-T1
S-L-1300-α600-t1.5-T1

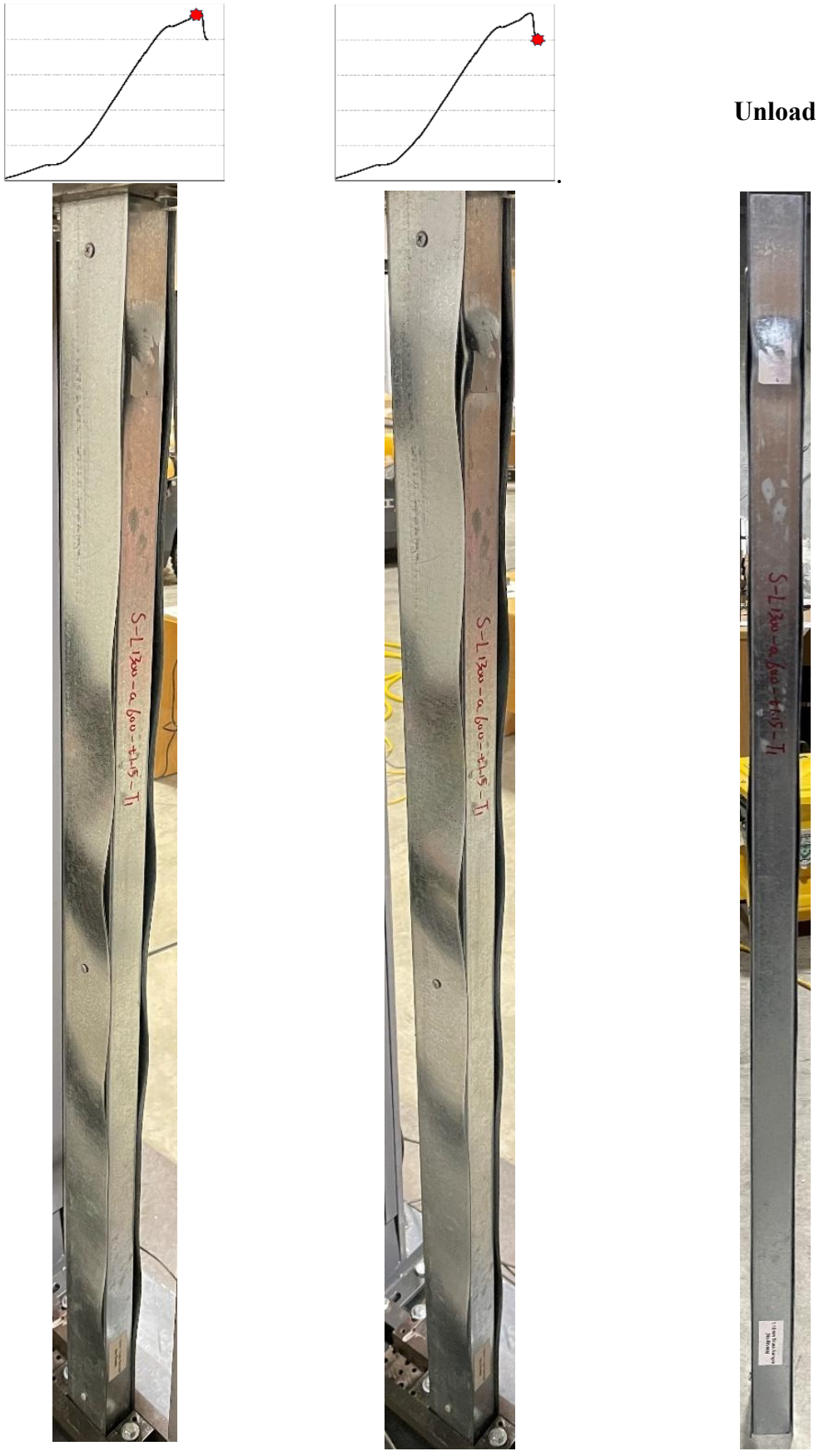

Figure 5-18 Failure progression of specimen SC-L1300-a600-t1.15-W1

SC-L700-a300-t0.95-W1

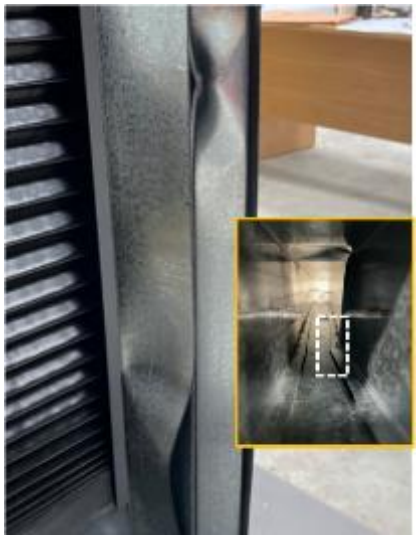

SC-L700-a600-t0.95-W1

SC-L700-a300-t1.15-W1

SC-L700-a600-t1.15-W1

(a) Specimen length of 700 mm

SC-L1300-a300-t0.95-W1

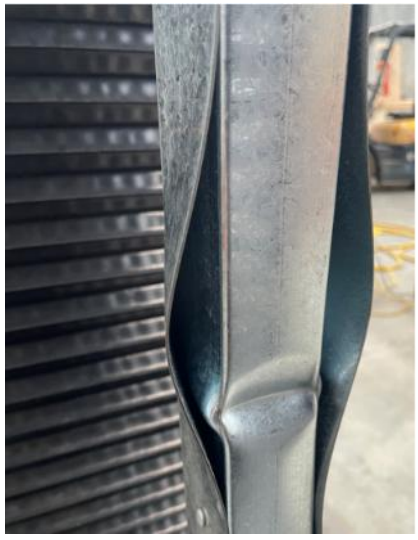

SC-L1300-a300-t0.95-W1

SC-L1300-a300-t1.15-W1

SC-L1300-a600-t1.15-W1

SC-L1300-a600-t0.95-W1

(b) Specimen length of 1300 mm

SC-L1900-a300-t0.95-W1

SC-L1900-a600-t0.95-W1

SC-L1900-a300-t1.15-W1

SC-L1900-a600-t1.15-W1

SC-L1900-a300-t0.95-W1

SC-L1900-a600-t0.95-W1

SC-L1900-a300-t1.15-W1

SC-L1900-a600-t1.15-W1

(c) Specimen length of 1900 mm

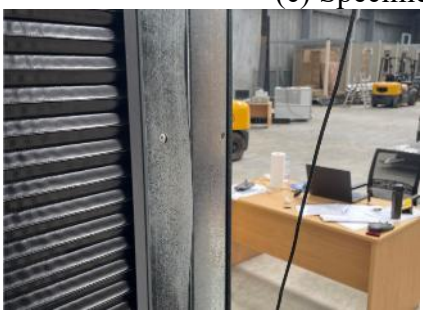

SC-L2500-a300-t0.95-W1

SC-L2500-a600-t0.95-W1

SC-L2500-a300-t1.15-W1

SC-L2500-a600-t1.15-W1

SC-L2500-a300-t0.95-W1

SC-L2500-a600-t0.95-W1

SC-L2500-a300-t1.15-W1

SC-L2500-a600-t1.15-W1

(d) Specimen length of 2500 mm

Figure 5-19 Failure modes of built-up box section columns

5.2.5.3. Comparison of specimens with screws and HRCs

A comparison was conducted between specimens with HRCs and screws, focusing on both loading-bearing capacity and failure modes. Specimens with HRCs did not exhibit the anticipated higher strength, primarily because the built-up box columns have relatively low demands on fastener connection strength. To fully utilize the advantages

of HRCs, they are better suited for regions where higher connection strength is required, such as CFS trusses and shear wall structures.

5.3. Numerical study

5.3.1. General description of FE model

The FE models were developed using ABAQUS, validated against the test results, and subsequently utilized for a parametric study. The average values of the stress-strain curves for the material properties described before, along with the measured cross-sectional dimensions, were incorporated into the FE model. The engineering stress-strain curves for different thicknesses were converted to the true stress-strain relationships according to ABAQUS manual, with the decreasing trends during the plastic stage not being considered in this study.

The S4R shell element was used to model the CFS built-up box section. A mesh sensitivity analysis was performed to investigate the effect of mesh sizes of 5 × 5, 10 × 10, and 15 × 15 mm on the ultimate load of the CFS C- and U-sections, as summarized in Table 5-9. To balance runtime and result accuracy, a mesh size of 10 × 10 mm was deemed suitable for the CFS sections, as illustrated in Figure 5-20.

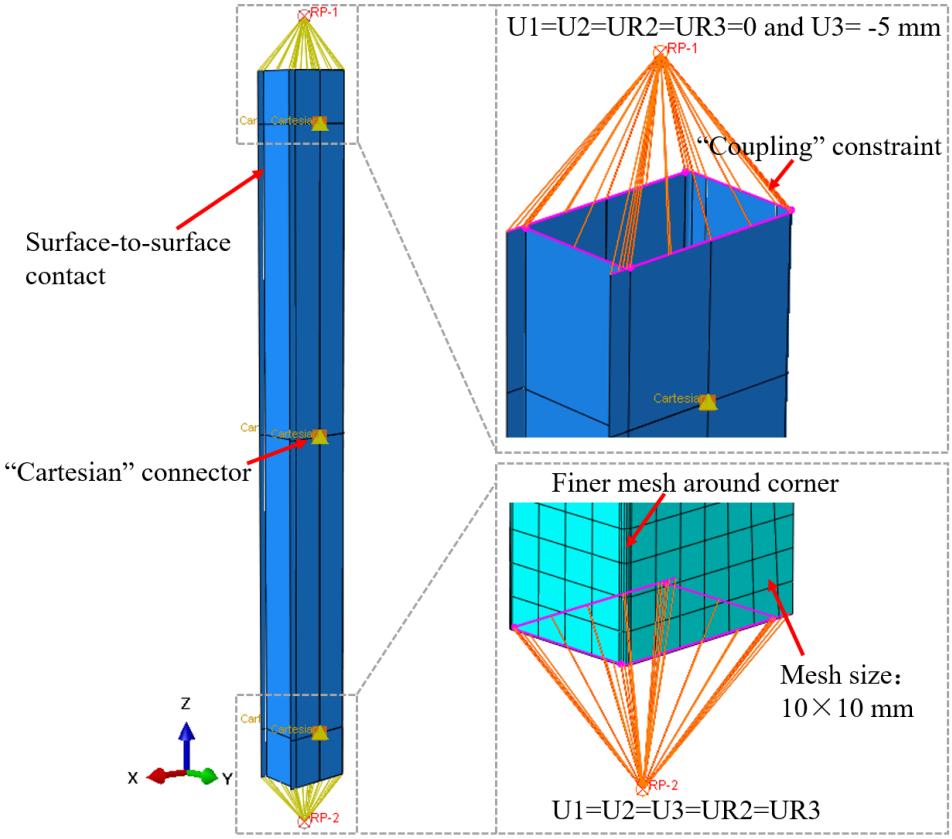

Figure 5-20 Mesh sizes, interactions, and boundary conditions used in the FE model

Table 5-9 Results of the mesh sensitivity analysis

Specimens	Test $\bar{P}_{EXP}$ kN	Ultimate strength obtained from FEA, P_{FEA}, kN			$\bar{P}_{EXP}/P_{FEA}$		
		Mesh sizes, mm			Mesh sizes, mm		
		5×5	10×10	15×15	5×5	10×10	15×15
L700-a300-t0.95	75.9	78.9	81.9	89.9	0.96	0.93	0.84
L700-a300-t1.15	99.8	100.4	104.7	112.0	0.99	0.95	0.89
L2500-a300-t0.95	45.0	48.2	48.3	48.8	0.93	0.93	0.92
L2500-a300-t1.15	60.4	62.6	62.0	62.5	0.96	0.97	0.97

Surface-to-surface contact with a friction coefficient of 0.1 was employed to model the interface between the C- and U-section components, with the inner surface of the U-section defined as the slave surface. Coupling constraints restricted both ends of the built-up column to reference points (RPs) placed 70 mm from the specimen ends. The boundary conditions at these RPs restricted rotation about the minor axis and vertical displacement at "RP-1", as depicted in Figure 5-20, where vertical displacement was applied to "RP-1". As previously mentioned, no failure modes such as self-drilling screw deformation, shearing, pulling, or tilting were observed during testing, indicating that the

screws provide sufficient connection strength at the screw connection area. The "Cartesian" connector available in ABAQUS is a specialized connector element defined by two nodes, suitable for various rigid linkages, particularly for fasteners that have not experienced shear failure or deformation (Wang et al. 2023, 2024). This connector allows users to prescribe translational and rotational degrees of freedom, as well as axial stiffness, between the connected nodes. To model the response of screws in the built-up section columns, the "Cartesian" connector was used with an infinite elasticity coefficient of 6000. The same setup for this type of connector used in CFS built-up columns to simulate screws was reported by Dai et al. (2024). As mentioned earlier, specimens with HRCs and those with screws did not exhibit significant differences in load-bearing capacity or failure modes, as no connection failure occurred. Therefore, the same connector was used in this FE study.

The linear buckling analysis in ABAQUS was performed to identify the potential critical buckling modes of the columns. Typical buckling shapes (see Figure 5-21) were selected and incorporated into the ideal models by modifying the relevant keywords, allowing the static analysis models to include these initial imperfections. The amplitude of the initial global imperfection was taken as the measured value, δ_{global}, while the amplitude of the initial local imperfection was set at 0.0055 times the plate width (Nie et al. 2020; Yang et al. 2022). Additionally, CFS members exhibit residual stresses due to the cold-forming process. However, these stresses were not considered in this study, as previous research (Vy et al. 2021a, 2021b; Ellobody et al. 2005) has demonstrated that their effect on the ultimate load-bearing capacity of CFS members is minimal.

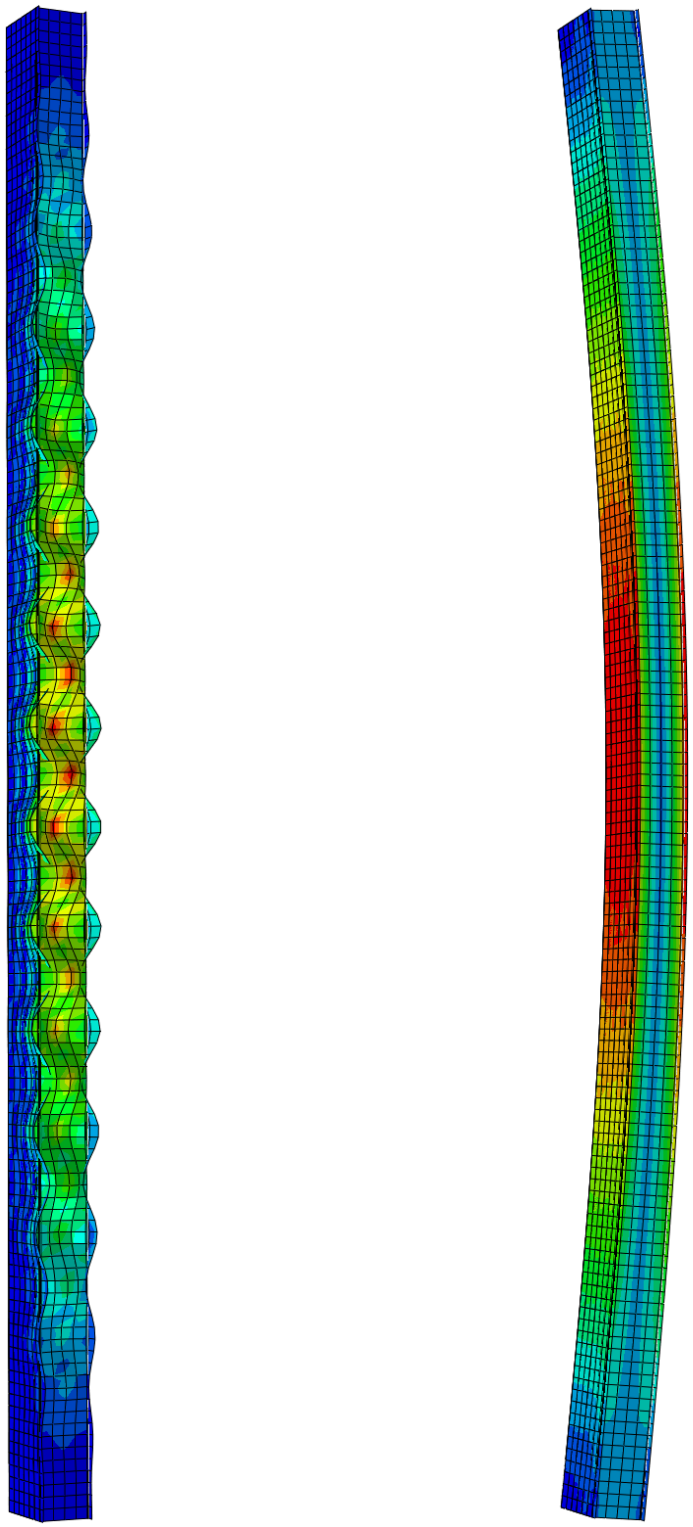

(a) Local buckling (b) Flexural buckling

Figure 5-21 Initial imperfection contours for the specimen L1300-a300-t0.95-W

5.3.2. Validation of FE model

This section validates the FE model by comparing its predictions to experimental results for built-up columns. Tables 5-6, 5-7, and 5-8 show that the average ratio of experimental ultimate strength (P_{EXP}) to FEA-predicted ultimate strength (P_{FEA}) is 0.97, with a COV of 0.07. This indicates close agreement between the model and the experimental data. Further validation is provided by comparing load-displacement curves and deformed shapes (Figures 5-22 and 5-23). While the FEA slightly overpredicts the initial stiffness of the load–displacement response, it closely matches the second slope of the curve. This discrepancy is mainly attributed to minor misalignment of the column components during the physical tests. In addition, it may also be influenced by the idealized boundary conditions adopted in the FE model, whereas such experimental details are difficult to fully capture in an idealized numerical model. Despite this minor difference, the FEA accurately predicts the failure modes and ultimate strengths, confirming its reliability for analysing built-up columns.

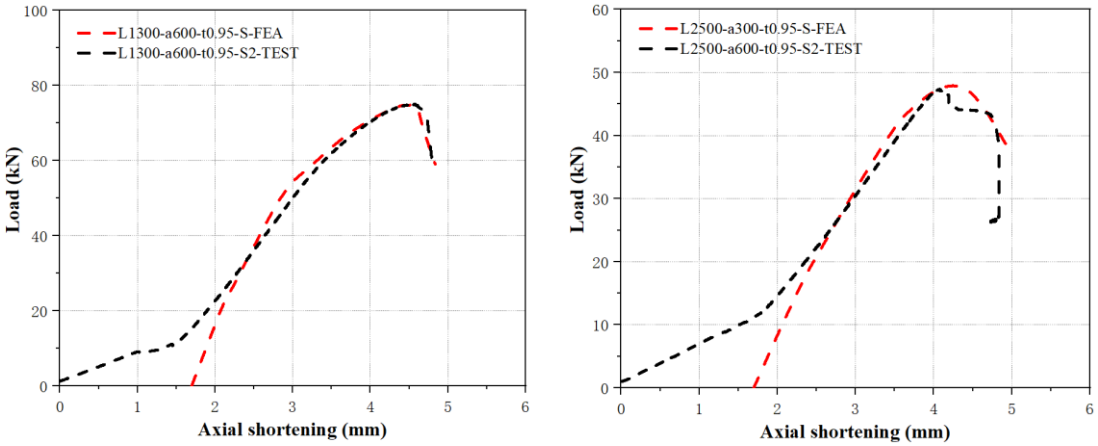

(a)HRC-L1300-a600-t0.95-S2 (b)HRC-L2500-a600-t0.95-S2

Figure 5-22 Comparison of load-axial shortening curves from tests and FEA

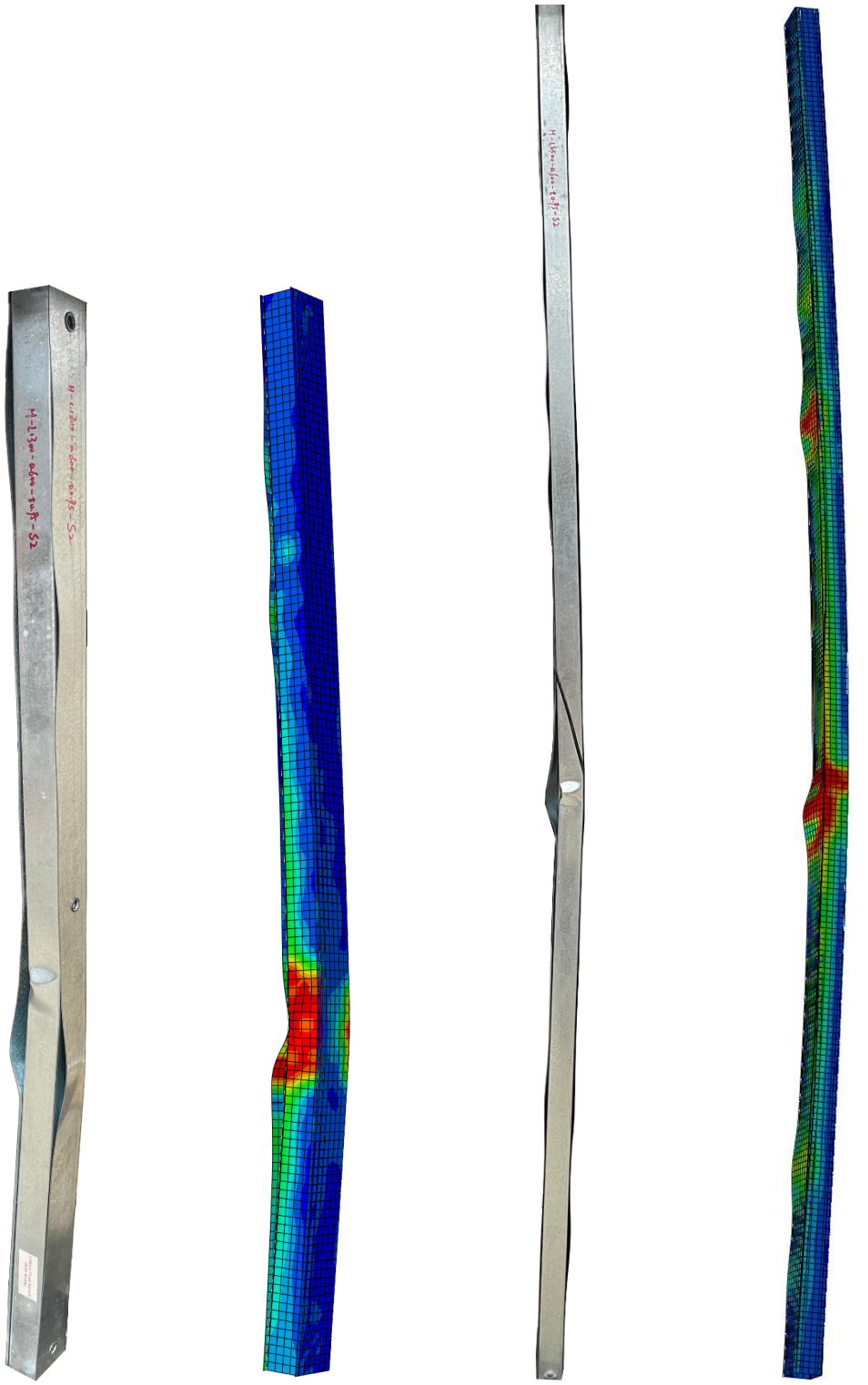

(a)HRC-L1300-a600-t0.95-S2 (b)HRC-L2500-a600-t0.95-S2

Figure 5-23 Comparison of deformed shapes from tests and FEA

5.4. Parametric study

A parametric study was conducted using the validated FE model to investigate how varying fastener spacing and cross-sectional shapes influence the axial strength of the

specimens. The material properties, slenderness ratios, thicknesses, and boundary conditions were kept consistent with those of the specimens used in the experimental tests.

In the experimental program, the cross-sectional configuration involved nesting a C-section within a U-section. Both the C- and U-sections were roll-formed from sheets of the same width, allowing them to be prefabricated using the same cold-forming equipment. For ease of modular installation, the lips of the C-section were tightly aligned with the web of the U-section, causing part of the U-section's flange to extend beyond the C-section's web. Various cross-sectional shapes were explored in this arrangement, as shown in Figure 5-24(a). The FE results, shown in Figure 5-24, indicate that there were no significant strength differences between the traditional box configuration and the configuration with the C-section nested within the U-section. However, the traditional box shape exhibited slightly lower strength, likely due to greater deformation in the lips of the C-section compared to the nested configuration.

Figure 5-25 and Table 5-10 illustrate the effect of different modified slenderness ratios on the load-carrying capacity for screw spacings of 300 mm and 600 mm. The results indicate that the load response is more pronounced for thicker specimens. When the screw spacing is 300 mm, the load decreases by 33% for specimens with a thickness of 0.75 mm as the slenderness ratio increases from 45 to 133. In contrast, for specimens with a thickness of 1.95 mm under a similar slenderness ratio variation, the load decreases by 52%.

The screw spacing varied from 100 to 600 mm, with the corresponding numerical results are depicted in Figure 5-26 and Table 5-10. It is evident that specimens with smaller slenderness ratios are more sensitive to screw spacing. For example, in specimen L700-t1.15, a decrease of 18% in ultimate strength is observed when the screw spacing is 600

mm compared to that of 100 mm, while the ultimate strength of specimen L2500-t0.95 varied by only 5% when the screw spacing changed from 600 mm to 100 mm. This is mainly because the failure mode of specimens with smaller slenderness ratios is predominantly governed by local buckling, and smaller screw spacing can effectively restrain the local deformation. In contrast, longer specimens are primarily controlled by global buckling and are therefore less sensitive to screw spacing. In summary, the screw spacings had minimal impact on the axial capacity of the built-up columns.

The variation in load with thickness is depicted in Figure 5-27. As expected, thickness has the most significant influence on the axial strength of the specimens, with the load increasing linearly as the specimen thickness increases. For example, for specimens L700-a300, the load increases by more than fivefold as the thickness increases from 0.75 mm to 1.95 mm.

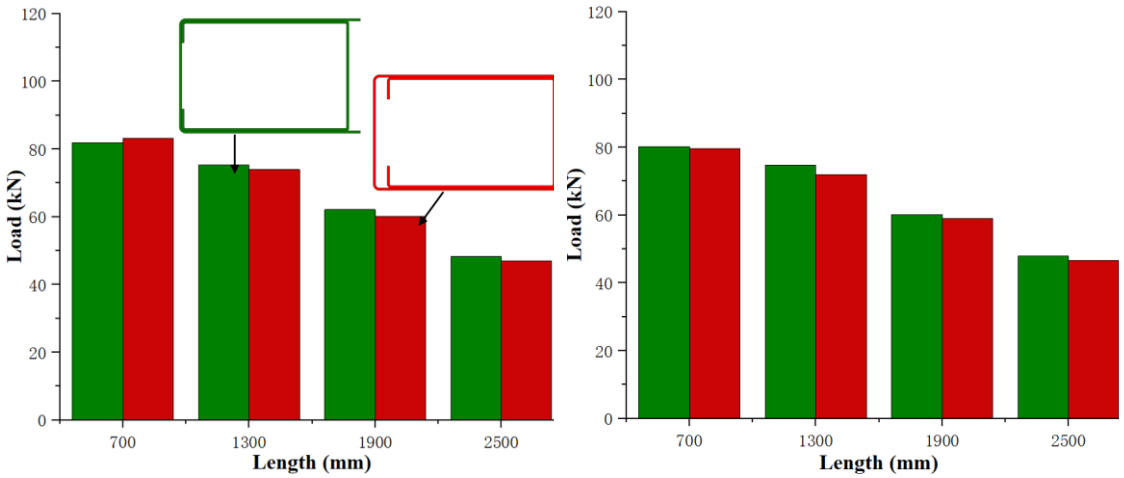

(a) a300-t0.95-W (b) a600-t0.95-W

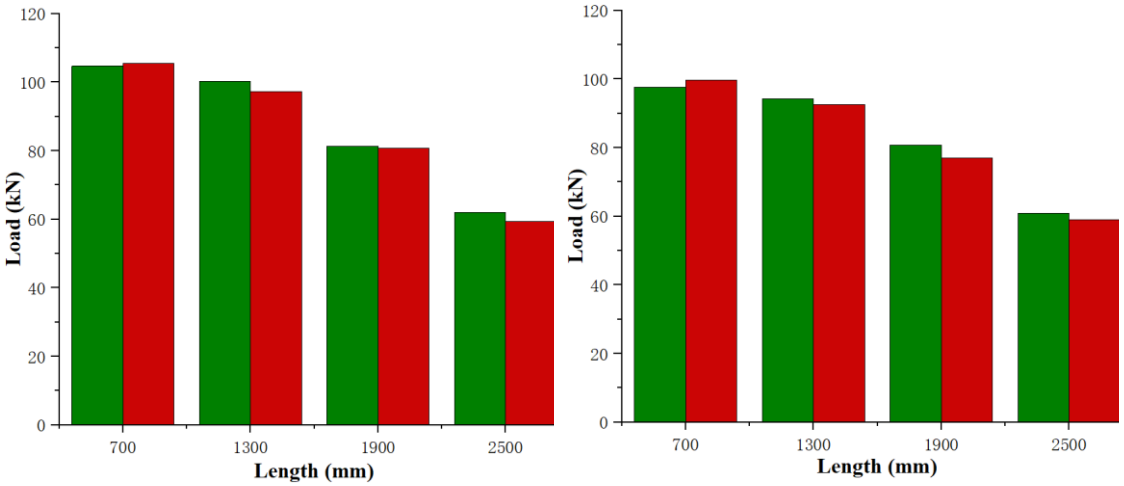

(c) a300-t1.15-W (d) a600-t1.15-W

Figure 5-24 Comparison of axial strengths for specimens with different cross-section shapes

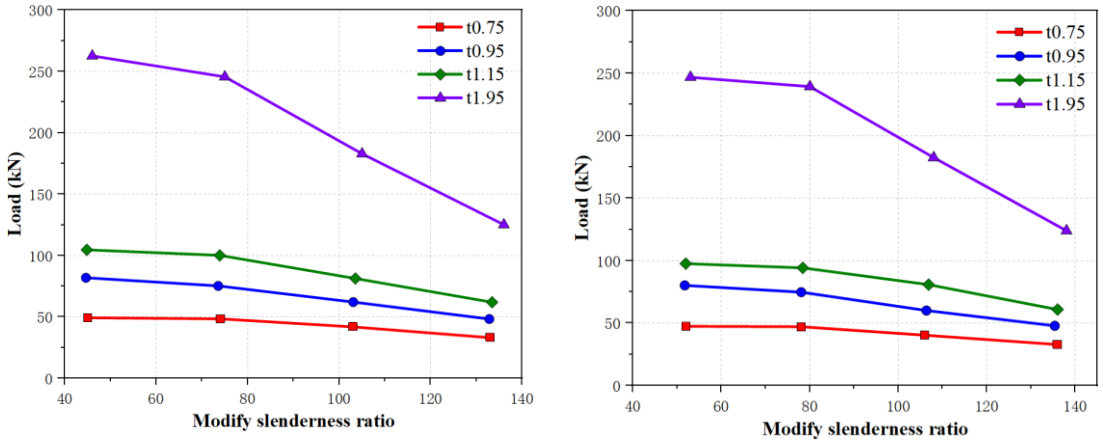

(a) a = 300 mm (b) a = 600 mm

Figure 5-25 Comparison of ultimate strengths of specimens with different modified slenderness ratio

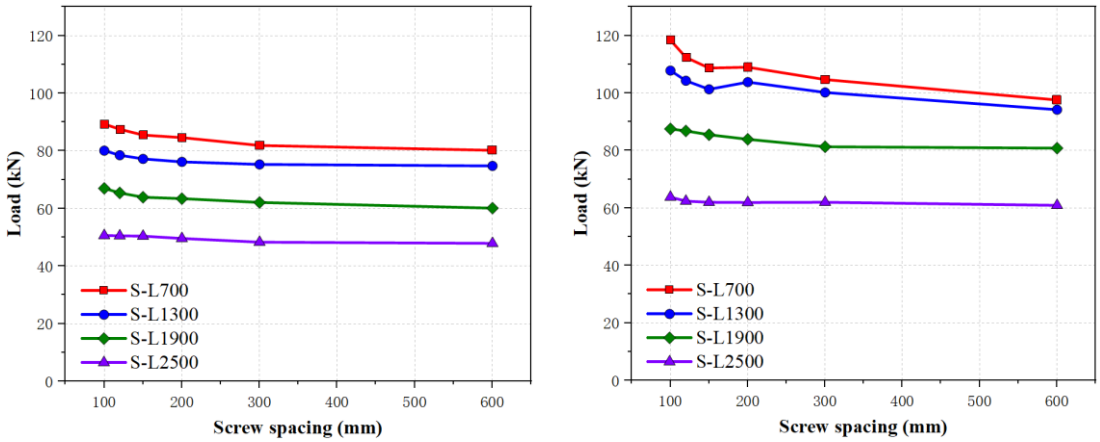

(a)t = 0.95 mm (b)t = 1.15 mm

Figure 5-26 Comparison of ultimate strengths of specimens with different screw spacing

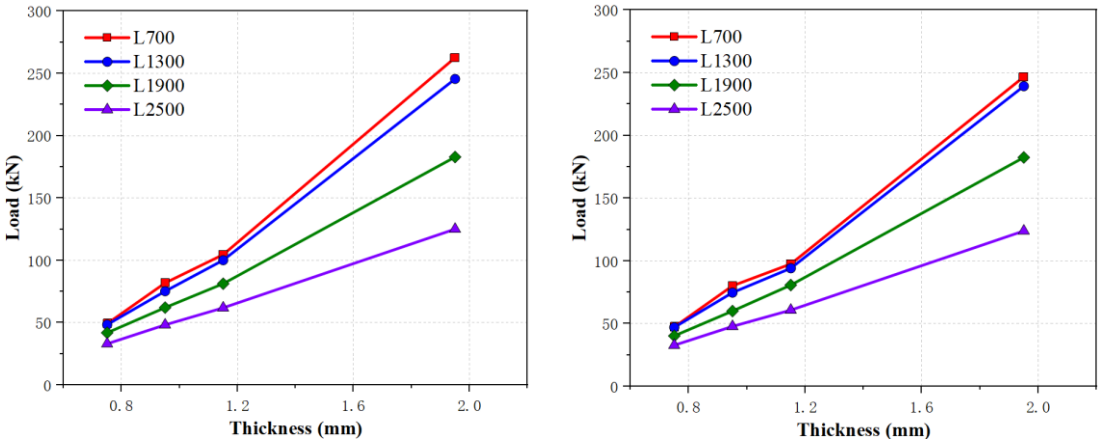

(a) a = 300 mm (b) a = 600 mm

Figure 5-27 Comparison of ultimate strengths of specimens with different thickness

Table 5-10 Parametric study results of CFS built-up box sections

Specimen ID	L mm	a mm	t mm	P_{FEA} kN
HRC-L700-a100-t0.75	700	100	0.75	55.66
HRC-L700-a120-t0.75	700	120	0.75	51.79
HRC-L700-a150-t0.75	700	150	0.75	51.02
HRC-L700-a200-t0.75	700	200	0.75	50.68
HRC-L700-a300-t0.75	700	300	0.75	49.36
HRC-L700-a600-t0.75	700	600	0.75	47.43
HRC-L700-a100-t0.95	700	100	0.95	89.30
HRC-L700-a120-t0.95	700	120	0.95	87.5
HRC-L700-a150-t0.95	700	150	0.95	85.5
HRC-L700-a200-t0.95	700	200	0.95	84.6
HRC-L700-a300-t0.95	700	300	0.95	81.9
HRC-L700-a600-t0.95	700	600	0.95	80.2
HRC-L700-a100-t1.15	700	100	1.15	118.4
HRC-L700-a120-t1.15	700	120	1.15	112.4
HRC-L700-a150-t1.15	700	150	1.15	108.7
HRC-L700-a200-t1.15	700	200	1.15	109
HRC-L700-a300-t1.15	700	300	1.15	104.7
HRC-L700-a600-t1.15	700	600	1.15	97.6
HRC-L700-a100-t1.95	700	100	1.95	287.46
HRC-L700-a120-t1.95	700	120	1.95	273.64
HRC-L700-a150-t1.95	700	150	1.95	266.77
HRC-L700-a200-t1.95	700	200	1.95	266.76
HRC-L700-a300-t1.95	700	300	1.95	262.64
HRC-L700-a600-t1.95	700	600	1.95	246.8
HRC-L1300-a100-t0.75	1300	100	0.75	55.26
HRC-L1300-a120-t0.75	1300	120	0.75	52.0
HRC-L1300-a150-t0.75	1300	150	0.75	50.04
HRC-L1300-a200-t0.75	1300	200	0.75	49.0
HRC-L1300-a300-t0.75	1300	300	0.75	48.48
HRC-L1300-a600-t0.75	1300	600	0.75	47.12
HRC-L1300-a100-t0.95	1300	100	0.95	80.10
HRC-L1300-a120-t0.95	1300	120	0.95	78.50
HRC-L1300-a150-t0.95	1300	150	0.95	77.20
HRC-L1300-a200-t0.95	1300	200	0.95	76.20
HRC-L1300-a300-t0.95	1300	300	0.95	75.30

HRC-L1300-a600-t0.95	1300	600	0.95	74.80
HRC-L1300-a100-t1.15	1300	100	1.15	107.8
HRC-L1300-a120-t1.15	1300	120	1.15	104.3
HRC-L1300-a150-t1.15	1300	150	1.15	101.3
HRC-L1300-a200-t1.15	1300	200	1.15	103.8
HRC-L1300-a300-t1.15	1300	300	1.15	100.2
HRC-L1300-a600-t1.15	1300	600	1.15	94.2
HRC-L1300-a100-t1.95	1300	100	1.95	264.72
HRC-L1300-a120-t1.95	1300	120	1.95	257.71
HRC-L1300-a150-t1.95	1300	150	1.95	254.82
HRC-L1300-a200-t1.95	1300	200	1.95	246.2
HRC-L1300-a300-t1.95	1300	300	1.95	245.57
HRC-L1300-a600-t1.95	1300	600	1.95	239.34
HRC-L1900-a100-t0.75	1900	100	0.75	44.8
HRC-L1900-a120-t0.75	1900	120	0.75	43.69
HRC-L1900-a150-t0.75	1900	150	0.75	43.61
HRC-L1900-a200-t0.75	1900	200	0.75	42.49
HRC-L1900-a300-t0.75	1900	300	0.75	41.97
HRC-L1900-a600-t0.75	1900	600	0.75	40.29
HRC-L1900-a100-t0.95	1900	100	0.95	67.0
HRC-L1900-a120-t0.95	1900	120	0.95	65.4
HRC-L1900-a150-t0.95	1900	150	0.95	63.9
HRC-L1900-a200-t0.95	1900	200	0.95	63.4
HRC-L1900-a300-t0.95	1900	300	0.95	62.1
HRC-L1900-a600-t0.95	1900	600	0.95	60.1
HRC-L1900-a100-t1.15	1900	100	1.15	87.5
HRC-L1900-a120-t1.15	1900	120	1.15	86.8
HRC-L1900-a150-t1.15	1900	150	1.15	85.5
HRC-L1900-a200-t1.15	1900	200	1.15	83.9
HRC-L1900-a300-t1.15	1900	300	1.15	81.3
HRC-L1900-a600-t1.15	1900	600	1.15	80.8
HRC-L1900-a100-t1.95	1900	100	1.95	209.6
HRC-L1900-a120-t1.95	1900	120	1.95	200.98
HRC-L1900-a150-t1.95	1900	150	1.95	191.05
HRC-L1900-a200-t1.95	1900	200	1.95	182.96
HRC-L1900-a300-t1.95	1900	300	1.95	182.94
HRC-L1900-a600-t1.95	1900	600	1.95	182.54
HRC-L2500-a100-t0.75	2500	100	0.75	36.06
HRC-L2500-a120-t0.75	2500	120	0.75	34.97
HRC-L2500-a150-t0.75	2500	150	0.75	34.6
HRC-L2500-a200-t0.75	2500	200	0.75	34.34
HRC-L2500-a300-t0.75	2500	300	0.75	33.12
HRC-L2500-a600-t0.75	2500	600	0.75	32.82
HRC-L2500-a100-t0.95	2500	100	0.95	50.6
HRC-L2500-a120-t0.95	2500	120	0.95	50.5
HRC-L2500-a150-t0.95	2500	150	0.95	50.4
HRC-L2500-a200-t0.95	2500	200	0.95	49.6
HRC-L2500-a300-t0.95	2500	300	0.95	48.3
HRC-L2500-a600-t0.95	2500	600	0.95	47.9
HRC-L2500-a100-t1.15	2500	100	1.15	63.8
HRC-L2500-a120-t1.15	2500	120	1.15	62.4
HRC-L2500-a150-t1.15	2500	150	1.15	62.0
HRC-L2500-a200-t1.15	2500	200	1.15	61.9
HRC-L2500-a300-t1.15	2500	300	1.15	62.0
HRC-L2500-a600-t1.15	2500	600	1.15	60.9
HRC-L2500-a100-t1.95	2500	100	1.95	154.9

HRC-L2500-a120-t1.95	2500	120	1.95	154.71
HRC-L2500-a150-t1.95	2500	150	1.95	154.67
HRC-L2500-a200-t1.95	2500	200	1.95	126.73
HRC-L2500-a300-t1.95	2500	300	1.95	125.11
HRC-L2500-a600-t1.95	2500	600	1.95	123.94

5.5. Evaluation of current design guidelines

AISI (2016) and AS/NZS (2018) recommend the EWM and the DSM for determining the axial capacity of CFS members. In the EWM, the nominal design strength of built-up columns is calculated using the effective cross-sectional area of the members. In contrast, the DSM determines design strength based on the critical elastic buckling stress, considering the entire cross-section. The specific calculation formulas for both methods are described in the following subsections. For built-up box section columns, the comparison between the test results (P_{EXP}) and the design strengths (P_{DSM} and P_{EWM}) determined from AISI (2016) and AS/NZS (2018) is presented in Table 5-11. The mean value of the P_{EXP}/P_{EWM} ratio for specimens with HRCs and with screws are 2.68 and 2.69, with COVs of 0.41 and 0.42, respectively. The comparison shows that the EWM is overly conservative, with mean experimental-to-design strength ratios exceeding 2.5, as shown in Figures 5-28, 5-29, and 5-30.

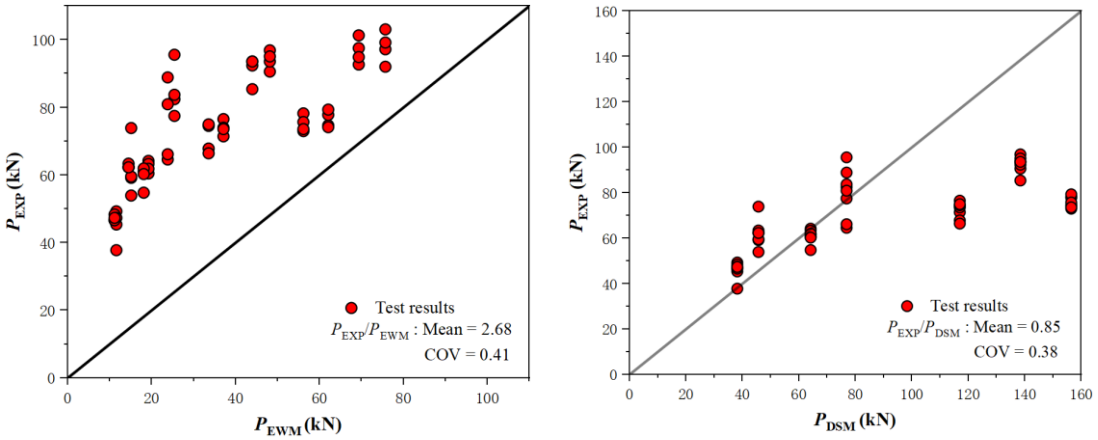

(a) P_{EWM} (b) P_{DSM}

Figure 5-28 Comparison of test results of specimens with HRCs and the design strengths

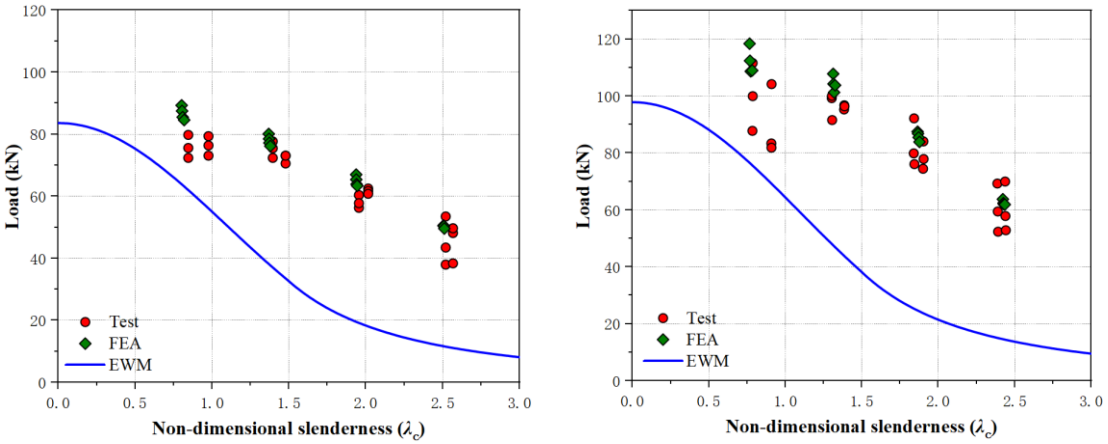

(i) Thickness of 0.95 mm (ii) Thickness of 1.15 mm

Figure 5-29 Comparison of test results of specimens with screws and the design strengths based on the EWM

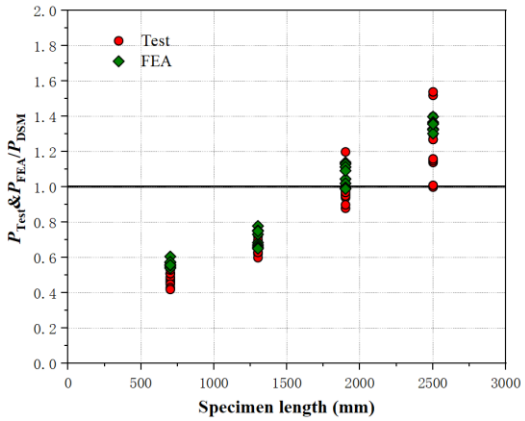

Figure 5-30 Comparison of test results of specimens with screws and the design strengths based on the DSM

Table 5-11 Comparison of test ultimate strength with design strength

Specimen ID	Test strength P_{EXP} kN	Design strength			P_{EXP} /P_{EWM}	P_{EXP} /P_{DSM}	P_{EXP} /P_{PROP}
		P_{EWM} kN	P_{DSM} kN	P_{PROP} kN			
Specimens with a thickness of 0.95 mm							
HRC-L700-a300-t0.95-W1	74.7	62.0	156.4	74.1	1.20	0.48	1.01
HRC-L700-a300-t0.95-W2	77.8	62.0	156.4	74.1	1.25	0.50	1.05
HRC-L700-a600-t0.95-W1	78.3	56.1	156.4	74.1	1.39	0.50	1.06
HRC-L700-a600-t0.95-W2	73.0	56.1	156.4	74.1	1.30	0.47	0.99
HRC-L1300-a300-t0.95-W1	76.6	37.1	116.9	74.1	2.07	0.65	1.03
HRC-L1300-a300-t0.95-W2	71.5	37.1	116.9	74.1	1.93	0.61	0.96
HRC-L1300-a600-t0.95-W1	67.9	33.5	116.9	74.1	2.02	0.58	0.92
HRC-L1300-a600-t0.95-W2	66.5	33.5	116.9	74.1	1.98	0.57	0.90
HRC-L1900-a300-t0.95-W1	60.5	19.2	64.1	70.5	3.15	0.94	0.86
HRC-L1900-a300-t0.95-W2	64.2	19.2	64.1	70.5	3.34	1.00	0.91
HRC-L1900-a600-t0.95-W1	54.8	18.1	64.1	66.2	3.03	0.85	0.83
HRC-L1900-a600-t0.95-W2	61.1	18.1	64.1	66.2	3.38	0.95	0.92
HRC-L2500-a300-t0.95-W1	37.8	11.6	38.1	42.5	3.27	0.99	0.89
HRC-L2500-a300-t0.95-W2	49.3	11.6	38.1	42.5	4.26	1.29	1.16
HRC-L2500-a600-t0.95-W1	46.6	11.1	38.1	40.9	4.18	1.22	1.14
HRC-L2500-a600-t0.95-W2	48.4	11.1	38.1	40.9	4.34	1.27	1.18

HRC-L700-a300-t0.95-S1	79.4	62.0	156.4	74.1	1.28	0.51	1.07
HRC-L700-a300-t0.95-S2	74.2	62.0	156.4	74.1	1.20	0.47	1.00
HRC-L700-a600-t0.95-S1	75.7	56.1	156.4	74.1	1.35	0.48	1.02
HRC-L700-a600-t0.95-S2	73.6	56.1	156.4	74.1	1.31	0.47	0.99
HRC-L1300-a300-t0.95-S1	74.0	37.1	116.9	74.1	2.00	0.63	1.00
HRC-L1300-a300-t0.95-S2	73.6	37.1	116.9	74.1	1.99	0.63	0.99
HRC-L1300-a600-t0.95-S1	74.6	33.5	116.9	74.1	2.22	0.64	1.01
HRC-L1300-a600-t0.95-S2	75.0	33.5	116.9	74.1	2.24	0.64	1.01
HRC-L1900-a300-t0.95-S1	63.3	19.2	64.1	70.5	3.30	0.99	0.90
HRC-L1900-a300-t0.95-S2	61.9	19.2	64.1	70.5	3.22	0.96	0.88
HRC-L1900-a600-t0.95-S1	62.0	18.1	64.1	66.2	3.43	0.97	0.94
HRC-L1900-a600-t0.95-S2	60.3	18.1	64.1	66.2	3.34	0.94	0.91
HRC-L2500-a300-t0.95-S1	47.4	11.6	38.1	42.5	4.10	1.24	1.11
HRC-L2500-a300-t0.95-S2	45.4	11.6	38.1	42.5	3.93	1.19	1.07
HRC-L2500-a600-t0.95-S1	46.7	11.1	38.1	40.9	4.19	1.22	1.14
HRC-L2500-a600-t0.95-S2	47.4	11.1	38.1	40.9	4.25	1.24	1.16
Specimens with a thickness of 1.15 mm							
HRC-L700-a300-t1.15-W1	92.1	75.7	195.3	101.6	1.22	0.47	0.91
HRC-L700-a300-t1.15-W2	97.2	75.7	195.3	101.6	1.28	0.50	0.96
HRC-L700-a600-t1.15-W1	101.3	69.3	195.3	101.6	1.46	0.52	1.00
HRC-L700-a600-t1.15-W2	97.6	69.3	195.3	101.6	1.41	0.50	0.96
HRC-L1300-a300-t1.15-W1	96.9	48.1	138.4	101.6	2.01	0.70	0.95
HRC-L1300-a300-t1.15-W2	90.6	48.1	138.4	101.6	1.88	0.65	0.89
HRC-L1300-a600-t1.15-W1	85.4	43.9	138.4	101.6	1.94	0.62	0.84
HRC-L1300-a600-t1.15-W2	93.6	43.9	138.4	101.6	2.13	0.68	0.92
HRC-L1900-a300-t1.15-W1	77.5	25.4	76.8	84.3	3.05	1.01	0.92
HRC-L1900-a300-t1.15-W2	95.6	25.4	76.8	84.3	3.77	1.24	1.13
HRC-L1900-a600-t1.15-W1	64.6	23.8	76.8	79.2	2.72	0.84	0.82
HRC-L1900-a600-t1.15-W2	66.2	23.8	76.8	79.2	2.78	0.86	0.84
HRC-L2500-a300-t1.15-W1	54.0	15.1	45.6	50.8	3.58	1.18	1.06
HRC-L2500-a300-t1.15-W2	73.9	15.1	45.6	50.8	4.90	1.62	1.46
HRC-L2500-a600-t1.15-W1	62.3	14.5	45.6	48.9	4.31	1.37	1.27
HRC-L2500-a600-t1.15-W2	62.4	14.5	45.6	48.9	4.31	1.37	1.28
HRC-L700-a300-t1.15-S1	103.1	75.7	195.3	101.6	1.36	0.53	1.01
HRC-L700-a300-t1.15-S2	99.2	75.7	195.3	101.6	1.31	0.51	0.98
HRC-L700-a600-t1.15-S1	92.7	69.3	195.3	101.6	1.34	0.47	0.91
HRC-L700-a600-t1.15-S2	94.9	69.3	195.3	101.6	1.37	0.49	0.93
HRC-L1300-a300-t1.15-S1	93.6	48.1	138.4	101.6	1.95	0.68	0.92
HRC-L1300-a300-t1.15-S2	95.1	48.1	138.4	101.6	1.98	0.69	0.94
HRC-L1300-a600-t1.15-S1	92.4	43.9	138.4	101.6	2.10	0.67	0.91
HRC-L1300-a600-t1.15-S2	93.6	43.9	138.4	101.6	2.13	0.68	0.92
HRC-L1900-a300-t1.15-S1	82.5	25.4	76.8	84.3	3.25	1.07	0.98
HRC-L1900-a300-t1.15-S2	83.8	25.4	76.8	84.3	3.30	1.09	0.99
HRC-L1900-a600-t1.15-S1	88.9	23.8	76.8	79.2	3.74	1.16	1.12
HRC-L1900-a600-t1.15-S2	81.0	23.8	76.8	79.2	3.40	1.05	1.02
HRC-L2500-a300-t1.15-S1	59.2	15.1	45.6	50.8	3.92	1.30	1.17
HRC-L2500-a300-t1.15-S2	59.6	15.1	45.6	50.8	3.95	1.31	1.17
HRC-L2500-a600-t1.15-S1	63.4	14.5	45.6	48.9	4.38	1.39	1.30
HRC-L2500-a600-t1.15-S2	62.3	14.5	45.6	48.9	4.31	1.37	1.27
Mean					2.68	0.85	1.01
COV					0.41	0.38	0.12

5.6. Proposed new design method and reliability analysis

For the EWM, there is currently no design approach to directly calculate the effective area of built-up sections. Instead, the effective areas of individual components are

calculated separately and then summed, thereby neglecting their composite action. For the DSM, software such as THIN-WALL-2 can be used for calculations, but it does not account for the influence of fastener spacing. Currently, the most common method for determining the elastic local buckling stress (P_{crl}) and distortional buckling stress (P_{crd}) of built-up sections is to perform a linear buckling analysis using ABAQUS. However, both DSM and EWM still lack the accuracy needed to calculate the axial strength of built-up columns, necessitating further development.

The DSM is more suitable for calculating the axial strength of individual channels, while the EWM, which superimposes the effective areas of individual channels, tends to be more conservative. This chapter proposes a novel design approach for CFS built-up section columns to address the inaccuracies in current standards. As shown in Figure 5-31, the proposed method integrates EWM and DSM by categorizing specimens into two groups: low slenderness ratios ($\lambda c \leq 1.5$) and high slenderness ratios ($\lambda c > 1.5$), with slenderness ratio calculations following the requirements of AISI (2016). For specimens with low slenderness ratios, the design strength of individual CFS components is calculated using DSM, considering the effective lengths (l_{ex}, l_{ey}, and l_{ez}). Here, l_{ex} represents the longitudinal effective length, defined as $l_{ex} = L$ for pin-end supports, according to AISI (2016), while l_{ey} and l_{ez} are fully laterally supported ($l_{ey} = l_{ez} = 0$) to account for interactions between components, including fastener connections and interfacial friction. The nominal design strength (P_{PORP}) is obtained by superimposing the individual channel strengths. For specimens with high slenderness ratios, where global buckling is the dominant failure mode, significant elastic local buckling is often recovered to its pre-loading state after unloading. This occurs because the failure is primarily due to global instability rather than material yielding. For this part of the design,

the formulaic structure of the EWM is referenced. However, instead of using the effective area (A_e), the full cross-sectional area (A) is applied in the calculations. Testing results, presented in Table 5-11 and Figure 5-32, show a mean P_{EXP}/P_{PROP} value of 1.01 with a COV of 0.12, indicating that the proposed method significantly enhances the accuracy of the design compared to current standards. It should be noted that the proposed equation is preliminarily validated for built-up columns with modified slenderness ratios ranging from 45 to 136. Its applicability to other slenderness ranges remains to be evaluated through further experimental and numerical studies.

Based on a reliability analysis, the β-value for design strength (P_{PROP}) was found to be 2.58, exceeding the desired value of 2.5. This confirms the reliability of the proposed equations in predicting the axial ultimate strength of these CFS built-up columns.

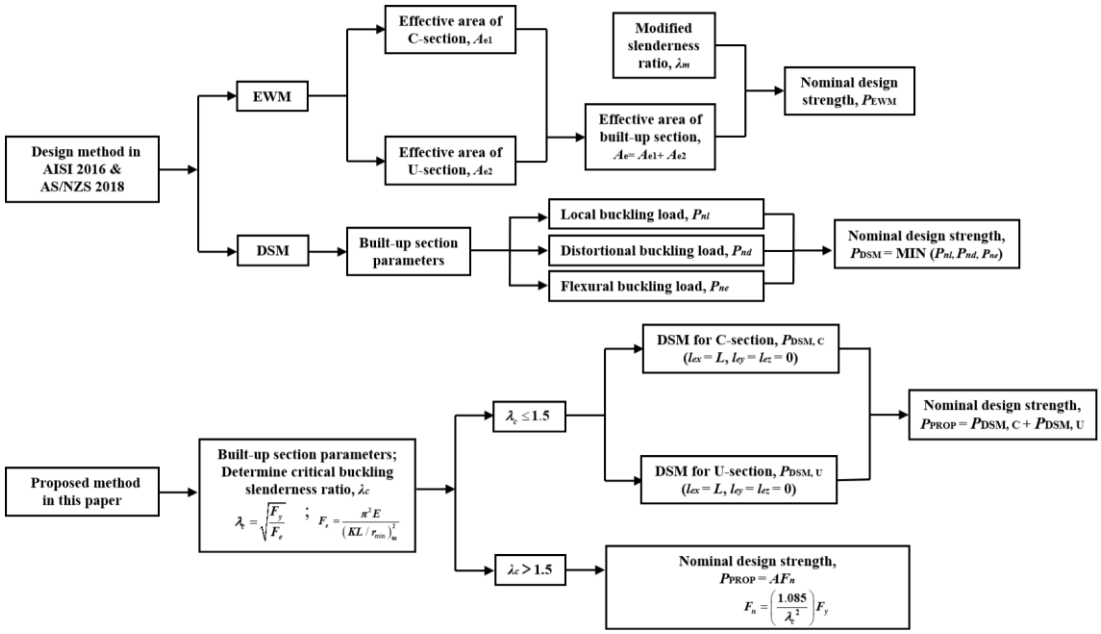

Figure 5-31 Flowchart for calculating design strengths

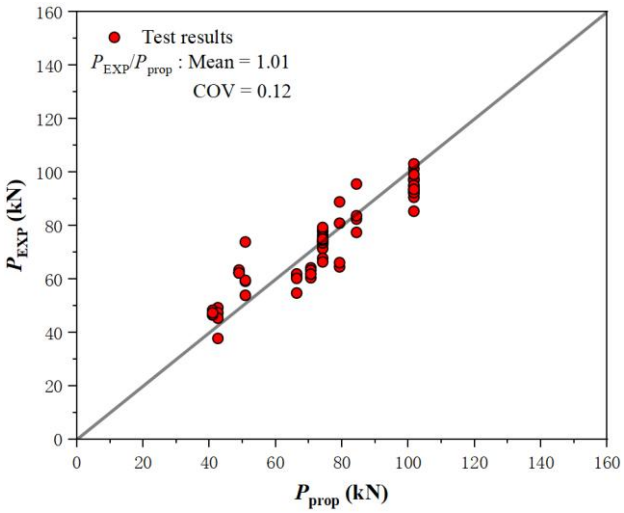

Figure 5-32 Comparison of test results and design strengths predicted by the proposed method

5.7. Summary

This chapter This chapter provides a comprehensive experimental and numerical investigation into the performance of CFS built-up box columns utilizing HRCs or traditional screws under pin-ended boundary conditions. The study evaluates the impact of various factors such as slenderness ratio, thickness, and fastener spacing on the buckling behaviour and axial capacity of the columns. Based on experimental testing and FE simulations, the following key findings and conclusions are drawn:

(1) Slenderness ratio and buckling behaviour: The study highlights that while fastener spacing and thickness have a minor influence on the overall buckling behaviour, the slenderness ratio is the key factor in determining the failure mode. No significant deformation or shear failure was observed in the HRCs or screws.

(2) Failure modes and axis rotation: Specimens exhibited flexural buckling that predominantly rotated about the weak axis, regardless of the type of end support. Thinner specimens (with a thickness of 0.95 mm) were more likely to experience strong-axis rotation failures

(3) Design methods and proposal for improvement: The study found that both the DSM and the EWM presented limitations in accurately predicting the axial strength of CFS built-up box columns. To address this, a new design approach combining DSM and EWM was proposed. This approach achieved a mean experimental-to-design strength ratio of 1.01, with a COV of 0.12, showing a notable improvement in design accuracy compared to existing methods. The proposed design approach significantly enhances the predictive accuracy of axial strength for CFS built-up box columns, demonstrating its potential to improve structural design practices. The statistical analysis supports the reliability of the new design equations, offering a more accurate tool for designing CFS built-up box columns.

Chapter 6 CFS telescopic studs under axial compression

6.1. Introductory remarks

CFS studs are widely used as vertical load-bearing members in light-gauge steel wall systems. In practical construction, studs may need to be connected or extended to accommodate construction tolerances, prefabrication requirements, or structural detailing. Telescopic stud systems have therefore been proposed as an efficient solution, allowing two CFS sections to overlap and be connected through screws to form a continuous load-bearing member. Despite their practical advantages, the structural behaviour and load-carrying capacity of telescopic studs, particularly the influence of screw configurations on connection performance, remain insufficiently understood.

This chapter presents a thorough experimental and numerical investigation into the structural behaviour of a novel CFS telescopic stud system under axial compression. In this study, "stud" denotes CFS vertical members primarily subjected to axial compression and commonly used in light-gauge steel wall systems. The term is defined based on structural function rather than specific geometric dimensions, as stud sizes may vary depending on design requirements and applications. A total of 40 specimens were tested, considering variations in screw configurations, steel grades, and section thicknesses. The test results revealed that tilting and bearing led to failure in all screw connections. In comparison to the single-screw connection with a gap at the middle of the web, the telescopic studs with 2 screws in the web, 2 screws in the flanges, and 4 screws in both the web and flanges showed approximately 35-37% higher strengths. A nonlinear explicit dynamic FE model was then developed and validated against the test results in terms of its connection strengths and failure modes. The experimental results were compared with the design strengths determined by the current design standards. The comparison results

revealed that the AISI (2016) and AS/NZS (2018) are conservative, underestimating the connection strengths of telescopic studs with different screw layouts by 1-13%.

6.2. Experimental Investigation

6.2.1. Test specimens

A total of 40 tests on telescopic stud connections (see Figure 6-1) were conducted. The telescopic stud connections were formed by combining two different CFS channel sections (see Figure 6-1), and they were connected using self-drilling screws (see Figure 6-2) on either the web or flanges of the channel sections. Figure 6-3 shows four different self-drilling screw layouts investigated in the current study. Two different thicknesses of CFS channels are considered: 0.75 mm and 1.2 mm. The steel grades of the sections are varied as G550 and G500. Table 6-1 illustrates the specimen dimensions and details, and the labelling of specimens is shown in Figure 6-4.

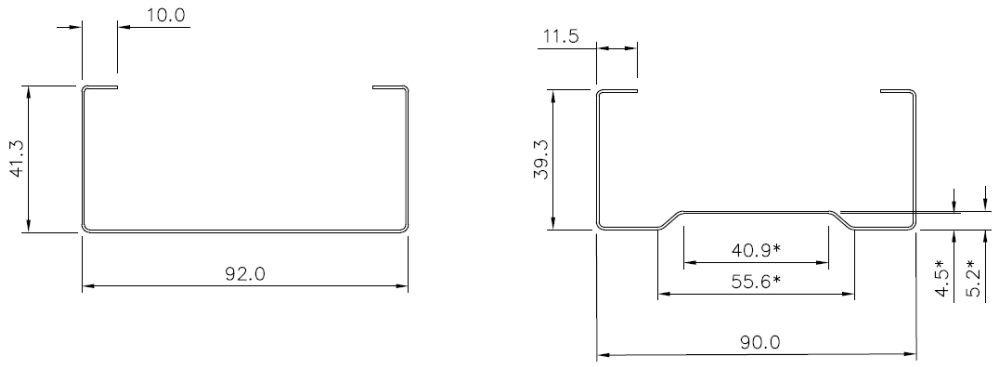

(a) CFS plain channel (b) CFS sigma channel

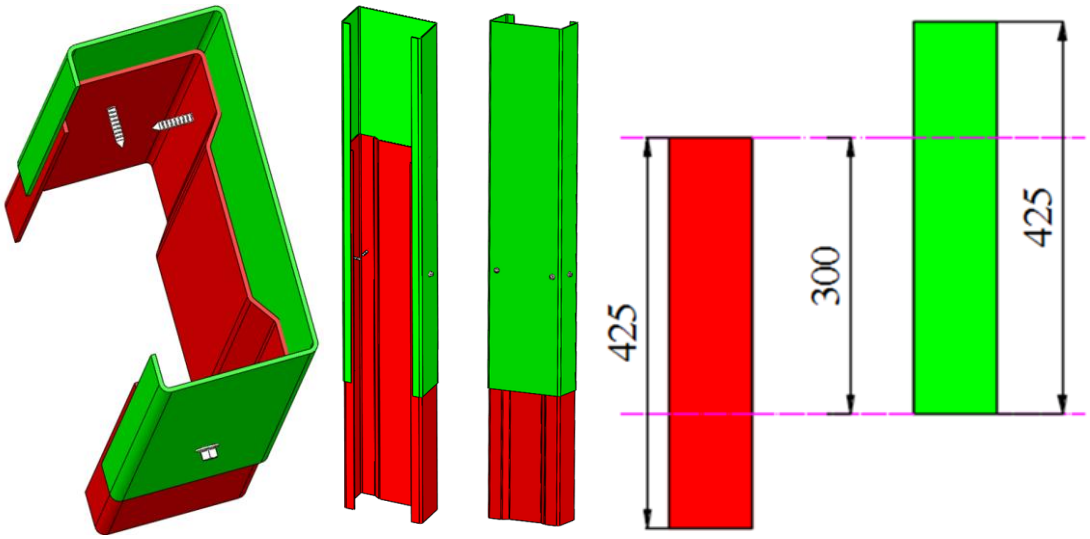

(c) Schematic views of telescopic studs

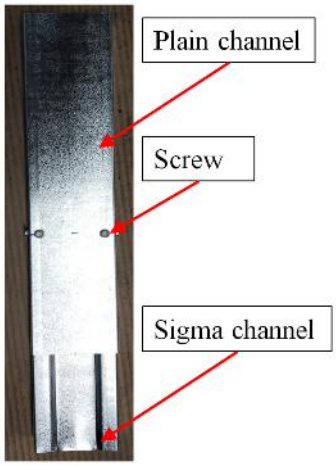

(d) Pictures of the telescopic studs with screws

Figure 6-1 Details of telescopic studs (all dimensions in mm)

Figure 6-2 ST10-16×16CL5 screws (screw diameter 3.5 mm)

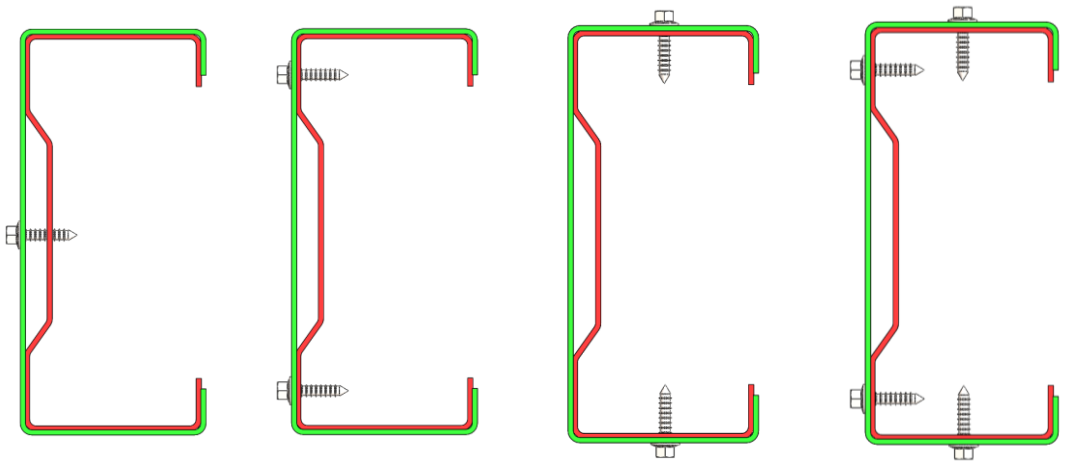

(a) S1 (b) S2 (c) S3 (d) S4

Figure 6-3 screw layouts

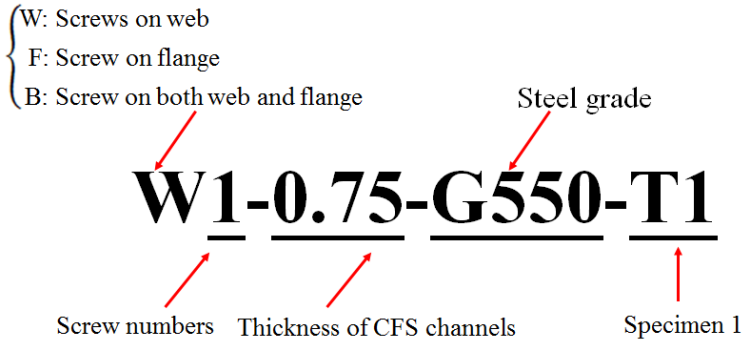

Figure 6-4 Specimen labelling

Table 6-1 Details of specimens and experimental loads

(a) 0.75 mm channel thickness

Specimen	Nominal thickness t (mm)	Screw numbers	Steel grade	Connection strengths P_{Exp} (kN)	Mean value P_{Exp} (kN)	P_{FEA} (kN)	P_{Exp}/P_{FEA}
Screws on web							
W1-0.75-G550-T1	0.75	1	G550	2.91			1.08
W1-0.75-G550-T2	0.75	1	G550	2.89			1.07
W1-0.75-G550-T3	0.75	1	G550	2.74	2.73	2.68	1.02
W1-0.75-G550-T4	0.75	1	G550	2.55			0.95
W1-0.75-G550-T5	0.75	1	G550	2.58			0.96
W2-0.75-G550-T1	0.75	2	G550	7.23			1.00
W2-0.75-G550-T2	0.75	2	G550	7.68			1.06
W2-0.75-G550-T3	0.75	2	G550	7.93	7.64	7.23	1.09
W2-0.75-G550-T4	0.75	2	G550	7.76			1.07
W2-0.75-G550-T5	0.75	2	G550	7.58			1.04
Screws on flanges							
F2-0.75-G550-T1	0.75	2	G550	7.67			1.00
F2-0.75-G550-T2	0.75	2	G550	7.26			0.94
F2-0.75-G550-T3	0.75	2	G550	7.81	7.60	7.69	1.02
F2-0.75-G550-T4	0.75	2	G550	7.85			1.02
F2-0.75-G550-T5	0.75	2	G550	7.43			0.97
Screws on both web and flanges							
B4-0.75-G550-T1	0.75	4	G550	13.71	13.82	13.47	1.02

B4-0.75-G550-T2	0.75	4	G550	13.44			1.00
B4-0.75-G550-T3	0.75	4	G550	13.87			1.03
B4-0.75-G550-T4	0.75	4	G550	14.03			1.04
B4-0.75-G550-T5	0.75	4	G550	14.07			1.04
Mean							1.02
COV							0.04

(b) 1.20 mm channel thickness

Specimen	Nominal thickness t (mm)	Screw numbers	Steel grade	Connection strengths P_{Exp} (kN)	Mean value P_{Exp} (kN)	P_{FEA} (kN)	P_{Exp}/P_{FEA}
Screw on web							
W1-1.2-G500-T1	1.20	1	G500	4.06			1.08
W1-1.2-G500-T2	1.20	1	G500	4.52			1.20
W1-1.2-G500-T3	1.20	1	G500	3.68	4.00	3.76	0.98
W1-1.2-G500-T4	1.20	1	G500	4.49			1.19
W1-1.2-G500-T5	1.20	1	G500	3.27			0.87
W2-1.2-G500-T1	1.20	2	G500	13.91			1.05
W2-1.2-G500-T2	1.20	2	G500	13.30			1.01
W2-1.2-G500-T3	1.20	2	G500	13.24	13.50	13.21	1.00
W2-1.2-G500-T4	1.20	2	G500	13.67			1.03
W2-1.2-G500-T5	1.20	2	G500	13.38			1.01
Screws on flanges							
F2-1.2-G500-T1	1.20	2	G500	13.97			1.12
F2-1.2-G500-T2	1.20	2	G500	12.28			0.98
F2-1.2-G500-T3	1.20	2	G500	12.39	13.09	12.49	0.99
F2-1.2-G500-T4	1.20	2	G500	13.44			1.08
F2-1.2-G500-T5	1.20	2	G500	13.38			1.07
Screws on both web and flanges							
B4-1.2-G500-T1	1.20	4	G500	25.31			1.02
B4-1.2-G500-T2	1.20	4	G500	26.74			1.08
B4-1.2-G500-T3	1.20	4	G500	27.45	26.64	24.79	1.11
B4-1.2-G500-T4	1.20	4	G500	26.56			1.07
B4-1.2-G500-T5	1.20	4	G500	27.15			1.10
Mean							1.05
COV							0.07

6.2.2. Material testing

The material properties of CFS channel sections were determined by the tensile coupon tests. Two sets of tensile coupons were cut from the untested specimens. A 100 kN Instron machine (see Figure 6-5) was used to conduct the tensile coupon tests. For steel grade G500, the average yield strength ($\sigma_{0.2}$) was 587.34 MPa and the ultimate strength was 599.56 MPa (see Figure 6-6), whereas for the steel grade G550, these values were 647.45 MPa and 651.23 MPa, respectively. The stress-strain curves for both steel grades are shown in Figure 6-7, and the results of tensile coupon tests are shown in Table 6-2.

Figure 6-5 Setup of tensile coupon tests

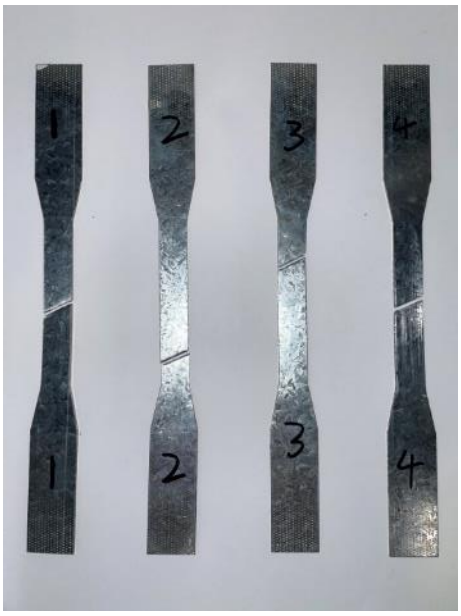

Figure 6-6 Deformed tensile coupons for G500 specimens

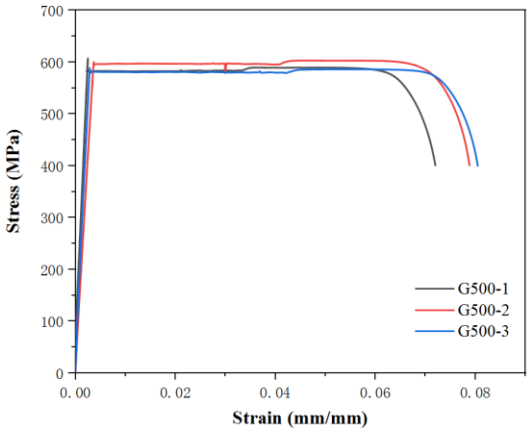

(a) Steel grade G500

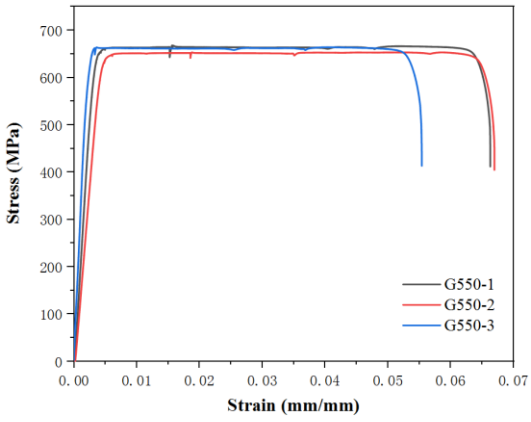

(b) Steel grade G550

Figure 6-7 Stress-strain curves obtained from the tensile coupon tests

Table 6-2 Material properties obtained from the tensile coupon tests

Coupon sample ID	Thickness t mm	Yield stress $\sigma_{0.2}$ MPa	Ultimate stress σ_u MPa
G500-1	1.22	582.53	607.23
G500-2	1.24	597.19	603.29
G500-3	1.21	582.30	588.60
Mean	1.22	587.34	599.56
G550-1	0.76	650.83	653.67
G550-2	0.77	640.73	645.54
G550-3	0.76	650.79	654.48
Mean	0.76	647.45	651.23

6.2.3. Testing-rig and loading procedure

A 200 kN Instron machine was used to perform the tests on telescopic studs. The specimens were subjected to compression loads through the bottom plate, and a displacement-controlled method with a loading rate of 1 mm/min was used to apply the loading. Figure 6-8 illustrates the test setup used for loading the telescopic studs. A data acquisition system was used to record the displacement and loads at regular intervals during the tests.

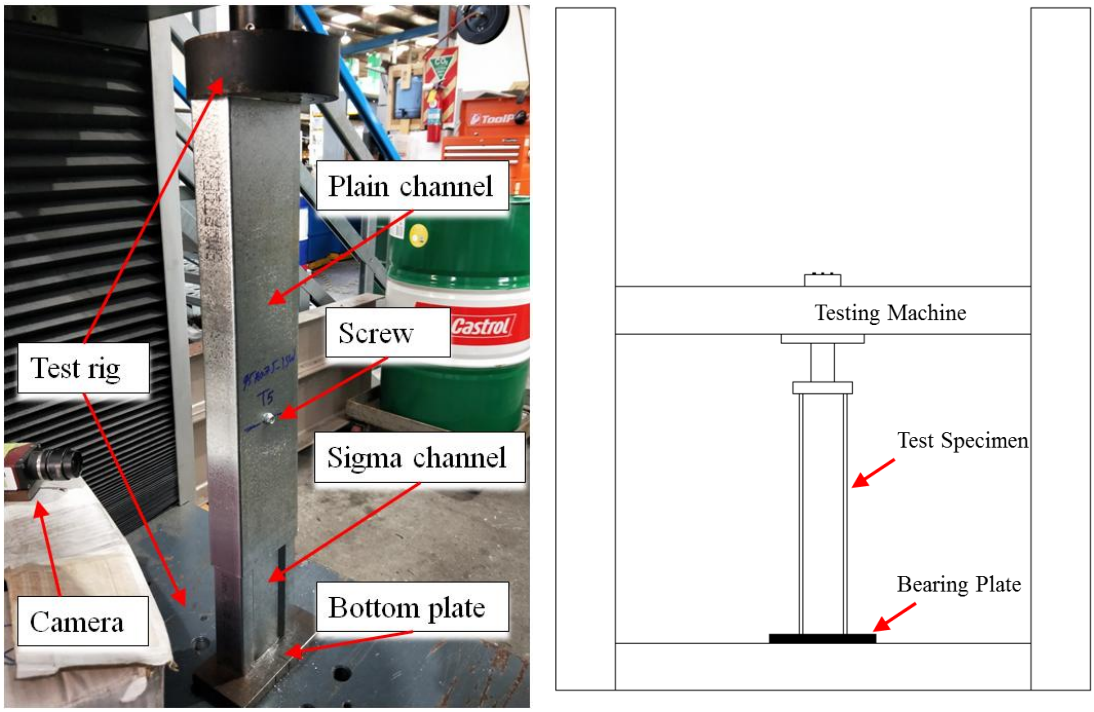

Figure 6-8 Test setup for telescopic studs

6.2.4. Test results and discussion

The structural behaviour of four different screw layouts in telescopic studs was investigated. As expected, the shear strengths of telescopic studs vary with the thickness and steel grades of CFS channel sections, as shown in Table 6-1. The combined tilting and bearing failure modes were observed in all tested specimens. Further information is detailed in the following paragraphs:

Table 6-1 summarises the experimental ultimate strengths (P_{Exp}) of telescopic stud connections. The test results show that the mean values of P_{Exp} have a small difference for the screws on the web or on the flanges. The connection strengths of the specimens with screw layout S2 are approximately 2.8 times greater than that of the specimens with screw layout S1 for 0.75mm thick specimens and approximately 3.3 times greater for the 1.20mm thick specimens. This indicates that the telescopic stud connections with a gap (S1) exhibit a lower single-screw connection strength compared to other screw layouts. This is primarily due to the increased susceptibility of the screw to tilting in the S1 configuration. Therefore, the telescopic studs should avoid using screw layout S1.

The load-displacement curves for all tested specimens are shown in Figure 6-9. The specimens with screw layout S1 (see Figures 6-9(a) and 6-9(e)) showed typical elastic deformation until reaching their ultimate strengths, followed by a notable and swift decline in the applied load. Compared to the specimens with screw layout S1, the load-displacement curves of other specimens showed a higher initial stiffness, and a non-linear curve was observed prior to their ultimate strengths. It can also be seen from Figure 6-9 that the specimens with a thickness of 0.75 mm exhibit superior ductility compared to those with a thickness of 1.20 mm, and the peak loads occurred at 5-10 mm displacement, especially for the specimens with screw layouts S2, S3, and S4. This occurrence can be attributed to the increased propensity for significant slipping between the CFS channel sections and screws, which occurred more prominently in thinner specimens.

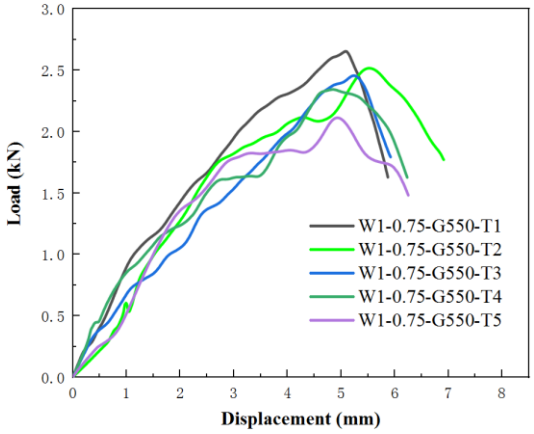

(a) W1-0.75-G550

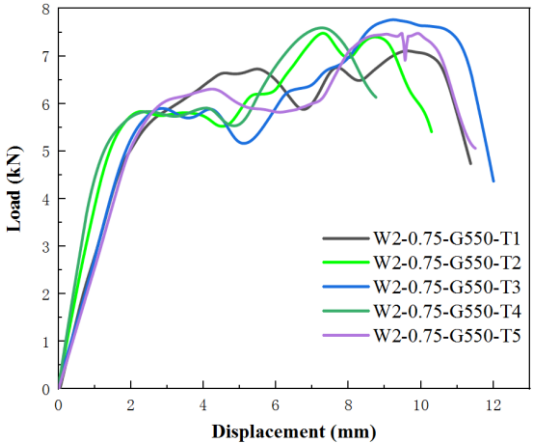

(b) W2-0.75-G550

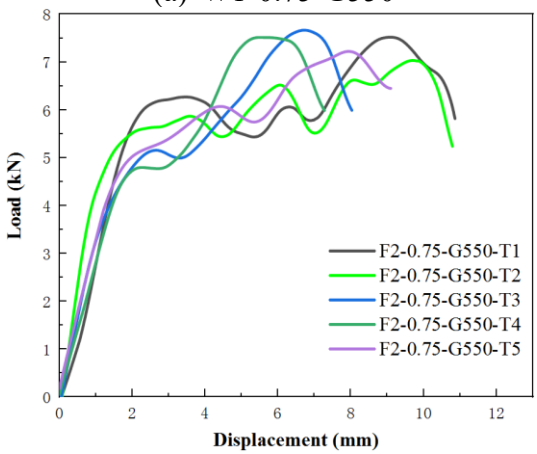

(c) F2-0.75-G550

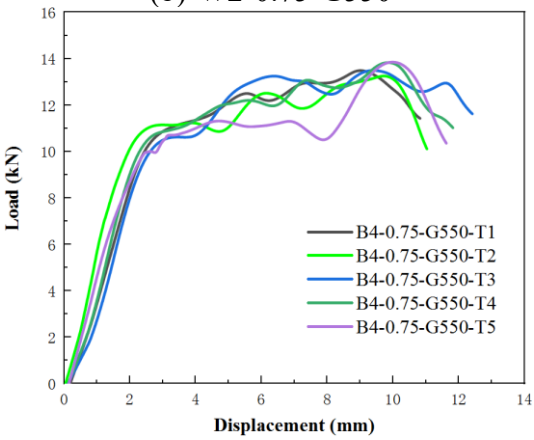

(d) B4-0.75-G550

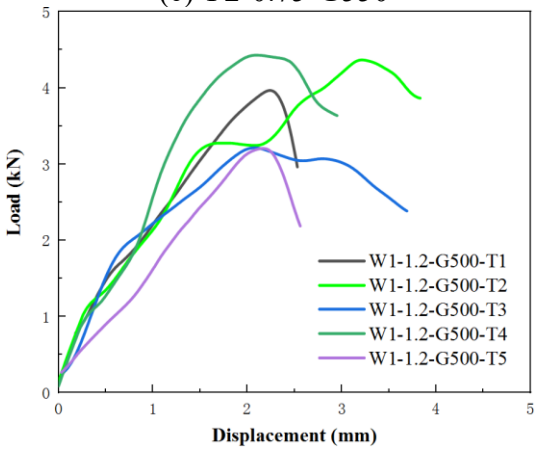

(e) W1-1.2-G500

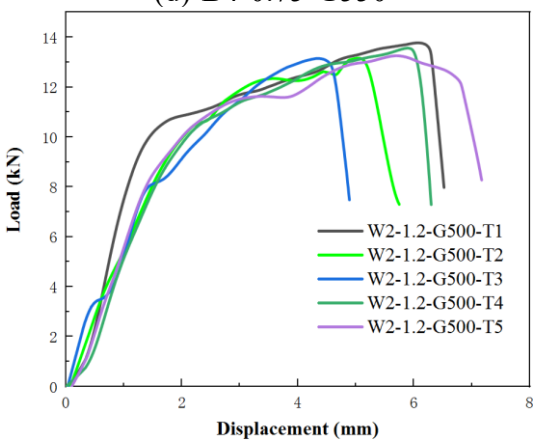

(f) W2-1.2-G500

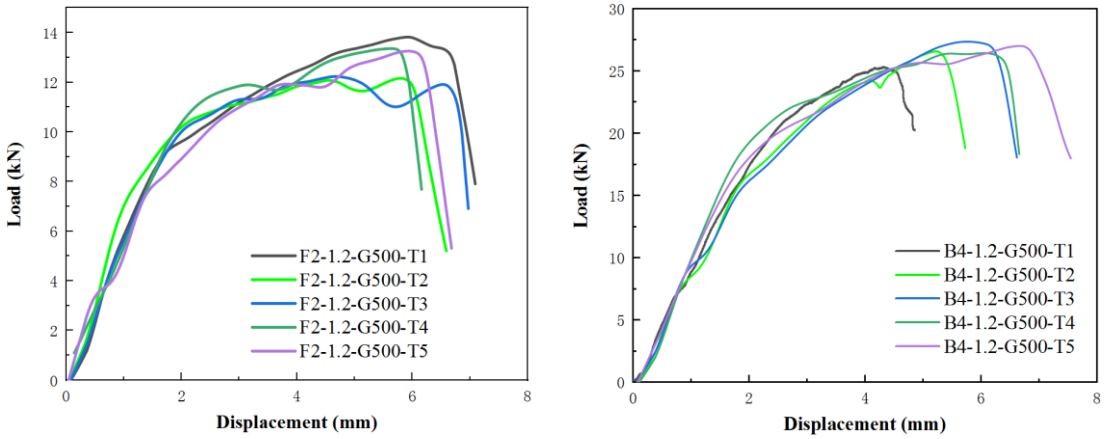

(g) F2-1.2-G500 (h) B4-1.2-G500

Figure 6-9 Load-displacement curves for telescopic stud connections

A simplified load-deformation response (see Figure 6-10) of telescopic studs was developed to show the stiffness and strength degradation in the current study. F_y and F_m represent the yield and peak strengths of telescopic studs, respectively. K_e, K_m, and K_r are the elastic, strain-hardening, and residual stiffness, respectively. The initial stiffness of all specimens is shown in Figure 6-11. The ratio of cap deformation (δ_m) to yield deformation (δ_y) can be used to denote ductility (Tao et al. 2016), and the higher ratio indicates better ductility. These parameters from the experimental results are summarised in Table 6-3. For the specimens with screw layout S1, there is no obvious strain-hardening stage due to premature screw tilting. For the specimens with screw layouts S2, S3, and S4, it can be seen from Table 6-3(b) and Figure 6-12 that the ratio of δ_m/δ_y is higher for thinner specimens, which means such specimens have better ductility.

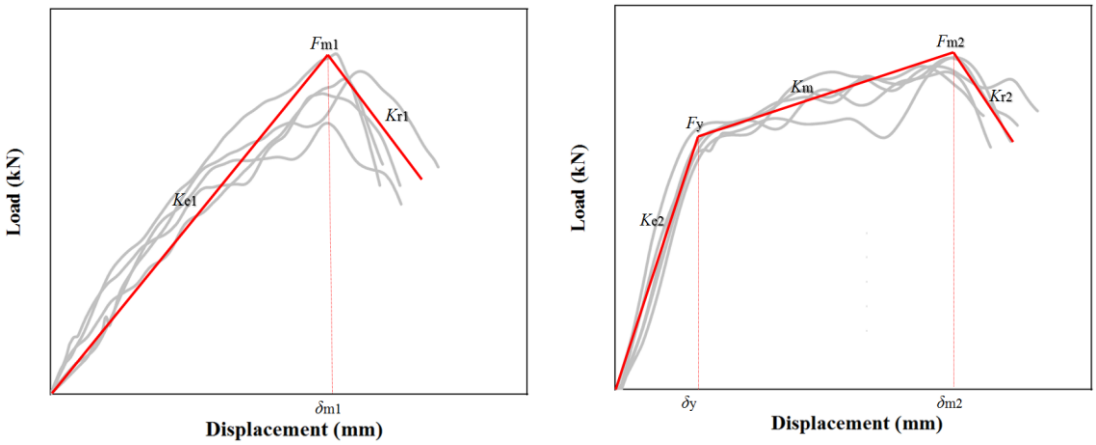

(a) Screw layout S1 (b) Screw layouts S2, S3, S4

Figure 6-10 Load-deformation response of specimens tested

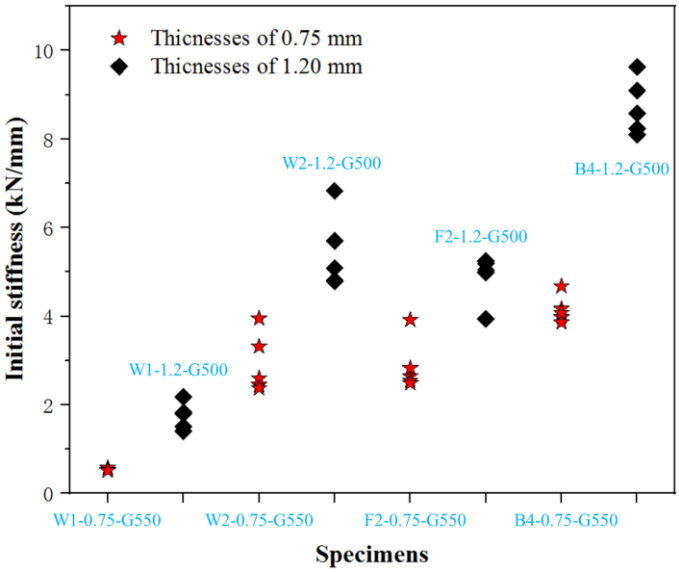

Figure 6-11 Comparison of initial stiffness

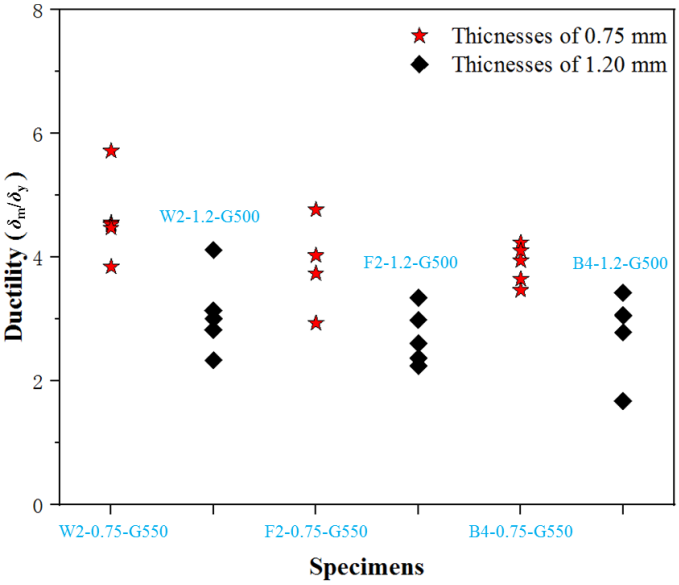

Figure 6-12 Comparison of ductility of specimens

Table 6-3 Parameter summary for simplified load-deformation response

(a) Screw layout S1

Specimen	F_{m1} kN	δ_{m1} mm	K_{e1} kN/mm	K_{r1} kN/mm
W1-0.75-G550-T1	2.91	5.03	0.58	-1.13
W1-0.75-G550-T2	2.89	5.42	0.53	-0.70
W1-0.75-G550-T3	2.74	5.29	0.52	-1.21
W1-0.75-G550-T4	2.55	4.75	0.54	-0.70
W1-0.75-G550-T5	2.58	4.98	0.52	-0.75
W1-1.2-G500-T1	4.06	2.22	1.83	-3.55
W1-1.2-G500-T2	4.52	3.21	1.41	-1.06
W1-1.2-G500-T3	3.68	2.05	1.80	-0.79
W1-1.2-G500-T4	4.49	2.06	2.18	-0.96
W1-1.2-G500-T5	3.27	2.16	1.51	-2.71

(b) Screw layouts S1, S2 and S3

Specimen	F_y kN	F_{m2} kN	δ_y mm	δ_{m2} mm	K_{e2} kN/mm	K_m kN/mm	K_{r2} kN/mm	δ_{m2}/δ_y
W2-0.75-G550-T1	5.17	7.23	2.11	9.62	2.45	0.27	-1.43	4.56
W2-0.75-G550-T2	5.34	7.68	1.61	7.29	3.32	0.44	-0.75	4.53
W2-0.75-G550-T3	5.32	7.93	2.05	9.19	2.60	0.36	-1.26	4.48
W2-0.75-G550-T4	5.02	7.76	1.27	7.27	3.95	0.38	-1.10	5.72
W2-0.75-G550-T5	5.54	7.58	2.33	8.97	2.38	0.23	-1.00	3.85
W2-1.2-G500-T1	10.11	13.91	1.48	6.10	6.83	0.62	-14.12	4.12
W2-1.2-G500-T2	10.34	13.30	2.15	5.04	4.81	0.59	-8.67	2.34
W2-1.2-G500-T3	7.87	13.24	1.38	4.34	5.70	1.24	-10.22	3.14
W2-1.2-G500-T4	9.96	13.67	2.08	5.89	4.79	0.63	-15.15	2.83
W2-1.2-G500-T5	9.73	13.38	1.91	5.75	5.09	0.63	-3.35	3.01
F2-0.75-G550-T1	5.94	7.67	2.24	9.02	2.65	0.19	-1.01	4.03
F2-0.75-G550-T2	4.63	7.26	1.18	9.7	3.92	0.27	-1.85	8.22
F2-0.75-G550-T3	4.57	7.81	1.79	6.69	2.55	0.48	-1.36	3.74
F2-0.75-G550-T4	4.61	7.85	1.85	5.43	2.49	0.60	-1.01	2.94
F2-0.75-G550-T5	4.70	7.43	1.66	7.91	2.83	0.35	-0.93	4.77
F2-1.2-G500-T1	9.24	13.97	1.76	5.89	5.25	0.80	-4.80	3.35
F2-1.2-G500-T2	10.07	12.28	1.94	5.81	5.19	0.38	-9.06	2.99
F2-1.2-G500-T3	9.90	12.39	1.96	4.65	5.05	0.54	-2.36	2.37
F2-1.2-G500-T4	10.87	13.44	2.18	5.68	4.99	0.45	-12.00	2.61
F2-1.2-G500-T5	10.45	13.38	2.65	5.97	3.94	0.49	-11.38	2.25
B4-0.75-G550-T1	10.31	13.71	2.59	8.98	3.98	0.38	-1.25	3.47
B4-0.75-G550-T2	10.72	13.44	2.29	9.7	4.68	0.28	-2.50	4.24
B4-0.75-G550-T3	9.87	13.87	2.56	9.35	3.86	0.43	-0.73	3.65
B4-0.75-G550-T4	10.43	14.03	2.5	9.87	4.17	0.36	-1.55	3.95
B4-0.75-G550-T5	9.88	14.07	2.42	9.95	4.08	0.42	-2.23	4.11
B4-1.2-G500-T1	20.81	25.31	2.57	4.32	8.10	1.04	-9.44	1.68
B4-1.2-G500-T2	16.04	26.74	1.87	5.22	8.58	2.05	-15.61	2.79
B4-1.2-G500-T3	15.74	27.45	1.91	5.84	8.24	2.01	-11.88	3.06
B4-1.2-G500-T4	19.16	26.56	1.99	6.11	9.63	1.21	-15.02	3.07
B4-1.2-G500-T5	17.73	27.15	1.95	6.69	9.09	1.41	-10.69	3.43

The whole process of failure for the specimen W1-0.75-G550-T1 is shown in Figure 6-3. As the load was applied initially, the screw tilting was observed in the specimen, followed by the slipping of the screw thread and the bearing failure (see Figure 6-14(a)). It is worth mentioning that the screw tilting throughout the loading process was accompanied by

contact separation between the CFS plain and sigma channel sections near the screw holes. The failure modes of some of the telescopic stud connections are shown in Figure 6-14. Failure in all screw connections was attributed to tilting and bearing, and the failure modes were not influenced by the screw numbers, screw layouts and section thickness. Notably, the test specimens exhibited elongation of holes and steel piling behaviour, as depicted in Figure 6-14, which were observed in most of the tested specimens.

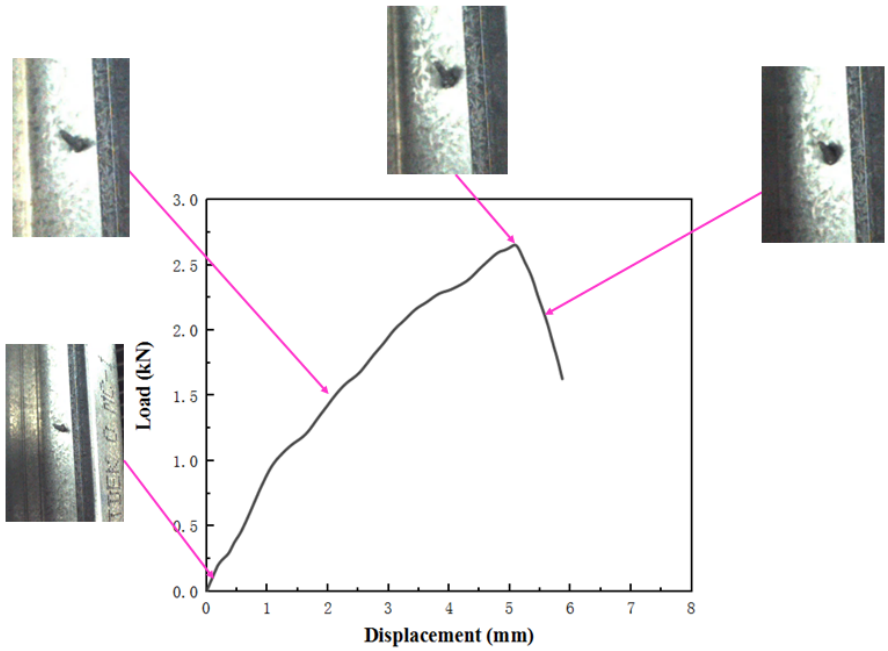

Figure 6-13 Whole process of failure for the specimen W1-0.75-G550-T1

(a) W1-0.75-G550-T1

(b) W2-0.75-G550-T1

(c) F2-0.75-G550-T1

(d) B4-0.75-G550-T1

(e) W1-1.2-G500-T1

(f) W2-1.2-G500-T1

(g) F2-1.2-G500-T1

(h) B4-1.2-G500-T1

Figure 6-14 Failure modes of telescopic studs

6.3. Numerical study

6.3.1. General description of FE model

A nonlinear elastic-plastic FE model was developed using ABAQUS. The FE model was based on the centre line dimensions of screws and telescopic studs. During the construction of the FE model, the interactions, boundary conditions, and screw connection of the telescopic studs were considered. Specific modelling techniques are described in the following paragraphs:

In the FE model, the full geometries of telescopic studs, including CFS channels and screws, were modelled. The material properties of CFS plain and sigma channels were obtained from the tensile coupon tests. For the screws, the material properties were determined using Roy et al. (2019)'s tensile test results, and the engineering stress-strain

curves were employed. As per the ABAQUS manual, the engineering stress-strain curves for both the channels and screws were converted into the true stress-strain curves by using ABAQUS manual. The true stress-strain curves for telescopic studs are shown in Figure 6-15.

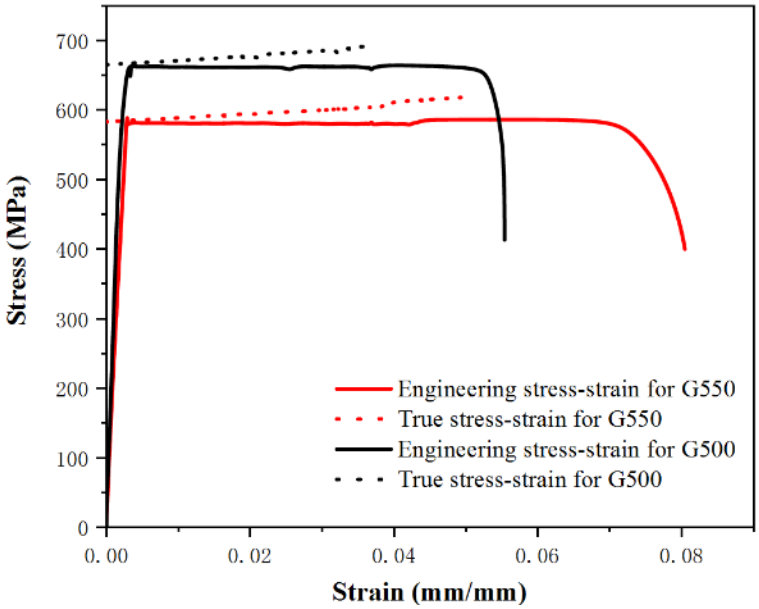

Figure 6-15 True material stress-strain curves for telescopic studs

The S4R shell element used to model the telescopic studs, while C3D8R solid elements were adopted to simulate the screws. The mesh size of 1 × 1 mm was used for screws, whereas the mesh size of 10 × 10 mm was selected for the CFS channels based on the results of a mesh sensitivity analysis. Mesh refinement was used around the screw holes and near the corners of the sections for more accurate FEA results. The FE meshing details are depicted in Figure 6-16(a).

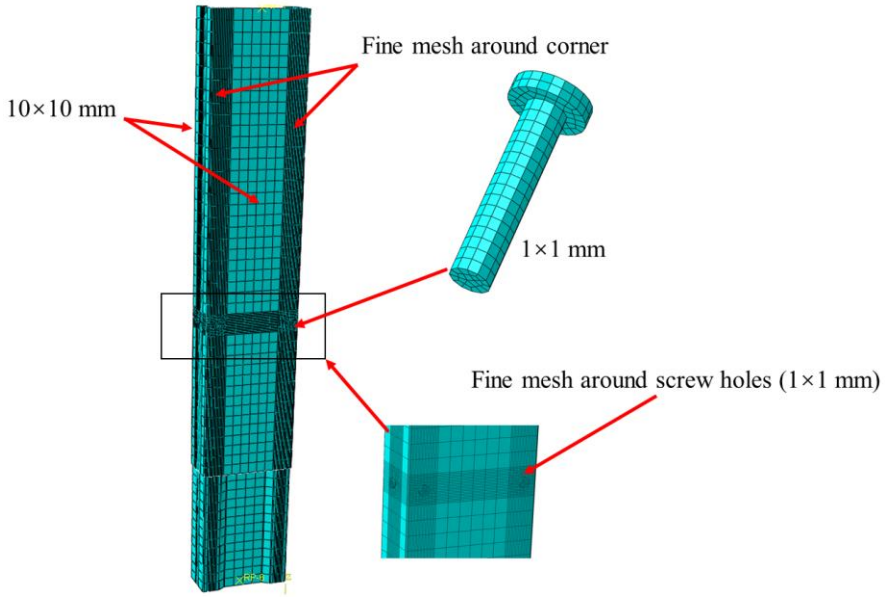

(a) FE meshing

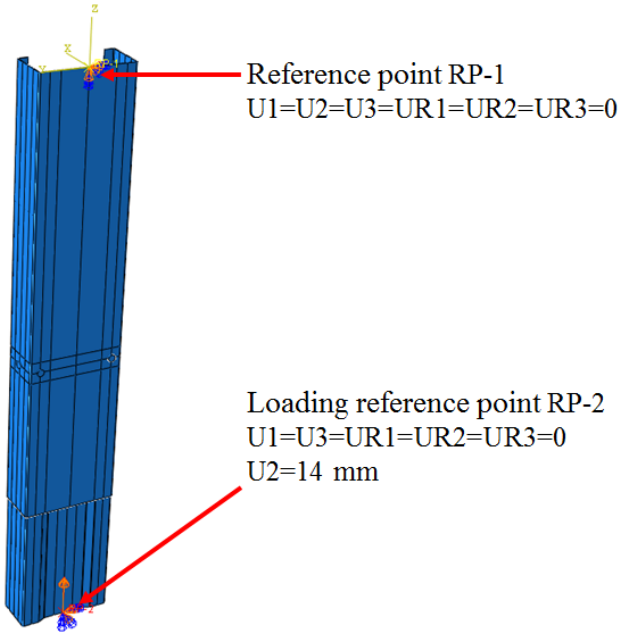

(b) Boundary conditions

Figure 6-16 Details of the FE model

The interface between the CFS plain and sigma channel sections was modelled by employing surface-to-surface contact, available in ABAQUS. The discretization method employed the node-to-surface approach for the interface between the channels and screws. The hard contact property was used to avoid the penetration of two contact surfaces. Apart

from the degrees of freedom associated with the direction of loading, all other degrees of freedom were constrained at the bottom reference point. A vertical displacement was applied to the bottom reference point. The boundary conditions used in the FE model are depicted in Figure 6-16 (b).

6.3.2. Validation of FE model

Table 6-1 summarises the ultimate shear strengths obtained from the test (P_{Exp}) and FEA (P_{FEA}) for all telescopic stud connections. The average values of P_{Exp}/ P_{FEA} are 1.02 and 1.05 for 0.75- and 1.2-mm specimens, respectively, with COVs of 0.04 and 0.07. The comparison of the load-displacement curves of tests and FEA is shown in Figure 6-17. The initial stiffness observed in the FEA results exceeded that of the test results. This difference can be attributed to the presence of initial slip between the CFS channel sections and screws. In contrast, the FEA modelling assumed idealized boundary conditions and interactions. Figure 6-18 compares the failure modes of the test and FEA, and the failure modes of combined tilting and bearing were observed in both. Overall, good agreement in terms of shear strengths and failure modes is shown between tests and FEA.

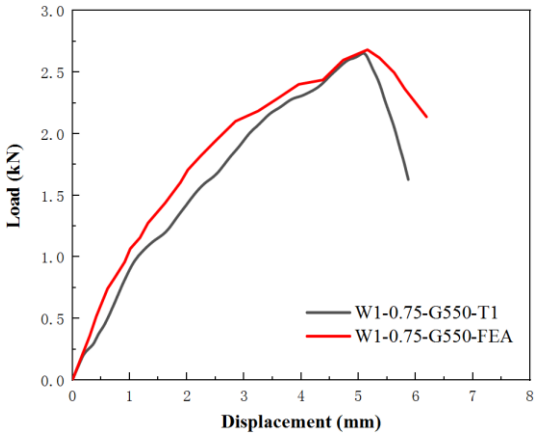

(a) W1-0.75-G550

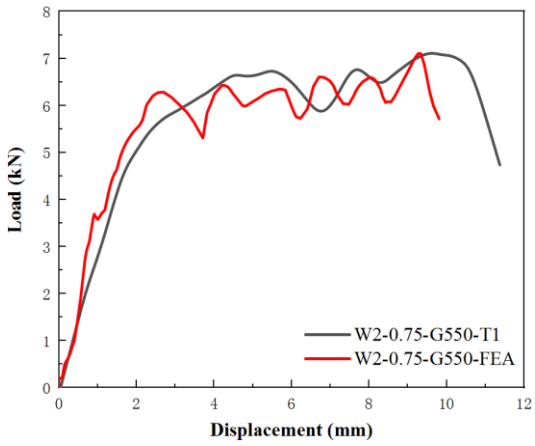

(b) W2-0.75-G550

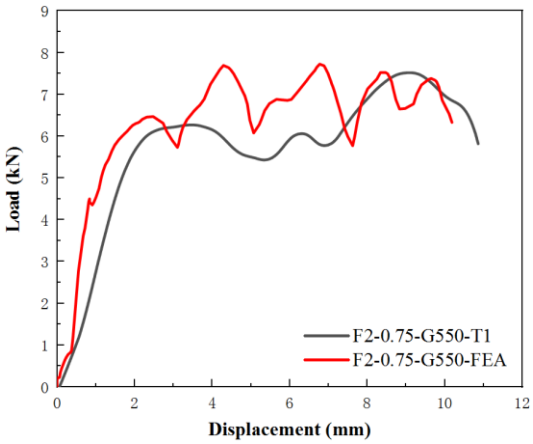

(c) F2-0.75-G550

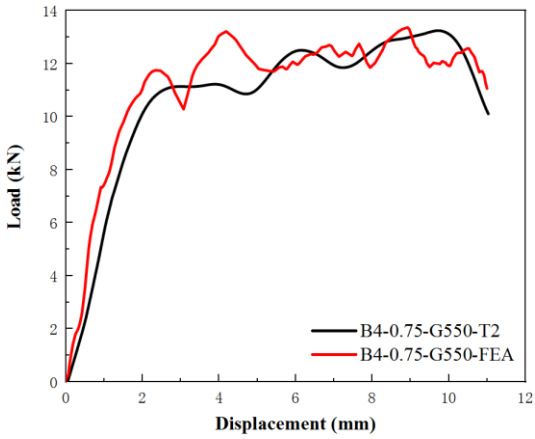

(d) B4-0.75-G550

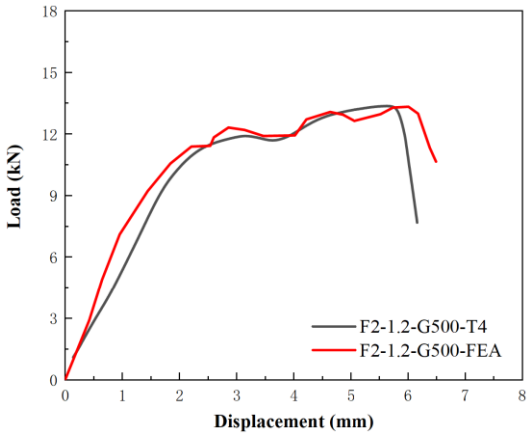

(e) F2-1.2-G500

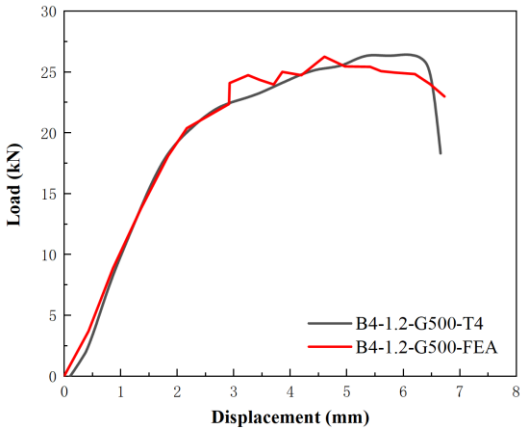

(f) B4-1.2-G500

Figure 6-17 Comparison of load-displacement curves obtained from the tests and FEA

(i) Experiment

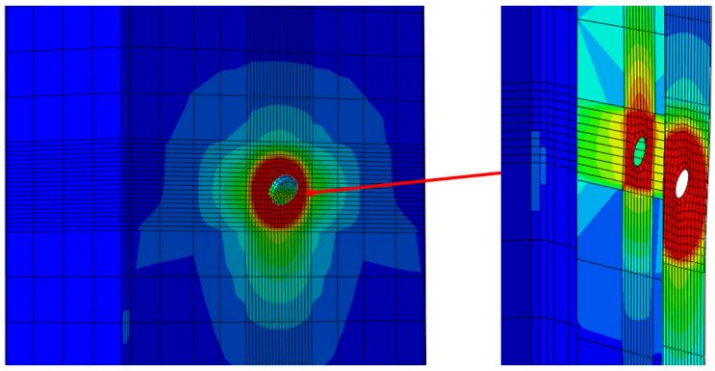

(ii) FEA

(a) W1-0.75-G550-T1

(i) Experiment

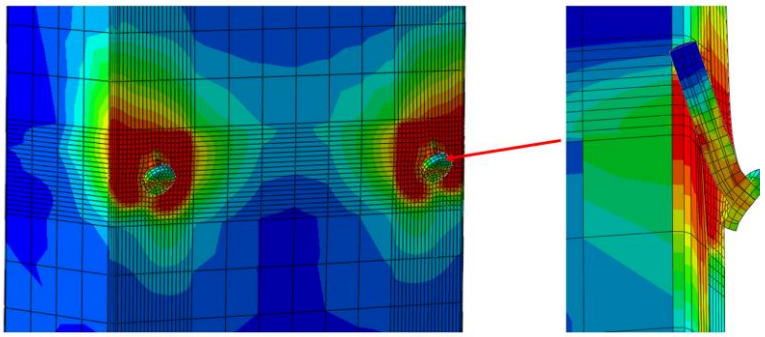

(ii) FEA

(b) W2-0.75-G550-T1

(i) Experiment

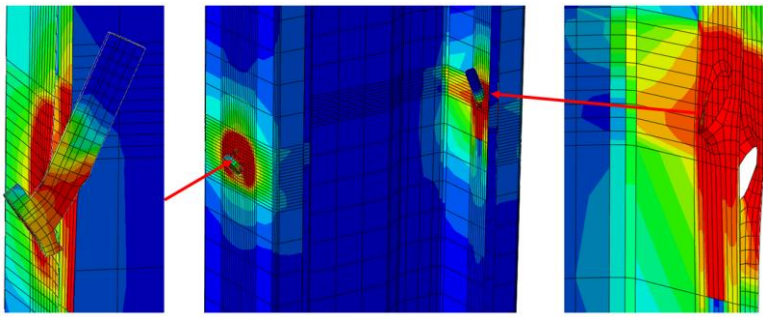

(ii) FEA

(c) F2-0.75-G550-T1

(i)Experiment

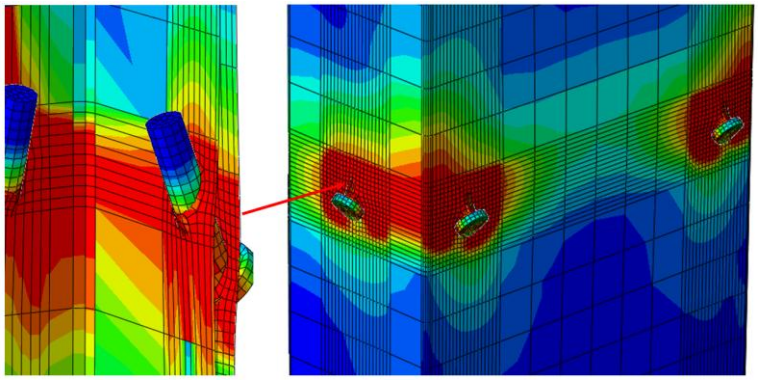

(ii) FEA

(d) B4-0.75-G550-T1

Figure 6-18 Failure modes of the specimens obtained from the experiments and FEA

6.4. Design procedure

6.4.1. Current design provisions

The design procedures outlined in design standards such as AISI (2016), AS/NZS (2018), Eurocode 3, BS5950-5, and GB50018 provide guidelines for determining the connection strengths of single screws. For multiple-screw connections, the shear strengths are obtained by multiplying the design strength of individual screws by the respective number of screws. Notably, the group effect (LaBoube et al. 2002), which refers to the collective influence of multiple screws, was not taken into consideration in this chapter due to the considerable spacing between screws in the telescopic stud connections. This chapter modifies some symbol nomenclature in some design equations of the AISI (2016).

6.4.2. Comparison of test and FEA results with the design strengths

The ultimate connection strengths of telescopic studs obtained from the tests and FEA were compared to the design strengths calculated by the design rules of current design standards. The comparison results are shown in Table 6-4 and in Figure 6-19. For specimens with screw layout S1, the connection strengths could be determined by Eurocode 3 and BS5950-5, and the mean values of P_{Exp}/P_{pred} are 0.96 and 0.94 with COVs of 0.16 and 0.14 for the results of tests and FEA, respectively. The AISI (2016), AS/NZS (2018), and GB50018 overestimate the design strengths of CFS telescopic stud connections, by up to 35%. The comparison of results for specimens with screw layouts S2, S3, and S4 reveals that the calculated ultimate design strengths, as per the AISI (2016) and AS/NZS (2018) design standards, demonstrate a conservative range of 1-13% for the test results and 4-10% for the FEA results.

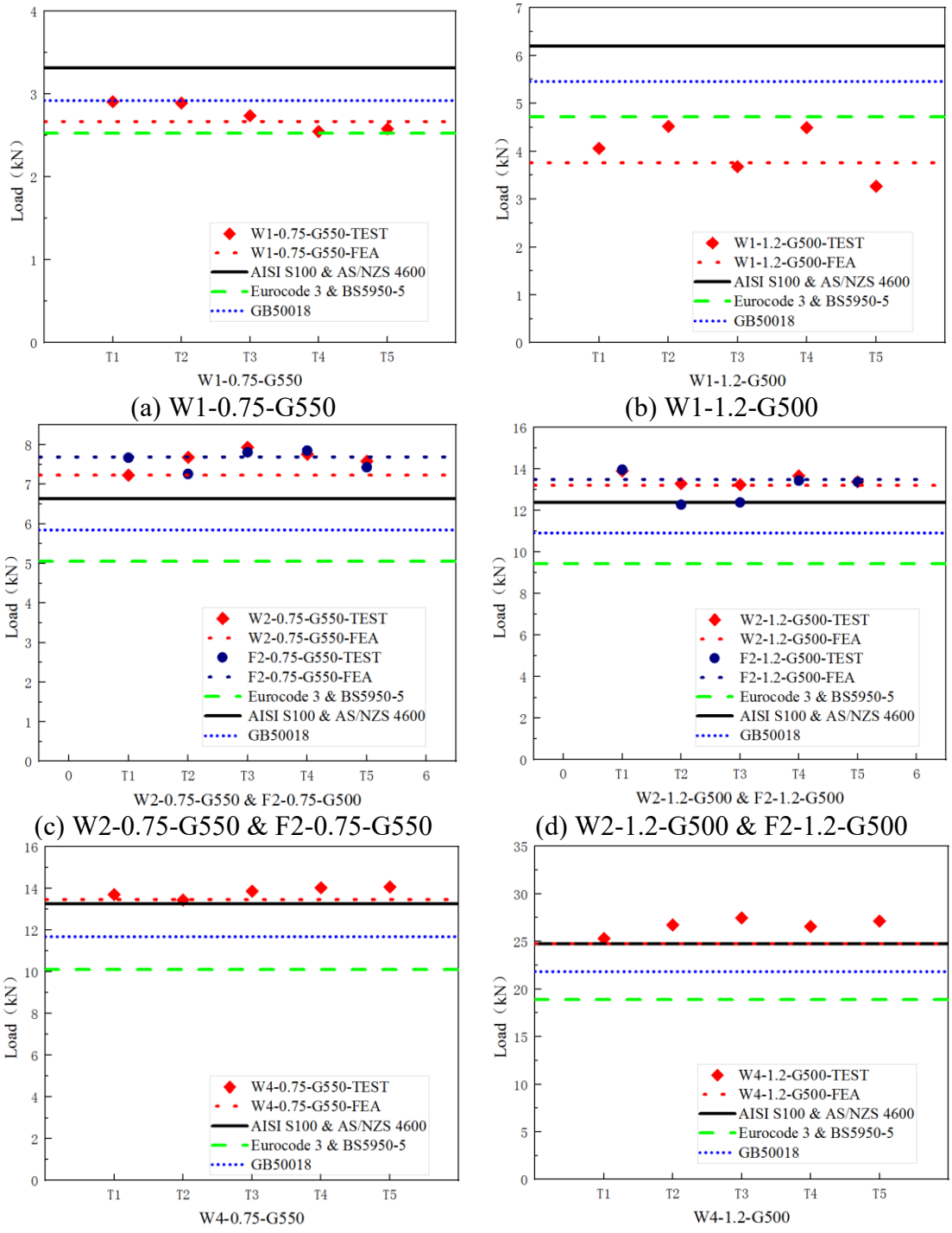

(a) W1-0.75-G550 (b) W1-1.2-G500

(c) W2-0.75-G550 & F2-0.75-G550 (d) W2-1.2-G500 & F2-1.2-G500

(e) W4-0.75-G550 (f) W4-1.2-G500

Figure 6-19 Comparison of design strengths with the experimental and FEA strengths

Table 6-4 Comparison of experimental and FEA results with design prediction

Specimens	P_{Exp} kN	P_{FEA} kN	AISI&AS/NZS			E3&BS-5			GB50018		
			P_{pred} kN	P_{Exp} /P_{pred}	P_{FEA} /P_{pred}	P_{pred} kN	P_{Exp} /P_{pred}	P_{FEA} /P_{pred}	P_{pred} kN	P_{Exp} /P_{pred}	P_{FEA} /P_{pred}
W1-0.75-G550-T1	2.91	2.68	3.31	0.88	0.81	2.53	1.15	1.06	2.92	1.00	0.92
W1-0.75-G550-T2	2.89	2.68	3.31	0.87	0.81	2.53	1.14	1.06	2.92	0.99	0.92
W1-0.75-G550-T3	2.74	2.68	3.31	0.83	0.81	2.53	1.08	1.06	2.92	0.94	0.92

W1-0.75-G550-T4	2.55	2.68	3.31	0.77	0.81	2.53	1.01	1.06	2.92	0.87	0.92
W1-0.75-G550-T5	2.58	2.68	3.31	0.78	0.81	2.53	1.02	1.06	2.92	0.88	0.92
W1-1.2-G500-T1	4.06	3.76	6.20	0.65	0.61	4.72	0.86	0.80	5.46	0.74	0.69
W1-1.2-G500-T2	4.52	3.76	6.20	0.73	0.61	4.72	0.96	0.80	5.46	0.83	0.69
W1-1.2-G500-T3	3.68	3.76	6.20	0.59	0.61	4.72	0.78	0.80	5.46	0.67	0.69
W1-1.2-G500-T4	4.49	3.76	6.20	0.72	0.61	4.72	0.95	0.80	5.46	0.82	0.69
W1-1.2-G500-T5	3.27	3.76	6.20	0.53	0.61	4.72	0.69	0.80	5.46	0.60	0.69
Mean				0.68	0.71		0.96	0.928		0.83	0.80
COV				0.17	0.15		0.16	0.15		0.16	0.15
W2-0.75-G550-T1	7.23	7.23	6.63	1.09	1.09	5.05	1.43	1.43	5.84	1.24	1.24
W2-0.75-G550-T2	7.68	7.23	6.63	1.16	1.09	5.05	1.52	1.43	5.84	1.32	1.24
W2-0.75-G550-T3	7.93	7.23	6.63	1.20	1.09	5.05	1.57	1.43	5.84	1.36	1.24
W2-0.75-G550-T4	7.76	7.23	6.63	1.17	1.09	5.05	1.54	1.43	5.84	1.33	1.24
W2-0.75-G550-T5	7.58	7.23	6.63	1.14	1.09	5.05	1.50	1.43	5.84	1.30	1.24
W2-1.2-G500-T1	13.91	13.21	12.40	1.12	1.07	9.44	1.47	1.40	10.92	1.27	1.21
W2-1.2-G500-T2	13.30	13.21	12.40	1.07	1.07	9.44	1.41	1.40	10.92	1.22	1.21
W2-1.2-G500-T3	13.24	13.21	12.40	1.07	1.07	9.44	1.40	1.40	10.92	1.21	1.21
W2-1.2-G500-T4	13.67	13.21	12.40	1.10	1.07	9.44	1.45	1.40	10.92	1.25	1.21
W2-1.2-G500-T5	13.38	13.21	12.40	1.08	1.07	9.44	1.42	1.40	10.92	1.23	1.21
F2-0.75-G550-T1	7.67	7.69	6.63	1.16	1.16	5.05	1.52	1.52	5.84	1.31	1.32
F2-0.75-G550-T2	7.26	7.69	6.63	1.10	1.16	5.05	1.44	1.52	5.84	1.24	1.32
F2-0.75-G550-T3	7.81	7.69	6.63	1.18	1.16	5.05	1.55	1.52	5.84	1.34	1.32
F2-0.75-G550-T4	7.85	7.69	6.63	1.18	1.16	5.05	1.55	1.52	5.84	1.34	1.32
F2-0.75-G550-T5	7.43	7.69	6.63	1.12	1.16	5.05	1.47	1.52	5.84	1.27	1.32
F2-1.2-G500-T1	13.97	12.49	12.40	1.13	1.01	9.44	1.48	1.32	10.92	1.28	1.14
F2-1.2-G500-T2	12.28	12.49	12.40	0.99	1.01	9.44	1.30	1.32	10.92	1.12	1.14
F2-1.2-G500-T3	12.39	12.49	12.40	1.00	1.01	9.44	1.31	1.32	10.92	1.13	1.14
F2-1.2-G500-T4	13.44	12.49	12.40	1.08	1.01	9.44	1.42	1.32	10.92	1.23	1.14
F2-1.2-G500-T5	13.38	12.49	12.40	1.08	1.01	9.44	1.42	1.32	10.92	1.23	1.14
B4-0.75-G550-T1	13.71	13.47	13.27	1.03	1.02	10.11	1.36	1.33	11.69	1.17	1.15
B4-0.75-G550-T2	13.44	13.47	13.27	1.01	1.02	10.11	1.33	1.33	11.69	1.15	1.15
B4-0.75-G550-T3	13.87	13.47	13.27	1.05	1.02	10.11	1.37	1.33	11.69	1.19	1.15
B4-0.75-G550-T4	14.03	13.47	13.27	1.06	1.02	10.11	1.39	1.33	11.69	1.20	1.15
B4-0.75-G550-T5	14.07	13.47	13.27	1.06	1.02	10.11	1.39	1.33	11.69	1.20	1.15
B4-1.2-G500-T1	25.31	24.79	24.79	1.02	1.00	18.89	1.34	1.31	21.84	1.16	1.14
B4-1.2-G500-T2	26.74	24.79	24.79	1.08	1.00	18.89	1.42	1.31	21.84	1.22	1.14
B4-1.2-G500-T3	27.45	24.79	24.79	1.11	1.00	18.89	1.45	1.31	21.84	1.26	1.14
B4-1.2-G500-T4	26.56	24.79	24.79	1.07	1.00	18.89	1.41	1.31	21.84	1.22	1.14
B4-1.2-G500-T5	27.15	24.79	24.79	1.10	1.00	18.89	1.44	1.31	21.84	1.24	1.14
Mean				1.09	1.06		1.44	1.39		1.24	1.20
COV				0.05	0.05		0.05	0.05		0.05	0.05

6.5. Summary

In this chapter, a comprehensive experimental and numerical study was carried out to investigate the connection strengths of telescopic studs under compression. A total of 40 specimens were tested, considering variations in screw configurations, steel grades, and sectional thicknesses. Experimental results showed that the screw tilting throughout the loading procedure was accompanied by contact separation between the CFS plain and sigma channel sections near the screw holes, and all specimens failed under combined

tilting and bearing failure modes. No curling effect of screws was found in the current study.

Compared with the single-screw connections with a gap in the middle of the web, telescopic stud connections with 2 screws in the web, 2 screws in the flanges, and 4 screws in both the web and flanges had around 35-77% higher strengths of single-screw connections. Therefore, screw connections without a gap will exhibit greater adaptability for such telescopic stud systems. Engineers or researchers can use the screw layouts developed in this chapter and determine the number of screws based on the structural needs and strength requirements.

A nonlinear explicit dynamic FE model was then developed and validated against the test results, demonstrating good agreement in terms of connection strengths and failure modes. The test and FEA results were compared with the design strengths calculated by the AISI (2016), AS/NZS (2018), Eurocode 3 (2006), BS5950-5 (1998), and GB50018 (2002). The comparison results showed that AISI (2016) and AS/NZS (2018) are conservative by 1-13%, when predicting the connection strengths of telescopic studs with different screw layouts. For the telescopic stud connections with a gap in the middle of the web, the connection strength could be predicted by Eurocode 3 (2006) and BS5950-5 (1998).

Chapter 7 CFS swaged section under axial compression

7.1. Introductory remarks

CFS columns are widely used in light-gauge steel structures as primary load-bearing members subjected to axial compression. In practical applications, geometric modifications such as swaged sections are sometimes introduced in CFS members to facilitate connections or improve structural detailing. A swaged section locally modifies the cross-sectional geometry of the member, which may influence its stiffness, stress distribution, and buckling behaviour under axial compression. However, the structural performance and design implications of CFS columns containing swaged sections have not been thoroughly investigated.

This chapter reports a total of 101 experimental results on the axial behaviour of CFS columns having a swaged section at the end or in the middle of channels under a fixed-fixed boundary. CFS columns with five different stud lengths and three different cross-sections were tested. A comparison between the experimental results and DSM predictions from the AISI (2016) and AS/NZS (2018) was conducted, indicating that the DSM is un-conservative by approximately 1.4% on average while predicting the axial capacities of CFS columns having a swaged section.

7.2. Experimental Investigation

7.2.1. Test specimens

A total of 101 compression tests were conducted. Five different specimen lengths (150 mm, 300 mm, 1000 mm, 1200 mm, and 1400 mm) and three different cross-sections (see Figure 7-1) with 2 different thicknesses (0.75 mm and 0.95 mm) were adopted in this study. As mentioned previously, CFS columns having a swaged section at the end and in

the middle of the channels were considered in this chapter. Table 7-1 illustrates the specimen details, and the specimen labelling is shown in Figure 7-2.

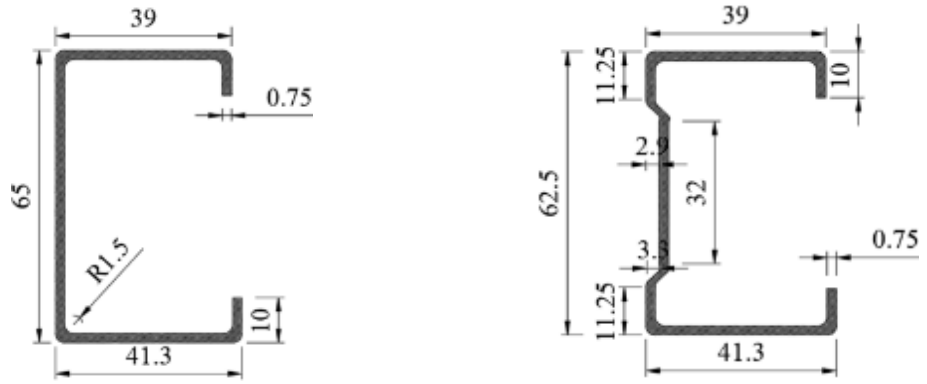

(i) Plain section (ii) Swaged section at the end or in the middle

(a) 65×41.3×0.75 mm

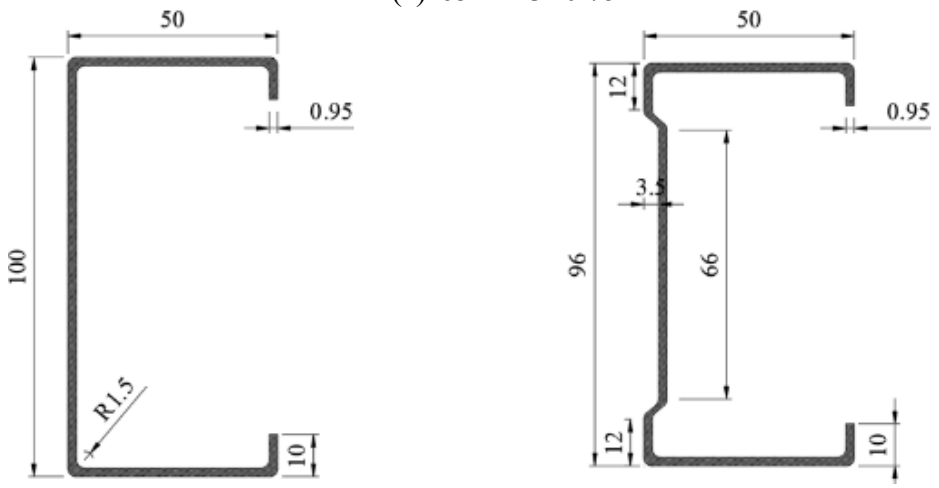

(i) Plain section (ii) Swaged section at the end or in the middle

(b) 100×50×0.95 mm

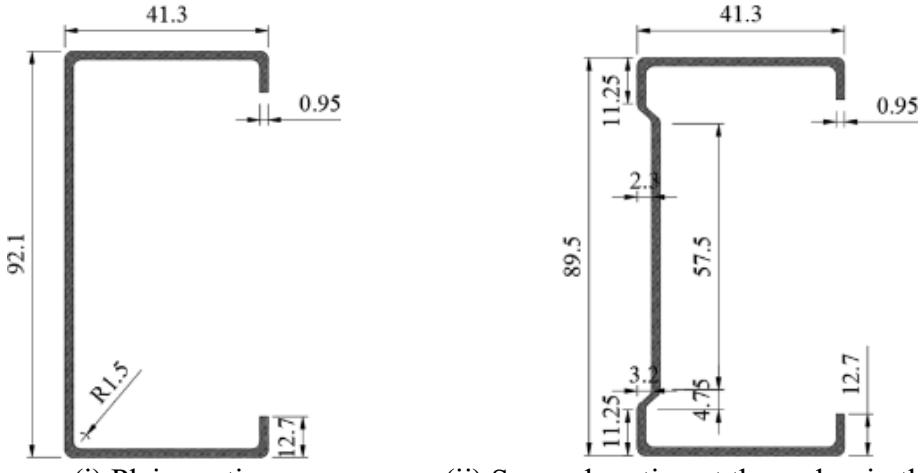

(i) Plain section (ii) Swaged section at the end or in the middle

(c) 92.1×41.3×0.95 mm

Figure 7-1 Nominal dimensions of investigated CFS channel sections (all dimensions are in mm)

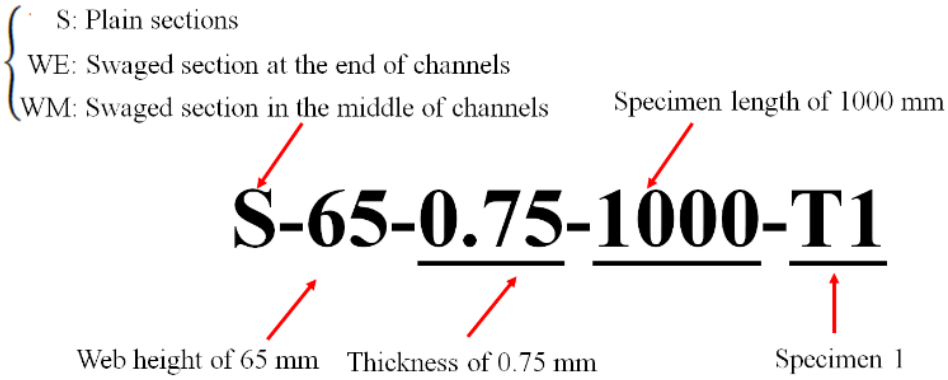

Figure 7-2 Specimen labelling

Table 7-1 Details of the test specimens and failure loads

(a) For CFS channel section: 65 × 41.3 × 0.75 mm

Specimen ID	Nominal Length L (mm)	Nominal thickness t (mm)	Swaging location	Failure modes	Ultimate load P_{Exp} (kN)	Mean value P_{Exp} (kN)
Plain section						
S-65-0.75-150-T1	150	0.75	-	L	33.41	
S-65-0.75-150-T2	150	0.75	-	L	33.16	
S-65-0.75-150-T3	150	0.75	-	L	32.88	33.23
S-65-0.75-150-T4	150	0.75	-	L	33.00	
S-65-0.75-150-T5	150	0.75	-	L	33.14	
S-65-0.75-150-T6	150	0.75	-	L	33.78	
S-65-0.75-1000-T1	1000	0.75	-	L + D + F	27.75	
S-65-0.75-1000-T2	1000	0.75	-	L + D + F	27.66	
S-65-0.75-1000-T3	1000	0.75	-	L + D + F	28.25	27.74
S-65-0.75-1000-T4	1000	0.75	-	L + D + F	27.97	
S-65-0.75-1000-T5	1000	0.75	-	L + D + F	27.06	
S-65-0.75-1200-T1	1200	0.75	-	D + F	27.02	
S-65-0.75-1200-T2	1200	0.75	-	L + D + F	26.76	
S-65-0.75-1200-T3	1200	0.75	-	L + D + F	26.94	
S-65-0.75-1200-T4	1200	0.75	-	L + D + F	27.99	26.84
S-65-0.75-1200-T5	1200	0.75	-	D + F	26.23	
S-65-0.75-1200-T6	1200	0.75	-	D + F	26.14	
S-65-0.75-1200-T7	1200	0.75	-	D + F	26.78	
S-65-0.75-1400-T1	1400	0.75	-	D + F	24.31	
S-65-0.75-1400-T2	1400	0.75	-	D + F	23.15	
S-65-0.75-1400-T3	1400	0.75	-	D + F	25.34	24.08
S-65-0.75-1400-T4	1400	0.75	-	D + F	23.92	
S-65-0.75-1400-T5	1400	0.75	-	D + F	23.70	
Swaged section						
WE-65-0.75-150-T1	150	0.75	End	L	31.92	
WE-65-0.75-150-T2	150	0.75	End	L	31.65	
WE-65-0.75-150-T3	150	0.75	End	L	31.85	31.93
WE-65-0.75-150-T4	150	0.75	End	L	32.10	
WE-65-0.75-150-T5	150	0.75	End	L	32.23	
WE-65-0.75-150-T6	150	0.75	End	L	31.81	
WM-65-0.75-1000-T1	1000	0.75	Middle	L + D + F	25.69	
WM-65-0.75-1000-T2	1000	0.75	Middle	L + D + F	25.54	
WM-65-0.75-1000-T3	1000	0.75	Middle	L + D + F	26.32	26.15
WM-65-0.75-1000-T4	1000	0.75	Middle	L + D + F	26.76	
WM-65-0.75-1000-T5	1000	0.75	Middle	L + D + F	26.46	

WM-65-0.75-1200-T1	1200	0.75	Middle	L + D + F	24.64	
WM-65-0.75-1200-T2	1200	0.75	Middle	L + D + F	24.51	
WM-65-0.75-1200-T3	1200	0.75	Middle	L + D + F	24.54	
WM-65-0.75-1200-T4	1200	0.75	Middle	L + D + F	24.40	24.56
WM-65-0.75-1200-T5	1200	0.75	Middle	L + D + F	24.69	
WM-65-0.75-1200-T6	1200	0.75	Middle	L + D + F	24.82	
WM-65-0.75-1200-T7	1200	0.75	Middle	L + D + F	24.34	
WM-65-0.75-1400-T1	1400	0.75	Middle	D + F	23.43	
WM-65-0.75-1400-T2	1400	0.75	Middle	D + F	22.84	
WM-65-0.75-1400-T3	1400	0.75	Middle	D + F	23.32	23.15
WM-65-0.75-1400-T4	1400	0.75	Middle	D + F	23.17	
WM-65-0.75-1400-T5	1400	0.75	Middle	D	23.00	

(b) For CFS channel section: 100 × 50 × 0.95 mm

Specimen ID	Nominal Length L (mm)	Nominal thickness t (mm)	Swaging location	Failure modes	Ultimate load P_{Exp} (kN)	Mean value $\overline{P_{Exp}}$ (Kn)
Plain section						
S-100-0.95-150-T1	150	0.95	-	L	57.25	
S-100-0.95-150-T2	150	0.95	-	L	57.26	
S-100-0.95-150-T3	150	0.95	-	L	57.58	57.45
S-100-0.95-150-T4	150	0.95	-	L	57.48	
S-100-0.95-150-T5	150	0.95	-	L	57.67	
S-100-0.95-1000-T1	1000	0.95	-	L + D + F	45.76	
S-100-0.95-1000-T2	1000	0.95	-	L + D + F	44.40	
S-100-0.95-1000-T3	1000	0.95	-	L + D + F	46.76	45.38
S-100-0.95-1000-T4	1000	0.95	-	L + D + F	44.86	
S-100-0.95-1000-T5	1000	0.95	-	L + D + F	45.14	
S-100-0.95-1200-T1	1200	0.95	-	L + D + F	43.06	
S-100-0.95-1200-T2	1200	0.95	-	L + D + F	43.06	
S-100-0.95-1200-T3	1200	0.95	-	L + D + F	42.91	42.73
S-100-0.95-1200-T4	1200	0.95	-	L + D + F	42.10	
S-100-0.95-1200-T5	1200	0.95	-	L + D + F	42.54	
S-100-0.95-1400-T1	1400	0.95	-	D + F	42.18	
S-100-0.95-1400-T2	1400	0.95	-	D + F	41.15	
S-100-0.95-1400-T3	1400	0.95	-	D + F	41.31	41.41
S-100-0.95-1400-T4	1400	0.95	-	D + F	41.07	
S-100-0.95-1400-T5	1400	0.95	-	D + F	41.37	
Swaged section						
WE-100-0.95-150-T1	150	0.95	End	L	51.06	
WE-100-0.95-150-T2	150	0.95	End	L	51.22	
WE-100-0.95-150-T3	150	0.95	End	L	51.14	51.06
WE-100-0.95-150-T4	150	0.95	End	L	50.93	
WE-100-0.95-150-T5	150	0.95	End	L	50.95	
WM-100-0.95-1000-T1	1000	0.95	Middle	L + D + F	43.66	
WM-100-0.95-1000-T2	1000	0.95	Middle	L + D + F	43.51	
WM-100-0.95-1000-T3	1000	0.95	Middle	L + D + F	44.08	43.90
WM-100-0.95-1000-T4	1000	0.95	Middle	L + D + F	43.86	
WM-100-0.95-1000-T5	1000	0.95	Middle	L + D + F	44.38	
WM-100-0.95-1200-T1	1200	0.95	Middle	L + D + F	41.98	
WM-100-0.95-1200-T2	1200	0.95	Middle	L + D + F	41.70	
WM-100-0.95-1200-T3	1200	0.95	Middle	L + D + F	41.30	41.66
WM-100-0.95-1200-T4	1200	0.95	Middle	L + D + F	41.51	
WM-100-0.95-1200-T5	1200	0.95	Middle	L + D + F	41.79	
WM-100-0.95-1400-1	1400	0.95	Middle	D + F	41.87	
WM-100-0.95-1400-2	1400	0.95	Middle	D + F	41.32	41.87
WM-100-0.95-1400-3	1400	0.95	Middle	D + F	42.61	

WM-100-0.95-1400-4	1400	0.95	Middle	D + F	41.93	
WM-100-0.95-1400-5	1400	0.95	Middle	D + F	41.62	

(c) For CFS channel section: 92.1 × 41.3 × 0.95 mm

Specimen ID	Nominal Length L (mm)	Nominal thickness t (mm)	Swaging location	Failure modes	Ultimate load P_{Exp} (kN)	Mean value $\overline{P_{Exp}}$ (kN)
Plain section						
S-92.1-0.95-300-T1	300	0.95	-	L	58.11	
S-92.1-0.95-300-T2	300	0.95	-	L	58.22	
S-92.1-0.95-300-T3	300	0.95	-	L	59.23	58.82
S-92.1-0.95-300-T4	300	0.95	-	L	58.80	
S-92.1-0.95-300-T5	300	0.95	-	L	59.74	
Swaged section						
WE-92.1-0.95-300-T1	300	0.95	End	L + D	55.01	
WE-92.1-0.95-300-T2	300	0.95	End	L + D	54.87	
WE-92.1-0.95-300-T3	300	0.95	End	L + D	56.18	55.05
WE-92.1-0.95-300-T4	300	0.95	End	L + D	54.62	
WE-92.1-0.95-300-T5	300	0.95	End	L + D	54.61	
WM-92.1-0.95-300-T1	300	0.95	Middle	L + D	57.90	
WM-92.1-0.95-300-T2	300	0.95	Middle	L + D	57.78	
WM-92.1-0.95-300-T3	300	0.95	Middle	L + D	57.88	57.65
WM-92.1-0.95-300-T4	300	0.95	Middle	L + D	57.99	
WM-92.1-0.95-300-T5	300	0.95	Middle	L + D	56.70	

Notes: L, D, and F represent local, distortional, and flexural-torsional buckling, respectively.

7.2.2. Material testing

In the current study, three different cross-sections were used, and their material properties were obtained by performing tensile coupon tests. All coupons were tested following the guidelines outlined in EN ISO 6892-1:2019. A total of three sets of coupons were longitudinally cut from the web plates of the untested specimens. The tensile coupon tests were conducted on a 100 kN Instron machine (see Figure 7-3) at a loading rate of 0.05 mm/min. The average yield ($\sigma_{0.2}$) and ultimate strengths (σ_u) of three sets of coupons are summarised in Table 7-2, and their failure modes and full stress-strain curves are depicted in Figures 7-4 and 7-5. In Table 7-2, the coupons are labelled based on the web height. For example, the number "65" on the label "C65-1" is the web height of section 65 × 41.3 × 0.75 mm.

Figure 7-3 Setup of tensile coupon tests

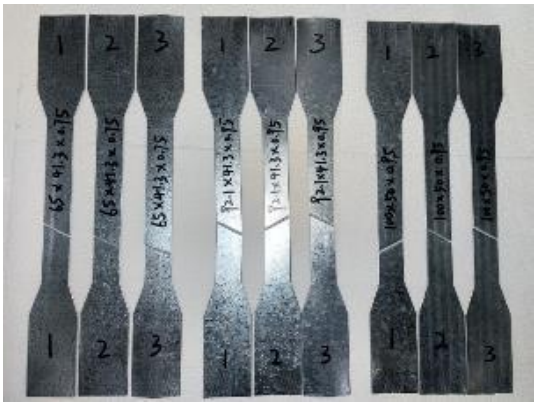

Figure 7-4 Tested tensile coupons

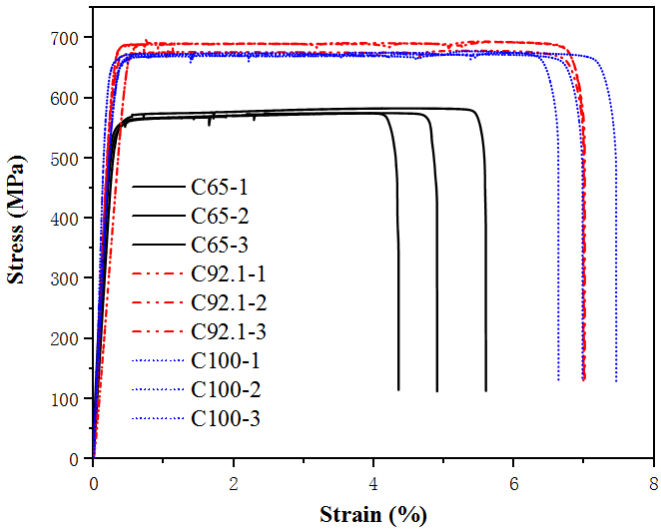

Figure 7-5 Stress-strain curves

Table 7-2 Material properties obtained from the tensile coupon tests

Specimen ID	Thickness t mm	Yield stress $\sigma_{0.2}$ MPa	Ultimate stress σ_u MPa
C65-1	0.78	566.20	574.76
C65-2	0.78	565.61	574.60
C65-3	0.77	573.89	582.68
Mean	0.78	568.57	577.35
COV	0.007	0.008	0.008
C92.1-1	0.97	690.15	696.09
C92.1-2	0.97	689.70	692.85
C92.1-3	0.98	676.26	678.54
Mean	0.97	685.37	689.16
COV	0.006	0.012	0.014
C100-1	0.97	671.37	674.81
C100-2	0.95	673.18	677.61
C100-3	0.95	669.13	672.68
Mean	0.96	671.23	675.03
COV	0.012	0.003	0.004

7.2.3. Testing-rig and loading procedure

A 200 kN Instron machine was used to perform the compression tests. The test setup is shown in Figure 7-6. The CFS columns were placed between the crossheads of a compression testing machine and loaded to failure. A displacement-controlled method with a loading rate of 1 mm/min was used to apply the compressive loads. The load through bearing plates was aligned with the geometric centre of the specimens. During the testing, a data collection system was used to periodically record the loads and displacements. Axial deformations and strains were measured using pressure sensors and displacement sensors integrated within the data acquisition system provided with the Instron machine. The previous test results of CFS single channels under axial compression have shown that the location of buckling is often difficult to determine, as it does not strictly occur at the mid-height of the column. Therefore, the current study did not measure lateral deformation but instead investigated buckling failure loads and ultimate axial capacities through extensive experimental tests.

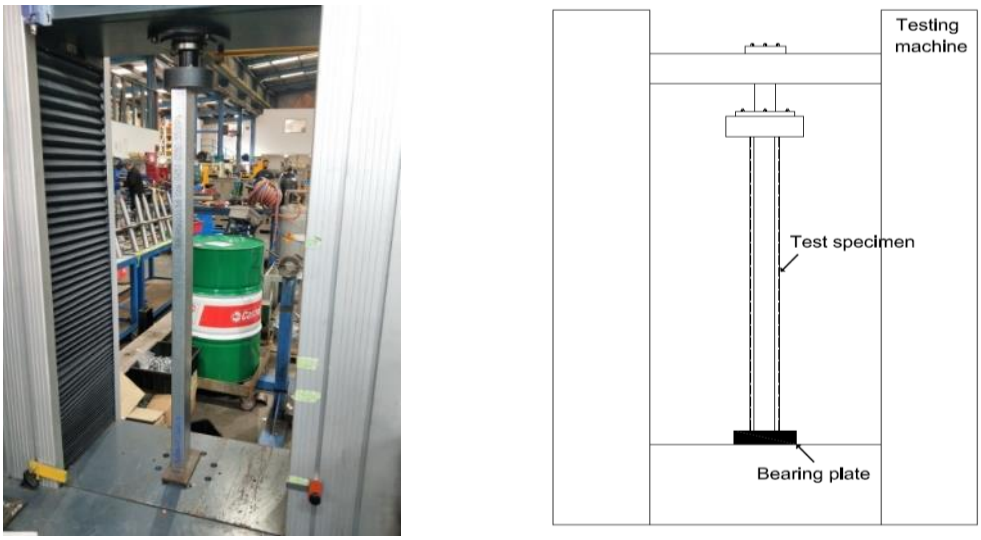

Figure 7-6 Test set-up for the specimen S-65-0.75-1000-T1

7.2.4. Test results and discussions

The structural behaviour of CFS columns having a swaged section was investigated in this study. The ultimate axial capacities and failure modes are summarized in Table 7-1. As the incorporation of swaged sections mainly affects the local buckling capacity, the present study concentrates on short columns, with specimen lengths limited to 1400 mm. For slender columns where global buckling governs the structural response, the influence of the swaged section is nearly insignificant. Further clarification is provided in the following paragraphs.

Figure 7-7 compares the ultimate axial capacities (P_{Exp}) of CFS columns having a swaged section with the axial capacities of plain channel sections. Compared to the CFS plain section, the average axial capacities of specimens having a swaged section are reduced by 5.5% for sections having the cross-section dimensions of 65 × 41.3 × 0.75 mm and 3.9% for sections having the cross-section dimensions of 100 × 50 × 0.95 mm, respectively. It is worth noting from Figure 7-7(c) that the CFS columns having a swaged section at the end of the channels exhibit a lower axial capacity than in the middle of the channels, showing an average reduction of 6.4% and 2.0%, respectively, when compared to the standard channels with the same specimen lengths.

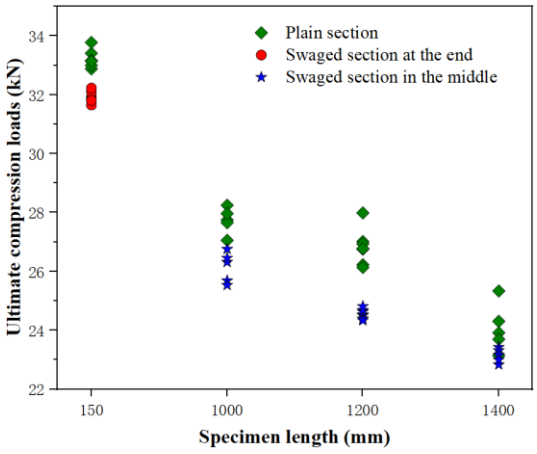

(a) Section 65 × 41.3 × 0.75 mm

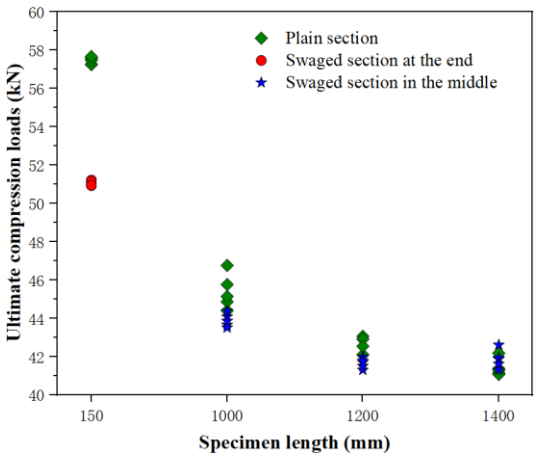

(b) Section 100 × 50 × 0.95 mm

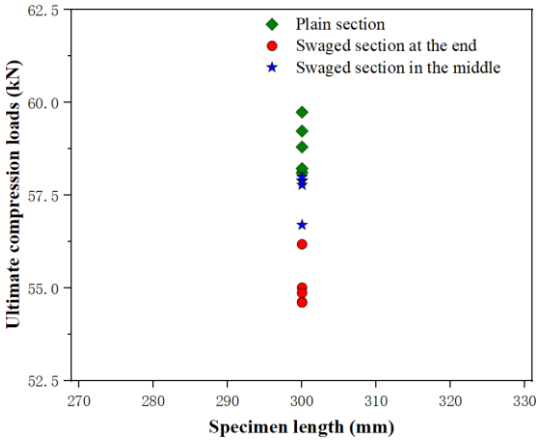

(c) Section 92.1 × 41.3 × 0.95 mm

Figure 7-7 Ultimate axial capacities

The load-displacement curves for all specimens are shown in Figures 7-8, 7-9, and 7-10, and the ultimate loads decrease with the increase of specimen lengths. Moreover, compared to the specimens with the plain section, the axial stiffness and compressive capacities of the CFS channels having a swaged section are lower. From Figure 7-10, when the swaged section is located at either end or in the middle of the channels, both its load-bearing capacity and elastic stiffness experience a certain degree of reduction compared to CFS plain channels. Notably, this reduction is more pronounced when the swaged section is positioned at the end.

For 1000 mm, 1200 mm, and 1400 mm long columns, there is a sudden drop in loads when the ultimate load is reached, and this behaviour indicates that their failure resulted mainly from the global buckling. The long columns having a swaged section demonstrate a slight decrease in elastic stiffness compared to those with a plain section, but not as significant as observed in short columns having a swaged section. This can be attributed to the fact that swaged sections primarily affect local buckling, which has less impact on long columns where global buckling predominates. For the short columns (lengths of 150 mm and 300 mm), their axial capacity-displacement curves declined relatively gradually, following the ultimate loading points. It can be concluded that the main reason for

controlling the global buckling of the specimens is not due to the presence of the swaged section, but rather the specimen lengths.

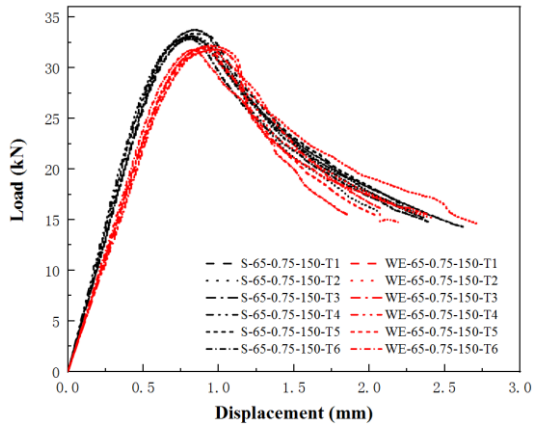

(a)S-65-0.75-150 & WE-65-0.75-150

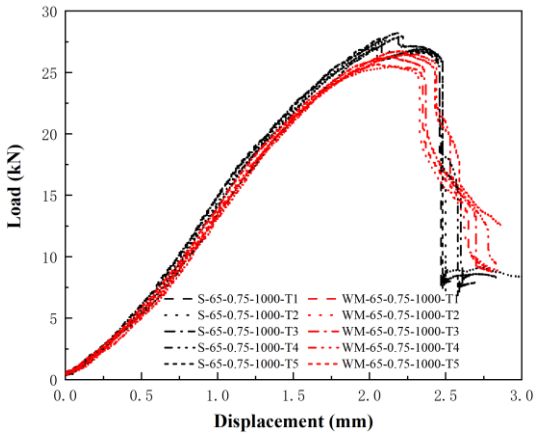

(b)S-65-0.75-1000 & WM-65-0.75-1000

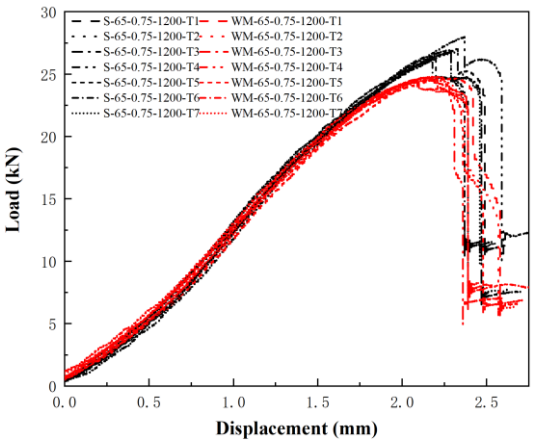

(c)S-65-0.75-1200 & WM-65-0.75-1200

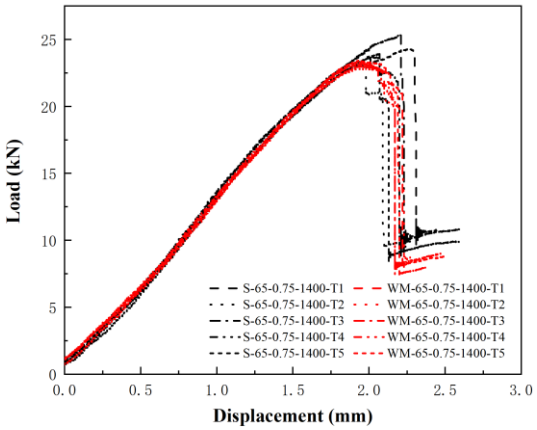

(d)S-65-0.75-1400 & WM-65-0.75-1400

Figure 7-8 Load-displacement curves for CFS columns 65 × 41.3 × 0.75 mm

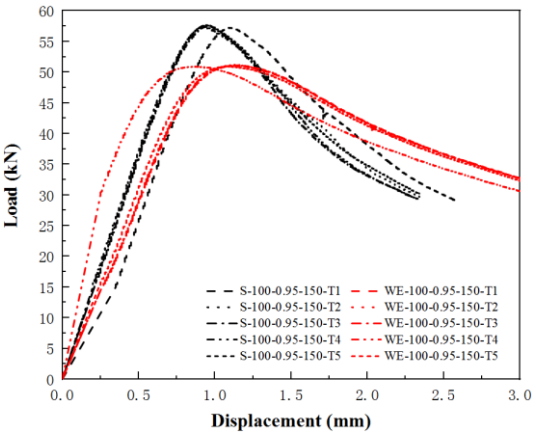

(a)S-100-0.95-150 & WE-100-0.95-150

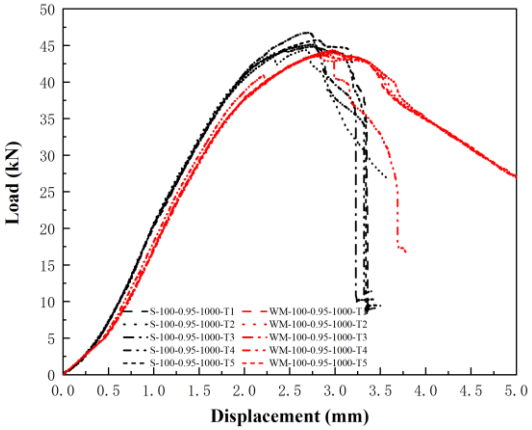

(b)S-100-0.95-1000 & WM-100-0.95-1000

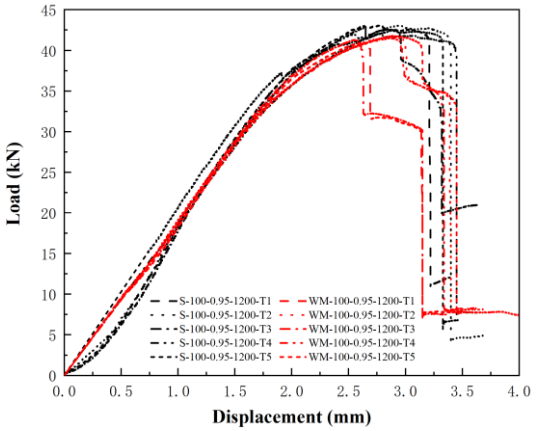

(c)S-100-0.95-1200 & WM-100-0.95-1200

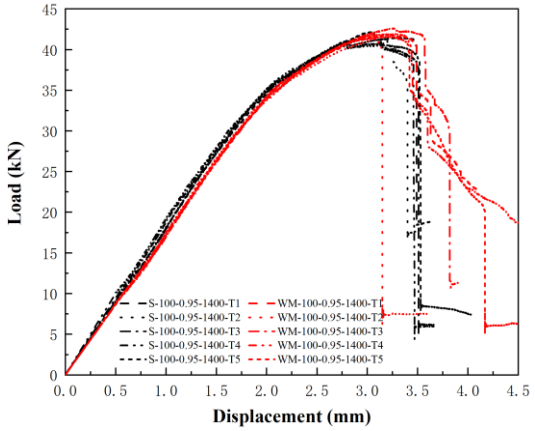

(d)S-100-0.95-1400 & WM-100-0.95-1400

Figure 7-9 Load-displacement curves for CFS columns with section: 100 × 50 × 0.95 mm

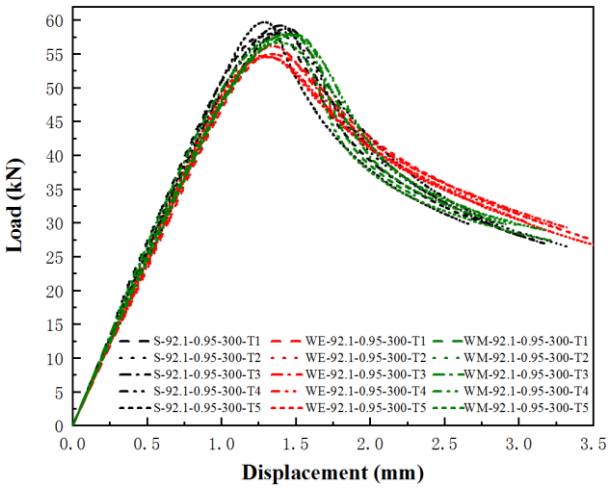

Figure 7-10 Load-displacement curves for CFS columns with section: 92.1 × 41.3 × 0.95 mm

CFS members are normally limited in wall thickness to less than 6mm, which makes them more susceptible to local, distortional, and flexural-torsional buckling, as well as their interactions (Ye et al. 2018). The deformed shapes of sections of 65 × 41.3 × 0.75 mm and 92.1 × 41.3 × 0.95 mm are shown in Figures 7-11 and 7-12, respectively. The failure modes of all specimens are summarized in Table 7-1.

The typical failure mode of short columns (150 mm and 300 mm) is local buckling, and no distortional buckling was visually recorded. For plain channel sections, local buckling occurred in an area near the end of columns, and the buckling half waves appeared along the length of columns. For columns having a swaged section, the local buckling

deformation mainly occurred at the junction of two different cross-sections (see Figures 7-11(a) and 7-12.

For 1000- and 1200-mm long columns, local buckling was initially observed, followed by eventual failure by the interaction of local, distortional, and flexural-torsional buckling. For plain channel columns, the yield lines were in an area near the mid-height (see Figures 7-11(b) and 7-11(d)). For columns having a swaged section, consistent with the failure of short columns, buckling deformation mainly occurred at the junction of two different cross-sections (see Figures 7-11(c) and 7-11(e)). Typical failure modes of long columns (1400 mm) were the interaction of distortional and flexural-torsional buckling, and no local buckling was observed.

It could be concluded that the buckling tends to occur at the junction between the swaged section and the plain section. Due to the special rolling process, the web of the swaged portion is not on the same plane as the web of sections, which increases the likelihood of stress concentration and buckling at the junction between the swaged section and the plain section. This factor likely contributes to the slightly reduced axial capacities.

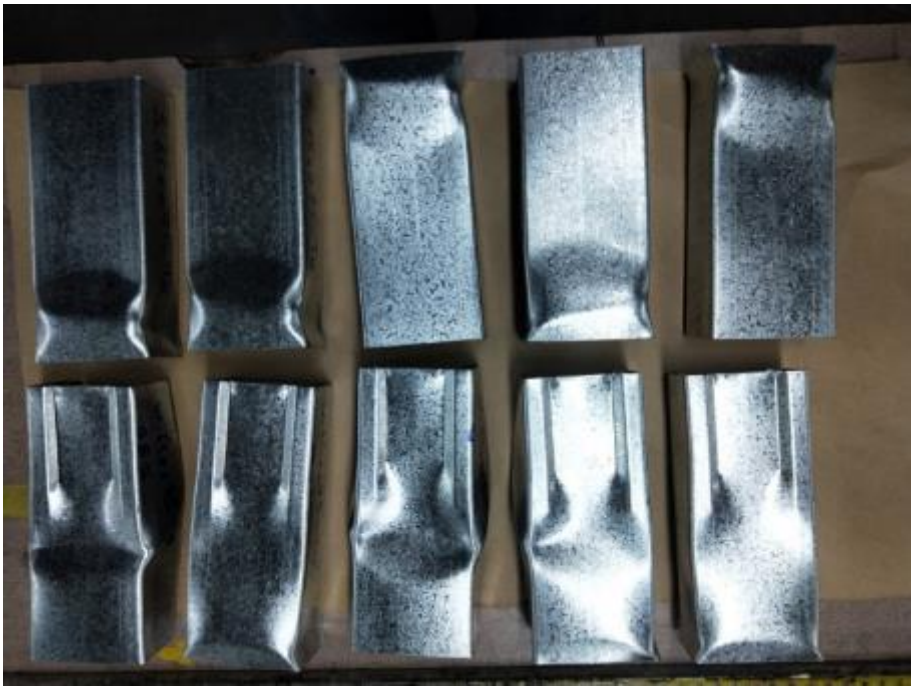

(a)S-65-0.75-150 & WE-65-0.75-150

(b)S-65-0.75-1000

(c)WM-65-0.75-1000

(d)S-65-0.75-1200

(e)WM-65-0.75-1200

(f)S-65-0.75-1400

(g)WM-65-0.75-1400

Figure 7-11 Failure modes of column having the cross-section of 65×41.3×0.75

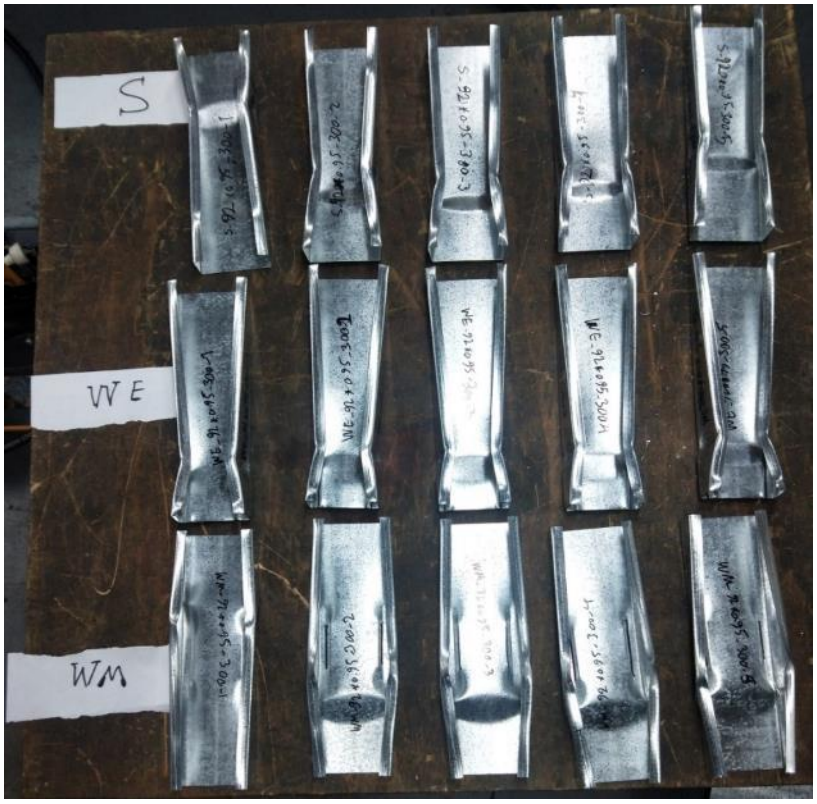

Figure 7-12 Failure modes of column having the cross-section of 92.1×42.3×0.95 mm

7.3. Design procedure

Using the direct strength method (DSM), the design procedures outlined in the design standards of AISI (2016) and AS/NZS (2018), the axial capacity of CFS plain channels can be determined. The axial capacity is the minimum of local buckling (P_{nl}), distortional buckling (P_{nd}), and flexural-torsional buckling (P_{ne}) strengths. The software Constrained and Unconstrained Finite Strip Method (CUFSM) was used to determine the elastic local buckling stress (P_{crl}) and distortional buckling stress (P_{crd}). In this chapter, three different cross-sections were adopted, and their signature curves (see Figure 7-13) were obtained by using CUFSM.

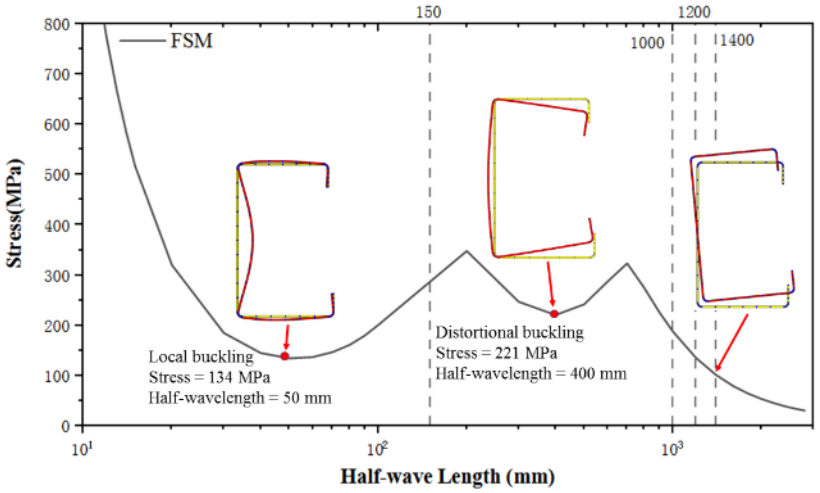

(a) Section: 65 × 41.3 × 0.75 mm

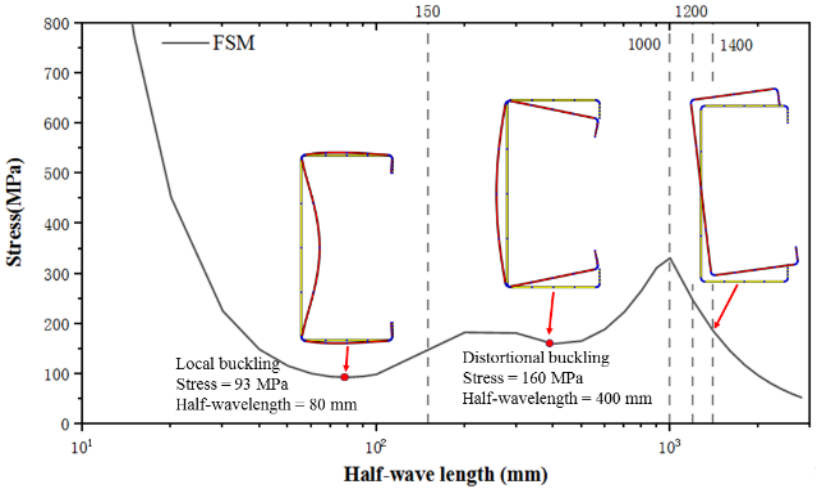

(b) Section:100 × 50 × 0.95 mm

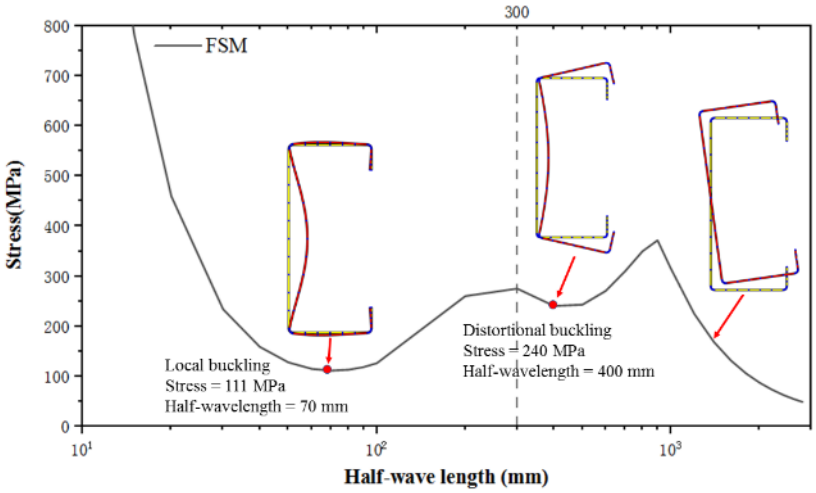

(c) Section: 92.1 × 41.3 × 0.95 mm

Figure 7-13 Signature curves obtained from the CUFSM

The ultimate axial capacities of CFS plain channel columns obtained from the tests were compared to the design strengths calculated by the DSM. The comparison results are shown in Table 7-3, and the mean value of P_{Exp}/P_{DSM} is 1.06 with a COV of 0.09.

For the case of axial capacities of columns having a swaged section, it cannot be directly calculated using DSM, and there is no design guidance for such sections. In the current study, the axial capacities of specimens having a swaged section at the end of the channels ($P_{Exp,WE}$) and in the middle of the channels ($P_{Exp,WM}$) are compared to those of the equivalent plain channel columns ($P_{DSM,plain}$) calculated using the DSM. The comparison results are shown in Figure 7-14, and the mean values of $P_{Exp,WE}/P_{DSM,plain}$ and $P_{Exp,WM}/P_{DSM,plain}$ are 1.07 and 1.00, with COVs of 0.06 and 0.08, respectively. The DSM predictions are conservative by about 5.8% and un-conservative by about 1.4% on average for plain channels and channels with swaged sections, respectively.

Table 7-3 Comparison between the test results and the DSM strengths

Specimen	Ultimate load P_{Exp} (kN)	Mean value P_{Exp} (kN)	Axial capacity P_{DSM} (kN)	P_{Exp}/P_{DSM}
S-65-0.75-150-T1	33.41	33.23	32.01	1.04
S-65-0.75-150-T2	33.16			1.04
S-65-0.75-150-T3	32.88			1.03
S-65-0.75-150-T4	33.00			1.03
S-65-0.75-150-T5	33.14			1.04
S-65-0.75-150-T6	33.78			1.06
S-65-0.75-1000-T1	27.75	27.74	27.77	1.00
S-65-0.75-1000-T2	27.66			1.00
S-65-0.75-1000-T3	28.25			1.02
S-65-0.75-1000-T4	27.97			1.01
S-65-0.75-1000-T5	27.06			0.97
S-65-0.75-1200-T1	27.02	26.84	25.54	1.06
S-65-0.75-1200-T2	26.76			1.05
S-65-0.75-1200-T3	26.94			1.05
S-65-0.75-1200-T4	27.99			1.10
S-65-0.75-1200-T5	26.23			1.03
S-65-0.75-1200-T6	26.14			1.02
S-65-0.75-1200-T7	26.78			1.05
S-65-0.75-1400-T1	24.31	24.08	23.15	1.05
S-65-0.75-1400-T2	23.15			1.00
S-65-0.75-1400-T3	25.34			1.09
S-65-0.75-1400-T4	23.92			1.03

S-65-0.75-1400-T5	23.70			1.02
S-100-0.95-150-T1	57.25			1.23
S-100-0.95-150-T2	57.26			1.23
S-100-0.95-150-T3	57.58	57.45	46.69	1.23
S-100-0.95-150-T4	57.48			1.23
S-100-0.95-150-T5	57.67			1.24
S-100-0.95-1000-T1	45.76			1.00
S-100-0.95-1000-T2	44.40			0.97
S-100-0.95-1000-T3	46.76	45.38	45.83	1.02
S-100-0.95-1000-T4	44.86			0.98
S-100-0.95-1000-T5	45.14			0.98
S-100-0.95-1200-T1	43.06			0.98
S-100-0.95-1200-T2	43.06			0.98
S-100-0.95-1200-T3	42.91	42.73	43.88	0.98
S-100-0.95-1200-T4	42.10			0.96
S-100-0.95-1200-T5	42.54			0.97
S-100-0.95-1400-T1	42.18			1.01
S-100-0.95-1400-T2	41.15			0.99
S-100-0.95-1400-T3	41.31	41.41	41.70	0.99
S-100-0.95-1400-T4	41.07			0.98
S-100-0.95-1400-T5	41.37			0.99
S-92.1-0.95-300-T1	58.11			1.20
S-92.1-0.95-300-T2	58.22			1.20
S-92.1-0.95-300-T3	59.23	58.82	48.44	1.22
S-92.1-0.95-300-T4	58.80			1.21
S-92.1-0.95-300-T5	59.74			1.23
Mean				1.06
COV				0.09

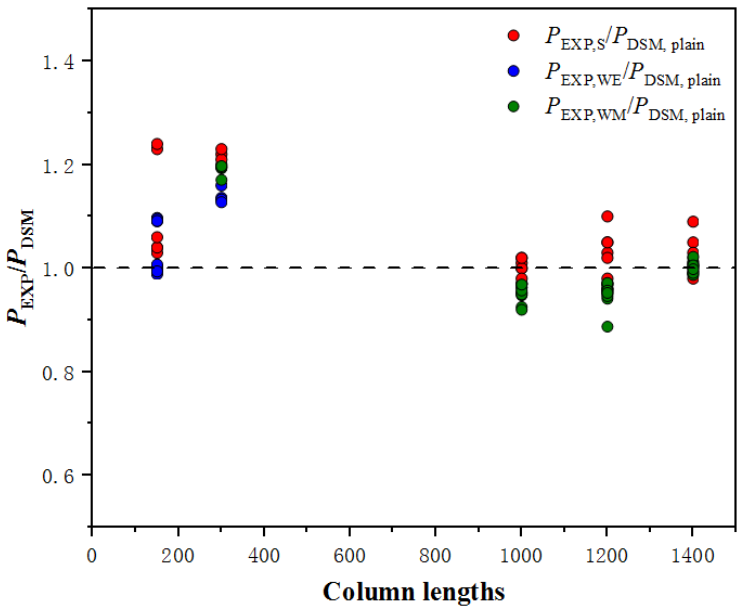

Figure 7-14 Comparisons of results between the test and DSM strengths (P_{Exp}/P_{DSM})

7.4. Summary

In this chapter, an experimental study was conducted to investigate the axial capacity of CFS fixed-fixed columns having a swaged section under compression. A total of 101

specimens were tested, considering variations in cross-section dimensions (CFS sections of 65 × 41.3 × 0.75 mm, 100 × 50 × 0.95 mm, and 92.1 × 41.3 × 0.95 mm), thicknesses of sections (0.75 mm and 0.95 mm), swaging locations (at the end and in the middle of channels), and specimen lengths (150 mm, 300 mm, 1000 mm, 1200 mm, and 1400 mm). The following conclusions can be drawn from the outcome of this chapter:

(1) Compared to the CFS plain section, the average axial capacities of columns having a swaged section are reduced by 5.5% and 3.9% for sections with a web depth of 65 mm and 100 mm, respectively. For columns having a swaged section, buckling tends to occur at the junction between the swaged section and the plain section.

(2) CFS channels having a swaged section at the end of the channels exhibit a lower axial capacity than in the middle of the channels, showing an average reduction of 6.4% and 2.0%, respectively, when compared to the plain channels with the same specimen lengths.

(3) For the columns with lengths of 1000 mm, 1200 mm, and 1400 mm, their failure is primarily due to global buckling, resulting in a sudden drop in loads when the ultimate load is reached. In contrast, the shorter columns (with lengths of 150 mm and 300 mm) primarily failed due to local buckling, and their load-displacement curves declined relatively gradually.

(4) Comparing the experimental results with the DSM predictions from the AISI (2016) and AS/NZS (2018) reveals that, on average, the DSM predictions are conservative by about 5.8% for plain channel columns and un-conservative by about 1.4% for CFS channels having swaged sections.

Chapter 8 Conclusions and future work

8.1. General

This research has focused on advancing the understanding of CFS structural systems across multiple topics, including web crippling behaviour of channels with elongated edge-stiffened web holes, moment capacity of truss with HRCs, axial strength of telescopic studs and locally swaged sections, and novel built-up sections under axial compression. Through rigorous experimental, numerical, and analytical investigations, this study has addressed critical gaps in existing design standards and proposed innovative solutions to enhance the structural efficiency, reliability, and applicability of CFS structures.

8.2. Conclusions

Web crippling behaviour: This research aimed to examine the web crippling behaviour of CFS channels with elongated un-stiffened and edge-stiffened web holes under four different loading cases. The validated FE model was used to conduct an extensive parametric study, exploring the influence of various geometric parameters on the web crippling behaviour of these channels. Results demonstrated that edge-stiffened elongated holes significantly reduce the adverse impact of web holes on web crippling strength. For instance, compared to unstiffened elongated holes, edge-stiffened configurations achieved strength reductions as low as 2% under ITF loading conditions. Based on the results of FEA, proposed design equations based on Direct Strength Method (DSM) effectively predict the web crippling strength of CFS channels with elongated holes, addressing the limitations of current standards such as AISI (2016) and AS/NZS (2018).

Moment capacity of truss: The introduction of HRCs for CFS trusses demonstrated superior connection performance, offering enhanced moment capacity and structural efficiency. Compared to using screw groups in CFS trusses, HRCs offer a novel alternative for truss design. Parametric studies revealed that factors such as span-to-height ratios, lateral support locations, and boundary conditions influence the strength and failure modes of trusses. Finally, the trusses with lipped section chords were designed according to the AISI (2016) and AS/NZS (2018), achieving an average test-to-design strength ratio of 0.86.

Axial strength of telescopic studs: A novel telescopic stud system was developed and tested, demonstrating higher axial strength and improved connection performance through optimized screw configurations. Results revealed that using multiple screws in strategic locations enhanced connection strength by up to 37%, compared to single-screw configurations with gaps. It should be noted that these findings are limited to the tested specimen configurations and parameter ranges considered in this study, primarily involving short studs where connection behavior governs the structural response. Furthermore, although current design standards such as AISI (2016) and AS/NZS (2018) appear conservative for the tested cases, broader experimental and numerical investigations are required before general design recommendations can be established.

Novel built-up sections under axial compression: For built-up box columns, the combination of C-sections and U-sections exhibited improved strength and stability under axial compression. The study highlights that while HRC spacing and thickness have a minor influence on the overall buckling behaviour, the slenderness ratio is the key factor in determining the failure mode. No significant deformation or shear failure was observed in the HRCs, indicating that the connectors provided adequate strength to

prevent slippage between the flanges. A novel hybrid DSM-EWM design approach was proposed, achieving better agreement with experimental results compared to existing methods. The proposed design equations combining DSM and EWM provided accurate predictions of axial strength, achieving a mean experimental-to-design strength ratio of 1.01. Statistical analyses confirmed the reliability of the proposed equations, ensuring their suitability for practical applications.

Axial strength of swaged sections: It was found that, compared with plain sections, the average axial capacities of specimens incorporating a swaged section were reduced by 5.5% for cross-sections of 65 × 41.3 × 0.75 and 3.9% for sections of 100 × 50 × 0.95, respectively. For columns with lengths of 1000, 1200, and 1400 mm, global buckling governed the failure response, whereas local buckling was dominant for short columns. A comparison between experimental results and direct strength method (DSM) predictions based on AISI (2016) and AS/NZS (2018) indicated that DSM slightly overestimated the axial capacities of CFS columns with swaged sections by approximately 1.4% on average.

It should be noted that the above conclusions are strictly applicable to the tested cross-sections and geometries considered in this study. Nevertheless, the validated FE model demonstrated good agreement with experimental responses in terms of failure modes and load–displacement behaviour, indicating its suitability for conducting parametric investigations on other cross-section configurations. Accordingly, the numerical models established herein may be employed to explore the influence of swaging on a broader range of CFS sections. However, further experimental verification is recommended before generalizing the proposed findings to other cross-sectional geometries.

Overall, the findings of this research significantly advance the understanding of CFS systems, providing innovative design recommendations that address existing limitations and promote the adoption of efficient and reliable CFS solutions in construction.

8.3. Future work

While this research has made substantial contributions to the field of CFS structures, several areas warrant further investigation to build upon the foundation established by this doctoral work. The following are potential directions for future research:

(1) Firstly, since no web crippling tests for elongated un-stiffened and edge-stiffened web holes are available, this study utilized experimental data from circular un-stiffened and edge-stiffened web holes to develop and validate the FE model. The validated models were then used to simulate elongated web holes and conduct extensive parametric studies. Future experimental investigations on web crippling of elongated holes should be conducted to develop more accurate validation models.

Secondly, this study proposes various predictive formulas for estimating the web crippling strength of elongated un-stiffened and edge-stiffened web holes and defines their applicable ranges. Within the specified parameters, these formulas demonstrate accuracy; however, their applicability outside these ranges remains uncertain. Further experimental or parametric studies, including those involving parameters beyond those used in this study, should be conducted to better establish the limits of these formulas. Finally, this study utilizes a specific form of elongated edge-stiffened web hole; however, additional forms of edge-stiffened holes should be optimized to provide more design options for practical engineering applications.

(2) For CFS trusses, this study highlights certain limitations and potential directions for future research. First, the findings revealed that CFS trusses with hat section chords exhibited distortional buckling in the diagonal members, with current standards failing to accurately predict their ultimate axial strength. This discrepancy may stem from diagonal-to-chord joints not behaving as fully hinged connections, potentially introducing additional moments that cause calculated loads to exceed experimentally measured values. Addressing this issue through further research is essential.

Second, while hat sections eliminate the need to cut lips at diagonal-to-chord joints, their protruding lips may restrict their application in scenarios requiring precise out-of-plane flatness, such as trusses integrated with cold-formed steel shear walls. Additionally, both past and present findings indicate that truss chords do not experience uniform axial loads, with sections farther from the neutral axis bearing higher stresses. Exploring the use of U-shaped channels with web or flange stiffeners could enhance the load-bearing capacity of the trusses, presenting a promising avenue for future studies.

(3) For built-up box sections, parametric studies focusing on optimizing cross-sectional geometry, connector configurations, and material utilization can enhance the structural efficiency and cost-effectiveness of built-up sections. Machine learning techniques can be explored to identify complex patterns in structural behaviour and optimize design parameters. Furthermore, the Effective Width Method (EWM) in current standards has limitations when calculating the effective area of complex built-up sections. Due to the intricate combinations and interactions within these sections, the approach of calculating the effective area of individual channels and summing them to determine the total effective area is clearly imprecise. Therefore, new

methods for determining effective areas need to be developed, particularly those that simplify the calculation process. For example, approximating the built-up section as a rectangular cross-section could be a practical approach. As for the Direct Strength Method (DSM), the associated coefficients require calibration, as the current coefficients are incapable of accurately predicting the DSM strength of channels with long flanges.

(4) For telescopic studs, the current research focuses on individual stud behaviour. Extending this understanding to structural systems, such as shear walls, requires further investigation.

References

A. Ahmadi, C. Mathieson, G. C. Clifton, R. Das, J.B.P. Lim. (2016). An experimental study on a novel cold-formed steel connection for light gauge open channel steel trusses. Journal of Constructional Steel Research, 122, 70–79.

Abbasi, M., Rasmussen, K. J. R., Khezri, M., & Schafer, B. W. (2023). Experimental investigation of the sectional buckling of built-up cold-formed steel columns. Journal of Constructional Steel Research, 203, 107803-.

AISI S214-12. North American Specification for Cold-Formed Steel Framing—Truss Design. American Iron and Steel Institute; 2012.

American Iron and Steel Institute (AISI) (2016). North American specification for the design of cold-formed steel structural members, 2016 Edition. AISI S100-16w, Washington, DC. USA.

American Iron and Steel Institute (AISI) (1996). Specification for the design of cold-formed steel structural members. Washington, DC. USA.

American Iron and Steel Institute (AISI) (2012). North American Specification for the Design of Cold-formed Steel Structural Members. Washington, DC, USA.

Ananthi, G. B. G., Roy, K., Ghosh, K., Pologanathan, K., & Lim, J. B. P. (2023). An investigation on stiffened cold-formed steel unequal angle box section columns. Journal of Building Engineering, 76, 106989-.

Ananthi, G. B. G., Roy, K., & Lim, J. B. P. (2021). Tests and Finite Element Modelling of Cold-Formed Steel Zed and Hat Section Columns Under Axial Compression. International Journal of Steel Structures, 21(4), 1305–1331.

Australian/New Zealand Standard (AS/NZS) (2018). Cold-formed steel structures. AS/NZS 4600:2018, Joint Technical Committee, Sydney.

BS5950-5: 1998. Structural use of steelwork in building-Part 5: Code of practice for design of cold-formed thin gauge section. London: British Standard.

Chen, B., Dai, Y., Wang, W., Wang, Y., Luo, L., Dai, P., Lim, J. (2024). An experimental study on web-bearing resistance of cold-formed steel sigma-shaped sections with web holes under interior-two-flange loading case. Thin-Walled Structures, 205, 112579.

Chen, B., Roy, K., Fang, Z., Uzzaman, A., Chi, Y., Lim, J. B. P. (2021). Web crippling capacity of fastened cold-formed steel channels with edge-stiffened web holes, un-stiffened web holes and plain webs under two-flange loading. Thin-Walled Structures, 163.

Chen, B., Roy, K., Uzzaman, A., Raftery, G., & Lim, J. B. P. (2020). Axial strength of back-to-back cold-formed steel channels with edge-stiffened holes, un-stiffened holes and plain webs. Journal of Constructional Steel Research, 174, 106313-.

Chen, B., Roy, K., Uzzaman, A., Raftery, G. M., & Lim, J. B. P. (2020). Parametric study and simplified design equations for cold-formed steel channels with edge-stiffened holes under axial compression. Journal of Constructional Steel Research, 172, 106161.

Chen, B., Roy, K., Uzzaman, A., Raftery, G. M., Nash, D., Clifton, G. C., Pouladi, P., & Lim, J. B. P. (2019). Effects of edge-stiffened web openings on the behaviour of cold-formed steel channel sections under compression. Thin-Walled Structures, 144, 106307.

Ç. Dizdar, B. Eray, T. Cem. (2019). Strength and stiffness of floor trusses fabricated from cold-formed steel lipped channels. Engineering Structures, 181, 437–457.

C. Mathieson. (2014). New Truss Joint Development Project (Master thesis). The University of Auckland.

C. Mathieson, G.C. Clifton, J.B.P. Lim. (2016). Novel pin-jointed connection for cold-formed steel trusses. Journal of Constructional Steel Research, 116, 173-182.

C. Mathieson, K. Roy, G.C. Clifton, A. Ahmadi, J.B.P. Lim. 2019. Failure mechanism and bearing capacity of cold-formed steel trusses with HRC connectors. Engineering Structures, 201, 109741.

Craveiro, H. D., Rahnavard, R., Laím, L., Simões, R. A., & Santiago, A. (2022). Buckling behavior of closed built-up cold-formed steel columns under compression. Thin-Walled Structures, 179, 109493-.

Dai, Y., Roy, K., Fang, Z., Chen, B., Raftery, G. M., & Lim, J. B. P. (2024). Buckling resistance of axially loaded cold-formed steel built-up stiffened box sections through experimental testing and finite element analysis. Engineering Structures, 302, 117379-.

Dar, M. A., Sahoo, D. R., Jain, A. K., & Sharma, S. (2021). Monotonic tests and numerical validation of cold-formed steel battened built-up columns. Thin-Walled Structures, 159, 107275-.

Dar, M. A., Verma, A., Anbarasu, M., Pang, S. D., & Dar, A. R. (2022). Design of cold-formed steel battened built-up columns. Journal of Constructional Steel Research, 193, 107291-.

Deepak, M. S., & Ananthi, G. B. G. (2021). Local buckling behaviour and capacities of Cold-Formed Steel Double-I-Box stub and short column sections. Structures (Oxford), 34, 1761–1784.

Duarte, A.P.C., Silvestre, N.M. (2014). A new slenderness-based approach for the web crippling design of plain channel steel beams. International Journal of Steel Structures, 421–434.

EN ISO 6892-1:2019, Metallic materials -Tensile testing-Part 1: Method of test at room temperature. BSI, London, 2019.

European code 3 Part 1.3 (ECS). 2006. Design of Steel Structures: Part 1.3: General Rules-Supplementary Rules for Cold-Formed Thin Gauge Members and Sheeting, European Committee for Standardization, Brussels, Belgium.

Ellobody, E., & Young, B. (2005). Behavior of Cold-Formed Steel Plain Angle Columns. Journal of Structural Engineering (New York, N.Y.), 131(3), 457–466.

Fratamico, D. C., Torabian, S., Zhao, X., Rasmussen, K. J. R., & Schafer, B. W. (2018). Experiments on the global buckling and collapse of built-up cold-formed steel columns. Journal of Constructional Steel Research, 144, 65–80.

GB50018: 2002. Technical code of cold-formed thin-wall steel structures. Wuhan: Hubei province development planning commission.

Gunalan, S., Mahendran, M. (2015). Web crippling tests of cold-formed steel channels under two flange load cases. Journal of Constructional Steel Research, 110, 1–15.

Guzmán, A., Guzmán, O., Arteta, C., & Carrillo, J. (2021). Experimental study of the influence of welding space in cold-formed built-up box flexural members. Engineering Structures, 228, 111541-.

Hetrakul, N., and Yu, W. W. (1978). Structural behavior of beam webs subjected to web crippling and a combination of web crippling and bending. Final Rep., Civ. Engrg. Study 78-4, University of Missouri-Rolla, Rolla, Mo.

Holesapple, M. W., LaBoube, R. A. (2003a). Web crippling of cold-formed steel beams at end supports. Engineering Structures, 25(9), 1211–1216.

H. Rajanayagam, K. Pologanathan, P. Gatheeshgar, G.E. Varelis, P. Sherlock, B. Nagaratnam, P. Hackney. (2021). A-state-of-the-art review on modular building connections. Structures, 34, 1903–1922.Howick Ltd. Floor joist system. Auckland, New Zealand.

Janarthanan, B., Gunalan S., and Mahendran, M., (2015). Bearing capacity of cold-formed unlipped channels with restrained flanges under EOF and IOF load cases. Steel Construction, 8,146-154.

Janarthanan, B., Sundararajah, L, Mahendran, M, Keerthan, P., Gunalan, S. (2019). Web crippling behaviour and design of cold-formed steel sections. Thin-Walled Struct., 140, 387-403

Keerthan, P., Mahendran, M., Steau, E. (2014). Experimental study of web crippling behaviour of hollow flange channel beams under two flange load cases. Thin-Walled Structures, 85, 207–219.

K. Roy, Ting, T. C. H., Lau, H. H., & Lim, J. B. P. (2019). Experimental and numerical investigations on the axial capacity of cold-formed steel built-up box sections. Journal of Constructional Steel Research, 160, 411–427.

K. Roy, H. Rezaeian, D. Lakshmanan, Z. Fang, B.G. Ananthi, J.B.P. Lim. (2023). Structural behaviour of cold-formed steel T-Stub connections with HRC and screws subjected to tension force. Engineering Structures, 283, 115922.

K. Roy, Mohammadjani, C., & Lim, J. B. P. (2019). Experimental and numerical investigation into the behaviour of face-to-face built-up cold-formed steel channel sections under compression. Thin-Walled Structures, 134, 291–309.

Lan, X., Zhang, J. J., Zhao, O. (2024). High strength steel unlipped channel sections subjected to ETF loading: Laboratory testing, numerical simulations and web crippling design. Engineering Structures, 319, 118852.

LaBoube, R.A., Sokol, M.A. (2002). Behaviour of screw connections in residential construction. Journal of Structural Engineering (New York, N.Y.), 128(1), 115–118.

Lian, Y., Uzzaman, A., Lim, J. B. P., Abdelal, G., Nash, D., Young, B. (2016). Effect of web holes on web crippling strength of cold-formed steel channel sections under end-one-flange loading condition – Part I: Tests and finite element analysis. Thin-Walled Structures, 107, 443–452.

Lian, Y., Uzzaman, A., Lim, J. B. P., Abdelal, G., Nash, D., & Young, B. (2017). Web crippling behaviour of cold-formed steel channel sections with web holes subjected to interior-one-flange loading condition-Part I: Experimental and numerical investigation. Thin-Walled Structures, 111, 103–112.

L. Gardner, X. Yun. (2018). Description of stress-strain curves for cold-formed steels. Construction & Building Materials, 189, 527–538.

Li, Y., Li, Y., Wang, S., & Shen, Z. (2014). Ultimate load-carrying capacity of cold-formed thin-walled columns with built-up box and I section under axial compression. Thin-Walled Structures, 79, 202–217.

Li, Y., Zhou, T., Zhang, L., Ding, J., & Zhang, X. (2021). Distortional buckling behavior of cold-formed steel built-up closed section columns. Thin-Walled Structures, 166, 108069-.

Li, Y., Zhou, T., Han, A., Li, W., & Xu, Y. (2024). Failure mechanism and reliability prediction of CFS built-up columns considering distortional buckling. Structures (Oxford), 69, 107337-.

Li, Q.-Y., & Young, B. (2022). Experimental and numerical investigation on cold-formed steel built-up section pin-ended columns. Thin-Walled Structures, 170, 108444-.

Liang, H., Roy, K., Fang, Z., & Lim, J. B. P. (2022). A Critical Review on Optimization of Cold-Formed Steel Members for Better Structural and Thermal Performances. Buildings (Basel), 12(1), 34-.

Mahar, A. M., Jayachandran, S. A., & Mahendran, M. (2023). Local-distortional interaction behaviour and design of cold-formed steel built-up columns. Journal of Constructional Steel Research, 200, 107654-.

Mahar, A. M., Jayachandran, S. A., & Mahendran, M. (2022). Design of locally buckling cold-formed steel built-up columns formed by unlipped channel sections. Thin-Walled Structures, 174, 109132-.

Macdonald M, Heiyantuduwa M.A., Kotelko, M., Rhodes, J. (2011). Web crippling behaviour of thin-walled lipped channel beams. Thin-Walled Struct. 49, 682–690.

Ma, C., Wei, C., Jiang, K., Zhao, O., & Su, A. (2024). Experimental and numerical investigations of high-strength cold-formed steel multi-limb built-up section columns. Engineering Structures, 309, 118012-.

Manikandan, P., Sukumar, S., & Kannan, K. (2018). Distortional buckling behaviour of intermediate cold-formed steel lipped channel section with various web stiffeners under compression. International Journal of Advanced Structural Engineering, 10(3), 189–198.

Natário, P., Silvestre, N., Camotim, D. (2016). Direct strength prediction of web crippling failure of beams under ETF loading. Thin-Walled Structures, 98, 360–374.

Natário, P., Silvestre, N., Camotim, D. (2017). Web crippling of beams under ITF loading: A novel DSM-based design approach. Journal of Constructional Steel Research, 128, 812–824.

Nguyen, V.V., Hancock, G.J., Pham, C.H. (2017). New developments in the direct strength method (DSM) for the design of cold-formed steel sections under localised loading. Steel Construction, 227–233.

Nie, S.-F., Zhou, T.-H., Zhang, Y., & Liu, B. (2020). Compressive behavior of built-up closed box section columns consisting of two cold-formed steel channels. Thin-Walled Structures, 151, 106762-.

N. Korcz-Konkol, P. Iwicki. (2023). Truss imperfections in the design of bar and diaphragm bracing systems. Journal of Constructional Steel Research, 206, 107936.

Nguyen, H. T., & Kim, S. E. (2009). Buckling of composite columns of lipped-channel and hat sections with web stiffener. Thin-Walled Structures, 47(11), 1149–1160.

Origin Lab (Version 8.5.1). Origin Lab Corporation, Northampton, MA, USA

Phan, D. K., Rasmussen, K. J. R., & Schafer, B. W. (2021). Tests and design of built-up section columns. Journal of Constructional Steel Research, 181, 106619-.

Pham, C. H., Hancock, G. J. (2015). Numerical investigation of longitudinally stiffened web channels predominantly in shear. Thin-Walled Structures, 86, 47–55.

Rasmussen, K. J. R., Khezri, M., Schafer, B. W., & Zhang, H. (2020). The mechanics of built-up cold-formed steel members. Thin-Walled Structures, 154, 106756-.

Rahnavard, R., Craveiro, H. D., Laím, L., Simões, R. A., & Napolitano, R. (2021). Numerical investigation on the composite action of cold-formed steel built-up battened columns. Thin-Walled Structures, 162, 107553-.

Rahnavard, R., Razavi, M., Fanaie, N., & Craveiro, H. D. (2023). Evaluation of the composite action of cold-formed steel built-up battened columns composed of two sigma-shaped sections. Thin-Walled Structures, 183, 110390-.

Reyes, W., & Guzmán, A. (2011). Evaluation of the slenderness ratio in built-up cold-formed box sections. Journal of Constructional Steel Research, 67(6), 929–935.

Sundararajah, L. (n.d.). Web Crippling Studies of Cold-formed Steel Channel Beams.

Sundararajah, L., Mahendran, M., Keerthan, P. (2017). New design rules for lipped channel beams subject to web crippling under two-flange load cases. Thin-Walled Structures, 119, 421–437.

Selvaraj, S., & Madhavan, M. (2022). Design of Cold-formed Steel Built-Up Closed Section Columns using Direct Strength Method. Thin-Walled Structures, 171, 108746-.

Uzzaman, A., Lim, J. B. P., Nash, D., Rhodes, J., Young, B. (2012a). Cold-formed steel sections with web openings subjected to web crippling under two-flange loading conditions - Part I: Tests and finite element analysis. Thin-Walled Structures, 56, 38–48.

Uzzaman, A., Lim, J. B. P., Nash, D., Rhodes, J., Young, B. (2012b). Web crippling behaviour of cold-formed steel channel sections with offset web holes subjected to interior-two-flange loading. Thin-Walled Structures, 50(1), 76–86.

Uzzaman, A., Lim, J. B. P., Nash, D., Rhodes, J., Young, B. (2013). Effect of offset web holes on web crippling strength of cold-formed steel channel sections under end-two-flange loading condition. Thin-Walled Structures, 65, 34–48.

Uzzaman, A., Lim, J. B. P., Nash, D., Roy, K. (2020a). Cold-formed steel channel sections under end-two-flange loading condition: Design for edge-stiffened holes, unstiffened holes and plain webs. Thin-Walled Structures, 147.

Uzzaman, A., Lim, J. B. P., Nash, D., Roy, K. (2020b). Web crippling behaviour of cold-formed steel channel sections with edge-stiffened and unstiffened circular holes under interior-two-flange loading condition. Thin-Walled Structures, 154.

Uzzaman, A., Lim, J. B. P., Nash, D., Young, B. (2017a). Effects of edge-stiffened circular holes on the web crippling strength of cold-formed steel channel sections under one-flange loading conditions. Engineering Structures, 139, 96–107.

Uzzaman, A., Lim, J. B. P., Nash, D., Young, B. (2017b). Effects of edge-stiffened circular holes on the web crippling strength of cold-formed steel channel sections under one-flange loading conditions. Engineering Structures, 139, 96–107.

Vy, S. T., & Mahendran, M. (2021a). Behaviour and design of slender built-up nested cold-formed steel compression members. Engineering Structures, 241, 112446-.

Vy, S. T., Mahendran, M., & Sivaprakasam, T. (2021b). Built-up nested cold-formed steel compression members subject to local or distortional buckling. Journal of Constructional Steel Research, 182, 106667-.

Santaputra, C., Parks, M. B., and Yu, W. W. (1989). Web crippling strength of cold-formed steel beams, J. Struct. Eng., 115, 2511–2527

Steau, E., Mahendran, M. and Keerthan, P. (2015). Web crippling tests of rivet fastened rectangular hollow flange channel beams under two flange load cases. Thin-Walled Struct., 95, 262–275.

Sundararajah, L., Mahendran, M., Keerthan, P. (2016). Experimental studies of lipped channel beams subject to web crippling under two-flange load cases. J. Struct. Eng., 142, 04016058.

Sundararajah, L., Mahendran, M., Keerthan, P. (2017). New design rules for lipped channel beams subject to web crippling under two-flange load cases. Thin-Walled Struct., 119,421–437.

Tao F., Moen, C D., Chatterjee, A. (2016). Monotonic and cyclic response of single shear cold-formed steel-to-steel and sheathing-to-steel connections.

Wang, W., Roy, K., Ananthi.G, B. G., Lu, L., Fang, Z., & Lim, J. B. P. (2024). Simplified Direct Strength Method for the design of cold-formed steel channels with circular web openings under two-flange loadings. Engineering Structures, 319, 118840-.

Wang, W., Roy, K., Fang, Z., Ananthi. G, B. G., & Lim, J. B. P. (2023). Web crippling behaviour of cold-formed steel channel sections having elongated edge-stiffened web holes under interior-two-flange loading condition. Engineering Structures, 294, 116757-.

Wing, B. A. (1981). Web crippling and the interaction of bending and web crippling of unreinforced multi-web cold-formed steel sections. M.Sc. Thesis, Department of Civil Enginneering, University of Waterloo.

Wang, C., Zhang, Z., Zhao, D., & Liu, Q. (2016). Compression tests and numerical analysis of web-stiffened channels with complex edge stiffeners. Journal of Constructional Steel Research, 116, 29–39.

Wang, C., Zhang, Z., Jia, L., & Yu, X. (2017). Bending tests and finite element analysis of lipped channels with complex edge stiffeners and web stiffeners. Journal of Central South University, 24(9), 2145–2153.

Wang, W., Rezaeian, H., Roy, K., Fang, Z., & Lim, J. B. P. (2024). Axial capacity of a novel cold-formed steel swaged section: Experimental tests and design. Journal of Building Engineering, 90, 109494-.

Yang, J., Luo, K., Wang, W., Shi, Y., & Li, H. (2024). Axial compressive behavior of cold-formed steel built-up box-shape columns with longitudinal stiffeners. Journal of Constructional Steel Research, 212, 108274-.

Yang, J., Xu, L., Shi, Y., & Wang, W. (2022). Experimental and Analytical Study of Flexural Buckling of Cold-Formed Steel Quadruple-Limb Built-Up Box Columns. Journal of Structural Engineering (New York, N.Y.), 148(1).

Ye, J., Hajirasouliha, I., & Becque, J. (2018a). Experimental investigation of local-flexural interactive buckling of cold-formed steel channel columns. Thin-Walled Structures, 125, 245–258.

Ye, J., Mojtabaei, S. M., & Hajirasouliha, I. (2018b). Local-flexural interactive buckling of standard and optimised cold-formed steel columns. Journal of Constructional Steel Research, 144, 106–118.

Yu, C. (2012). Cold-formed steel flexural member with edge stiffened holes: Behavior, optimization, and design. Journal of Constructional Steel Research, 71, 210–218.

Young, B., and Hancock, G. J. (1998). Web crippling behaviour of cold-formed unlipped channels. 14th Int. Spec. Conf. Cold-formed Steel Struct., 127–149.

Young, B., and Hancock, G. J. (2000). Tests and design of cold-formed unlipped channels subjected to web crippling, 15th Int. Spec. Conf. Cold-formed Steel Struct., 43–70.

Young, B., and Hancock, G. J. (2001). Design of cold-formed channels subjected to web crippling. J. Struct. Eng.,127, 1137–1144.

Young, B., and Hancock, G. J. (2004). Web crippling of cold-formed unlipped channels with flanges restrained. Thin-Walled Struct., 42, 911–930.

Zhou, X., Xiang, Y., Shi, Y., Xu, L., & Zou, Y. (2021). Simplified design method of cold-formed steel columns with built-up box sections. Engineering Structures, 228, 111532-.

Zhou X., M. T, Zhou Q., & Liu Y. (2002). Study on the plate-assembly effects on edge-stiffened plate elements in design approach of effective width-to-thickness ratio. J Build Struct, 03:37–43 (In Chinese).

Zhong, Y., Su, A., & Zhao, O. (2023). Post-fire local buckling behaviour of cold-formed S700 high strength steel circular hollow sections under axial compression: Experiments, modelling and design. Thin-Walled Structures, 184, 110511-.

Appendix A

Web crippling strength predicted from FEA under the ITF loading case

(a) CFS channel sections 190×45×15-t1.5

Bearing length	Elongated web holes		Web crippling strength per web predicted from FEA, P_{FEA} (kN)											
					With edge-stiffened hole									
					Q0.02		Q0.06				Q0.10			
N (mm)	d_w/d_1	b_w/d_w	Plain web	With un-stiffened hole	r_q=2 (mm)	r_q=3 (mm)	r_q=2 (mm)	r_q=3 (mm)	r_q=4 (mm)	r_q=6 (mm)	r_q=2 (mm)	r_q=3 (mm)	r_q=4 (mm)	r_q=6 (mm)
50.00	0.30	2.00	8.16	7.24	7.58	6.44	7.01	7.03	7.03	7.08	7.20	7.22	7.24	7.30
50.00	0.30	2.50	8.16	6.89	6.15	6.13	6.72	6.74	6.74	6.79	6.99	7.01	7.04	7.12
50.00	0.30	3.00	8.16	6.52	5.83	5.82	6.41	6.43	6.43	6.49	6.73	6.75	6.79	6.88
75.00	0.30	2.00	8.28	6.96	7.62	7.60	8.20	8.21	8.21	8.26	8.45	8.46	8.48	8.52
75.00	0.30	2.50	8.28	6.61	6.78	6.76	7.35	7.36	7.36	7.41	7.65	7.67	7.69	7.76
75.00	0.30	3.00	8.28	6.27	6.45	6.41	7.02	7.03	7.02	7.07	7.35	7.37	7.39	7.46
100.00	0.30	2.00	9.12	7.66	7.69	7.68	8.26	8.27	8.27	8.32	8.50	8.51	8.53	8.59
100.00	0.30	2.50	9.12	7.31	7.36	7.35	7.94	7.95	7.95	7.99	8.24	8.25	8.27	8.34
100.00	0.30	3.00	9.12	6.94	7.05	7.03	7.61	7.62	7.61	7.66	7.94	7.96	7.98	8.05
50.00	0.50	2.00	8.16	5.51	5.32	5.47	6.85	6.89	6.90	7.01	7.26	7.30	7.35	7.50
50.00	0.50	2.50	8.16	4.95	4.95	4.92	6.31	6.34	6.34	6.45	6.70	6.74	6.79	6.94
50.00	0.50	3.00	8.16	4.43	4.44	4.42	5.81	5.84	5.85	5.97	6.18	6.22	6.27	6.40
75.00	0.50	2.00	8.28	5.41	5.67	5.65	6.84	6.87	6.87	6.96	7.23	7.25	7.29	7.39
75.00	0.50	2.50	8.28	4.88	5.13	5.11	6.29	6.32	6.32	6.42	6.67	6.70	6.74	6.86
75.00	0.50	3.00	8.28	4.38	4.62	4.60	5.79	5.82	5.83	5.93	6.15	6.18	6.22	6.33
100.00	0.50	2.00	9.12	6.04	6.22	6.19	7.39	7.42	7.42	7.50	7.77	7.79	7.83	7.93
100.00	0.50	2.50	9.12	5.46	5.66	5.64	6.84	6.87	6.87	6.96	7.22	7.25	7.29	7.39
100.00	0.50	3.00	9.12	4.93	5.16	5.13	6.35	6.37	6.38	6.47	6.71	6.73	6.77	6.89
50.00	0.70	2.00	8.16	3.80	3.95	3.97	6.35	6.41	6.44	6.63	6.66	6.72	6.80	6.99
50.00	0.70	2.50	8.16	3.18	3.53	3.55	5.79	5.84	5.89	6.06	5.99	6.04	6.11	6.30
50.00	0.70	3.00	8.16	2.63	3.00	2.99	5.16	5.18	5.25	5.46	5.34	5.45	5.52	5.67
75.00	0.70	2.00	8.28	3.83	4.12	4.09	6.27	6.32	6.36	6.53	6.61	6.65	6.74	6.92

75.00	0.70	2.50	8.28	3.24	3.63	3.61	5.73	5.79	5.81	5.98	5.98	6.03	6.09	6.26
75.00	0.70	3.00	8.28	2.70	3.17	3.21	5.31	5.37	5.43	5.60	5.55	5.60	5.67	5.82
100.00	0.70	2.00	9.12	4.36	4.62	4.59	6.81	6.86	6.89	7.05	7.14	7.20	7.27	7.45
100.00	0.70	2.50	9.12	3.71	4.01	4.03	6.24	6.30	6.34	6.47	6.51	6.57	6.64	6.81
100.00	0.70	3.00	9.12	3.13	3.59	3.61	5.70	5.75	5.78	5.90	5.93	5.98	6.05	6.18

(b) CFS channel sections 240×45×15-t1.5

Bearing length	Elongated web holes		Web crippling strength per web predicted from FEA, P_{FEA}(kN)											
					With edge-stiffened hole									
					Q0.02		Q0.06				Q0.10			
N (mm)	d_w/d_1	b_w/d_w	Plain web	With un-stiffened hole	r_q=2 (mm)	r_q=3 (mm)	r_q=2 (mm)	r_q=3 (mm)	r_q=4 (mm)	r_q=6 (mm)	r_q=2 (mm)	r_q=3 (mm)	r_q=4 (mm)	r_q=6 (mm)
50.00	0.30	2.00	7.50	6.45	8.05	8.04	8.24	8.24	8.25	8.24	8.30	8.30	8.31	8.31
50.00	0.30	2.50	7.50	6.12	7.86	7.84	8.15	8.15	8.15	8.14	8.26	8.26	8.27	8.27
50.00	0.30	3.00	7.50	5.80	7.62	7.60	8.02	8.02	7.99	8.02	8.20	8.19	8.20	8.20
75.00	0.30	2.00	9.45	7.35	7.77	7.74	8.44	8.44	8.43	8.46	8.74	8.75	8.76	8.81
75.00	0.30	2.50	9.45	6.92	7.35	7.32	8.03	8.03	8.02	8.05	8.37	8.38	8.40	8.46
75.00	0.30	3.00	9.45	6.52	6.95	6.93	7.64	7.64	7.62	7.66	7.99	8.01	8.03	8.09
100.00	0.30	2.00	9.52	7.44	7.83	7.81	8.50	8.51	8.50	8.52	8.80	8.81	8.83	8.88
100.00	0.30	2.50	9.52	7.02	7.42	7.40	8.09	8.10	8.08	8.12	8.43	8.44	8.45	8.51
100.00	0.30	3.00	9.52	6.62	7.03	7.00	7.70	7.71	7.70	7.74	8.05	8.06	8.08	8.14
50.00	0.50	2.00	7.50	4.83	6.25	6.23	7.49	7.51	7.49	7.51	7.82	7.85	7.87	7.92
50.00	0.50	2.50	7.50	4.32	5.65	5.65	6.92	6.93	6.91	6.94	7.29	7.30	7.32	7.38
50.00	0.50	3.00	7.50	3.84	5.33	5.29	6.41	6.41	6.41	6.43	6.71	6.72	6.77	6.84
75.00	0.50	2.00	9.45	5.11	5.54	5.51	7.05	7.09	7.11	7.25	7.49	7.53	7.58	7.72
75.00	0.50	2.50	9.45	4.55	4.97	4.94	6.57	6.61	6.64	6.77	6.90	6.94	6.99	7.13
75.00	0.50	3.00	9.45	4.05	4.44	4.42	6.13	6.17	6.20	6.33	6.39	6.43	6.48	6.62
100.00	0.50	2.00	9.52	5.29	5.69	5.67	7.23	7.27	7.29	7.41	7.65	7.69	7.74	7.89
100.00	0.50	2.50	9.52	4.73	5.13	5.10	6.72	6.76	6.79	6.92	7.06	7.10	7.15	7.29
100.00	0.50	3.00	9.52	4.24	4.62	4.59	6.27	6.32	6.35	6.47	6.55	6.59	6.64	6.78
50.00	0.70	2.00	7.50	3.20	4.48	4.52	6.48	6.51	6.52	6.62	6.75	6.79	6.83	6.95
50.00	0.70	2.50	7.50	2.64	3.96	3.97	5.84	5.86	5.89	5.98	6.04	6.07	6.11	6.20
50.00	0.70	3.00	7.50	2.12	3.44	3.45	5.24	5.26	5.29	5.39	5.41	5.44	5.48	5.57

(c) CFS channels 190×45×15 - *t*1.5

Bearing length N (mm)	Elongated web holes ratio		With edge stiffened holes Q (q/d_1)	Edge-stiffener fillet radius r_q (mm)	Web crippling strength P_{FEA} (kN)	R_{FEA}/R_{P1}
	d_w/d_1	b_w/d_w				
50.00	0.7	2	Q0.020	2.00	3.95	0.76
50.00	0.7	2	Q0.020	3.00	3.97	0.76
50.00	0.7	2	Q0.025	2.00	4.89	0.93
50.00	0.7	2	Q0.025	3.00	4.91	0.92
50.00	0.7	2	Q0.030	2.00	5.36	1.00
50.00	0.7	2	Q0.030	3.00	5.41	1.00
50.00	0.7	2	Q0.035	2.00	5.81	1.07
50.00	0.7	2	Q0.035	3.00	5.87	1.07
50.00	0.7	2	Q0.040	2.00	6.20	1.12
50.00	0.7	2	Q0.040	3.00	6.28	1.13
50.00	0.7	2	Q0.045	2.00	6.36	1.14
50.00	0.7	2	Q0.045	3.00	6.42	1.13
50.00	0.7	2	Q0.050	2.00	6.45	1.14
50.00	0.7	2	Q0.050	3.00	6.48	1.13
50.00	0.7	2	Q0.055	2.00	6.49	1.13
50.00	0.7	2	Q0.055	3.00	6.50	1.12
50.00	0.7	2	Q0.060	2.00	6.35	1.09
50.00	0.7	2	Q0.060	3.00	6.41	1.09
50.00	0.7	2	Q0.060	4.00	6.44	1.08
50.00	0.7	2	Q0.060	5.00	6.65	1.11
50.00	0.7	2	Q0.060	6.00	6.63	1.09
50.00	0.7	2	Q0.060	7.00	6.80	1.11
50.00	0.7	2	Q0.060	8.00	6.87	1.11
50.00	0.7	2	Q0.060	9.00	6.94	1.11
50.00	0.7	2	Q0.060	10.00	7.00	1.11
50.00	0.7	2	Q0.060	11.00	7.05	1.11

Appendix B

Detials of elastic critical buckling analyses for ITF loading condition

d	r_i	t	N	d_w	b_w	r_q	q	$P_{b,cr}$	k_{FEA}	k_{prop}	k_{FEA}/k_{prop}
190	3.0	1.50	50	57	114.0	3.0	7.6	7.71	2.53	2.63	0.96
190	3.0	1.50	50	57	142.5	3.0	7.6	7.42	2.43	2.47	0.98
190	3.0	1.50	50	95	190.0	3.0	7.6	6.75	2.21	2.42	0.91
190	3.0	1.50	50	95	237.5	3.0	7.6	6.24	2.04	2.20	0.93
190	3.0	1.50	50	133	266.0	3.0	7.6	6.19	2.03	2.20	0.92
190	3.0	1.50	50	133	332.5	3.0	7.6	5.64	1.85	1.92	0.96
190	3.0	1.50	50	57	114.0	0	0	6.98	2.29	2.55	0.90
190	3.0	1.50	50	57	142.5	0	0	6.62	2.17	2.40	0.90
190	3.0	1.50	50	95	190.0	0	0	5.16	1.69	1.88	0.90
190	3.0	1.50	50	95	237.5	0	0	4.56	1.50	1.71	0.88
190	3.0	1.50	50	133	266.0	0	0	3.42	1.12	1.41	0.79
190	3.0	1.50	50	133	332.5	0	0	2.80	0.92	1.23	0.75
190	3.0	1.50	50	57	114.0	3.0	5.7	7.58	2.49	2.61	0.95
190	3.0	1.50	50	57	114.0	3.0	9.5	7.79	2.55	2.65	0.96
190	3.0	1.50	50	57	114.0	3.0	11.4	7.87	2.58	2.67	0.97
190	3.0	1.50	50	57	114.0	3.0	13.3	7.92	2.60	2.69	0.97
190	3.0	1.50	50	57	114.0	3.0	15.2	7.96	2.61	2.70	0.97
190	3.0	1.50	50	57	114.0	3.0	17.1	7.99	2.62	2.72	0.96
190	3.0	1.50	50	57	114.0	3.0	19.0	8.03	2.63	2.73	0.96
190	3.0	1.50	25	57	114.0	3.0	7.6	6.15	2.02	2.38	0.85
190	3.0	1.50	30	57	114.0	3.0	7.6	6.62	2.17	2.44	0.89
190	3.0	1.50	35	57	114.0	3.0	7.6	7.04	2.31	2.49	0.93
190	3.0	1.50	40	57	114.0	3.0	7.6	7.37	2.42	2.54	0.95
190	3.0	1.50	45	57	114.0	3.0	7.6	7.58	2.49	2.59	0.96
190	3.0	1.50	55	57	114.0	3.0	7.6	7.80	2.56	2.68	0.96
190	3.0	1.50	60	57	114.0	3.0	7.6	7.87	2.58	2.72	0.95
190	3.0	1.50	65	57	114.0	3.0	7.6	7.95	2.61	2.76	0.95
190	3.0	1.50	70	57	114.0	3.0	7.6	8.03	2.63	2.79	0.94
190	3.0	1.50	75	57	114.0	3.0	7.6	8.09	2.65	2.83	0.94
190	3.0	1.50	80	57	114.0	3.0	7.6	8.16	2.67	2.86	0.93
190	3.0	1.50	85	57	114.0	3.0	7.6	8.21	2.69	2.90	0.93
190	3.0	1.50	90	57	114.0	3.0	7.6	8.29	2.72	2.93	0.93
190	3.0	1.50	95	57	114.0	3.0	7.6	8.34	2.73	2.96	0.92
190	3.0	1.50	100	57	114.0	3.0	7.6	8.42	2.76	2.99	0.92
190	3.0	2.00	50	57	114.0	3.0	7.6	13.77	1.90	1.68	1.14
190	3.0	2.50	50	57	114.0	3.0	7.6	21.66	1.53	1.07	1.43
190	3.0	3.00	50	57	114.0	3.0	7.6	31.30	1.28	0.67	1.92
190	3.5	1.50	50	57	114.0	3.0	7.6	7.23	2.37	2.46	0.96
190	4.0	1.50	50	57	114.0	3.0	7.6	6.84	2.24	2.30	0.97
190	4.5	1.50	50	57	114.0	3.0	7.6	6.48	2.12	2.15	0.99
190	5.0	1.50	50	57	114.0	3.0	7.6	6.17	2.02	2.01	1.00
190	5.5	1.50	50	57	114.0	3.0	7.6	5.88	1.93	1.88	1.02
190	6.0	1.50	50	57	114.0	3.0	7.6	5.62	1.84	1.76	1.05
190	3.0	1.50	50	57	114.0	3.5	11.4	7.87	2.58	2.67	0.97
190	3.0	1.50	50	57	114.0	4.0	11.4	7.86	2.58	2.66	0.97
190	3.0	1.50	50	57	114.0	4.5	11.4	7.87	2.58	2.66	0.97
190	3.0	1.50	50	57	114.0	5.0	11.4	7.88	2.58	2.66	0.97
190	3.0	1.50	50	57	114.0	5.5	11.4	7.88	2.58	2.65	0.97
190	3.0	1.50	50	57	114.0	6.0	11.4	7.89	2.59	2.65	0.98
190	3.0	1.50	50	57	114.0	6.5	11.4	7.90	2.59	2.64	0.98
190	3.0	1.50	50	57	114.0	7.0	11.4	7.91	2.59	2.64	0.98

240	3.0	1.5	50	72	114.0	3.0	7.6	8.32	3.44	3.30	1.04
240	3.0	1.5	50	72	180.0	3.0	7.6	8.10	3.35	3.06	1.10
240	3.0	1.5	50	120	240.0	3.0	7.6	6.97	2.89	2.95	0.98
240	3.0	1.5	50	120	300.0	3.0	7.6	6.44	2.66	2.61	1.02
240	3.0	1.5	50	168	336.0	3.0	7.6	5.88	2.43	2.58	0.94
240	3.0	1.5	50	168	420.0	3.0	7.6	5.28	2.19	2.14	1.02
240	3.0	1.5	50	72	144.0	0	0	7.87	3.26	3.00	1.09
240	3.0	1.5	50	72	180.0	0	0	7.57	3.14	2.78	1.13
240	3.0	1.5	50	120	240.0	0	0	5.59	2.31	2.07	1.12
240	3.0	1.5	50	120	300.0	0	0	4.99	2.07	1.83	1.13
240	3.0	1.5	50	168	336.0	0	0	3.51	1.46	1.44	1.01
240	3.0	1.5	50	168	420.0	0	0	2.91	1.20	1.20	1.00
240	3.0	1.5	50	72	144.0	3.0	5.7	8.24	3.41	3.28	1.04
240	3.0	1.5	50	72	144.0	3.0	9.5	8.37	3.47	3.33	1.04
240	3.0	1.5	50	72	144.0	3.0	11.4	8.42	3.49	3.35	1.04
240	3.0	1.5	50	72	144.0	3.0	13.3	8.46	3.50	3.37	1.04
240	3.0	1.5	50	72	144.0	3.0	15.2	8.48	3.51	3.39	1.04
240	3.0	1.5	50	72	144.0	3.0	17.1	8.51	3.52	3.41	1.03
240	3.0	1.5	50	72	144.0	3.0	19	8.53	3.53	3.43	1.03
240	3.0	1.5	25	72	144.0	3.0	7.6	6.20	2.57	2.99	0.86
240	3.0	1.5	30	72	144.0	3.0	7.6	6.70	2.77	3.06	0.91
240	3.0	1.5	35	72	144.0	3.0	7.6	7.17	2.97	3.13	0.95
240	3.0	1.5	40	72	144.0	3.0	7.6	7.61	3.15	3.19	0.99
240	3.0	1.5	45	72	144.0	3.0	7.6	7.96	3.30	3.25	1.01
240	3.0	1.5	55	72	144.0	3.0	7.6	8.45	3.50	3.36	1.04
240	3.0	1.5	60	72	144.0	3.0	7.6	8.58	3.55	3.41	1.04
240	3.0	1.5	65	72	144.0	3.0	7.6	8.70	3.60	3.46	1.04
240	3.0	1.5	70	72	144.0	3.0	7.6	8.79	3.64	3.50	1.04
240	3.0	1.5	75	72	144.0	3.0	7.6	8.86	3.67	3.55	1.03
240	3.0	1.5	80	72	144.0	3.0	7.6	8.93	3.70	3.59	1.03
240	3.0	1.5	85	72	144.0	3.0	7.6	9.00	3.73	3.63	1.03
240	3.0	1.5	90	72	144.0	3.0	7.6	9.07	3.76	3.68	1.02
240	3.0	1.5	95	72	144.0	3.0	7.6	9.13	3.78	3.72	1.02
240	3.0	1.5	100	72	144.0	3.0	7.6	9.21	3.81	3.75	1.02
240	3.0	2.0	50	72	144.0	3.0	7.6	14.11	2.46	2.25	1.10
240	3.0	2.5	50	72	144.0	3.0	7.6	21.72	1.94	1.56	1.25
240	3.0	3.0	50	72	144.0	3.0	7.6	30.92	1.60	1.09	1.47
240	3.5	1.5	50	72	144.0	3.0	7.6	7.62	3.16	3.09	1.02
240	4.0	1.5	50	72	144.0	3.0	7.6	7.13	2.95	2.90	1.02
240	4.5	1.5	50	72	144.0	3.0	7.6	6.70	2.77	2.72	1.02
240	5.0	1.5	50	72	144.0	3.0	7.6	6.33	2.62	2.55	1.03
240	5.5	1.5	50	72	144.0	3.0	7.6	6.03	2.50	2.38	1.05
240	6.0	1.5	50	72	144.0	3.0	7.6	5.77	2.39	2.23	1.07
240	3.0	1.5	50	72	144.0	3.5	11.4	8.36	3.46	3.35	1.03
240	3.0	1.5	50	72	144.0	4.0	11.4	8.35	3.46	3.34	1.04
240	3.0	1.5	50	72	144.0	4.5	11.4	8.35	3.46	3.34	1.04
240	3.0	1.5	50	72	144.0	5.0	11.4	8.35	3.46	3.33	1.04
240	3.0	1.5	50	72	144.0	5.5	11.4	8.35	3.46	3.33	1.04
240	3.0	1.5	50	72	144.0	6.0	11.4	8.35	3.46	3.32	1.04
240	3.0	1.5	50	72	144.0	6.5	11.4	8.35	3.46	3.32	1.04
240	3.0	1.5	50	72	144.0	7.0	11.4	8.35	3.46	3.31	1.04

Appendix C

Detials of elastic critical buckling analyses for ETF loading condition

(a) Un-stiffened

d_w	b_w	r_i	N	q	r_q	Thickness 1.0mm				Thickness 1.2mm				Thickness 1.5mm			
						$P_{b,cr}$	k_{FEA}	k_{prop}	k_{FEA}/k_{prop}	$P_{b,cr}$	k_{FEA}	k_{prop}	k_{FEA}/k_{prop}	$P_{b,cr}$	k_{FEA}	k_{prop}	k_{FEA}/k_{prop}
55.2	110.4	3	50	-	-	0.84	0.90	0.96	0.94	1.34	0.83	0.87	0.96	2.37	0.75	0.76	0.99
55.2	124.2	3	50	-	-	0.83	0.89	0.92	0.96	1.32	0.82	0.84	0.98	2.33	0.74	0.74	1.01
55.2	138.0	3	50	-	-	0.81	0.87	0.89	0.98	1.30	0.80	0.81	0.99	2.30	0.73	0.72	1.02
55.2	151.8	3	50	-	-	0.79	0.85	0.85	1.00	1.27	0.79	0.78	1.01	2.26	0.72	0.70	1.03
55.2	165.6	3	50	-	-	0.78	0.83	0.82	1.02	1.24	0.77	0.76	1.02	2.22	0.70	0.68	1.04
92.0	184.0	3	50	-	-	0.73	0.78	0.79	1.00	1.18	0.73	0.73	1.00	2.11	0.67	0.66	1.01
92.0	207.0	3	50	-	-	0.70	0.75	0.74	1.02	1.13	0.70	0.69	1.01	2.03	0.64	0.63	1.02
92.0	230.0	3	50	-	-	0.67	0.72	0.69	1.04	1.08	0.67	0.66	1.02	1.95	0.62	0.61	1.02
92.0	253.0	3	50	-	-	0.64	0.68	0.65	1.06	1.03	0.64	0.62	1.03	1.86	0.59	0.58	1.02
92.0	276.0	3	50	-	-	0.60	0.65	0.60	1.07	0.98	0.61	0.59	1.03	1.77	0.56	0.56	1.01
128.8	257.6	3	50	-	-	0.61	0.65	0.64	1.01	0.99	0.61	0.62	0.99	1.79	0.57	0.58	0.98
128.8	289.8	3	50	-	-	0.56	0.60	0.58	1.03	0.91	0.57	0.58	0.98	1.66	0.53	0.55	0.96
128.8	322.0	3	50	-	-	0.50	0.53	0.53	1.00	0.81	0.50	0.53	0.94	1.46	0.47	0.51	0.91
128.8	354.2	3	50	-	-	0.46	0.49	0.48	1.03	0.75	0.46	0.49	0.94	1.36	0.43	0.48	0.89
128.8	386.4	3	50	-	-	0.40	0.43	0.42	1.01	0.65	0.40	0.45	0.90	1.19	0.38	0.45	0.83
92.0	184.0	3	30	-	-	0.71	0.76	0.74	1.02	1.13	0.70	0.69	1.01	2.02	0.64	0.63	1.02
92.0	184.0	3	40	-	-	0.72	0.77	0.76	1.01	1.15	0.72	0.71	1.00	2.06	0.65	0.64	1.02
92.0	184.0	3	60	-	-	0.75	0.80	0.81	0.99	1.20	0.75	0.75	0.99	2.16	0.68	0.68	1.01
92.0	184.0	3	70	-	-	0.76	0.82	0.83	0.99	1.23	0.76	0.77	0.99	2.21	0.70	0.69	1.02
92.0	184.0	3	80	-	-	0.78	0.83	0.84	0.99	1.26	0.78	0.78	1.00	2.26	0.72	0.70	1.02
92.0	184.0	3	90	-	-	0.79	0.85	0.86	0.99	1.28	0.80	0.80	1.00	2.31	0.73	0.71	1.03
92.0	184.0	3	100	-	-	0.81	0.87	0.87	0.99	1.31	0.81	0.81	1.01	2.37	0.75	0.72	1.04
92.0	184.0	2	50	-	-	0.78	0.84	0.84	0.99	1.27	0.79	0.78	1.01	2.29	0.73	0.70	1.04
92.0	184.0	2.5	50	-	-	0.75	0.81	0.81	0.99	1.22	0.76	0.76	1.00	2.19	0.70	0.68	1.03

92.0	184.0	3.5	50	-	-	0.71	0.76	0.76	1.00	1.14	0.71	0.71	0.99	2.04	0.65	0.64	1.00
92.0	184.0	4	50	-	-	0.70	0.75	0.74	1.01	1.11	0.69	0.69	0.99	1.97	0.63	0.63	0.99
92.0	184.0	4.5	50	-	-	0.68	0.73	0.72	1.01	1.08	0.67	0.68	0.99	1.91	0.61	0.62	0.98
92.0	184.0	5	50	-	-	0.66	0.71	0.70	1.02	1.06	0.65	0.66	0.99	1.85	0.59	0.60	0.97
92.0	184.0	5.5	50	-	-	0.65	0.70	0.68	1.03	1.03	0.64	0.64	0.99	1.80	0.57	0.59	0.97
92.0	184.0	6	50	-	-	0.64	0.68	0.66	1.03	1.01	0.62	0.63	0.99	1.76	0.56	0.58	0.96

(b) Edge-stiffened

d_w	b_w	r_i	N	q	r_q	Thickness 1.0mm				Thickness 1.2mm				Thickness 1.5mm			
						$P_{b,cr}$	k_{FEA}	k_{prop}	k_{FEA}/k_{prop}	$P_{b,cr}$	k_{FEA}	k_{prop}	k_{FEA}/k_{prop}	$P_{b,cr}$	k_{FEA}	k_{prop}	k_{FEA}/k_{prop}
55.2	110.4	3	50	7.36	3	0.94	1.01	1.03	0.98	1.48	0.92	0.92	1.00	2.54	0.81	0.80	1.01
55.2	124.2	3	50	7.36	3	0.93	1.00	1.01	0.99	1.47	0.91	0.90	1.01	2.52	0.80	0.79	1.02
55.2	138.0	3	50	7.36	3	0.92	0.99	1.00	0.99	1.45	0.90	0.89	1.01	2.50	0.79	0.78	1.02
55.2	151.8	3	50	7.36	3	0.91	0.98	0.99	0.99	1.44	0.89	0.88	1.01	2.48	0.79	0.77	1.02
55.2	165.6	3	50	7.36	3	0.90	0.96	0.97	0.99	1.42	0.88	0.87	1.01	2.45	0.78	0.76	1.02
92.0	184.0	3	50	7.36	3	0.94	1.00	1.01	1.00	1.45	0.90	0.90	1.00	2.48	0.79	0.79	1.00
92.0	207.0	3	50	7.36	3	0.91	0.98	0.99	0.99	1.43	0.88	0.88	1.00	2.45	0.78	0.77	1.00
92.0	230.0	3	50	7.36	3	0.89	0.96	0.97	0.99	1.40	0.87	0.87	1.00	2.41	0.77	0.76	1.01
92.0	253.0	3	50	7.36	3	0.87	0.93	0.95	0.98	1.37	0.85	0.85	1.00	2.37	0.75	0.75	1.00
92.0	276.0	3	50	7.36	3	0.85	0.91	0.93	0.98	1.34	0.83	0.84	0.99	2.32	0.74	0.74	0.99
128.8	257.6	3	50	7.36	3	0.93	1.00	0.98	1.02	1.43	0.89	0.88	1.01	2.36	0.75	0.77	0.97
128.8	289.8	3	50	7.36	3	0.92	0.99	0.96	1.03	1.41	0.87	0.86	1.01	2.31	0.73	0.76	0.97
128.8	322.0	3	50	7.36	3	0.90	0.96	0.93	1.03	1.37	0.85	0.84	1.00	2.24	0.71	0.75	0.95
128.8	354.2	3	50	7.36	3	0.88	0.94	0.91	1.03	1.34	0.83	0.83	1.01	2.19	0.69	0.73	0.95
128.8	386.4	3	50	7.36	3	0.85	0.92	0.89	1.03	1.30	0.81	0.81	0.99	2.10	0.67	0.72	0.93
92.0	184.0	3	30	7.36	3	0.90	0.96	0.94	1.02	1.39	0.86	0.85	1.02	2.37	0.75	0.74	1.01
92.0	184.0	3	40	7.36	3	0.92	0.98	0.98	1.01	1.42	0.88	0.88	1.01	2.42	0.77	0.77	1.00
92.0	184.0	3	60	7.36	3	0.95	1.02	1.03	0.99	1.48	0.92	0.92	1.00	2.54	0.81	0.80	1.00
92.0	184.0	3	70	7.36	3	0.97	1.04	1.06	0.99	1.52	0.94	0.94	1.00	2.60	0.83	0.82	1.01
92.0	184.0	3	80	7.36	3	1.00	1.07	1.08	0.99	1.55	0.96	0.96	1.00	2.66	0.85	0.83	1.01
92.0	184.0	3	90	7.36	3	1.02	1.09	1.10	0.99	1.59	0.98	0.98	1.01	2.74	0.87	0.85	1.02
92.0	184.0	3	100	7.36	3	1.04	1.11	1.12	1.00	1.63	1.01	1.00	1.01	2.81	0.89	0.86	1.03

92.0	184.0	2	50	7.36	3	0.98	1.05	1.07	0.98	1.54	0.95	0.95	1.00	2.64	0.84	0.83	1.01
92.0	184.0	2.5	50	7.36	3	0.96	1.03	1.04	0.99	1.49	0.93	0.93	1.00	2.56	0.81	0.81	1.01
92.0	184.0	3.5	50	7.36	3	0.91	0.98	0.98	1.00	1.41	0.88	0.88	1.00	2.41	0.76	0.77	0.99
92.0	184.0	4	50	7.36	3	0.89	0.96	0.95	1.00	1.38	0.85	0.86	1.00	2.34	0.74	0.75	0.99
92.0	184.0	4.5	50	7.36	3	0.87	0.94	0.93	1.01	1.34	0.83	0.84	1.00	2.28	0.72	0.74	0.98
92.0	184.0	5	50	7.36	3	0.86	0.92	0.91	1.01	1.31	0.82	0.82	0.99	2.22	0.71	0.72	0.97
92.0	184.0	5.5	50	7.36	3	0.84	0.90	0.88	1.01	1.29	0.80	0.80	0.99	2.17	0.69	0.71	0.97
92.0	184.0	6	50	7.36	3	0.82	0.88	0.86	1.02	1.26	0.78	0.79	0.99	2.17	0.69	0.70	0.98
92.0	184.0	3	50	7.36	2	0.93	1.00	1.01	0.99	1.45	0.90	0.90	0.99	2.47	0.79	0.79	1.00
92.0	184.0	3	50	7.36	2.5	0.93	1.00	1.01	0.99	1.45	0.90	0.90	1.00	2.48	0.79	0.79	1.00
92.0	184.0	3	50	7.36	3.5	0.94	1.00	1.01	1.00	1.45	0.90	0.90	1.00	2.48	0.79	0.79	1.00
92.0	184.0	3	50	7.36	4	0.94	1.01	1.01	1.00	1.45	0.90	0.90	1.00	2.48	0.79	0.78	1.00
92.0	184.0	3	50	7.36	4.5	0.94	1.01	1.00	1.00	1.46	0.90	0.90	1.01	2.48	0.79	0.78	1.01
92.0	184.0	3	50	7.36	5	0.94	1.01	1.00	1.01	1.46	0.90	0.90	1.01	2.49	0.79	0.78	1.01
92.0	184.0	3	50	7.36	5.5	0.94	1.01	1.00	1.01	1.46	0.91	0.90	1.01	2.49	0.79	0.78	1.01
92.0	184.0	3	50	7.36	6	0.94	1.01	1.00	1.01	1.46	0.91	0.90	1.01	2.49	0.79	0.78	1.01
92.0	184.0	3	50	9.2	3	0.94	1.01	1.01	1.00	1.46	0.90	0.91	1.00	2.49	0.79	0.79	1.00
92.0	184.0	3	50	11.0	3	0.95	1.01	1.02	1.00	1.47	0.91	0.91	1.00	2.50	0.80	0.79	1.00
92.0	184.0	3	50	12.9	3	0.95	1.02	1.02	1.00	1.47	0.91	0.91	1.00	2.52	0.80	0.80	1.00
92.0	184.0	3	50	14.7	3	0.95	1.02	1.03	1.00	1.48	0.92	0.92	1.00	2.53	0.80	0.80	1.00
92.0	184.0	3	50	16.6	3	0.96	1.03	1.03	1.00	1.49	0.92	0.92	1.00	2.54	0.81	0.80	1.00
92.0	184.0	3	50	18.4	3	0.96	1.03	1.03	1.00	1.49	0.93	0.92	1.00	2.55	0.81	0.81	1.00

Appendix D

Web crippling strengths per web predicted from FEA under the IOF loading condition

(a) Bearing length of 50 mm

Thickness	Elongated web holes		Web crippling strengths per web predicted from FEA, P_{FEA} (kN)										
					With edge-stiffened holes								
					Q0.02			Q0.04			Q0.06		
t (mm)	d_w/d_1	b_w/d_w	Plain web	With un-stiffened hole	r_q=2 (mm)	r_q=3 (mm)	r_q=4 (mm)	r_q=2 (mm)	r_q=3 (mm)	r_q=4 (mm)	r_q=2 (mm)	r_q=3 (mm)	r_q=4 (mm)
1.50	0.20	1.40	9.34	9.32	9.36	9.35	9.37	9.32	9.36	9.36	9.35	9.35	9.36
1.50	0.20	1.80	9.34	9.27	9.31	9.26	9.31	9.32	9.30	9.32	9.32	9.32	9.32
1.50	0.20	2.20	9.34	9.23	9.31	9.26	9.31	9.32	9.30	9.32	9.32	9.32	9.32
1.50	0.40	1.40	9.34	9.14	9.31	9.32	9.28	9.32	9.32	9.32	9.33	9.33	9.26
1.50	0.40	1.80	9.34	9.04	9.29	9.29	9.29	9.29	9.29	9.29	9.30	9.30	9.29
1.50	0.40	2.20	9.34	8.87	9.25	9.18	9.23	9.21	9.25	9.26	9.28	9.29	9.29
1.50	0.60	1.40	9.34	8.74	9.32	9.30	9.27	9.31	9.31	9.31	9.32	9.33	9.33
1.50	0.60	1.80	9.34	7.99	9.13	9.13	9.18	9.25	9.23	9.24	9.25	9.27	9.27
1.50	0.60	2.20	9.34	6.70	8.84	8.83	8.85	9.05	9.04	9.03	9.10	9.08	9.10
2.00	0.20	1.40	16.23	16.22	16.22	16.20	16.23	16.22	16.19	16.22	16.20	16.20	16.13
2.00	0.20	1.80	16.23	16.09	16.04	16.15	16.18	16.09	16.18	16.16	16.16	16.10	16.19
2.00	0.20	2.20	16.23	16.11	16.04	16.15	16.18	16.09	16.18	16.16	16.16	16.10	16.19
2.00	0.40	1.40	16.23	16.03	16.00	16.16	16.18	16.15	16.16	16.11	16.09	16.12	16.18
2.00	0.40	1.80	16.23	15.88	16.10	16.14	16.08	16.12	16.11	16.18	16.11	16.18	16.17
2.00	0.40	2.20	16.23	15.59	15.94	16.08	16.07	16.07	16.11	16.13	16.11	16.13	16.12
2.00	0.60	1.40	16.23	15.38	16.13	16.14	16.10	16.14	16.16	16.10	16.15	16.16	16.15
2.00	0.60	1.80	16.23	13.47	15.97	15.95	15.94	16.02	15.98	16.04	15.93	15.96	15.95
2.00	0.60	2.20	16.23	10.92	15.28	15.29	15.29	15.72	15.67	15.72	15.79	15.74	15.81
2.50	0.20	1.40	24.62	24.61	24.62	24.38	24.63	24.56	24.63	24.61	24.51	24.52	24.61
2.50	0.20	1.80	24.62	24.47	24.41	24.41	24.58	24.40	24.41	24.58	24.61	24.57	24.58
2.50	0.20	2.20	24.62	24.48	24.41	24.41	24.58	24.40	24.41	24.58	24.61	24.57	24.58
2.50	0.40	1.40	24.62	24.49	24.38	24.56	24.49	24.59	24.56	24.54	24.59	24.59	24.56
2.50	0.40	1.80	24.62	24.38	24.55	24.53	24.54	24.54	24.54	24.54	24.56	24.56	24.55
2.50	0.40	2.20	24.62	24.07	24.45	24.48	24.48	24.50	24.51	24.39	24.51	24.41	24.45
2.50	0.60	1.40	24.62	23.81	24.46	24.41	24.46	24.44	24.48	24.39	24.54	24.36	24.43
2.50	0.60	1.80	24.62	20.61	24.17	24.02	24.20	24.11	24.33	24.33	24.38	24.40	24.37
2.50	0.60	2.20	24.62	16.36	23.02	23.01	23.02	23.65	23.78	23.73	23.91	23.96	23.79

(b) Bearing length of 75 mm

Thickness	Elongated web holes		Web crippling strengths per web predicted from FEA, P_{FEA} (kN)										
					With edge-stiffened holes								
					Q0.02			Q0.04			Q0.06		
t (mm)	d_w/d_1	b_w/d_w	Plain web	With un-stiffened hole	r_q=2 (mm)	r_q=3 (mm)	r_q=4 (mm)	r_q=2 (mm)	r_q=3 (mm)	r_q=4 (mm)	r_q=2 (mm)	r_q=3 (mm)	r_q=4 (mm)
1.50	0.20	1.40	10.66	10.59	10.66	10.66	10.65	10.66	10.66	10.66	10.66	10.67	10.67
1.50	0.20	1.80	10.66	10.54	10.59	10.60	10.60	10.60	10.60	10.59	10.60	10.60	10.62
1.50	0.20	2.20	10.66	10.46	10.56	10.55	10.56	10.57	10.58	10.58	10.58	10.59	10.59
1.50	0.40	1.40	10.66	10.13	10.60	10.61	10.61	10.61	10.61	10.64	10.64	10.63	10.65
1.50	0.40	1.80	10.66	9.74	10.51	10.51	10.52	10.54	10.55	10.55	10.57	10.58	10.58
1.50	0.40	2.20	10.66	9.25	10.32	10.34	10.33	10.42	10.43	10.43	10.46	10.47	10.47
1.50	0.60	1.40	10.66	8.94	10.56	10.56	10.57	10.61	10.60	10.62	10.63	10.64	10.65
1.50	0.60	1.80	10.66	8.94	10.21	10.21	10.23	10.37	10.37	10.38	10.42	10.42	10.40
1.50	0.60	2.20	10.66	6.47	9.39	9.41	9.44	9.88	9.87	9.87	10.00	9.99	10.02
2.00	0.20	1.40	18.72	18.60	18.70	18.71	18.71	18.71	18.72	18.72	18.71	18.71	18.73
2.00	0.20	1.80	18.72	18.52	18.64	18.64	18.63	18.66	18.66	18.66	18.67	18.67	18.67
2.00	0.20	2.20	18.72	18.43	18.54	18.55	18.61	18.63	18.63	18.59	18.64	18.64	18.64
2.00	0.40	1.40	18.72	17.93	18.61	18.62	18.59	18.65	18.63	18.62	18.67	18.67	18.67
2.00	0.40	1.80	18.72	17.23	18.45	18.47	18.47	18.52	18.52	18.51	18.55	18.54	18.56
2.00	0.40	2.20	18.72	16.22	18.18	18.20	18.20	18.32	18.32	18.32	18.37	18.37	18.38
2.00	0.60	1.40	18.72	15.60	18.35	18.34	18.34	18.44	18.44	18.44	18.47	18.45	18.46
2.00	0.60	1.80	18.72	15.60	17.67	17.68	17.70	17.99	17.98	17.94	18.05	18.06	18.02
2.00	0.60	2.20	18.72	10.65	16.13	16.13	16.15	16.93	16.93	16.93	17.22	17.22	17.14
2.50	0.20	1.40	28.42	28.18	28.37	28.30	28.30	28.39	28.39	28.25	28.26	28.26	28.39
2.50	0.20	1.80	28.42	28.22	28.26	28.24	28.24	28.15	28.15	28.15	28.27	28.31	28.27
2.50	0.20	2.20	28.42	28.15	28.18	28.19	28.24	28.22	28.21	28.21	28.25	28.23	28.23
2.50	0.4	1.40	28.42	27.58	28.12	28.12	28.11	28.22	28.15	28.10	28.16	28.16	28.22
2.50	0.4	1.80	28.42	26.59	27.93	27.92	27.89	28.01	28.01	28.00	28.03	28.03	28.02
2.50	0.4	2.20	28.42	25.28	27.63	27.61	27.60	27.74	27.63	27.73	27.73	27.79	27.78
2.50	0.6	1.4	28.42	24.41	27.49	27.56	27.56	27.63	27.69	27.68	27.74	27.75	27.74
2.50	0.6	1.80	28.42	24.41	26.30	26.39	26.34	26.67	26.82	26.81	27.01	27.02	26.95
2.50	0.6	2.20	28.42	16.21	23.81	23.79	23.76	25.06	24.94	24.97	25.55	25.49	25.42

(c) Bearing length of 100 mm

Thickness	Elongated web holes		Web crippling strengths per web predicted from FEA, P_{FEA} (kN)										
					With edge-stiffened holes								
					Q0.02			Q0.04			Q0.06		
t (mm)	d_w/d_1	b_w/d_w	Plain web	With un-stiffened hole	r_q=2 (mm)	r_q=3 (mm)	r_q=4 (mm)	r_q=2 (mm)	r_q=3 (mm)	r_q=4 (mm)	r_q=2 (mm)	r_q=3 (mm)	r_q=4 (mm)
1.50	0.20	1.40	11.64	11.52	11.34	11.35	11.36	11.36	11.37	11.38	11.38	11.38	11.39
1.50	0.20	1.80	11.64	11.46	11.21	11.21	11.20	11.21	11.22	11.24	11.24	11.23	11.23
1.50	0.20	2.20	11.64	11.35	11.15	11.17	11.18	11.19	11.20	11.21	11.21	11.22	11.22
1.50	0.40	1.40	11.64	10.85	11.26	11.27	11.28	11.31	11.32	11.33	11.33	11.34	11.35
1.50	0.40	1.80	11.64	10.33	11.05	11.07	11.08	11.16	11.16	11.18	11.21	11.22	11.23
1.50	0.40	2.20	11.64	9.74	10.69	10.72	10.75	10.91	10.94	10.94	11.01	11.00	11.04
1.50	0.60	1.40	11.64	9.28	11.23	11.25	11.26	11.33	11.34	11.35	11.38	11.38	11.40
1.50	0.60	1.80	11.64	7.99	10.54	10.59	10.63	10.91	10.93	10.95	11.01	11.03	11.03
1.50	0.60	2.20	11.64	6.69	9.40	9.45	9.49	10.07	10.10	10.12	10.31	10.32	10.34
2.00	0.20	1.40	20.52	20.31	19.99	19.99	20.02	20.02	20.01	20.03	20.02	20.03	20.04
2.00	0.20	1.80	20.52	20.18	19.83	19.83	19.84	19.83	19.86	19.87	19.87	19.90	19.90
2.00	0.20	2.20	20.52	19.91	19.77	19.77	19.78	19.79	19.77	19.82	19.83	19.83	19.86
2.00	0.40	1.40	20.52	19.16	19.86	19.85	19.86	19.91	19.93	19.91	19.96	19.96	19.97
2.00	0.40	1.80	20.52	18.24	19.54	19.59	19.57	19.70	19.70	19.75	19.79	19.80	19.80
2.00	0.40	2.20	20.52	16.95	19.10	19.13	19.15	19.40	19.37	19.37	19.50	19.51	19.52
2.00	0.60	1.40	20.52	16.17	19.49	19.54	19.55	19.65	19.66	19.61	19.78	19.78	19.79
2.00	0.60	1.80	20.52	13.59	18.44	18.42	18.43	18.95	18.92	18.96	19.15	19.14	19.08
2.00	0.60	2.20	20.52	11.16	16.34	16.39	16.39	17.43	17.42	17.42	17.82	17.82	17.81
2.50	0.20	1.40	31.33	30.84	30.37	30.37	30.37	30.39	30.39	30.39	30.41	30.41	30.41
2.50	0.20	1.80	31.33	30.73	30.38	30.39	30.39	30.39	30.43	30.43	30.23	30.20	30.42
2.50	0.20	2.20	31.33	30.77	30.24	30.23	30.24	30.37	30.37	30.37	30.39	30.39	30.42
2.50	0.40	1.40	31.33	29.82	30.21	30.25	30.25	30.16	30.16	30.33	30.08	30.11	30.11
2.50	0.40	1.80	31.33	28.34	29.74	29.76	29.77	29.86	29.87	29.89	29.93	29.93	29.93
2.50	0.40	2.20	31.33	26.47	29.18	29.08	29.08	29.56	29.54	29.59	29.69	29.74	29.65
2.50	0.60	1.40	31.33	25.46	29.39	29.21	29.36	29.64	29.54	29.65	29.54	29.81	29.79
2.50	0.60	1.80	31.33	21.14	27.33	27.36	27.44	28.11	28.22	28.23	28.40	28.50	28.45
2.50	0.60	2.20	31.33	17.05	24.18	24.21	24.15	25.83	25.82	25.67	26.53	26.50	26.40

Appendix E

Web crippling strengths per web predicted from FEA under the EOF loading condition

(a) Bearing length of 50 mm

Thickness	Elongated web holes		Web crippling strengths per web predicted from FEA, P_{FEA} (kN)										
			Plain web	With un-stiffened hole	With edge-stiffened holes								
					Q0.02			Q0.04			Q0.06		
t (mm)	d_w/d_1	b_w/d_w			r_q=2mm	r_q=3mm	r_q=4mm	r_q=2mm	r_q=3mm	r_q=4mm	r_q=2mm	r_q=3mm	r_q=4mm
1.50	0.20	1.40	3.79	3.12	3.78	3.78	3.78	3.79	3.79	3.79	3.80	3.79	3.79
1.50	0.20	1.80	3.79	3.11	3.78	3.78	3.78	3.79	3.79	3.79	3.79	3.79	3.79
1.50	0.20	2.20	3.79	3.08	3.49	3.49	3.49	3.50	3.49	3.49	3.51	3.51	3.50
1.50	0.40	1.40	3.79	2.95	3.41	3.41	3.41	3.43	3.43	3.43	3.45	3.44	3.44
1.50	0.40	1.80	3.79	2.84	3.37	3.36	3.36	3.40	3.40	3.39	3.42	3.41	3.41
1.50	0.40	2.20	3.79	2.71	3.31	3.31	3.30	3.35	3.35	3.34	3.38	3.37	3.37
1.50	0.60	1.40	3.79	2.64	3.21	3.21	3.21	3.26	3.25	3.24	3.28	3.28	3.27
1.50	0.60	1.80	3.79	2.41	3.06	3.06	3.05	3.12	3.11	3.11	3.16	3.15	3.15
1.50	0.60	2.20	3.79	2.14	2.84	2.84	2.83	2.93	2.92	2.92	2.98	2.97	2.96
2.00	0.20	1.40	5.98	4.84	5.96	5.95	5.96	5.96	5.97	5.95	5.98	5.96	5.97
2.00	0.20	1.80	5.98	4.81	5.95	5.94	5.93	5.95	5.96	5.96	5.97	5.96	5.97
2.00	0.20	2.20	5.98	4.76	5.60	5.61	5.61	5.63	5.62	5.63	5.63	5.64	5.64
2.00	0.40	1.40	5.98	4.57	5.49	5.48	5.48	5.52	5.51	5.51	5.53	5.53	5.53
2.00	0.40	1.80	5.98	4.39	5.40	5.40	5.40	5.45	5.43	5.43	5.47	5.47	5.47
2.00	0.40	2.20	5.98	4.17	5.27	5.28	5.27	5.35	5.34	5.33	5.39	5.38	5.37
2.00	0.60	1.40	5.98	4.08	5.12	5.12	5.10	5.20	5.19	5.18	5.25	5.24	5.23
2.00	0.60	1.80	5.98	3.68	4.78	4.78	4.77	4.92	4.91	4.89	4.99	4.99	4.97
2.00	0.60	2.20	5.98	3.21	4.35	4.35	4.35	4.54	4.52	4.51	4.64	4.62	4.62
2.50	0.20	1.40	8.76	7.04	8.70	8.70	8.69	8.71	8.69	8.70	8.73	8.72	8.71
2.50	0.20	1.80	8.76	6.99	8.66	8.68	8.65	8.69	8.66	8.68	8.72	8.69	8.70
2.50	0.20	2.20	8.76	6.94	8.33	8.33	8.32	8.35	8.35	8.36	8.38	8.34	8.37
2.50	0.40	1.40	8.76	6.65	8.14	8.15	8.15	8.20	8.19	8.16	8.22	8.23	8.19
2.50	0.40	1.80	8.76	6.36	7.99	7.99	8.00	8.07	8.07	8.05	8.10	8.11	8.10
2.50	0.40	2.20	8.76	6.03	7.79	7.80	7.80	7.91	7.91	7.89	7.99	7.97	7.94
2.50	0.60	1.40	8.76	5.90	7.53	7.54	7.54	7.70	7.68	7.65	7.77	7.76	7.75
2.50	0.60	1.80	8.76	5.24	6.91	6.93	6.91	7.19	7.17	7.13	7.31	7.30	7.29
2.50	0.60	2.20	8.76	4.47	6.17	6.17	6.14	6.50	6.47	6.46	6.66	6.65	6.62

(b) Bearing length of 75 mm

Thickness t (mm)	Elongated web holes		Web crippling strengths per web predicted from FEA, P_{FEA} (kN)									
			Plain web	With un-stiffened hole	With edge-stiffened holes							
					Q0.02			Q0.04			Q0.06		
	d_w/d_1	b_w/d_w			r_q=2 (mm)	r_q=3 (mm)	r_q=4 (mm)	r_q=2 (mm)	r_q=3 (mm)	r_q=4 (mm)	r_q=2 (mm)	r_q=3 (mm)	r_q=4 (mm)
1.50	0.20	1.40	4.05	3.29	4.30	4.30	4.30	4.30	4.30	4.30	4.31	4.31	4.31
1.50	0.20	1.80	4.05	3.27	4.29	4.30	4.29	4.30	4.30	4.30	4.31	4.30	4.31
1.50	0.20	2.20	4.05	3.25	4.28	4.29	4.29	4.30	4.30	4.29	4.31	4.31	4.30
1.50	0.40	1.40	4.05	3.12	4.19	4.19	4.19	4.22	4.22	4.22	4.23	4.24	4.23
1.50	0.40	1.80	4.05	3.00	4.14	4.14	4.13	4.17	4.17	4.16	4.20	4.19	4.19
1.50	0.40	2.20	4.05	2.88	4.06	4.07	4.05	4.11	4.11	4.10	4.14	4.13	4.14
1.50	0.60	1.40	4.05	2.81	3.93	3.94	3.93	3.99	3.98	3.98	4.03	4.02	4.01
1.50	0.60	1.80	4.05	2.58	3.73	3.73	3.73	3.82	3.81	3.80	3.87	3.86	3.85
1.50	0.60	2.20	4.05	2.34	3.45	3.45	3.46	3.58	3.57	3.56	3.64	3.63	3.62
2.00	0.20	1.40	6.38	5.13	6.78	6.77	6.75	6.78	6.77	6.77	6.78	6.79	6.76
2.00	0.20	1.80	6.38	5.09	6.76	6.75	6.75	6.77	6.76	6.76	6.78	6.77	6.75
2.00	0.20	2.20	6.38	5.05	6.71	6.71	6.74	6.76	6.76	6.76	6.77	6.77	6.75
2.00	0.40	1.40	6.38	4.86	6.59	6.61	6.61	6.65	6.63	6.64	6.66	6.66	6.65
2.00	0.40	1.80	6.38	4.69	6.52	6.51	6.52	6.57	6.57	6.55	6.59	6.60	6.59
2.00	0.40	2.20	6.38	4.49	6.40	6.39	6.39	6.47	6.46	6.46	6.52	6.51	6.50
2.00	0.60	1.40	6.38	4.40	6.19	6.19	6.18	6.29	6.27	6.27	6.33	6.34	6.32
2.00	0.60	1.80	6.38	4.01	5.75	5.75	5.75	5.93	5.92	5.90	6.02	6.00	5.99
2.00	0.60	2.20	6.38	3.57	5.21	5.21	5.21	5.46	5.44	5.41	5.57	5.56	5.54
2.50	0.20	1.40	9.39	7.45	10.01	10.00	10.00	10.01	10.01	10.01	10.05	10.03	10.02
2.50	0.20	1.80	9.39	7.40	9.98	9.97	9.98	9.99	9.99	10.00	10.00	10.01	9.99
2.50	0.20	2.20	9.39	7.36	9.95	9.96	9.96	9.97	9.98	9.95	10.00	10.00	9.99
2.50	0.40	1.40	9.39	7.08	9.73	9.73	9.73	9.80	9.79	9.77	9.83	9.81	9.82
2.50	0.40	1.80	9.39	6.82	9.56	9.55	9.55	9.63	9.63	9.63	9.67	9.70	9.66
2.50	0.40	2.20	9.39	6.51	9.31	9.30	9.32	9.45	9.45	9.45	9.53	9.54	9.53
2.50	0.60	1.40	9.39	6.39	8.97	8.95	8.97	9.16	9.15	9.14	9.26	9.23	9.23
2.50	0.60	1.80	9.39	5.75	8.20	8.20	8.21	8.49	8.48	8.45	8.67	8.63	8.62
2.50	0.60	2.20	9.39	5.03	7.29	7.28	7.27	7.65	7.62	7.59	7.87	7.84	7.80

(c) Bearing length of 100 mm

Thickness t (mm)	Elongated web holes		Web crippling strengths per web predicted from FEA, P_{FEA} (kN)										
					With edge-stiffened holes								
					Q0.02			Q0.04			Q0.06		
	d_w/d_1	b_w/d_w	Plain web	With un-stiffened hole	r_q=2 (mm)	r_q=3 (mm)	r_q=4 (mm)	r_q=2 (mm)	r_q=3 (mm)	r_q=4 (mm)	r_q=2 (mm)	r_q=3 (mm)	r_q=4 (mm)
1.50	0.20	1.4	4.28	3.44	4.53	4.53	4.53	4.54	4.54	4.54	4.54	4.54	4.55
1.50	0.20	1.80	4.28	3.43	4.52	4.53	4.53	4.53	4.53	4.54	4.54	4.54	4.54
1.50	0.20	2.20	4.28	3.40	4.50	4.50	4.50	4.53	4.53	4.53	4.54	4.54	4.54
1.50	0.40	1.40	4.28	3.28	4.43	4.43	4.43	4.46	4.45	4.45	4.47	4.46	4.45
1.50	0.40	1.80	4.28	3.16	4.37	4.37	4.37	4.41	4.39	4.38	4.43	4.43	4.42
1.50	0.40	2.20	4.28	3.04	4.30	4.29	4.29	4.34	4.34	4.34	4.38	4.37	4.36
1.50	0.60	1.40	4.28	2.98	4.17	4.17	4.17	4.23	4.22	4.22	4.26	4.25	4.25
1.50	0.60	1.80	4.28	2.74	3.94	3.94	3.95	4.04	4.03	4.02	4.08	4.08	4.08
1.50	0.60	2.20	4.28	2.56	3.66	3.66	3.67	3.80	3.79	3.77	3.86	3.85	3.85
2.00	0.20	1.40	6.74	5.38	7.13	7.13	7.12	7.14	7.14	7.14	7.14	7.14	7.15
2.00	0.20	1.80	6.74	5.35	7.12	7.10	7.12	7.14	7.13	7.12	7.14	7.15	7.14
2.00	0.20	2.20	6.74	5.30	7.10	7.10	7.10	7.12	7.13	7.11	7.13	7.13	7.14
2.00	0.40	1.40	6.74	5.14	6.97	6.97	6.96	6.99	7.00	6.97	7.03	7.02	7.01
2.00	0.40	1.80	6.74	4.97	6.86	6.86	6.87	6.92	6.90	6.89	6.94	6.96	6.92
2.00	0.40	2.20	6.74	4.77	6.75	6.73	6.75	6.83	6.82	6.81	6.87	6.86	6.86
2.00	0.60	1.40	6.74	4.69	6.53	6.54	6.54	6.65	6.63	6.62	6.69	6.68	6.66
2.00	0.60	1.80	6.74	4.30	6.09	6.09	6.09	6.28	6.27	6.24	6.37	6.36	6.34
2.00	0.60	2.20	6.74	3.86	5.53	5.53	5.53	5.77	5.75	5.74	5.90	5.88	5.86
2.50	0.20	1.40	9.95	7.81	10.59	10.60	10.58	10.62	10.61	10.57	10.63	10.63	10.63
2.50	0.20	1.80	9.95	7.79	10.58	10.54	10.54	10.58	10.57	10.60	10.59	10.60	10.58
2.50	0.20	2.20	9.95	7.73	10.55	10.52	10.56	10.58	10.56	10.57	10.59	10.59	10.59
2.50	0.40	1.40	9.95	7.48	10.31	10.33	10.31	10.36	10.34	10.37	10.42	10.42	10.37
2.50	0.40	1.80	9.95	7.22	10.14	10.15	10.09	10.23	10.19	10.20	10.30	10.29	10.28
2.50	0.40	2.20	9.95	6.90	9.89	9.87	9.86	10.02	10.02	10.00	10.12	10.10	10.08
2.50	0.60	1.40	9.95	6.81	9.48	9.48	9.50	9.71	9.67	9.66	9.81	9.79	9.76
2.50	0.60	1.80	9.95	6.15	8.67	8.67	8.65	8.97	8.93	8.89	9.12	9.11	9.07
2.50	0.60	2.20	9.95	5.43	7.72	7.70	7.68	8.04	8.00	7.98	8.27	8.23	8.19

Appendix F

Detials of elastic critical buckling analyses for one-flange loading condition

d_w	b_w	r_i	N	q	r_q	Thickness of 1.50 mm				Thickness of 2.00 mm				Thickness of 2.50 mm			
						IOF		EOF		IOF		EOF		IOF		EOF	
						$P_{b,cr}$	k_{FEA}/k_{prop}	$P_{b,cr}$	k_{FEA}/k_{prop}	$P_{b,cr}$	k_{FEA}/k_{prop}	$P_{b,cr}$	k_{FEA}/k_{prop}	$P_{b,cr}$	k_{FEA}/k_{prop}	$P_{b,cr}$	k_{FEA}/k_{prop}
(a) Un-stiffened																	
46.80	65.52	3.0	75	-	-	9.05	0.89	3.47	0.92	20.63	0.94	8.19	0.95	39.22	0.99	15.90	0.98
46.80	84.24	3.0	75	-	-	8.95	0.94	3.45	0.96	20.40	0.99	8.13	0.98	38.78	1.03	15.79	1.00
46.80	102.96	3.0	75	-	-	8.82	0.99	3.42	1.00	20.10	1.02	8.06	1.01	38.21	1.06	15.67	1.03
93.60	131.04	3.0	75	-	-	8.31	0.97	3.31	0.97	18.95	0.99	7.82	0.98	36.05	1.01	15.20	1.00
93.60	168.48	3.0	75	-	-	7.73	1.02	3.19	1.01	17.62	1.01	7.54	1.01	33.51	1.02	14.67	1.02
93.60	205.92	3.0	75	-	-	7.03	1.06	3.04	1.04	16.00	1.01	7.20	1.02	30.38	1.00	14.01	1.02
140.40	196.56	3.0	75	-	-	6.98	0.98	3.02	0.98	15.88	0.94	7.14	0.96	30.16	0.94	13.91	0.97
140.40	252.72	3.0	75	-	-	5.82	0.99	2.75	1.00	13.15	0.90	6.50	0.96	24.86	0.87	12.59	0.94
140.40	308.88	3.0	75	-	-	4.62	0.98	2.38	0.97	10.36	0.82	5.53	0.89	19.48	0.76	10.64	0.86
93.60	168.48	3.0	30	-	-	7.13	1.03	2.45	1.05	16.17	1.00	5.79	1.03	30.67	1.00	11.27	1.03
93.60	168.48	3.0	40	-	-	7.25	1.02	2.60	1.02	16.47	1.00	6.15	1.00	31.25	1.00	11.98	1.01
93.60	168.48	3.0	50	-	-	7.38	1.02	2.76	1.01	16.78	1.00	6.53	0.99	31.87	1.00	12.72	1.00
93.60	168.48	3.0	60	-	-	7.52	1.02	2.93	1.01	17.12	1.01	6.93	0.99	32.52	1.01	13.48	1.00
93.60	168.48	3.0	70	-	-	7.67	1.02	3.10	1.01	17.47	1.01	7.33	1.00	33.21	1.02	14.27	1.01
93.60	168.48	3.0	80	-	-	7.82	1.03	3.28	1.02	17.83	1.02	7.75	1.01	33.92	1.03	15.08	1.02
93.60	168.48	3.0	90	-	-	7.98	1.04	3.46	1.03	18.21	1.03	8.17	1.02	34.66	1.04	15.90	1.04
93.60	168.48	3.0	100	-	-	8.15	1.04	3.64	1.04	18.61	1.04	8.60	1.04	35.42	1.05	16.73	1.05
93.60	168.48	2.0	75	-	-	7.73	1.03	3.19	1.02	17.62	1.02	7.53	1.01	33.52	1.03	14.65	1.02
93.60	168.48	2.5	75	-	-	7.73	1.03	3.19	1.02	17.62	1.02	7.54	1.01	33.51	1.02	14.66	1.02
93.60	168.48	3.5	75	-	-	7.73	1.02	3.19	1.01	17.62	1.01	7.55	1.00	33.50	1.02	14.68	1.01
93.60	168.48	4.0	75	-	-	7.74	1.02	3.19	1.01	17.62	1.01	7.55	1.00	33.49	1.01	14.69	1.01
93.60	168.48	4.5	75	-	-	7.75	1.01	3.19	1.01	17.62	1.00	7.55	1.00	33.48	1.01	14.70	1.01
93.60	168.48	5	75	-	-	7.76	1.01	3.20	1.01	17.63	1.00	7.56	1.00	33.48	1.01	14.71	1.01
(b) Edge-stiffened																	
46.80	65.52	3.0	75	14.04	3	9.25	1.02	3.52	0.97	21.10	1.02	8.29	0.97	40.11	1.02	16.08	0.99
46.80	84.24	3.0	75	14.04	3	9.23	1.02	3.51	0.98	21.05	1.02	8.27	0.99	40.01	1.02	16.04	1.00
46.80	102.96	3.0	75	14.04	3	9.19	1.01	3.50	1.00	20.97	1.01	8.24	1.00	39.85	1.01	15.99	1.01
93.60	131.04	3.0	75	14.04	3	9.27	1.00	3.50	0.98	21.15	1.00	8.24	0.99	40.18	1.00	15.97	0.99
93.60	168.48	3.0	75	14.04	3	9.19	0.99	3.45	1.00	20.97	0.99	8.12	1.00	39.81	0.99	15.74	1.00

93.60	205.92	3.0	75	14.04	3	9.11	0.97	3.39	1.01	20.74	0.98	7.97	1.00	39.31	0.98	15.43	1.00
140.40	196.56	3.0	75	14.04	3	9.52	1.01	3.46	0.99	21.70	1.01	8.13	0.99	41.12	1.01	15.70	0.99
140.40	252.72	3.0	75	14.04	3	9.69	1.02	3.33	1.00	21.99	1.02	7.82	0.99	41.43	1.01	15.10	0.98
140.40	308.88	3.0	75	14.04	3	10.0	1.05	3.15	0.98	22.47	1.04	7.40	0.96	41.78	1.02	14.27	0.95
93.60	168.48	3.0	30	14.04	3	8.72	1.02	2.72	1.05	19.86	1.01	6.40	1.03	37.66	1.01	12.39	1.02
93.60	168.48	3.0	40	14.04	3	8.78	1.00	2.87	1.01	20.02	1.00	6.75	1.00	37.97	0.99	13.07	1.00
93.60	168.48	3.0	50	14.04	3	8.87	0.99	3.03	1.00	20.24	0.99	7.12	0.99	38.40	0.99	13.79	0.99
93.60	168.48	3.0	60	14.04	3	8.99	0.99	3.19	0.99	20.51	0.99	7.51	0.99	38.93	0.99	14.55	0.99
93.60	168.48	3.0	70	14.04	3	8.99	0.97	3.37	1.00	20.51	0.97	7.92	1.00	38.93	0.98	15.34	1.00
93.60	168.48	3.0	80	14.04	3	9.29	0.99	3.54	1.00	21.20	0.99	8.33	1.00	40.24	1.00	16.15	1.01
93.60	168.48	3.0	90	14.04	3	9.47	1.00	3.72	1.01	21.60	1.00	8.76	1.02	41.01	1.00	16.97	1.02
93.60	168.48	3.0	100	14.04	3	9.66	1.00	3.91	1.03	22.04	1.01	9.20	1.03	41.86	1.01	17.81	1.04
93.60	168.48	2.0	75	14.04	3	9.19	0.98	3.45	1.00	20.98	0.98	8.11	1.00	39.85	0.99	15.71	1.00
93.60	168.48	2.5	75	14.04	3	9.19	0.98	3.45	1.00	20.97	0.99	8.12	1.00	39.83	0.99	15.73	1.00
93.60	168.48	3.5	75	14.04	3	9.20	0.99	3.45	1.00	20.97	0.99	8.13	1.00	39.79	0.99	15.75	1.00
93.60	168.48	4.0	75	14.04	3	9.21	1.00	3.46	1.00	20.98	1.00	8.13	1.00	39.79	1.00	15.76	1.00
93.60	168.48	4.5	75	14.04	3	9.23	1.00	3.46	1.00	20.99	1.00	8.14	1.00	39.80	1.00	15.77	1.00
93.60	168.48	5.0	75	14.04	3	9.26	1.01	3.46	1.00	21.02	1.00	8.14	1.00	39.81	1.00	15.78	1.00
93.60	168.48	3.0	75	9.36	3	9.07	1.00	3.43	1.00	20.62	1.00	8.05	1.00	39.01	0.99	15.58	1.00
93.60	168.48	3.0	75	11.70	3	9.14	1.00	3.44	1.00	20.82	1.00	8.09	1.00	39.49	1.00	15.67	1.00
93.60	168.48	3.0	75	16.38	3	9.24	1.00	3.46	1.00	21.10	1.00	8.15	1.00	40.07	1.00	15.80	1.00
93.60	168.48	3.0	75	18.72	3	9.29	1.00	3.48	1.00	21.22	1.00	8.18	1.00	40.31	1.00	15.85	1.00
93.60	168.48	3.0	75	21.06	3	9.34	1.00	3.49	1.00	21.33	1.00	8.20	1.00	40.55	1.00	15.90	1.00
93.60	168.48	3.0	75	23.40	3	9.39	1.00	3.50	1.00	21.44	1.00	8.23	1.00	40.77	1.00	15.95	1.00
93.60	168.48	3.0	75	14.04	2	9.18	1.00	3.45	1.00	20.95	1.00	8.12	1.00	39.78	1.00	15.74	1.00
93.60	168.48	3.0	75	14.04	2.5	9.19	1.00	3.45	1.00	20.96	1.00	8.12	1.00	39.79	1.00	15.74	1.00
93.60	168.48	3.0	75	14.04	3.5	9.20	1.00	3.45	1.00	20.98	1.00	8.12	1.00	39.83	1.00	15.74	1.00
93.60	168.48	3.0	75	14.04	4	9.20	1.00	3.45	1.00	20.99	1.00	8.12	1.00	39.85	1.00	15.74	1.00
93.60	168.48	3.0	75	14.04	4.5	9.21	1.00	3.45	1.00	21.01	1.00	8.12	1.00	39.88	1.00	15.74	1.00
93.60	168.48	3.0	75	14.04	5	9.22	1.00	3.45	1.00	21.02	1.00	8.13	1.00	39.91	1.00	15.74	1.00